NASA Contractor Report 3538

Tone-Excited Jet

Theory and Experiments

K. K. Ahuja, J. Lepicovsky, C. K. W. Tam,
P. J. Morris, and R. H. Burrin

CONTRACT NAS3-21987
NOVEMBER 1982

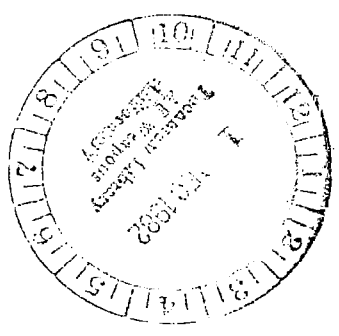

NASA

NASA Contractor Report 3538

Tone-Excited Jet
Theory and Experiments

K. K. Ahuja and J. Lepicovsky
Lockheed-Georgia Company
Marietta, Georgia

C. K. W. Tam
The Florida State University
Tallahassee, Florida

P. J. Morris
Pennsylvania State University
University Park, Pennsylvania

R. H. Burrin
Lockheed-Georgia Company
Marietta, Georgia

Prepared for
Lewis Research Center
under Contract NAS3-21987

NASA
National Aeronautics
and Space Administration

Scientific and Technical
Information Branch

1982

CONTENTS

CONTENTS (Cont'd)

CONTENTS (Cont'd)

SUMMARY

The major objective of this investigation is to obtain an understanding of the mechanism of broadband jet-noise augmentation due to upstream excitation. This understanding is desired in terms of the relationship between the excitation characteristics, the changes in the large-scale and/or small-scale turbulence structure of the jet, and the sound radiated to the far field under both static and simulated forward-velocity conditions.

To achieve this objective, a systematic set of acoustic measurements have been made for a range of flow conditions in the acoustic research facilities of the Lockheed-Georgia Company.

Following the analyses of the acoustic results, turbulence measurements have been made using Lockheed's laser velocimeter for those jet conditions at which jet noise-amplification is found to be important.

To increase our understanding further, a few optical pictures (schlieren) of the excited jets are also obtained. Flow visualization of of the large-scale turbulence structure has been made by the method of ensemble-averaging.

A theory to explain the results obtained in this investigation is also developed both for the static as well as the flight simulation conditions.

Results for a 5.08-cm diameter nozzle are presented for both unheated and heated jets for a range of excitation frequencies and levels, and for two mode orders-- the zero order and the first order spinning mode. Results of measurements of the large-scale instability waves within the excited jet are also described. Changes in the radiated noise and the flow structure and their inter-relationship are then discussed.

Broadband jet-noise amplifications of up to 5 dB have been observed in the present study. These amplification levels could have been much higher if the excitation levels were higher than those used here.

After all the experimental results and the theoretical models are put together, the jet-noise amplification can be fairly well described by the schematic representation shown below.

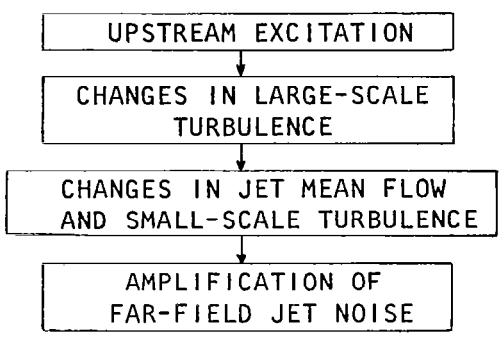

The salient conclusions derived primarily from the results for the unheated jets can be listed as follows:

1. Excited large-scale structure indeed exists (within extremely narrow band of frequency), and its center frequency is equal to that of the excitation signal itself.

2. The preferential Strouhal number at which maximum broadband jet-noise amplification is obtained (at a fixed excitation level) lies between 0.4 and 0.8, depending upon whether one is considering 1/3-octave band SPLs and PWLs or the OASPLs and OAPWLs, or for that matter the angle of noise measurements. $S_e = 0.5$ can be considered to be a reasonable mean Strouhal number for maximum amplification.

3. With increasing excitation levels: (a) the mean velocities decay faster, (b) turbulence intensities increase, and (c) broadband jet-noise amplifications increase.

4. Threshold levels for jet-noise amplification can be taken to be 0.08% of the jet dynamic head, but only for the unheated jets.

5. For a fixed excitation level, jet noise amplification decreases as the jet Mach number increases.

6. Limited data acquired for the heated jets showed little effect of upstream excitation on broadband jet noise.

7. Excited large-scale structure amplitudes are not affected by flight velocity.

8. Broadband jet-noise amplification is obtained for the flight condition also, and its magnitude is equal to that obtained for the stationary jets.

9. For jets under forward motion, the relative velocity effects are the same for both the unexcited and the excited jets.

10. It is the small-scale turbulence, and not the large-scale turbulence that generates the additional broadband noise upon excitation by upstream discrete tones.

1.0 INTRODUCTION

Since the introduction of jet engines for aircraft propulsion some 30 years ago, the noise generated by a jet exhaust has been studied in great detail, both theoretically and experimentally. The majority of the fundamental experimental research studies during this period have been conducted by using model-scale nozzles, and, in fact, prediction methods for jet noise have also been derived using the results generated from these model-scale experiments. As a result of the advances made in recent years, it has now become possible to predict the noise field of model-scale jets, both stationary and in forward motion, and indeed the theory to substantiate and explain these predictions is now available.

The fundamental understanding of jet-noise generating processes and prediction methods obtained from model-scale controlled experiments can in principle be applied to full-scale engines, simply by using the universally accepted scaling procedures. In many cases, this transformation from the model-scale idealized situation to the full-scale real situation is found to be quite satisfactory. However, in recent years, two types of anomalies have emerged, one for the static case, and the other for jets in forward motion. These anomalies are as follows:

For the static case, it was first observed that the measured noise levels from full-scale engines were higher than the noise levels projected from model-scale jets; the difference between the two varying from one engine configuration to another (e.g., see refs. 1 and 2). In many cases, this difference can be largely explained (especially at low jet efflux velocities) by accounting for the contributions to the total noise levels made by engine internal noise sources, which are of course, not significant in a well-designed jet rig used in the model-scale laboratory experiments. However, for some engines, even the best estimates of the internal noise levels are not large enough to explain these differences completely, and a small but consistent discrepancy remains to be resolved.

Turning now to the flight case, it has been observed that, while the model-scale flight simulation experiments provide a reduction in jet noise with forward velocity at all angles and frequencies, some full-scale aircraft flight tests show a distinctly different behavior, with little or no change in noise levels at 90° to the jet axis, and some increase in noise levels in the forward quadrant (ref. 3). Here also, the observed discrepancies in some cases can be explained by taking proper account of the contributions made by engine internal noise sources in conjunction with the pure jet-noise contribution. In addition, within the last five years, other effects have also been postulated to reconcile the observed differences. These include the engine installation effects (both acoustic and aerodynamic) and the airframe noise, all of which are not present in controlled model-scale flight simulation experiments. Although many full-scale flight results can be adequately explained by one or more of these effects, the gap between the remaining full-scale flight results

available at the present time and the model-scale flight simulation results is still large, and needs to be resolved urgently.

The two anomalies discussed above then raise the question as to what else can possibly lead to such differences in the noise features between model-scale jets and certain full-scale engines. One possible answer to this question is the effect of upstream excitation on jet-noise amplification, which is the subject of the present study.

It has been recognized for some time that the structure of a jet is sensitive to upstream excitation. In a jet engine, there are many possible sources of excitation. These include the large thermal, acoustic,and turbulent fluctuations produced by flow separation or eddy shedding from exhaust struts or centerbodies. In model-scale jet-noise experiments, on the other hand, the rig is normally designed with great care to avoid these complications, and therefore,the measurements are essentially free of any upstream excitation effects. The importance of the role played by upstream excitation in jet noise, and the associated background are discussed further in the following subsection.

1.1 ROLE PLAYED BY UPSTREAM EXCITATION IN JET NOISE

In recent years, several studies have been initiated both in the U. S. and in Europe (refs. 4-9) to examine the sensitivity of turbulent air jets to upstream excitation using model-scale jet nozzles. In most cases, the upstream excitation is provided in the form of acoustic waves using loudspeakers. It has been observed that when the jet is artificially excited by a low-level acoustic source, the instability wave (i.e., the latent motions of the jet flow, commonly referred to as the large-scale structure) tends to lock onto it, and produces a response which is in agreement with linear shear-layer instability theory. At higher excitation levels, the wave extracts considerable energy from the jet mean flow, and the response becomes nonlinear as some of this energy is converted to turbulent energy, which changes the jet turbulence structure, and hence the radiated jet noise. An acoustic tone or broadband source can, therefore, change the broadband jet noise significantly without being detected in the far field.

This phenomenon of the excitation of a jet by sound has actually been known since the mid-nineteenth century (refs. 10 and 11). It was not until the 1970's, however, that it became clear that forcing of a jet by a loudspeaker upstream of the nozzle exit can not only increase the strength and regularity of the jet's coherent structures, but it also increases the radiated sound. One striking feature of the change in jet-noise level with upstream excitation is that the amplification is essentially uniform at all frequencies,and is virtually independent of observation angle. Furthermore, the level of acoustic excitation (i.e. fluctuating pressure at the nozzle exit) at which the amplification commences is found to be only 0.08% of the jet dynamic head (ref. 6). This excitation threshold is lower than the excitation levels that may be present on full-scale jet engines, and hence this

phenomenon has great practical importance.

In the well-controlled experiments conducted by Bechert and Pfizenmaier (ref. 5) in Germany, Moore (ref. 6) in England, and Deneuville and Jacques (ref. 7) in France, it has been observed that the level of broadband jet noise can be increased (above the unexcited jet noise level) by up to 7 dB by upstream acoustic excitation at the preferred Strouhal number. The amplification is totally repeatable, and it has also been shown that if the jet is excited by higher-order cut-off duct modes, the broadband noise is amplified with no distinguishable evidence of the excitation signal in the far field.

There is no doubt about the existence of the broadband jet-noise amplification outlined above. However, from a practical standpoint, the following two questions need to be answered:

(1) *What is responsible for jet-noise amplification -- the large-scale jet structure or the small-scale turbulence?*

In the case of an unexcited, clean jet flow, it is now well accepted that the large-scale jet structure plays an important part in the control of the mixing process (with the ambient air) and hence in the control of the small-scale turbulence and the radiated noise. With upstream acoustic excitation, although it is known that the large-scale, orderly structure becomes phase-locked to the excitation signal, it is not clear whether it is this phase-locked large-scale structure that radiates the amplified noise directly or whether it is the modified small-scale (and random) turbulence structure (i.e., last link in the chain) that leads to the noise amplification. Since the observed jet-noise amplification is almost uniform at all frequencies, it tends to indicate that it is perhaps the change in small-scale turbulence that leads to the noise amplification. However, this needs to be verified experimentally.

(2) *Are the relative velocity effects the same for the excited and the unexcited jets?*

In considering the flight effects on jet noise, previous studies have established beyond any doubt that for an *unexcited* clean-jet configuration, the turbulent mixing noise should decrease in level with forward velocity at all angles. Furthermore, the observed relative-velocity effects at 90° to the jet axis have been correlated or explained in terms of the changes in turbulence structure with forward velocity (ref. 12). It remains to be established whether or not the amplified broadband-jet noise from an excited jet displays the same relative-velocity effects as those for an unexcited jet. If the effects of forward motion on the excited jet are found to be different, the outcome may well explain the currently observed anomalies (refs. 3 and 12) between some full-scale flyover-noise data and the model-scale flight-simulation data.

To provide answers to the two specific aspects discussed above, a systematic research program was thus initiated to study the process of broadband jet-noise amplification due to upstream excitation, first for a static jet,

and then for the same jet operated in a free-jet flight simulation facility.

1.2 SCOPE OF THE PRESENT STUDY

The major objective of the program described here was to obtain an understanding of the mechanism of broadband jet-noise augmentation due to upstream excitation. This understanding was desired in terms of the relationship between the excitation characteristics, the changes in the large-scale and/or small-scale turbulence structure of the jet, and the sound radiated to the far field under both static and simulated forward-velocity conditions.

To achieve this objective, a systematic set of acoustic measurements were made for a range of flow conditions in the acoustic-research facilities of the Lockheed Georgia Company. Following the analysis of the acoustic results, turbulence measurements were made with Lockheed's laser velocimeter for those jet conditions at which jet-noise amplification was found to be important.

To increase our understanding further, a few optical pictures (schlieren) of the excited jets were also obtained.

Theory to explain the results obtained in this investigation was also developed, both for the static as well as the flight-simulation conditions.

The technical approach adopted to accomplish the objective is summarized in section 2.0. This is followed by a description of the facilities, and test procedures used for the experiments. Effects of upstream excitation on the jet-flow structure are described first qualitatively in section 4.0 with the aid of schlieren photographs. Schlieren photographs showing the shape of the excited large-scale turbulence structure, obtained by a unique photographic-averaging technique, are also presented here. Quantitative results from the turbulence and the acoustic measurements are described separately in sections 5.0 and 6.0, respectively. The theoretical model, developed to explain the effects of acoustic excitation on jet-flow structure and far-field noise, is described in section 7.0. Finally, the general discussion and conclusions are presented in section 8.0.

Two aspects of this study were funded by Lockheed's internal research and development program. These were: (1) the theoretical investigation, and (2) the schlieren studies.

Dr. Harry E. Plumbee, Jr., initiated the program, and Mr. D. F. Blakney and Mr. W. H. Brown helped in data acquisition and analysis. Mr. M. C. Whiffen developed the Lockheed schlieren system used in this study.

2.0 TECHNICAL APPROACH

The major objectives of this program were accomplished by conducting work under the following 7 tasks:

Task 1: Theory for Jet-Noise Amplification for Static Jets
Task 2: Theory for Jet-Noise Amplification with Forward Velocity
Task 3: Acoustic Measurements for Static Jets
Task 4: Turbulence Measurements for Static Jets
Task 5: Acoustic Measurements with Forward Velocity
Task 6: Turbulence Measurements with Forward Velocity
Task 7: Flow Visualization of the Excited Jets

Before discussing the detailed technical approach of these tasks, it is worthwhile to present some background information and the method of approach for the complete program, so that the role played by each task in meeting the overall objectives of this program will become clear.

2.1 OVERALL TECHNICAL APPROACH

As mentioned briefly in section 1.0 (Introduction), the complete process of broadband jet-noise amplification by upstream excitation is considered to involve three parts or steps which are linked in a logical fashion as illustrated schematically in figure 2.1.

In the first part of the process, the large-scale instability wave, inherent even in an unexcited jet, can be modified by upstream disturbances, leading to an amplification of this instability wave. The magnitude of this modification depends upon the detailed excitation characteristics, which, in the case of acoustic excitation, can be defined in terms of excitation level, frequency, etc., as will be discussed later. Several physical descriptions and mathematical models of this phenomenon are available in the literature, while from the experimental viewpoint, some of the best evidence is given in the work of Moore (ref. 6), who used elaborate "eduction" techniques to observe the changes in large-scale jet structure with upstream excitation.

The second part of the process involves the coupling between the large-scale jet structure and the fine-scale turbulence, based on the premise that even in the case of an unexcited jet, these two are intimately related. If the large-scale jet structure controls the mixing process (with ambient air) and hence the mean- and turbulent-flow properties in an unexcited jet, then the augmented coherent structure in an excited jet can be expected to produce significant changes in the fine-scale turbulence values. Although not examined from such a coupling viewpoint, Schmidt (ref. 8) has recently obtained some measurements which indeed show that the jet spreading rate and turbulence intensities in an excited jet are significantly higher than those in an unexcited jet.

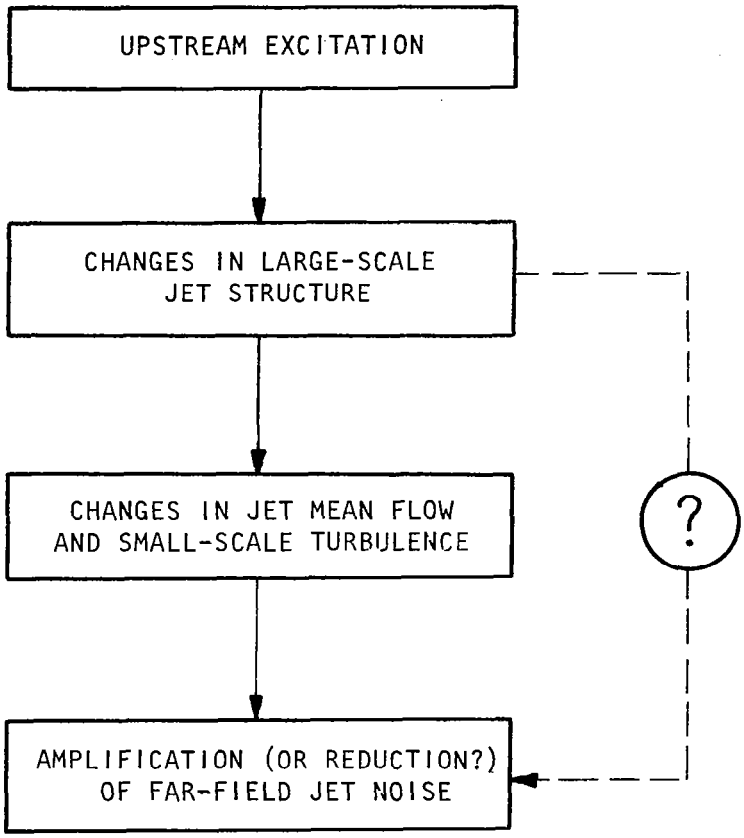

Figure 2.1 Schematic representation of jet-noise augmentation by upstream excitation

The final link in the process concerns the relationship between the jet-flow characteristics and the noise radiated to the far field. Here, on the basis of classical aerodynamic-noise theories, it is straightforward and logical to infer that an excited jet with significantly modified mean flow and turbulence levels will generate *different* noise levels compared to an unexcited jet. The word "different" is emphasized here to indicate that the excited jet-noise levels can be higher as well as lower than the corresponding unexcited jet-noise levels, the net result being a function of several relevant parameters and effects considered together.

The existence of the changes in large-scale and small-scale jet-flow properties with upstream excitation (i.e., the first two parts of the noise augmentation process) is acknowledged widely by jet-noise researchers, but when it comes to the changes in the noise fields between excited and unexcited jets, two schools of thought have clearly emerged recently. In one case, it is argued that the increase in jet noise is a direct result of the amplified large-scale jet structure, while the small-scale turbulence plays a relatively weaker role in the noise *generation* process. This is the explanation put forward in a recent theoretical study by Ffowcs Williams and Kempton (ref. 13). On the other hand, the position taken by other researchers places more importance on the increase in small-scale turbulence in an excited jet. Here, it is argued that although the phase-locked large-scale jet structure is at the root of the noise-amplification process, the actual *noise-generation mechanism* lies in the small-scale turbulence.

The second explanation appears to be more plausible for two reasons. First, except for hot jets and unheated jets with relatively high-supersonic Mach number (M>1.5), the phase velocity of the excited large-scale instability waves is *subsonic* relative to the ambient fluid. It can be shown by the theory of Morris and Tam (ref. 14) that such subsonic instability waves are very inefficient in generating sound waves directly. Second, the broadband jet-noise amplification observed in practice is almost uniform at all frequencies. If it was the large-scale jet structure that was *directly* responsible for the noise augmentation, the noise increase would occur only over a narrow frequency band centered around the natural frequency or Strouhal number of the instability wave, which, in the case of maximum amplification, will also correspond to the frequency or Strouhal number of the upstream excitation signal.

Although the above discussion of the jet-noise amplification process represents a highly simplified picture, it does reveal some of the complexities of the problem. In order to obtain a thorough understanding of the complete process, each part or step in the process as outlined above needs to be investigated, both experimentally and theoretically, so that the underlying mechanisms can be identified and quantified. To understand these phenomena for a static jet, both acoustic and jet-flow (or turbulence) measurements are required, first for the unexcited jet, and then in the presence of upstream excitation. These measurements have been obtained under Tasks 3 and 4 listed at the beginning of this section. To study the jet-noise amplification effects under flight conditions, corresponding acoustic and turbulence measurements are also required with the unexcited and excited jets operated in clean forward-velocity simulation facilities. These experiments have been conducted

under Tasks 5 and 6, respectively.

Although the major emphasis in this program is on experimental work, Lockheed believes that a theoretical effort parallel with the experimental program is necessary, not only to guide the experiments, but also so that the results of the program can be based on a firm physical basis, and hence, have a lasting value. A systematic analytical study has, therefore, been carried out to develop theoretical models, first for the static jets and then for the jets operated under flight simulation.

A detailed description of the theoretical work is given separately in section 7.0. The supporting background and approach of this analytical work are, however, given in the next subsection to provide a logical introduction to the technical approach for the experimental work, which is presented in the subsequent subsections.

2.2 THEORETICAL INVESTIGATION (TASKS 1 & 2)

At the time this investigation was initiated, the following three important reasons were kept in mind for conducting the theoretical work:

(1) It would help in coordinating the various tasks of the experimental program. For instance, in making turbulence measurements of the unexcited and excited jets, numerous types of data can be gathered. Theoretical input would be helpful in selecting the types of data which would seem to be the most important and relevant towards understanding the broadband jet-noise amplification mechanism.

(2) It would serve to provide a framework for the interpretation of measured data.

(3) The results of the theoretical study would provide a working model for the underlying mechanism of turbulence and jet-noise enhancement by upstream tones. When properly verified by comparison with experimental results, it allows a better understanding of the cause of the observed broadband jet-noise augmentation phenomenon.

The approach for the theoretical investigation is described below and consists of developing an analytical model encompassing the various kinds of interactions outlined in section 2.1 above. This model is capable of calculating the amplitude of the excited large-scale turbulence structure and also the intensity of the fine-scale turbulence. It can also be used to interpret the enhancement of broadband noise radiation. The analytical model is comprised of *two essential parts* for the static case.

2.2.1 Coupling Between Upstream Tones and Excited Large-Scale Instability Waves

The excitation of instability waves in a flow by externally imposed disturbances such as sound waves, free-stream turbulence or entropy waves is

generally referred to in the literature as the receptivity problem; for example, see the discussion given by Reshotko (ref. 15). Although it is perceived as an important problem by many interested in hydrodynamic stability and transition theories, a proper formulation of the mathematical problem and its solution were not available until the most recent work of Tam (ref. 16). Tam studied the problem of excitation of instability waves in a two-dimensional free shear layer by sound. The problem was formulated as an inhomogeneous boundary-value problem which was solved by means of a local Green's function technique. The Green's function provided the coupling constants between the incident sound wave and the excited instability waves by which the amplitude of the forced instability wave could be calculated. This theory was applied to a study of wheel-well cavity tones by Tam and Block (ref. 17). These tones are generated by a feedback loop involving the excitation of the instability waves in the shear layer spanning the open end of the cavity by acoustic waves produced at the downstream end of the cavity. The predicted tone frequencies were found to agree favorably with experimental results, thus lending support to the validity of the theory. In a more recent study, the theory was applied by Tam (ref. 18) to the excitation of Tollmien-Schlichting waves in a flat-plate boundary layer by sound. Good agreement between the calculated Tollmien-Schlichting wave amplitude and the measurements of Shapiro (ref. 19) was obtained. In this work it was also shown that if the boundary layer was excited by free-stream turbulence, only the turbulent-velocity component normal to the plate could excite the unstable Tollmien-Schlichting waves. This important finding is in agreement with the experiments of Kachanov et al (ref. 20), further supporting the validity of the local Green's function theory.

In the present investigation, Tam's theory (refs. 16 and 18) has been extended to calculate the excitation of large-scale instability waves in a jet flow by upstream tones. The coupling constants between the upstream tones and the instability waves at the jet-operating conditions to be used in the experimental program have been calculated. This involved frequency variation at different modal numbers, Mach numbers, and temperatures. After these coupling constants have been computed, they may be used to determine the spatial amplitudes of the excited large-scale instability waves. Comparisons between calculated and measured results have been carried out to assess the accuracy of the prediction.

2.2.2 Enhancement of the Fine-Scale Turbulence by the Large-Scale Instability Waves

Having calculated the characteristics of the large-scale instability wave, a reasonably accurate estimate of the fine-scale turbulence intensity in a jet under the excitation of upstream tones has been developed. A model of this kind was first employed by Ko et al (ref. 21) to describe the role of instability waves in wake flows. Similar models have since been used by Tam (ref. 22), Chan (ref. 23), Liu (ref. 24), and Morris (ref. 25) to account for the nonlinear interaction between mean flow and large-scale instability waves in jets. In these models, the mean flow and the fine-scale turbulence distribution of the jet are represented by shape profiles characterized by a number of, as yet undetermined, parameters. These parameters may be determined by a set of nonlinear ordinary differential equations. These equations are

obtained by integrating the moments of the Navier-Stokes equations across the cross-section of the jet, very similar to the integral methods of turbulent-boundary layer theories. The two lowest moments, namely, the conservation of momentum flux and energy have been used. The coupling between the upstream tones and excited instability waves have also been incorporated in the model. By numerically integrating the resultant set of equations, it is possible to obtain the level of the enhanced fine-scale turbulence distribution in the jet under various excitation conditions, i.e., different frequencies, modal numbers, Mach numbers,and jet temperatures. Once again the results from this analytical model have been compared with measurements to ascertain its accuracy.

2.2.3 Broadband Jet-Noise Augmentation

The final link in the theoretical model requires a method of relating the predicted changes in the flow structure, particularly the increase in the fine-scale turbulence levels and the jet volume, to the changes in the radiated noise. In spite of almost 30 years of effort, there still remains no concensus as to the physical processes by which a turbulent flow radiates noise, and no satisfactory model to compute the radiated noise has yet evolved. For the case of a round jet exhausting into stationary air, arguments based on dimensional analysis have provided a good correlation of experimental data. However, such arguments, involving the characteristic length and time scales of the turbulence, are inappropriate when the turbulence is subjected to a periodic forcing which adds an additional time scale to the problem. In spite of these reservations, an attempt has been made to find an integral property of the fine-scale turbulence which permits a correlation of the observed noise changes with changes in the flow structure.

2.2.4 Forward Flight Effects

Effort to assess the effects of flight on the phenomenon of broadband jet-noise amplification by upstream-tone excitation has been carried out. The influence of an ambient flow on the mean flow velocity profile of the jet, the spatial growth of the excited instability waves, and the receptivity of these waves to upstream-tone excitation have been examined separately. The role of jet temperature and mode number of the excitation tone have also been briefly investigated. The combined effect of all these changes on the radiated noise of a jet in forward flight will be discussed in a later section of this report.

2.2.5 Summary

To summarize, theoretical investigation of the phenomenon of broadband jet-noise amplification by upstream tones has been carried out in two major parts. The calculated results of each part has been compared with measurements. Since each part of the investigation has involved one basic link of the noise-amplification process, an accurate assessment of the validity of each link has been possible. It is felt that the results of this investigation have contributed significantly to the understanding of the mechanism of the total phenomenon.

The remaining parts of this section are now devoted to the experimental effort (Tasks 3-7), which, as was mentioned earlier, constitutes the major portion of this research program. Before presenting the details of the five specific tasks involving the experimental work, it is useful to make some overall observations as well as to discuss some pertinent aspects which are common to two or more of the five tasks.

2.3 EXPERIMENTAL WORK

The acoustic experiments, for both static and simulated forward-velocity conditions, were conducted in the Lockheed anechoic free-jet facility, while the corresponding jet-flow measurements were performed in the Lockheed turbulence facility, which was suitably modified to provide the necessary forward-velocity conditions. The two experimental setups, including the upstream-excitation source sections, were made as compatible as possible. These facilities are described in detail in section 3.0.

Since our overall technical approach for this program indicated that an understanding of the noise-amplification mechanism could be satisfactorily and effectively obtained by conducting the relatively simpler time-independent measurements of the jet mean-flow and turbulence characteristics, no time-dependent measurements were therefore made.

In the experimental program, there is obviously a large number of parameters which need to be considered in order to obtain a thorough understanding of the broadband jet-noise augmentation process. Collectively, these parameters characterize (a) the jet-operating conditions, (b) the forward-velocity conditions, and (c) the upstream-excitation conditions.

The following list gives the relevant parameters which define a particular test condition to study jet-noise amplification:

Jet-operating conditions -

Nozzle-pressure ratio (ξ) and Stagnation temperature (t_r)

Forward-velocity conditions -

Free-jet velocity (V_t)

Upstream excitation conditions -

Frequency (f_e), Level (L_e), and Circumferential mode number (m)

In view of the fact that there are six general parameters for each test condition, and that each parameter ought to be varied over a realistic range, the experimental conditions needed to be chosen carefully. The problem is particularly severe for the turbulence measurements, where the jet flow needs to be surveyed in great detail. Thus the acoustic and turbulence tests were carefully planned to provide the maximum amount of

useful information within the available level of effort. The following five subsections describe the technical approach that was adopted to carry out the experimental work.

2.3.1 Task 3 - Acoustic Measurements for Static Jets

The *objective* of this task was to conduct a series of acoustic measurements to verify and establish the phenomenon of broadband jet-noise augmentation by upstream acoustic excitation.

The noise-augmentation characteristics were measured for unheated and heated jets at both subsonic and supersonic conditions. The amount of broadband jet-noise amplification was measured as a function of (a) excitation frequency, (b) excitation level (including the determination of an excitation threshold and/or saturation level, if any), and (c) excitation-signal modal structure. The results from these experiments were used to select the test conditions (i.e. combinations of jet-operating conditions and excitation characteristics) for detailed turbulence measurements conducted under Task 4 and also to select the test conditions for acoustic and turbulence measurements under simulated forward-velocity conditions conducted in Tasks 5 and 6, respectively.

The following items describe the details of this task:

(1) These static experiments were conducted in the Lockheed anechoic free-jet wind tunnel with nominally zero free-jet or tunnel velocity, V_t. The specifications of this facility are given in section 3.0.

(2) The diameter of the primary-jet nozzle (D_j) was 5.08 cm.

(3) Far-field acoustic data was acquired using 0.63 cm (1/4 in) microphones placed on an arc of radius 48 D_j. The measurements were made from 60° to 160° relative to the nozzle inlet axis at 10° intervals. The data was recorded on a multi-channel Honeywell tape recorder for subsequent processing.

(4) The recorded data were played back through a one-third octave analyzer, and using a specially-developed data-reduction computer program to apply corrections for atmospheric-attenuation and microphone frequency-response, 1/3-octave lossless-SPL spectra over the frequency range from 200 Hz to 80 KHz were generated for all measurements. Limited amount of data were also analyzed through a real-time analyzer for narrow-band analysis.

(5) Majority of the acoustic measurements were obtained at nozzle-pressure ratios of 1.25 and 1.5, and stagnation temperatures equal to the ambient temperature and also 800K. Data for few additional test points of higher pressure ratios of 1.8 and 3.04 were also obtained.

(6) A special source section was designed and installed to provide controlled frequency, level and modal structure of the upstream acoustic excitation. The source section consisted of 4 acoustic drivers, the signals from each of which were independently controllable with respect to phase and amplitude. The source section is described in detail in section 3.0.

(7) The frequency of the excitation signal was varied between 2 octaves below and 2 octaves above the peak frequency of the "unexcited" broadband jet noise.

(8) The level of the excitation signal was varied over a sufficiently broad range to include representative levels encountered in actual jet engines.

(9) The measurements were concentrated for two mode orders - the zero-order (plane wave) mode, and the first-order circumferential (spinning) mode. A mode detection scheme using multiple microphones, circumferentially distributed just upstream of the nozzle exit, was utilized. To determine the mode structure at the nozzle exit, modal analysis of the resulting pressure measurements was conducted. The mode detection method used here is described separately in section 3.0.

(10) To select the optimum operating acoustic excitation parameters the following steps were adopted to obtain the maximum amount of information within the given limitations. To start with, one jet-operating condition (say, pressure ratio of 1.5 and ambient temperature) was selected, and the effects of excitation frequency, level, and modal structure on broadband jet-noise amplification were investigated parametrically in detail. From the results of these tests, the excitation characteristics in terms of nondimensional frequency and level and the mode order at which the amplification effects were found to be the most interesting were isolated. Then, these "optimum" excitation conditions were used to conduct tests at other nozzle-pressure ratios and the 800K jet temperature.

(11) The results from these experiments were analyzed by subtracting the "unexcited" or baseline jet-noise levels from the "excited" or amplified jet-noise levels. The amount of broadband jet-noise augmentation as a fuction of frequency, level,and modal structure of the upstream excitation were determined for subsequent comparison with theory.

2.3.2 Task 4 - Turbulence Measurements for Static Jets

A turbulence measurement program for stationary jets with and without upstream acoustic excitation was conducted to obtain the relationship between the changes in jet-turbulence structure with upstream excitation and the corresponding increases in far-field radiated jet noise.

(1) The test conditions, in particular the excitation frequency, level, and modal structure, for this task were selected on the basis of the results generated under Task 3. Test points chosen for detailed turbulence measurements, included nozzle-pressure ratios of 1.25 and 1.5 for the unheated jet, and 1.5 pressure ratio for heated (800K stagnation temperature) jet.

(2) The measurements (for both excited and unexcited jets) consisted of radial distributions of mean velocity and turbulence intensity at several axial locations in the jet flow, and the data were processed to obtain the spectra of the velocity fluctuations. In addition, for the unheated jets, the pressures associated with the large-scale turbulence structure were also measured at various axial locations. Most of the pressure measurements were made along the centerline of the jet. Limited measurements along the lip line together with a few radial profiles of the large-scale turbulence pressure levels were also made.

2.3.3 Task 5 - Acoustic Measurements with Forward Velocity

A series of acoustic experiments using unexcited jets under simulated forward-velocity conditions were conducted to determine whether or not the phenomenon of jet-noise augmentation by upstream acoustic excitation is enhanced (or diminished) by relative-velocity effects.

(1) The experiments were conducted at two free-jet velocities of 45 m/sec and 90 m/sec.

(2) The diameter of the free-jet (flight simulation) nozzle was 0.7 m, which provided an area ratio of 200 between the free-jet and the model-jet nozzle.

(3) The experiments were conducted at nozzle-pressure ratios of 1.25 and 1.5,and stagnation temperatures equal to the ambient temperature and also 800K.

(4) The upstream excitation conditions (i.e. frequency, level, and mode order) used in this task were determined on the basis of Task 3 results.

(5) The data acquisition and reduction procedure were identical to those used in the static jet acoustic experiments. However, in the present task, since the measurements were conducted in the presence of the free-jet flow, all data were transformed to those for the ideal wind-tunnel conditions using a scheme developed at Lockheed (ref. 3).

2.3.4 Task 6 - Turbulence Measurements with Forward Velocity

A turbulence measurement program for unexcited and excited jets under simulated forward-velocity (flight) conditions was conducted to investigate the effects of forward speed on the changes in jet-turbulence structure resulting from upstream acoustic excitation.

(1) The experiments were conducted at two simulated forward velocities of 45 m/sec and 90 m/sec (nominal).

(2) The outer nozzle to provide the flight simulation flow was 25 cm in diameter, which provided an outer-nozzle to model-jet area ratio of 25.

(3) The upstream excitation conditions for this task were determined on the basis of the results obtained from Tasks 3, 4 and, 5. As for the static case, turbulence measurements under flight simulation were made at nozzle-pressure ratios of 1.25 and 1.5 for the unheated jet. The 1.5 pressure ratio case was also investigated at 800K stagnation temperature.

(4) The flow quantities measured in this task were identical to those measured in Task 4.

2.3.5 Task 7 - Flow Visualization of the Excited Jets

During the course of conducting the experiments of Tasks 3 thru 6, an optical setup was developed at Lockheed-Georgia for a program not related to this one. Opportunity was, however, taken to utilize this optical setup to obtain schlieren pictures of the excited jet. In particular, it enables one to extract the shape of the excited large-scale turbulence structure, hidden behind the fine-scale turbulence, through the use of a time-averaging method described later in section 4.0.

Since this optical setup was not especially catered for the present program, the test conditions for the optical study, in particular the flow velocities, could not be kept identical to those used for the previous tasks. For example, only low-velocity jets, operated at 20.5 m/s (67 ft/s) and 45.7 m/s (150 ft/s), were used for this flow-visualization study. Inspite of these limitations, these flow-visualization photographs provided a wealth of qualitative information. In particular, these photographs revealed the shape and spacing of the large-scale structure in an excited jet. Because of the importance of these photographs in understanding the experimental and theoretical results of the first six tasks, a separate section (Section 4.0) has been devoted to the description of these flow-visualization results.

This completes the description of the technical approach adopted to conduct this study.

3.0 FACILITIES AND TEST PROCEDURE

Two separate facilities were used to accomplish the experimental program. All acoustic tests were conducted in the anechoic free-jet wind tunnel. All turbulence data were acquired in the turbulence facility. All turbulence measurements were made with Lockheed's unique laser velocimeter facility. Further details of these facilities are given below.

3.1 ACOUSTIC FACILITIES

3.1.1 The Anechoic Free-Jet Wind Tunnel

This facility is powered by a jet ejector and is capable of providing continuous free-jet velocities up to 95 m/s with a circular test section of diameter 0.71 m. A planview schematic of the complete facility is shown in figure 3.1. Starting from the left, air is drawn into the intake, through the honeycomb and screens to the contraction, across the anechoic room (test section) to the collector, through the diffuser, the two right-angle corners with turning vanes, and through the duct silencers to the transition section. The exhaust and entrainment flows of the jet ejector (diameter = 8.6 cm) are diffused through a 17.1 m long muffler/diffuser section shown on the right in figure 3.1.

The air supply to the jet ejector originates from the main 2.07×10^6 N/m^2 compressor which supplies dry air to all research-center facilities. In addition, storage tanks retain approximately 5500 kg of air at 2.07×10^6 N/m^2 for higher demands.

The basic anechoic room surrounding the free-jet test section is 4.3 m long, 4.3 m wide, and 6.1 m high between wedge tips. The interior is lined with polyurethane foam wedges. The chamber is completely isolated from the rest of the acoustics laboratory since it is mounted on massive springs. A spring-tensioned cable floor, suspended from the walls, provides easy access to the interior of the chamber for instrumentation and hardware changes and for calibration purposes.

Because of the high noise levels generated by the jet-ejector drive system for the free jet, being operated at pressure ratios up to 8 to induce flows through the working section of up to 95 m/s, a significant amount of acoustic treatment has been incorporated in the tunnel ducting between the anechoic room and the jet ejector.

The free-jet nozzle is 0.71 m in diameter. In order to have an option of utilizing the existing rectangular free-jet nozzle, the round free-jet nozzle has been designed to fit inside the rectangular nozzle section, as shown in figure 3.2. The inlet diameter of the round nozzle is 1.9 m and the inner contour has been designed such that a flat velocity profile is

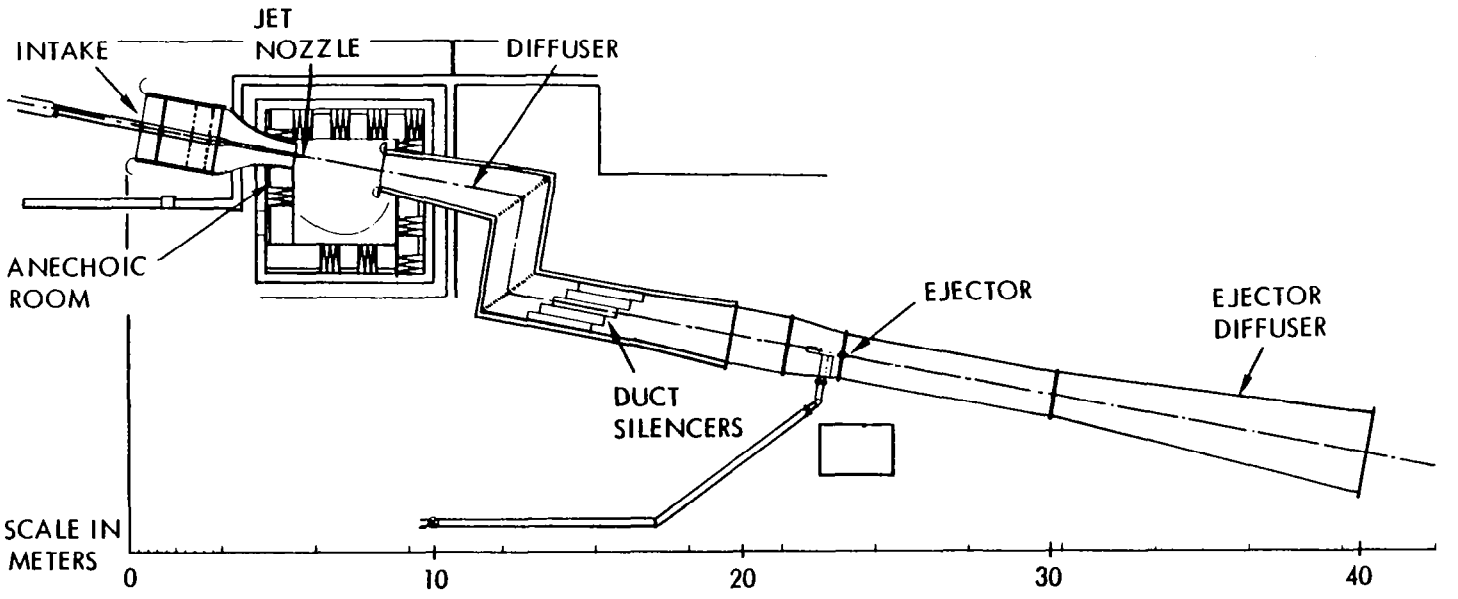

Figure 3.1 Planview schematic of the anechoic open-jet wind tunnel.

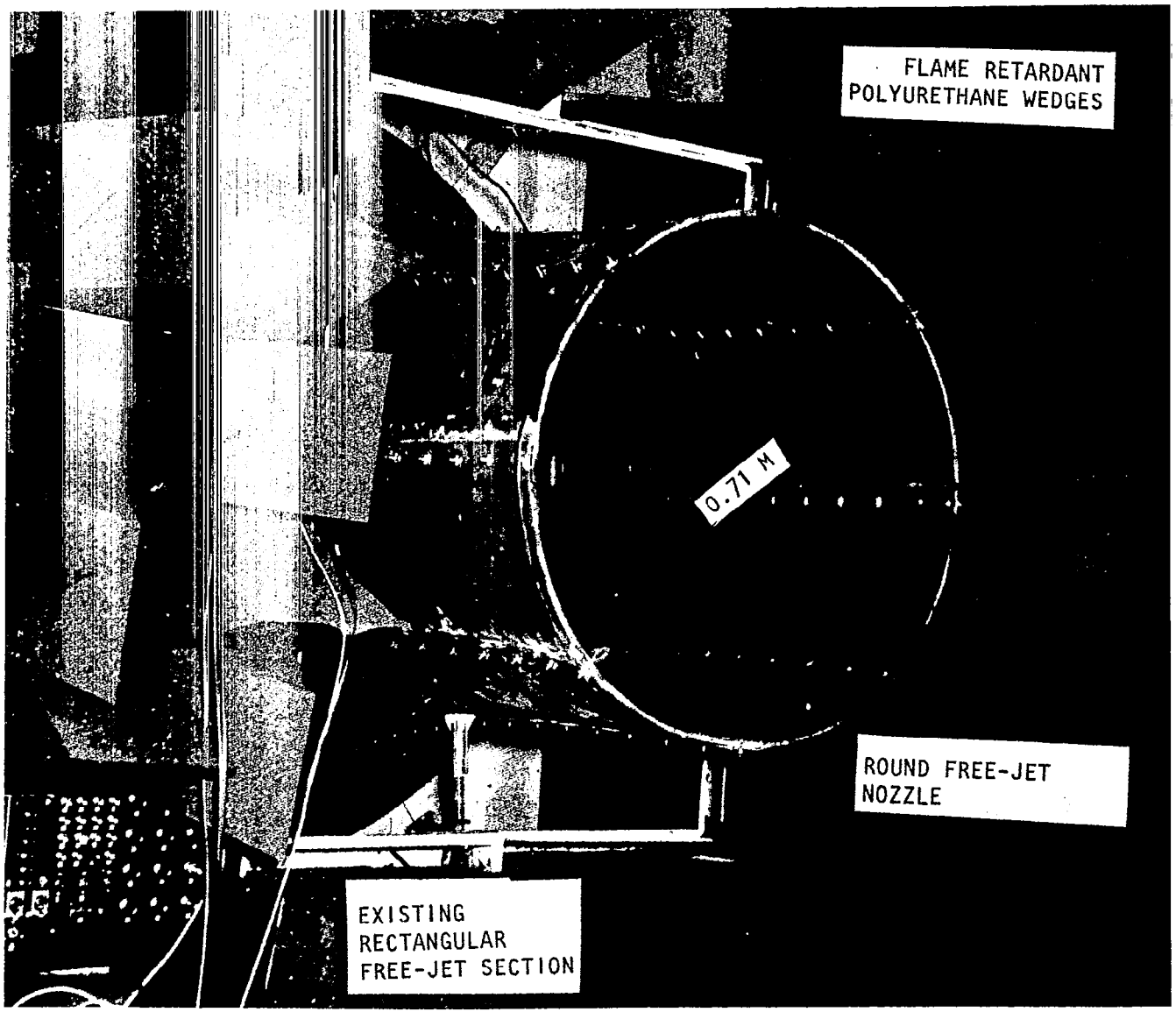

Figure 3.2 Round free-jet nozzle

obtained at the exit plane. The total length of the nozzle contraction section is 2.44 m.

3.1.2 The Primary-Jet Nozzle

The primary-jet nozzle used in this study is a 5.08-cm (2 in.) diameter convergent nozzle. This is a unique nozzle in that it is provided with 12 acoustic-pressure sensing ports around the inner periphery, near the exit plane, as shown in figure 3.3. The outer surface of the nozzle has been machined for slots needed to accommodate the miniature Knowles microphones and microphone probes. This special feature enables the measurement of acoustic levels and acoustic modes at the jet exit plane by a mode detection method described separately in appendix A. The microphones are actually positioned on an oval shaped water-carrying copper tube to keep the microphones cool when the jet is heated. These slots are filled with a high temperature cement to render the outer surface of the nozzle smooth. This nozzle mounted in the anechoic free-jet wind tunnel is shown in figure 3.4.

The nozzle is connected to a 10-cm diameter supply duct. For minimum blockage (and therefore minimum flow disturbance) in the working section, the air-supply ducting for the model jet is installed in the free-jet intake/contraction section rather than through a swept pylon mounted on the anechoic room wall. The ducting is designed to avoid any flow separation within the accelerating free-jet flow in the contraction section, a totally welded construction being adopted for this purpose. The ducting is aligned by using a low-power laser, placed at the end of the collector/diffuser and aimed along the free-jet centerline, ensuring that the model jet would exhaust axially in the free stream.

For heated jet noise tests, the air is first heated to approximately 1000K by a Marquardt Sudden Expansion (SUE) Propane Burner located outside the laboratory building. The air is then passed through a muffler section. The muffler section is highly effective in minimizing upstream internal noise levels.

3.1.3 Upstream Acoustic Excitation Source

The source section used for the acoustic experiments is shown schematically in figure 3.5. It is centered around a 10-cm diameter duct and utilizes four electro-acoustic 100 watt Altec drivers. Each driver is enclosed in a pressure vessel to equalize the pressure across the driver diaphragm. To protect the diaphragms during high temperature tests, tubes connecting the drivers to the source section have provisions to provide cooling air. The source section is located in a constant 10-cm diameter pipe section, six meters upstream of the nozzle exit plane.

The most critical feature of the source section is the requirement to generate modes in isolation. To achieve this, the input signal for each driver is passed through individual power amplifiers with provision for input *amplitude and phase* control in order to ensure generation of the plane-wave mode, (1,0) mode, or (2,0) mode in isolation.

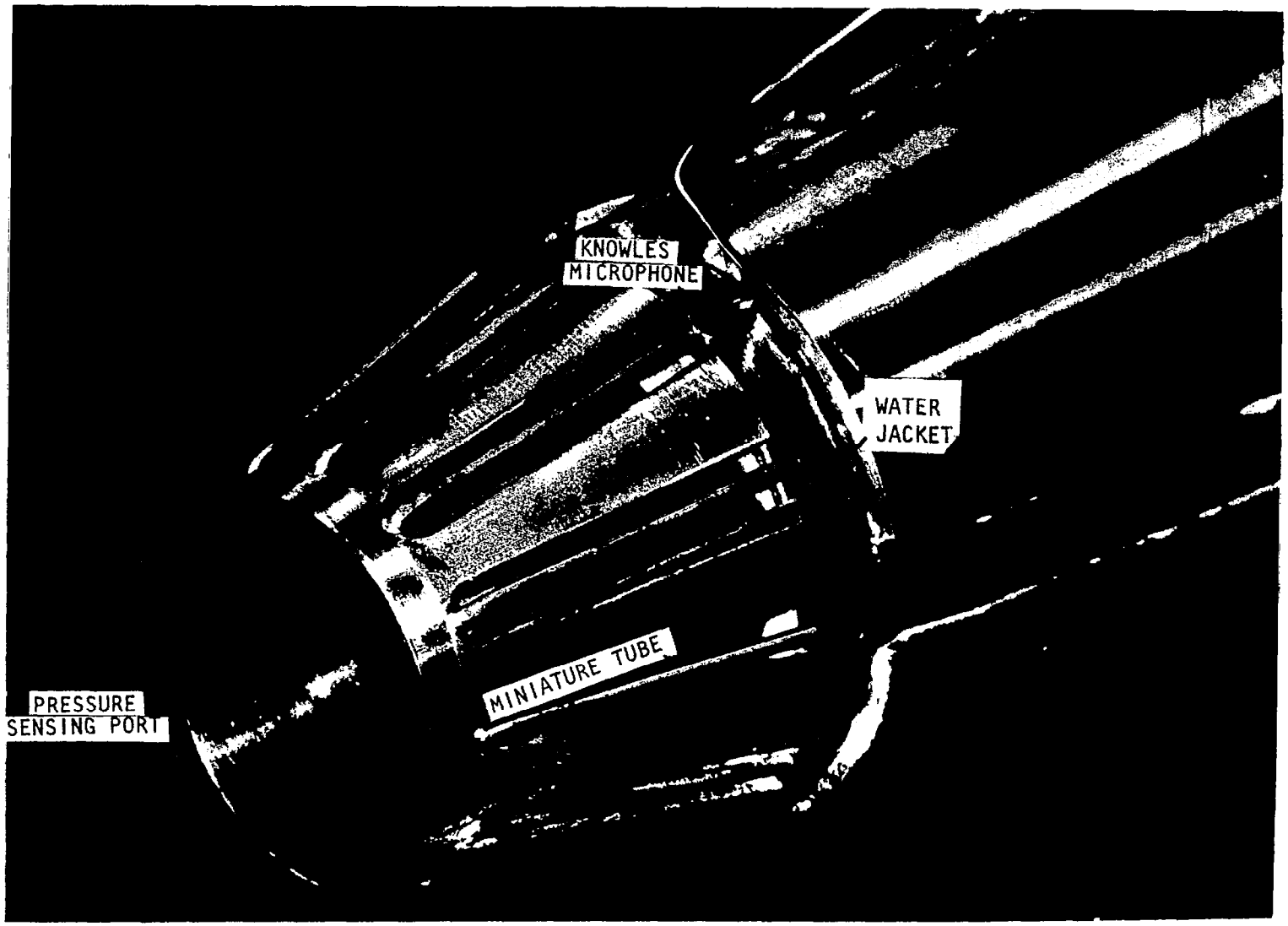

Figure 3.3 Photographic view of the nozzle with 12 miniature probe tubes used for mode detection. (Only one microphone is shown connected here.)

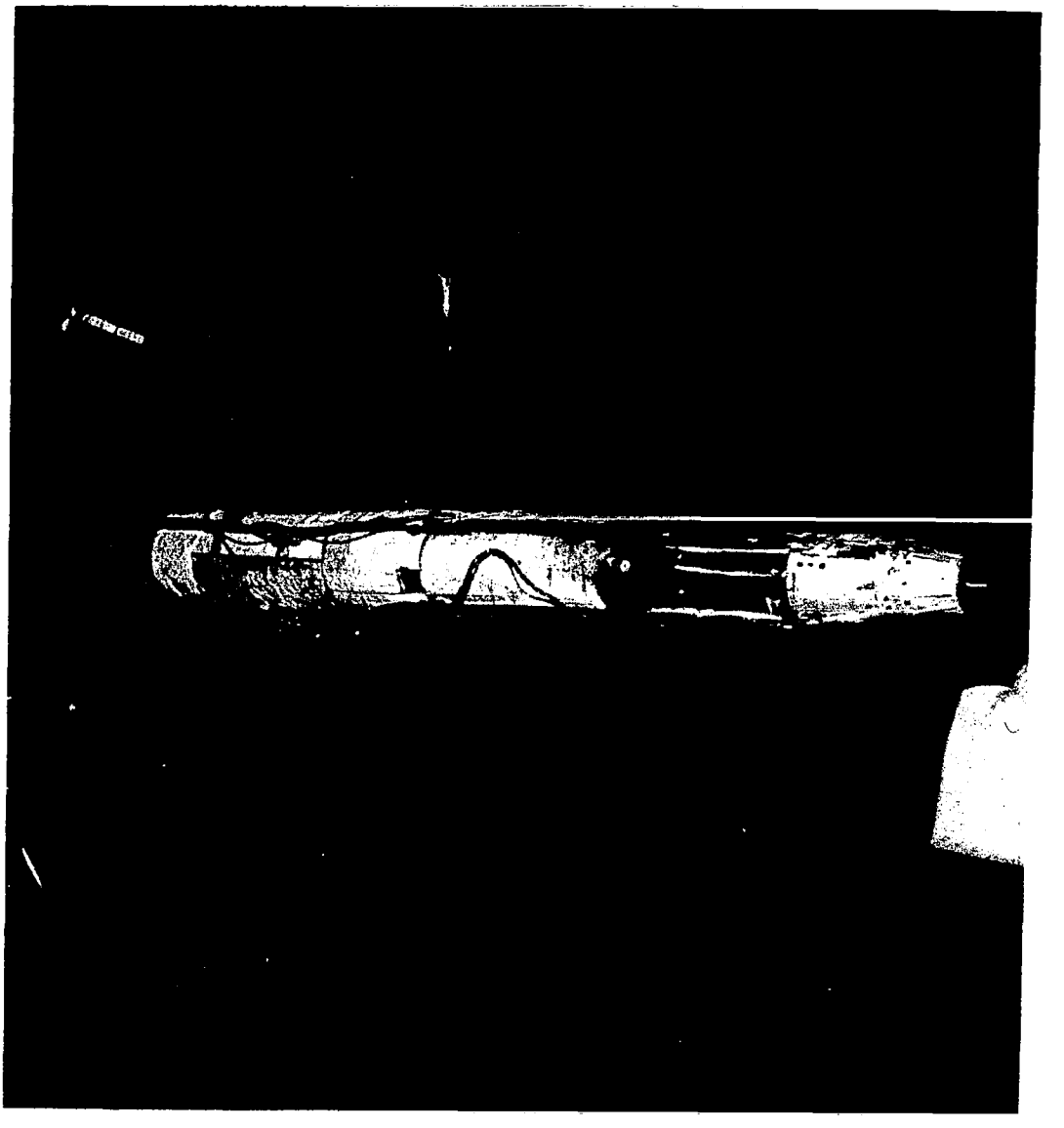

Figure 3.4 Test nozzle mounted in the anechoic open-jet wind tunnel.

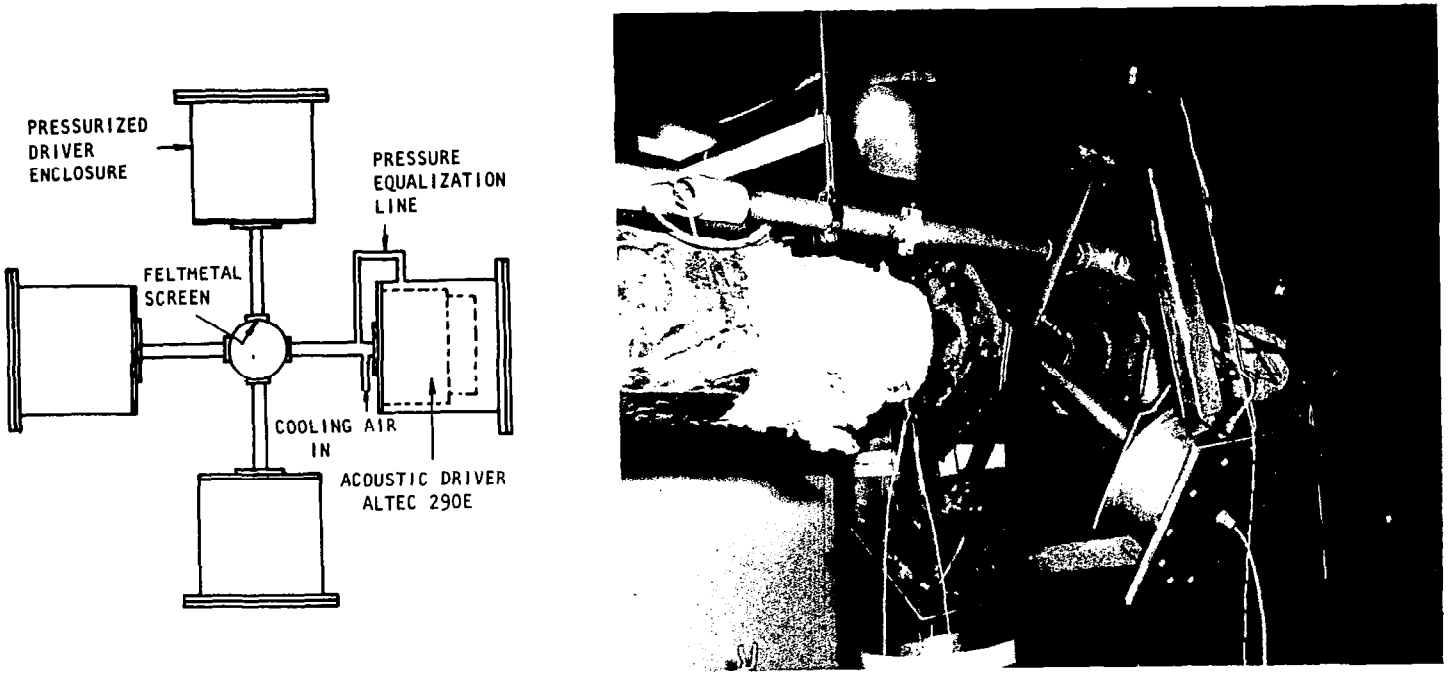

Figure 3.5 Source section for upstream acoustic excitation.

3.2 TURBULENCE FACILITY

For efficient operation of Lockheed's facilities, turbulence measurements for this investigation were made in a facility which was similar to, but physically different from, that used for the acoustic measurements. The turbulence facility used for this study is housed in a building adjacent to the acoustic facility. The building also contains the laser velocimeter system.

3.2.1 The Jet System

The turbulence facility is designed to produce parallel, low-turbulence coaxial flows (fig. 3.6). It has two plenums arranged coaxially. The primary flow enters through a 25.4-cm diameter pipe followed by an initial contraction to a 10-cm diameter duct to which is attached the 5.08-cm diameter test nozzle.

In order to simulate flight effects in the turbulence facility, the outer flow enters from one side into an initial coannular plenum with a cross-sectional area of 0.21 m^2. Flow then passes through eight 10-cm diameter ports covered by screens to another coannular plenum of the same cross-sectional area. The outer flow is then contracted to 0.045 m^2 to simulate flight effects. The upstream end of this nozzle is 71 cm in diameter, and it contracts to 25.4 cm-diameter at the exit plane. This results in an annular area contraction ratio of 4.6.

A photographic view of this facility is shown in figure 3.7.

3.2.2 Upstream Excitation Source

The upstream excitation source used in the turbulence facility is somewhat different from that used in the acoustic facility, but basically provides the same acoustic characteristics at the jet exit. The source configuration is shown schematically in figure 3.6. The acoustic drivers and pressurized enclosures are identical to those in the acoustic facility. The only difference, however, is in the length and shape of the pipe used to connect the driver to the 10-cm diameter section just upstream of the jet nozzle.

3.2.3 Laser Velocimeter System

The mean velocities and the turbulence intensities were measured by Lockheed's laser velocimeter system, which has been used extensively in the past to make both single jet- and coannular jet-flow surveys. A detailed description of this facility is given in reference 26, and the salient features are summarized below.

The laser velocimeter consists essentially of a transmitting optical system which sends out two pairs (one green and the other blue) of coherent laser beams that intersect at the measurement point in the jet. The beams are oriented in such a way that the two sets of fringes formed at the measurement volume are normal to each other. Thus, velocities in two

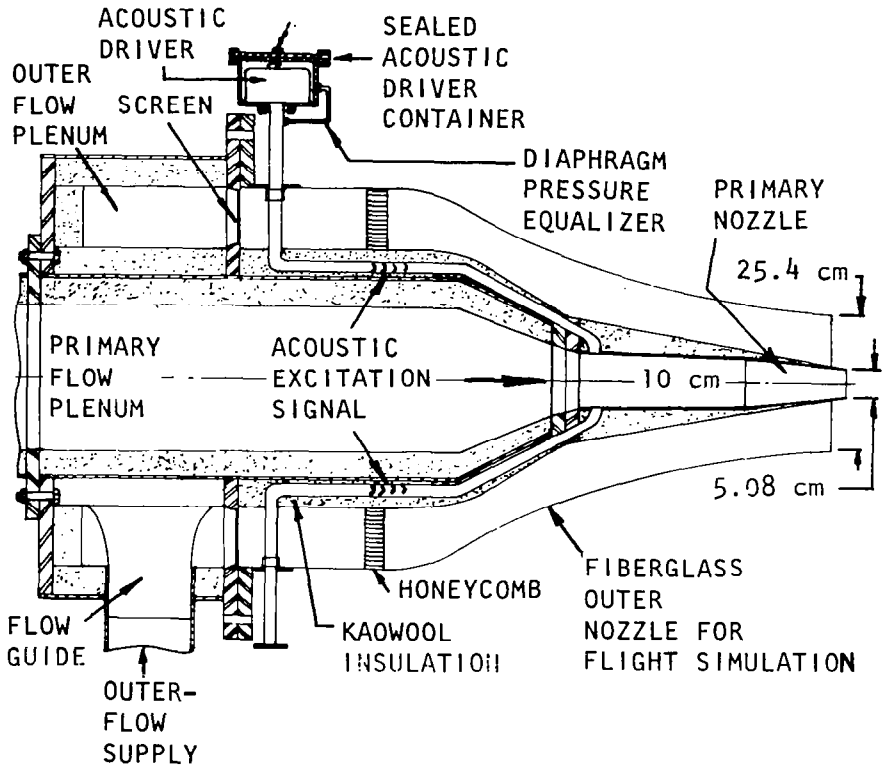

Figure 3.6 Cross-sectional view of the turbulence facility

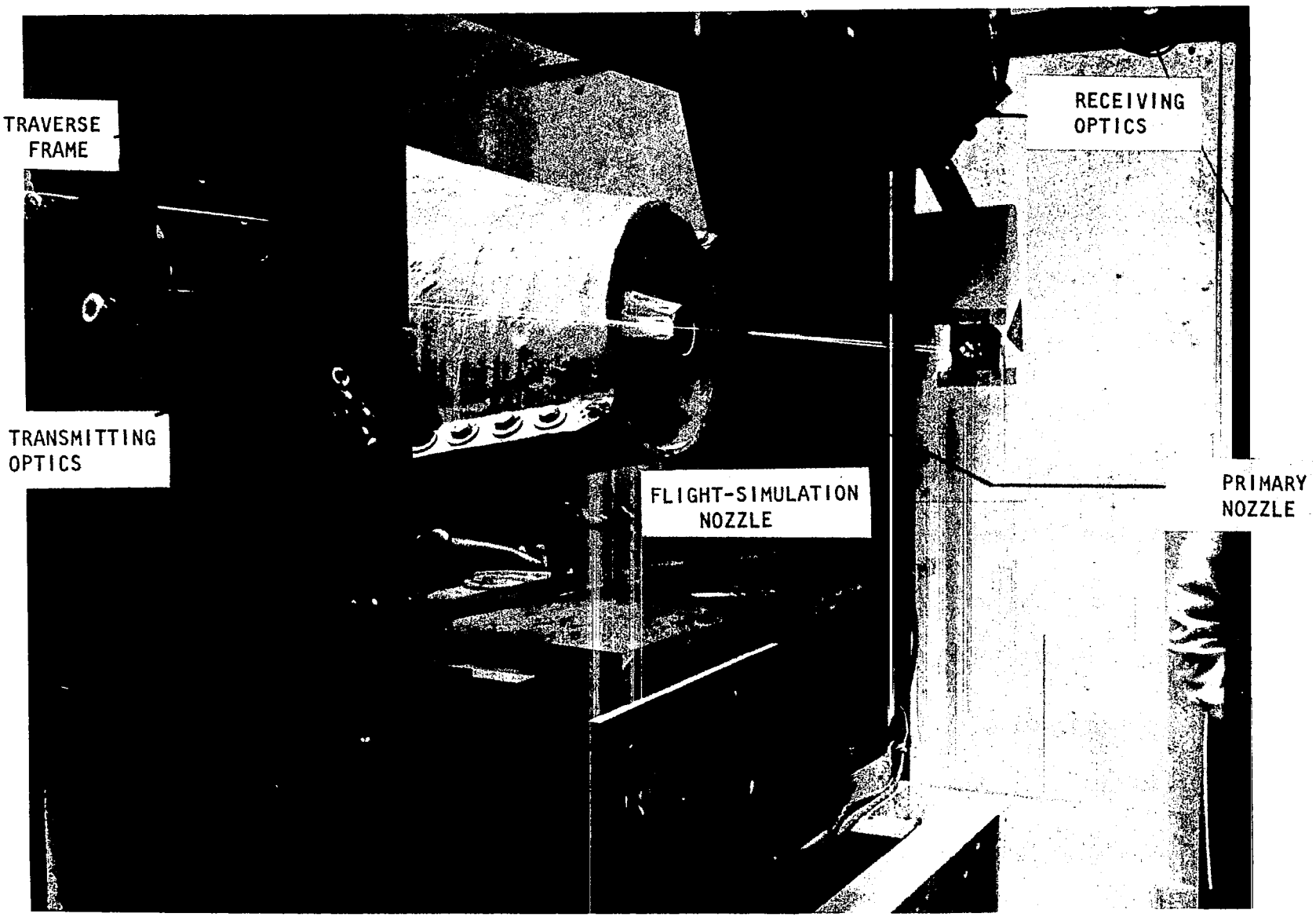

Figure 3.7 Photographic view of the turbulence facility

orthogonal directions are obtained. The fringes are made to move within the measurement volume by means of frequency shifting induced with an acousto-optical transducer (Bragg cell).

The alternating light scattered by the individual particles of aluminum oxide powder seeded in the flow is detected by the receiving optical system placed at about 30° to the transmitting beams. A color separator, which allows separation of the green and blue light, detected at the measurement volume, is placed in the receiving optical system across the path of the scattered light. The alternating green and blue light signals are then converted into alternating voltages of photomultiplier tubes (PMT), and these voltages are processed in an electronic processor. Validation circuits are incorporated in the processor to ensure that the signals are the signals arising out of the passage of single seeding particles, the validated signals are analyzed by a digital computer to give results on mean velocity, turbulence level, and covariance of the velocity components. The raw data on instantaneous velocities may also be recorded on magnetic tape for subsequent analysis to give results on spectra and auto- and cross-correlations.

A set of the transmitting and receiving optics is mounted securely on each of the two traversing frames shown in figure 3.8. The measurement volumes are therefore fixed relative to their respective frames, and their positioning is accomplished by moving the frames. The frames are mounted on a large platform which is free to move axially. They are also arranged so that the downstream frame may move relative to the other frame, and each frame has transverse motion in two orthogonal directions. By the use of absolute positioning encoders, the location of the measurement volume can be determined to an accuracy of better than 0.25 mm. The frame movement is controlled by the computer, and is fully automated.

3.3 COMPATIBILITY BETWEEN THE TWO FACILITIES

It would be ideal to make both the acoustic and turbulence measurements in the same facility. This would guarantee that identical phenomena in terms of excitation, flow mixing, and flight simulation mechanisms are present in both sets of experiments. Since various constraints dictated the use of two separate facilities, it was important to carry out tests to ensure that the various flow and acoustic parameters of interest, in both facilities, did not differ significantly. Extensive validation tests were, therefore, carried out which showed that, for all intents and purposes, the two facilities are quite compatible. It was found that for both facilities :(1) the turbulence intensity at the nozzle-exit center is about 0.6%; (2) the velocity profiles at the nozzle exit are almost identical (see figure 3.9); and, (3) the (0,0) mode and the (1,0) mode can be set up in isolation in each jet even though the source sections are somewhat different in the two facilities.

Since for a fixed primary jet diameter, the flight-simulation nozzles for the two facilities have different diameters it is important to ascertain that the flight effects can be simulated with reasonable accuracy in both facilities.

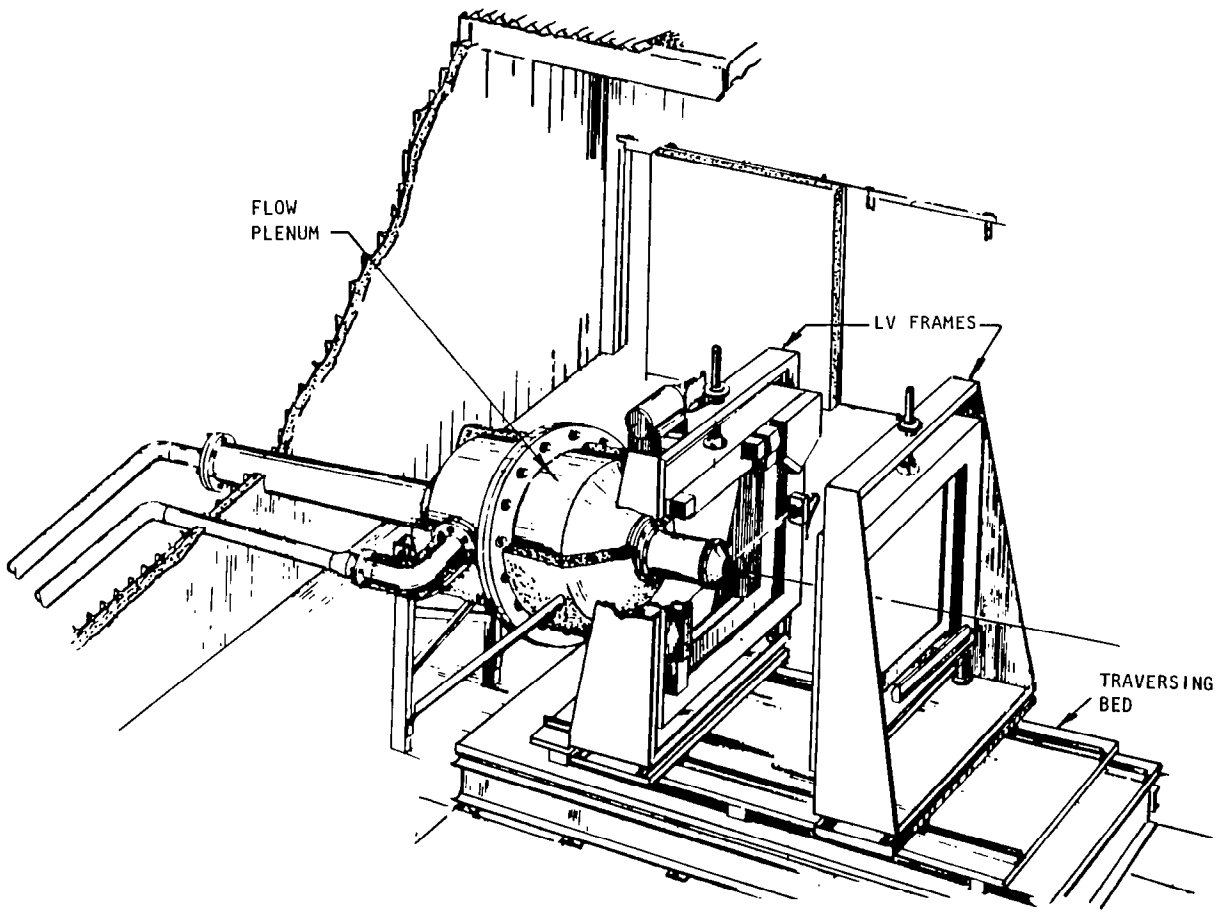

Figure 3.8 Jet turbulence facility with LV traversing bed and frames

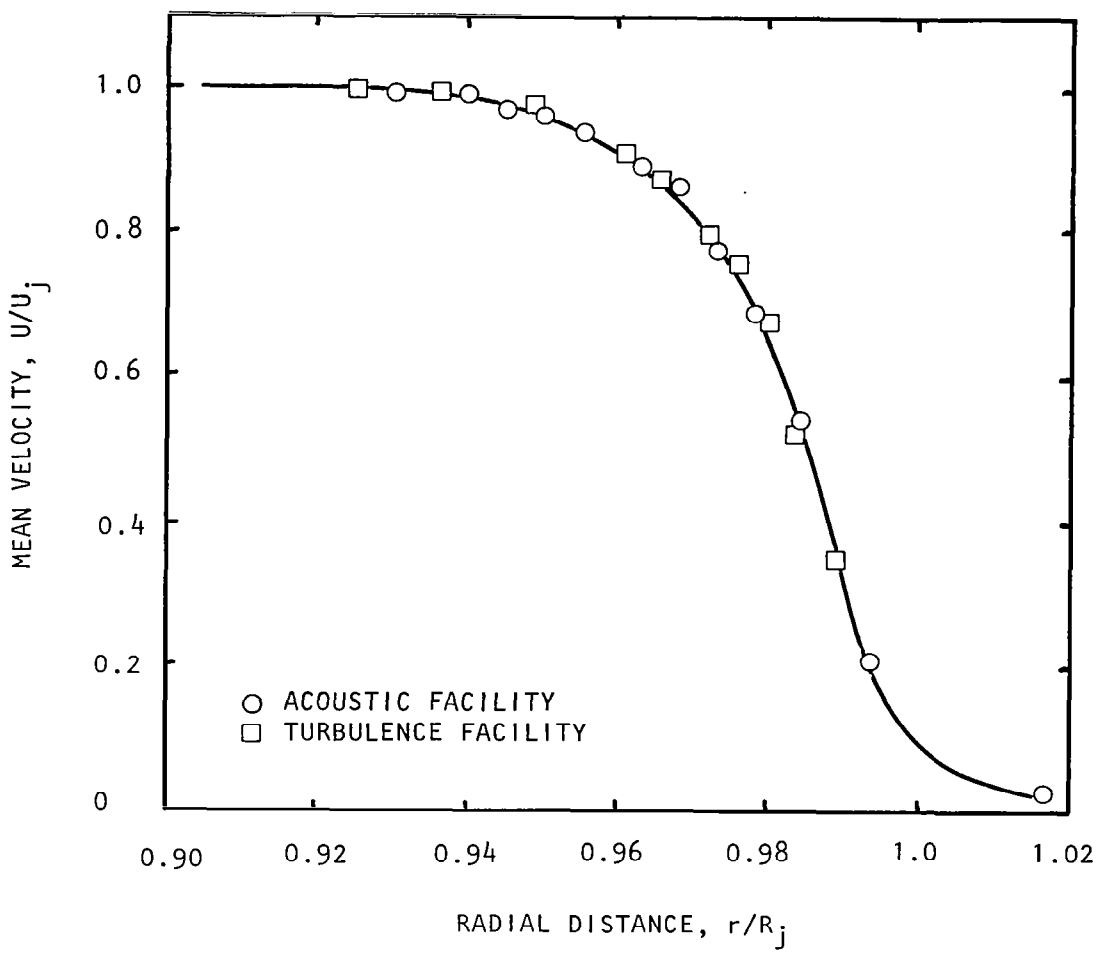

Figure 3.9 Comparison of exit-velocity profiles near the nozzle lip for the acoustic and the turbulence facility.

(Momentum thickness ≈ 0.17 mm)

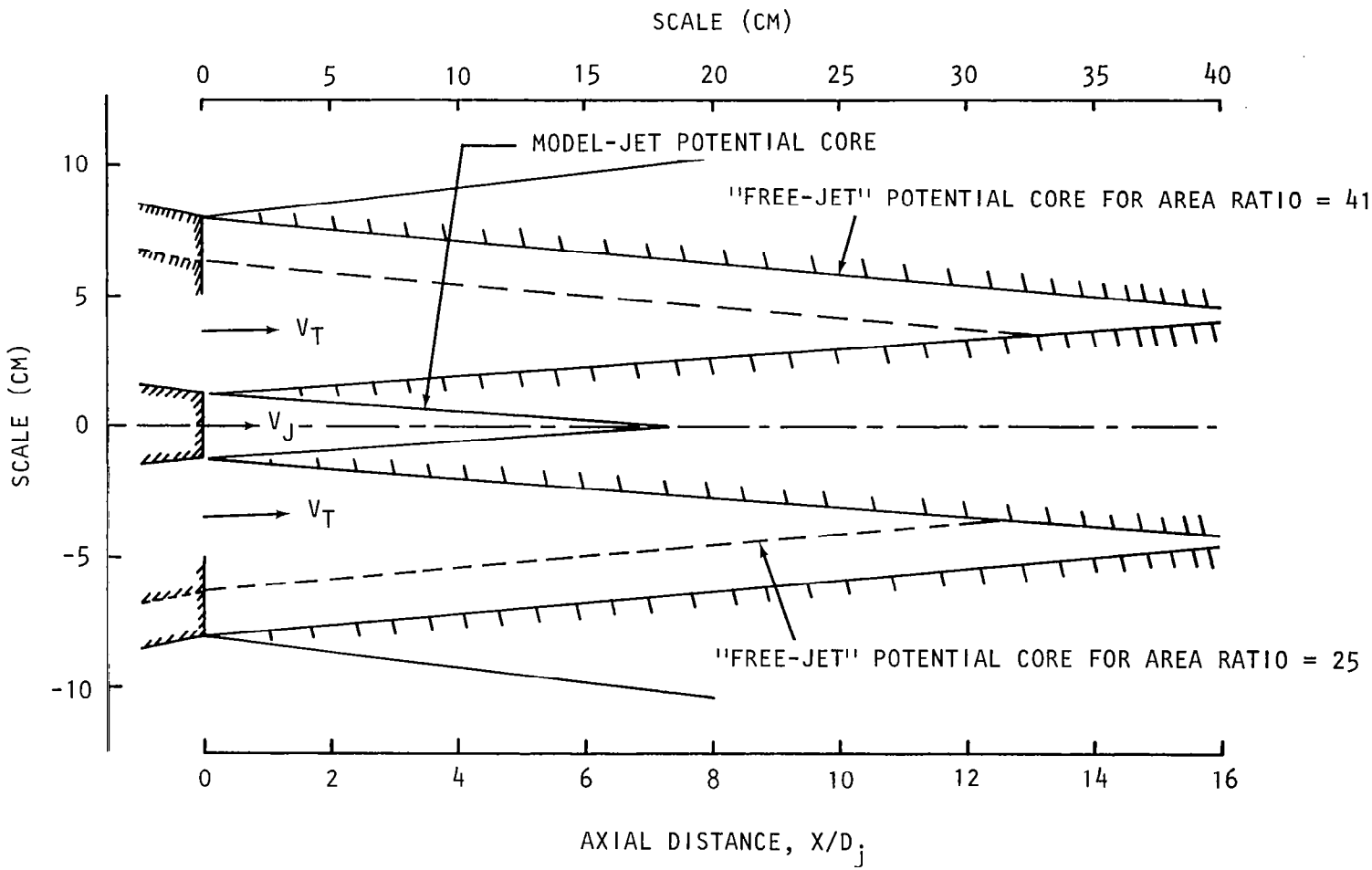

Figure 3.10 Boundaries of potential cores and shear layers of a model jet immersed in a larger surrounding jet, as measured by Lockheed LV.

The outer nozzle in the acoustic facility has an exit diameter of 71 cm, while that used in the turbulence facility has a diameter of 25 cm. For a 5-cm diameter primary-jet nozzle, these provide an outer-jet to inner-jet area ratio of 196 for the acoustic facility and 25 for the turbulence facility. Now, although this area ratio of 25 for the turbulence facility appears to be rather small at first sight, and indeed it is unacceptable for *acoustic* tests, we have gathered sufficient experimental evidence to show that it is adequate for the proposed *turbulence* measurements. The justification is as follows:

In order to determine the extent (i.e. maximum value of x/D_j) of the model-jet flow that can be adequately simulated (for forward motion) by using a coannular nozzle system, LV measurements have been conducted with two combinations of inner and outer nozzles to determine the boundaries of the inner and outer shear layers. The outer-to-inner nozzle area ratios were 41 and 10 in these tests. The inner diameter for the primary nozzle was 2.54 cm. Also, the inner and outer nozzles were operated at 300 m/sec and 90 m/sec, respectively. The boundaries of the potential cores and shear layers for the inner and outer jets for the area ratio of 41 case are shown in figure 3.10. It can be seen that at this area ratio, the model jet can be adequately simulated up to $x/D_j \doteq 16$, with no interference from the outer shear layer. It was also observed that as long as the Mach numbers in the two jets remained unchanged, the inner boundary of outer shear layer remained parallel, as the area ratio was reduced from 41 to 10. Based on this observation, this boundary for an area ratio of 25 is shown in figure 3.10 as a dashed line. For this case, it is clear that the primary jet can be accurately simulated from the nozzle-exit plane to $x/D_j \doteq 12$, which was considered adequate.

3.4 TEST PROCEDURE AND DATA ACQUISITION

3.4.1 Mode Generation and Detection

In the present study, both the plane-wave (0,0) and the first-order (1,0) spinning mode were generated in isolation by controlling the amplitudes and phases of the four acoustic drivers in the source-section. To ensure that a given-order mode was obtained, both phases and amplitudes of sound at the nozzle exit plane were measured by 12 miniature microphones as shown in figure 3.3. The flow noise was rejected from the measured data by using cross-spectral analysis (for details see appendixes A and B).

The mode detection scheme proposed by Plumblee (ref. 27) was used in this study. An outline of the scheme is as follows. The measured pressure distribution in the duct was digitized at equal angular intervals. This pressure distribution was represented as a complex set, $p(\psi)$. The Fourier coefficients were then derived using a least-square analysis formulated as

$$E(\psi) = p(\psi) - \sum_{n=0}^{N} (A_n \cos n\psi + B_n \sin n\psi) \qquad (3\text{-}1)$$

here $E(\psi)$ is the difference between the measured pressure $p(\psi)$ at angle ψ and the sum of the Fourier components, and A_n and B_n are complex constants to be determined.

If the magnitude of E is summed over all the points ψ, and then minimized with respect to the real and imaginary components of A_n and B_n, the Fourier coefficients can be determined from the resulting set of simultaneous equations. Having determined A_n and B_n, the peak amplitudes of individual mode components are determined by rearranging the Fourier components of each mode in terms of a circumferential spinning and standing wave. This is represented as

$$p(\psi) = \sum_{n=0}^{N} C_n e^{-in\psi} + D_n \cos(n\psi - \phi_n) \qquad (3\text{-}2)$$

Here, C_n and D_n are the complex amplitudes of the spinning wave and the standing wave respectively, and ϕ_n is the phase shift of the standing mode. C_n, D_n, and ϕ_n can be expressed in terms of A_n and B_n (see ref. 27) which enables one to determine the peak amplitudes of individual mode component.

A computer program was developed to detect the modes at the exit of the nozzle, on-line.

The mode detection scheme was used extensively in the acoustic facility. In the turbulence facility, however, due to the blockage of the sound-sensing ports by seeding particles normally used in laser velocimetry, this method was not found to be sufficiently accurate. A survey of sound levels and phases at the nozzle exit plane,with simultaneous iterative adjustments of the voltage and phase of the four acoustic drivers,was therefore made to set up and detect the desired modes.

3.4.2 Far-field Acoustic Measurements

Far-field acoustic measurements were made using 0.635-cm, B&K microphones on a polar arc of radius 3.5 m at every 10° in the range 20° to 120° with the jet exhaust. The sound-pressure levels were analyzed on a one-third-octave band analyzer over the frequency range from 200 Hz to 80 kHz, and the results were recorded on an incremental digital tape recorder. The recorded levels were subsequently converted into lossless 1/3-octave SPLs by using a data-reduction program which applies microphone frequency response corrections and atmospheric absorption corrections.

The jet noise measured under flight simulation was corrected to ideal wind tunnel (IWT) conditions (ref. 3), and extrapolated to 100 equivalent diameters (5.08 m).

3.4.3 Turbulence Measurements

All mean velocity and turbulence measurements were made using Lockheed's forward scatter, two color, four channel, laser velocimeter used extensively in the past for jet-noise studies (ref. 26). Both mean axial velocity and axial and radial components of turbulence intensity were measured.

3.4.4 Large-Scale Turbulence Pressure Measurements

The pressures associated with large-scale turbulence were measured using a 0.635-cm, B&K microphone fitted with a nose cone and mounted on a faired microphone support. The levels were derived from the cross-spectra between the electronic input to the acoustic driver and the microphone signal. (See appendix B for details.)

3.5 FLOW VISUALIZATION SETUP

Because of the importance of the flow visualization results obtained under a separate internal research and development program of the Lockheed-Georgia Company, a separate section (section 4.0) is being devoted to these results. For the sake of completeness, the setup for these flow visualization studies is described in section 4.0.

4.0 FLOW VISUALIZATION

Most shadowgraphs and schlieren photographs, particularly those for axisymmetric flows, display a certain degree of confused detail resulting from small-scale turbulence in the jet, and from thermal convection in the ambient air. A method of removing these sometimes unwanted details, and thereby highlighting essential characteristics, is the application of a photographic averaging technique (for example see Moore, ref. 6). This is an effective methed for revealing large-scale structure in a jet. The method involves repeated triggering of a light source and superposition of all the schlieren images on a single photographic film. By this means, the images of the coherent structure at the trigger frequency are reinforced, and those from the random turbulence tend to cancel.

The above method was used in the present experiments, but a new and very simple method of synchronizing the source of light was used (ref. 28). The laser beam passing through a Bragg cell was the source of light. The Bragg-cell shutter was synchronized with the excitation signal itself, thus the strobe frequency was the same frequency as that of the acoustic signal used to excite the jet. Some optical schlieren pictures obtained in this way are discussed in this section.

4.1 TEST SETUP

A block diagram of the optical facility is shown in figure 4.1. A photographic view is shown in figure 4.2. It features a Bragg cell that pulses the light beam from a CW Argon laser. The combination of the spatial filter and the first lens forms a collimated beam through the jet flow. The second lens focuses the collimated light at the knife edge, and images the flow area on the film plane, as in the conventional schlieren arrangement. Since the laser-light source is coherent, a graduated knife edge consisting of a reflection coating on glass, is used to avoid image degradation by diffraction. An on-axis type camera shutter is placed at the film plane to obtain the final schlieren photographs.

In operation, the Bragg cell acts as a shutter blocking the laser beam. In this application, when the cell is excited by a known frequency signal, the light beam is deflected, and thus aligned with the schlieren optics. A pulsed shutter is obtained by using a diode switch to interrupt the excitation except when activated by the pulse generator.

Two modes of operation are available with the present arrangement. In the multiple-pulse mode, the Bragg cell is continually pulsed by the acoustic signal, and the camera shutter is adjusted to average the light from several pulses to illuminate the large-scale structure. In the single-pulse mode, the camera shutter is used to limit exposure to background

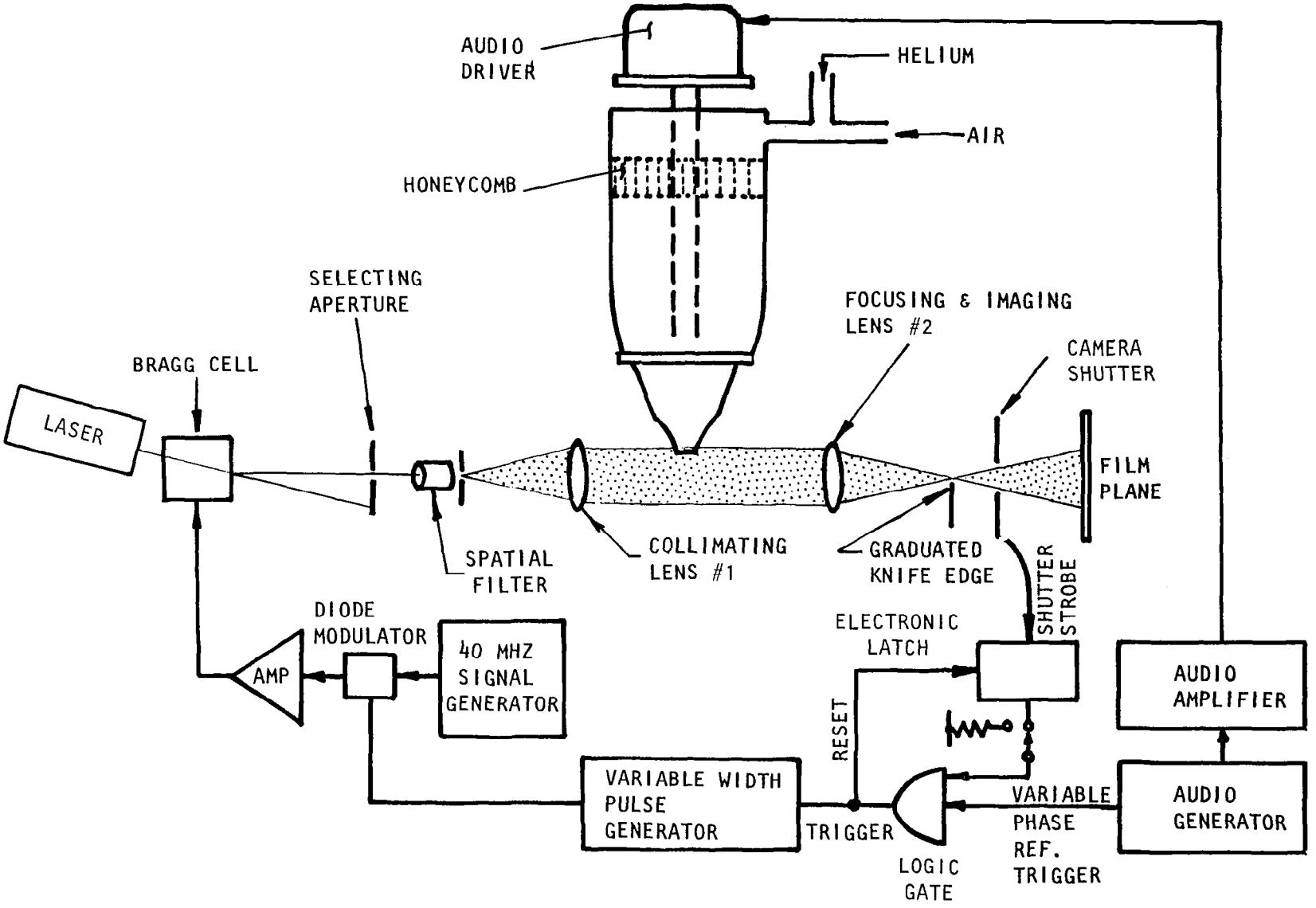

Figure 4.1 Schematic of the flow-visualization setup and the associated electronics.

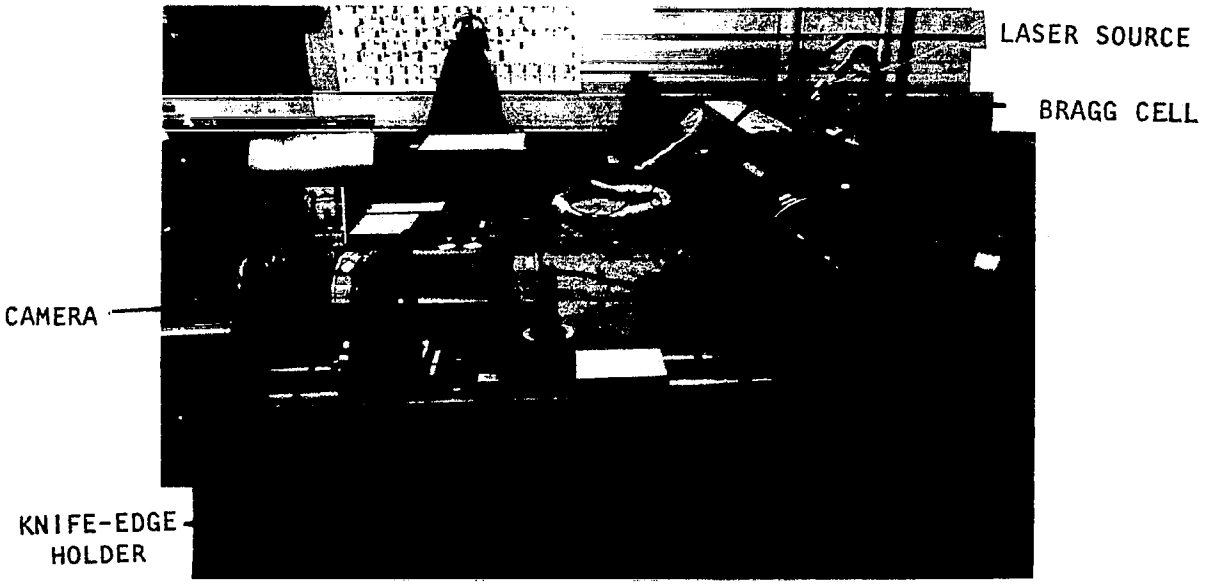

Figure 4.2 Photographic view of the optical setup

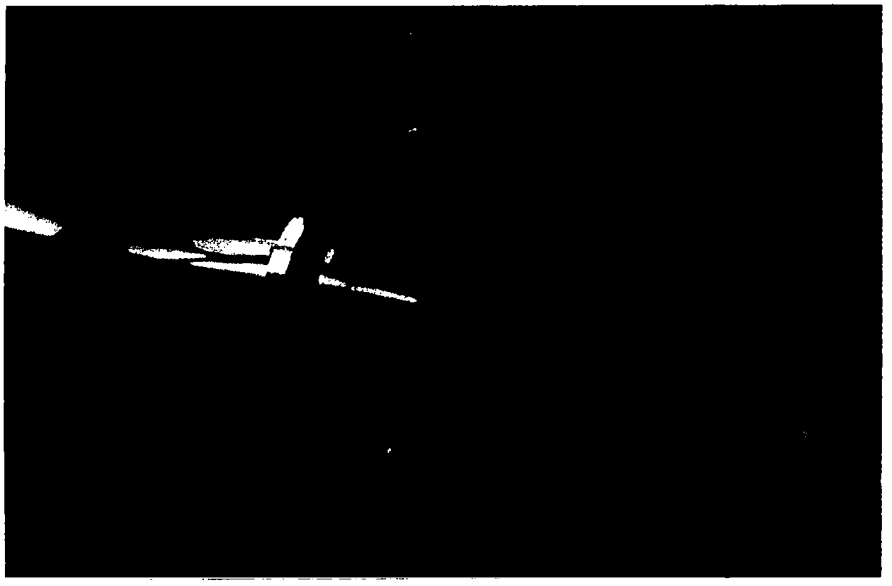

Figure 4.3 View of the 1.25 cm diameter nozzle and the heated wire used for flow-visualization studies.

light (some residual light comes through the selecting aperture) and the shutter strobe opens a latch that allows the next audio trigger to pulse the Bragg cell.

The power level of the laser-light source is adjustable up to several watts, and this provides excellent film exposure control.

The jet, for this part of the study, exhausted from a conical nozzle of 1.25 cm exit diameter. The nozzle was connected to a 25.4 cm diameter plenum chamber. This provides an area ratio between the plenum and the nozzle of 400. Thus, the flow through the nozzle was quite clean, and the velocities in the plenum chamber were almost insignificant. The air to the jet was supplied by the shop air.

Since the jet velocities were low, air density variations were too small to be recorded. Therefore, either helium or a heated nichrome wire as shown in figure 4.3 was used to produce the refraction changes necessary to make the flow visible.

4.2 RESULTS

Figure 4.4 shows typical schlieren photographs of an unexcited jet and an excited jet. Here the light source was synchronized with the acoustic signal but the film plate was exposed only once. These photographs show quite clearly how the jet plume has widened considerably as a result of upstream excitation. In addition to a general disruption in the movement of the small-scale turbulence, new large-scale vortices appear some distance downstream of the exit. These vortices travel downstream, and their position in the schlieren photographs depends upon the phase relationship between this orderly vortex structure and the strobe signal.

To prove that these vortices are indeed orderly, the film plate was exposed 30 times, using the above mentioned technique of photographic averaging, and the resulting photograph is shown in figure 4.5. The vortex structure seen here is the so-called large-scale turbulence structure, also called the "instability wave" by some in the published literature.

The photograph of the large-scale turbulence shown in figure 4.5 was obtained at a nondimensional frequency $f_e D_j/U_j$ equal to 0.5. (Here, f_e is the excitation frequency in Hz, and D_j and U_j are the jet diameter and exit velocity, respectively.) If this excitation frequency is doubled, a different normal mode of the naturally existing large-scale turbulence structure is excited, and the resultant photograph, again obtained by averaging, has a different structure, as shown in figure 4.6. Here the frequency of the large-scale structure is also doubled, and there are now twice as many vortices in a given volume. Since small-scale turbulence accompanies this large-scale turbulence, it can be inferred that the behavior of the small-scale turbulence will be affected by the behavior of these large-scale structures.

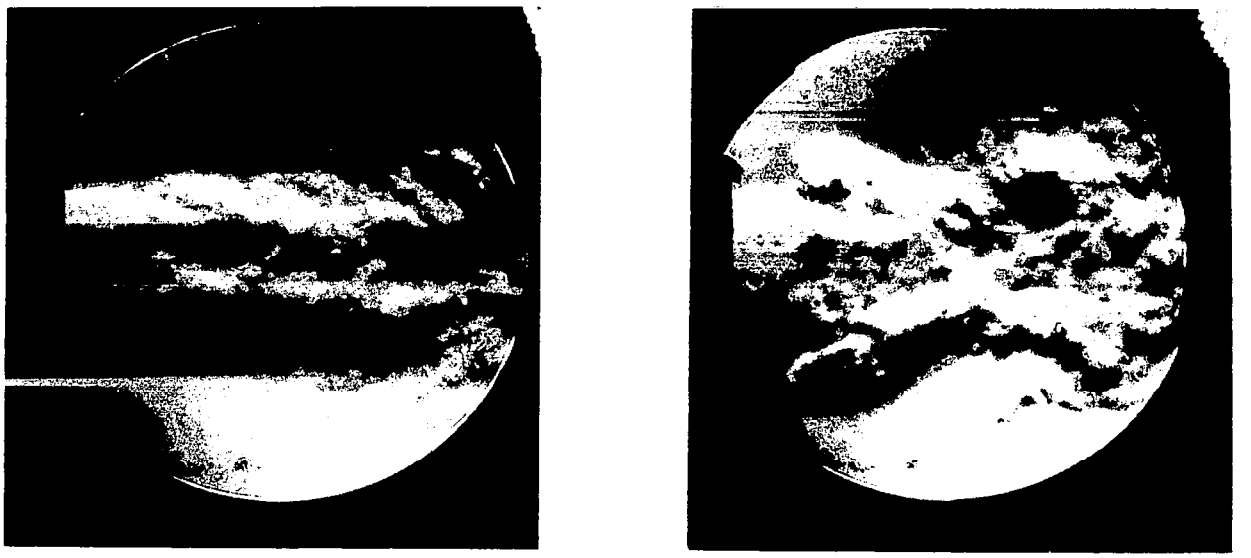

(a) (b)

Figure 4.4 Schlieren photographs of (a) an unexcited and (b) an excited jet.

Figure 4.5 Photographic averaging of the excited jet shown in Figure 4.4(b).

Figure 4.6 Photographically averaged schlieren photograph of a jet excited at twice the frequency of excitation used in Figure 4.5.

Due to the interesting nature of these results, other schlieren photographs, taken by the photographic averaging technique described above, are shown in figures 4.7 thru 4.9. Four schlieren photographs are shown in each figure. Each successive photograph in each figure was taken by delaying the light-strobing phase by 90°. The motion of the large-scale structure with respect to time and space thus becomes quite clear.

The excitation Strouhal numbers in figures 4.7 thru 4.9 were 0.25, 0.5, and 1.0, respectively. The laser-light strobe frequency was the same as the excitation frequency, and hence the large-scale structure in each figure is occurring at the excitation frequency or at a frequency that is harmonically related to the excitation frequency. However, through detailed frequency domain measurements of the pressure associated with these large-scale structures, described in section 5.0, it was concluded that the large-scale structure is excited at the frequency of excitation itself.

The effect of increasing the excitation level on the jet structure is shown in the schlieren photographs of figure 4.10. Here, similar to the photograph shown in figure 4.4, the photograph was exposed only once, primarily to see the changes in the small-scale turbulence surrounding the large-scale structure. As the excitation voltage (peak-to-peak), and thus the excitation level, is increased, the excited large-scale structure appears to become more dominant and the jet appears to widen, indicating enhanced mixing in the jet.

Quantitative results alluding to the qualitative results presented above are presented in the next section.

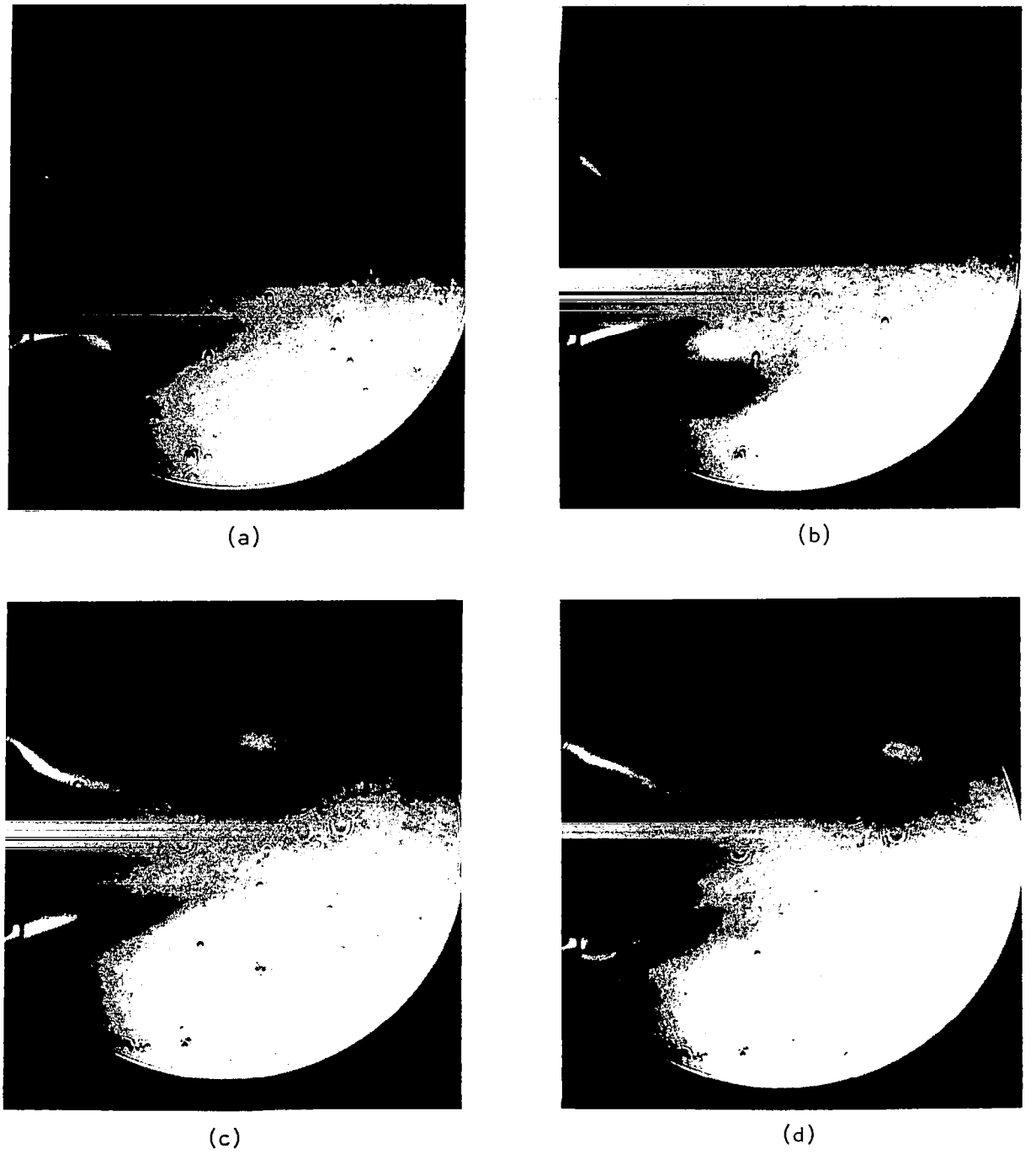

Figure 4.7 Ensemble-averaged schlieren photographs of an excited jet with figures (a) thru (d) successively delayed by 90° in phase. S_e = 0.25, Driver-peak-to-peak voltage = 40V, V_j = 21 m/s.

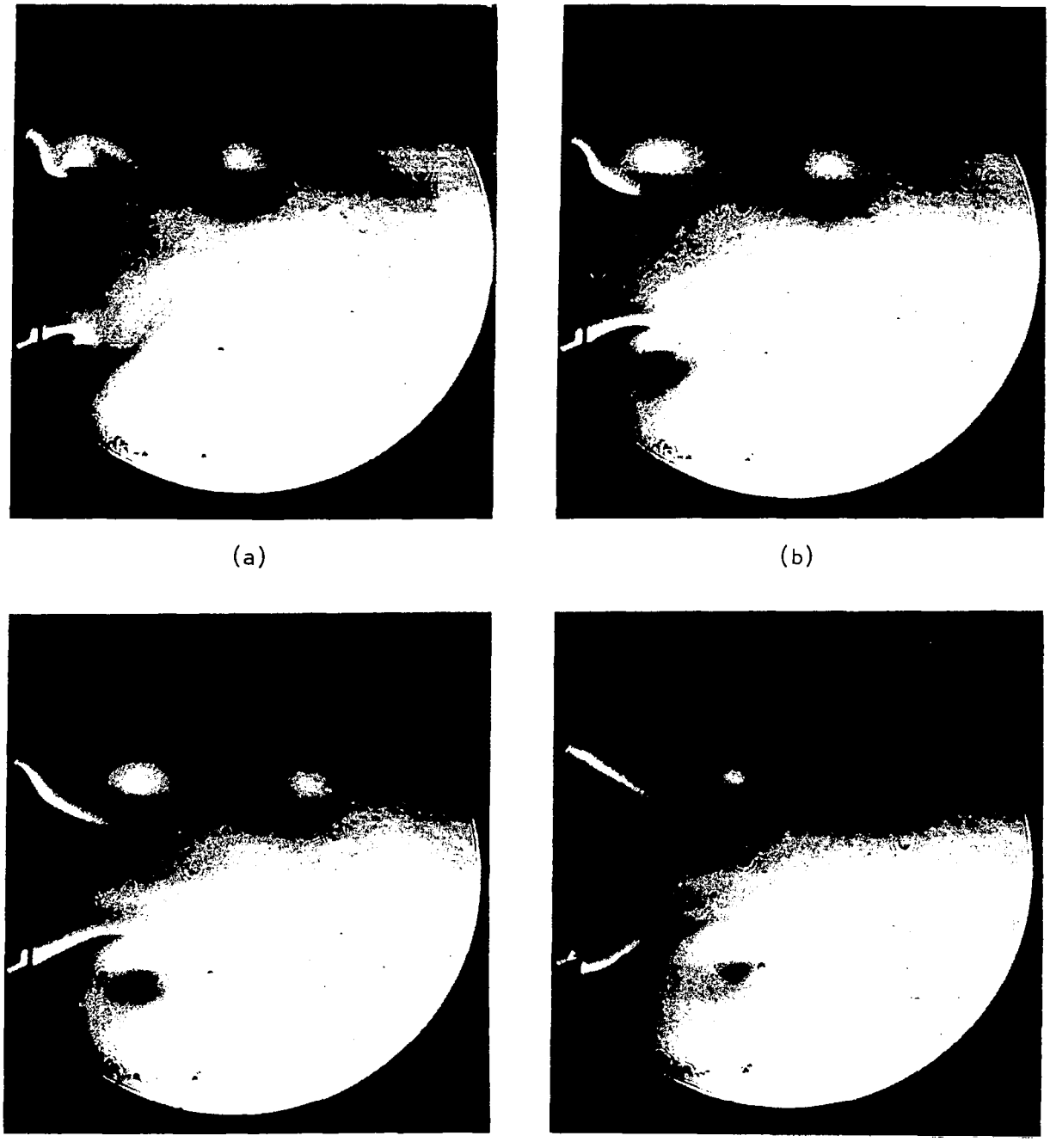

Figure 4.8 Ensemble-averaged schlieren photographs of an excited jet with figure (a) thru (d) successively delayed by 90° in phase. $S_e = 0.5$, Driver-peak-to-peak voltage = 40V, V_j = 21 m/s.

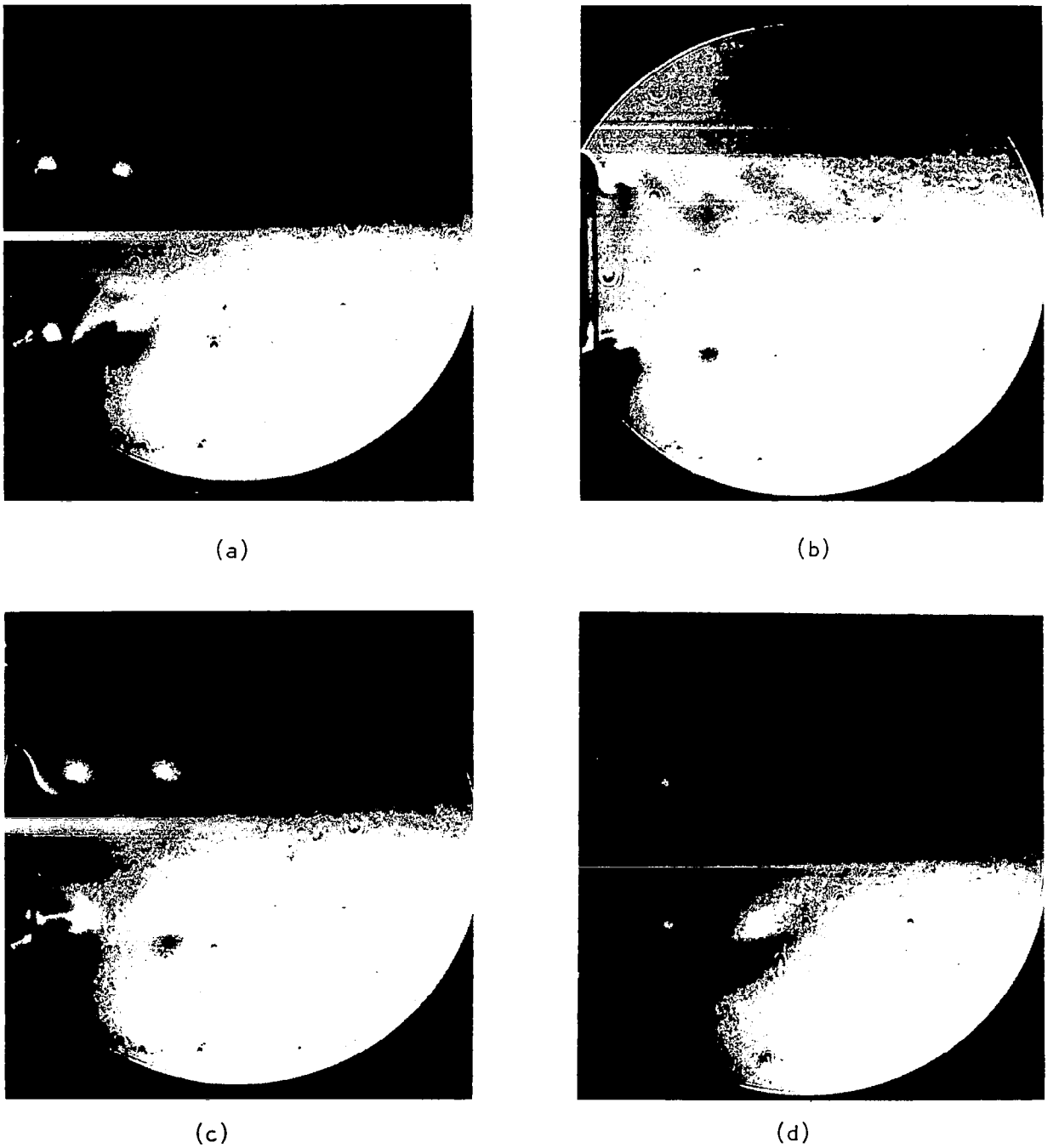

Figure 4.9 Ensemble-averaged schlieren photographs of an excited jet with figures (a) thru (d) successively delayed by 90° in phase. S_e = 1.0, Driver peak-to-peak voltage = 40V, V_j = 21 m/s.

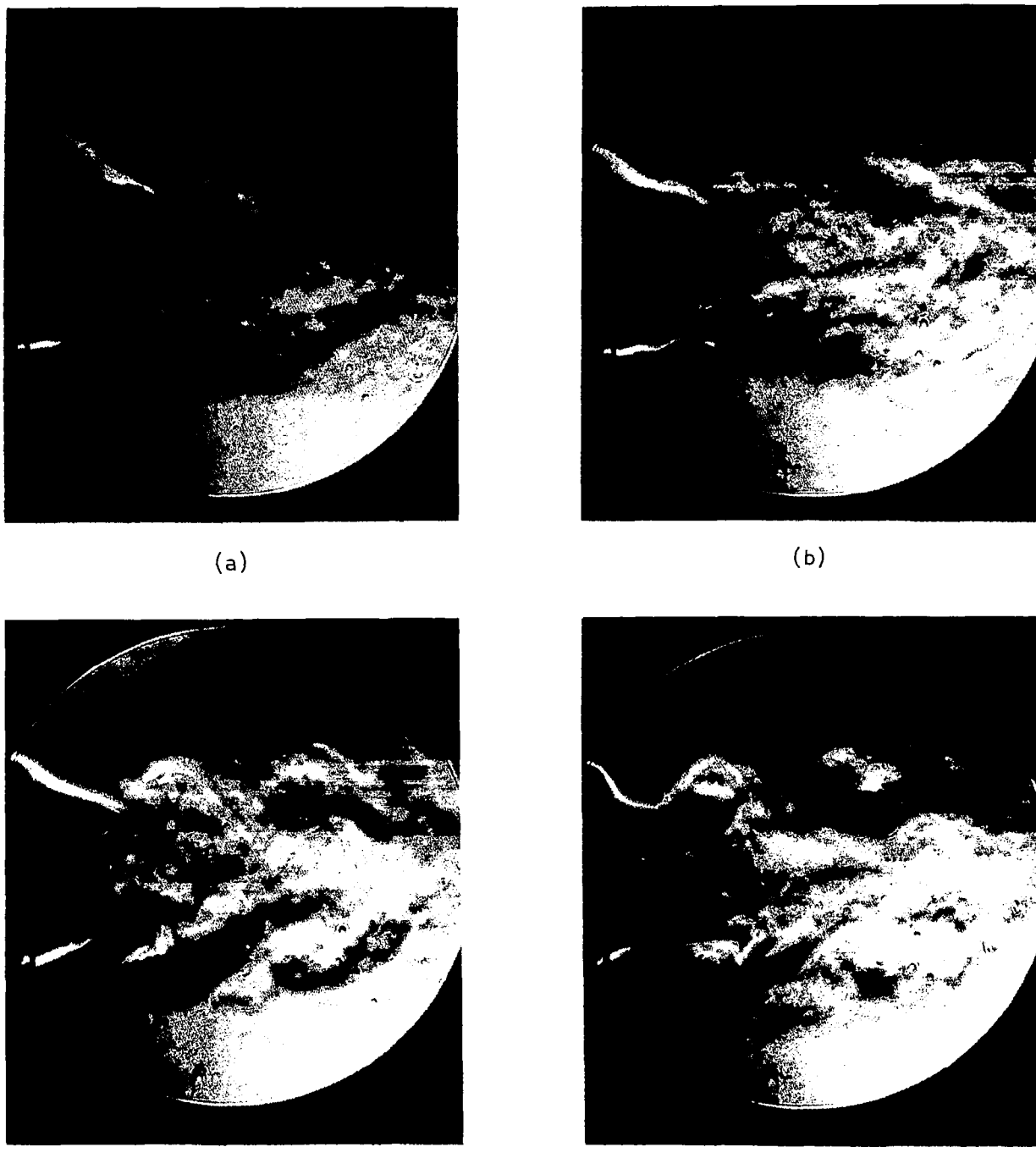

Figure 4.10 Effect of increasing the excitation levels on jet structure at S_e = 0.5 and V_j = 21 m/s. Driver peak-to-peak voltage: (a) unexcited, (b) 1V, (c) 10V, (d) 40V.

5.0 TURBULENCE RESULTS

Because of the time-consuming nature of turbulence-data acquisition, the flow and excitation parameters for which the turbulence data were acquired, were dictated by those conditions that provided maximum jet-noise amplification. As shown in the next section on acoustic results, maximum amplification was obtained when the jet was excited at a Strouhal number of 0.5. The majority of the data were, therefore, acquired at this Strouhal number. Data for two jet Mach numbers (M_j = 0.58 and 0.79) and two temperatures (unheated and 800K) were obtained. The majority of the results presented here are, however, for the unheated condition.

To preserve clarity of the plotted turbulence results, it has been decided to show smooth curves through the measured points, instead of all the individually measured points. For the sake of completeness, however, representative plots of actual measured points together with these smooth curves are given separately in appendix D. The maximum deviation of the measured points from the best fitting curve is ±0.04 for the dimensionless mean velocity and ±1.0% for the turbulence intensity, throughout the whole range of the experimental conditions.

Before presenting the detailed mean-velocity and turbulence-intensity results, pressures associated with the large-scale turbulence, excited by upstream sound, are presented. It is felt that these results, together with the flow-visualization results already presented, will provide adequate background to explain the mean-velocity and turbulence-intensity results presented in subsections 5.2 thru 5.7.

To save repetition, it is worth pointing out here that all the results up to subsection 5.4 are for the unheated jet operated under static conditions and the plane wave (0,0) mode only. Mode-order effects, flight-simulation effects, and the temperature effects are described separately in subsections 5.5, 5.6 and 5.7, respectively.

5.1 LARGE-SCALE TURBULENCE PRESSURES

As already seen in the schlieren photographs presented in section 4.0, the large-scale turbulence structure in the excited jet is quite well defined. From measurements of the fluctuating pressure within the flow, both radially and axially, it was found that the frequency of the excited large-scale structure was the same as that of the acoustic excitation signal. An interesting feature was that the frequency bandwidth of this pressure fluctuation was extremely narrow, for example see figure 5.1.

Figure 5.2 shows a typical variation of the large-scale turbulence pressure magnitude (p'_e) with distance, along the axis. Here the jet was excited with a discrete tone at Strouhal number, S_e = 0.5. The top curve was obtained at an excitation level of 141 dB. On the same figure is

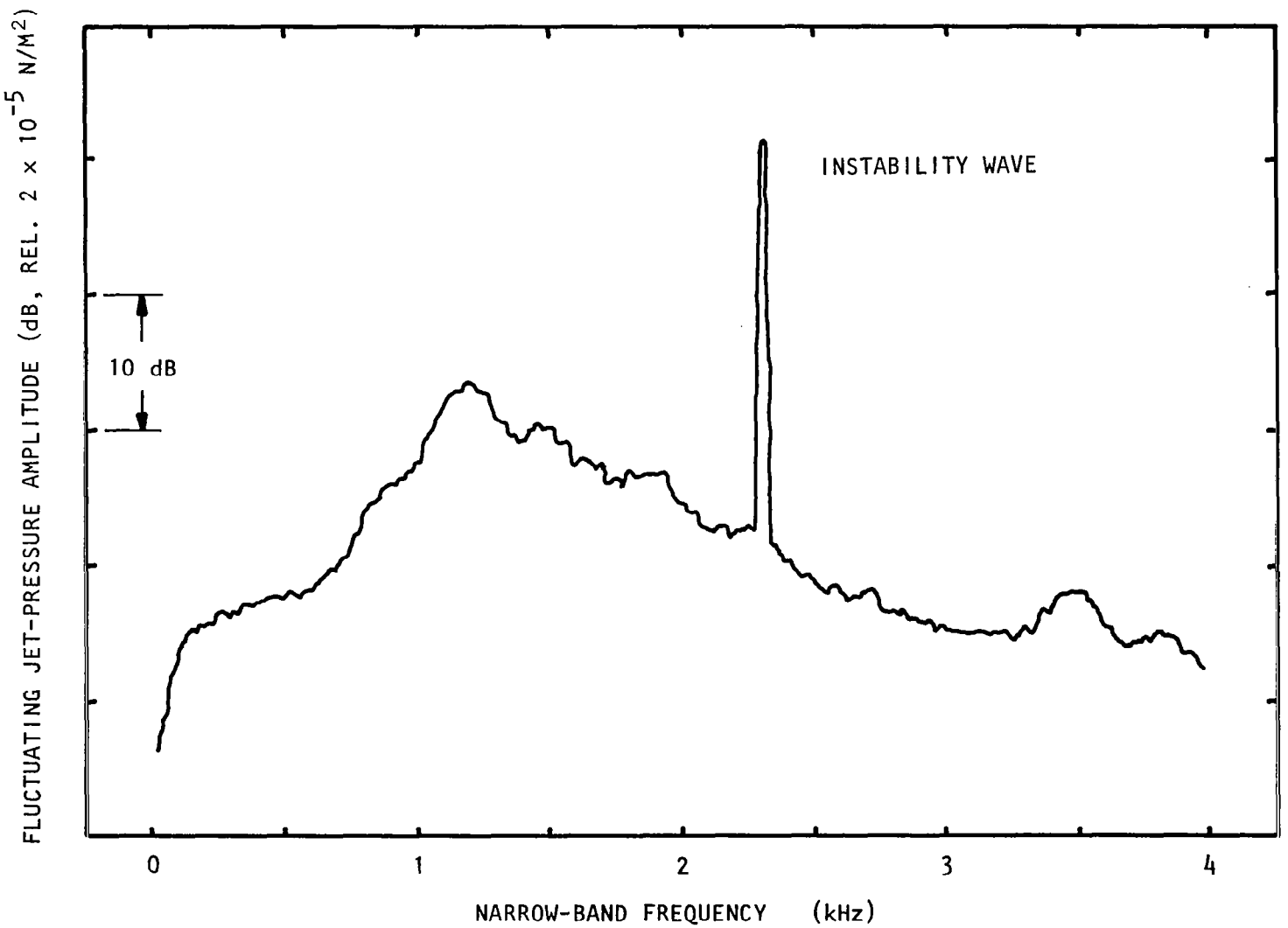

Figure 5.1 Typical spectrum of the jet-centerline pressure at $x/D_j = 3.0$. $M_j = 0.58$, Unheated, Static, $f_e = 2330$ Hz, $S_e = 0.6$, $L_e = 136$ dB, analysis bandwidth $\Delta f = 10$ Hz.

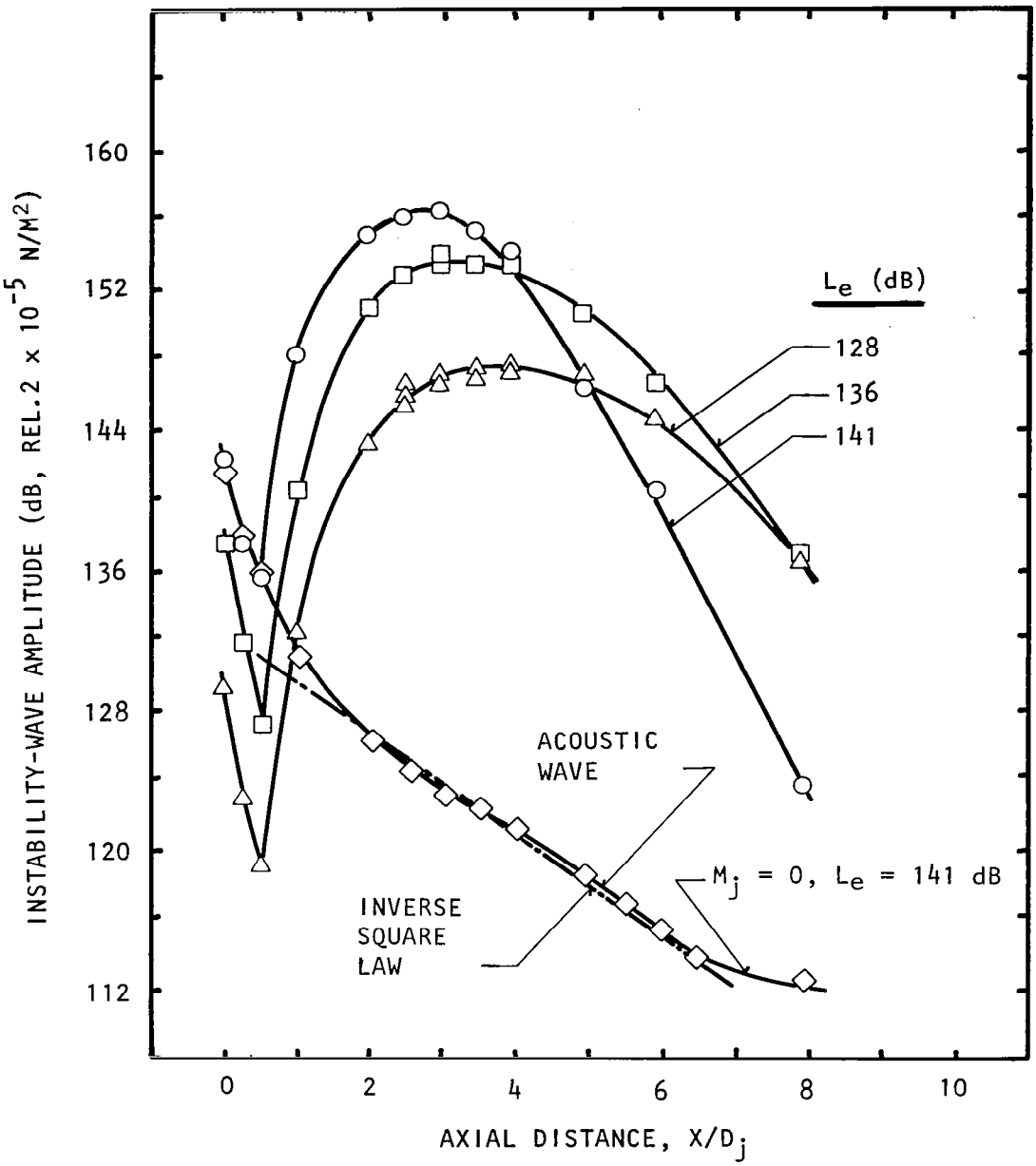

Figure 5.2 Centerline variation of instability-wave pressure amplitude at various excitation levels. M_j = 0.58, U_j = 195 m/s, Unheated, Static, S_e = 0.5, (0,0) Mode.

shown the pressure variation with the flow turned off but with the excitation level kept at 141 dB. It is clear from this figure that, in the presence of the jet flow, the acoustic signal is dominant close to the nozzle exit up to about 1/2 diameter. Thereafter, the hydrodynamic-wave magnitude starts rising very rapidly, reaches a peak, and is then followed by a gradual decrease in level. The fluctuating pressure due to the large-scale structure is about 35 decibels higher than that due to the acoustic signal.

Curves of the large-scale instability wave are not necessarily parallel to each other for various excitation levels as seen in figure 5.2 for three different excitation levels, namely, 141 dB, 136 dB, and 128 dB. Close to the nozzle exit the behavior is linear, but further downstream there is considerably less amplification at the higher excitation levels. At large distances downstream, in fact, there is even a decrease in the measured pressure levels of the large-scale turbulence for an increase in excitation level.

Detailed explanations of the above behavior are given in section 7.0. To understand the results presented in the remaining part of this section, however, a summary of these explanations is given below.

When the jet is excited by a low-level acoustic source, the large-scale instability wave tends to lock onto it, and produces a response that is in agreement with the linear shear-layer instability theory. It extracts energy from the mean flow in the initial region of the jet, indicated by the initial rise of the curve in figure 5.2. However, further downstream, due to larger jet width, the growth rate of the instability wave is decreased, and as the wave decays, part of its energy is transferred back to the mean flow. Thus, at low excitation levels, there is basically a back-and-forth exchange of energy between the instability wave and the mean flow. At higher excitation levels, however, the wave extracts considerable energy from the jet mean flow, and the response becomes nonlinear as some of this energy is converted into small-scale turbulence energy. This interaction involves both the generation of random turbulence and its transport.

The increase in the level of the random, turbulent kinetic energy causes a more rapid spreading of the jet flow through an increase in turbulent stresses. Thus, for high level excitation, some distance downstream of the nozzle exit (e.g. beyond the peak of the upper curve in figure 5.2), the wave transfers more energy to the random turbulence than it gains from the mean flow, and it begins to decay rapidly. Based upon these results, the effect of nonlinearity is to lower the peak of the amplification curve, and move it back toward the nozzle. The severity of this effect depends upon the strength and frequency of the excitation and the mean velocity of the jet flow. This can be seen in figure 5.3, where similar plots for $S_e = 0.5$ but for a higher jet Mach number ($M_j = 0.78$) are plotted. Here, even though there is some tendency for nonlinearity at the highest excitation level of 141 dB, this nonlinearity is, nevertheless, considerably less severe than that seen in figure 5.2 for the lower jet Mach number. Similar results are obtained for a different Strouhal number, for example $S_e = 0.4$, as shown in figure 5.4.

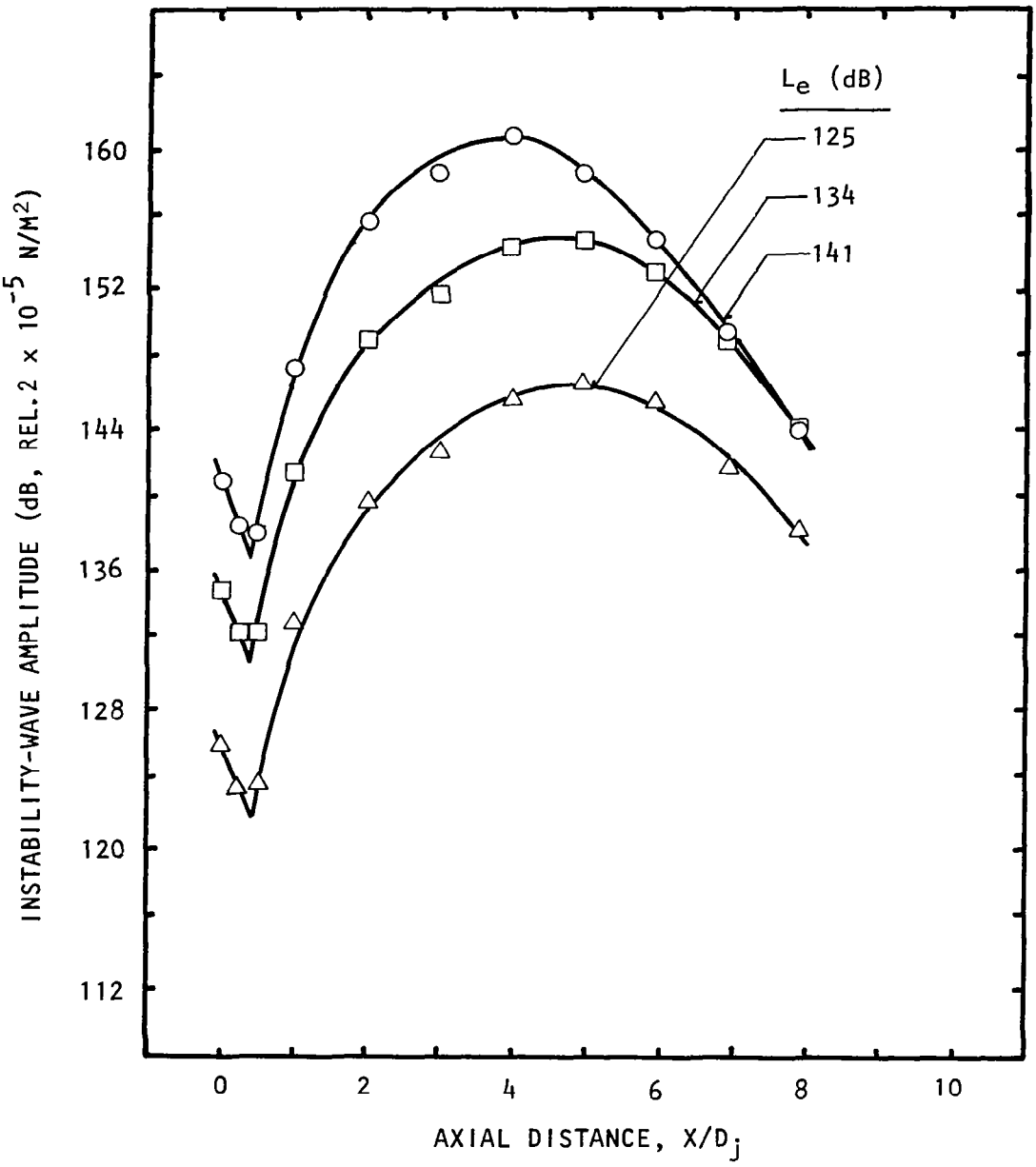

Figure 5.3 Centerline variation of instability-wave pressure amplitude at various excitation levels. M_j = 0.78, U_j = 255 m/s, Unheated, Static, S_e = 0.5, (0,0) Mode.

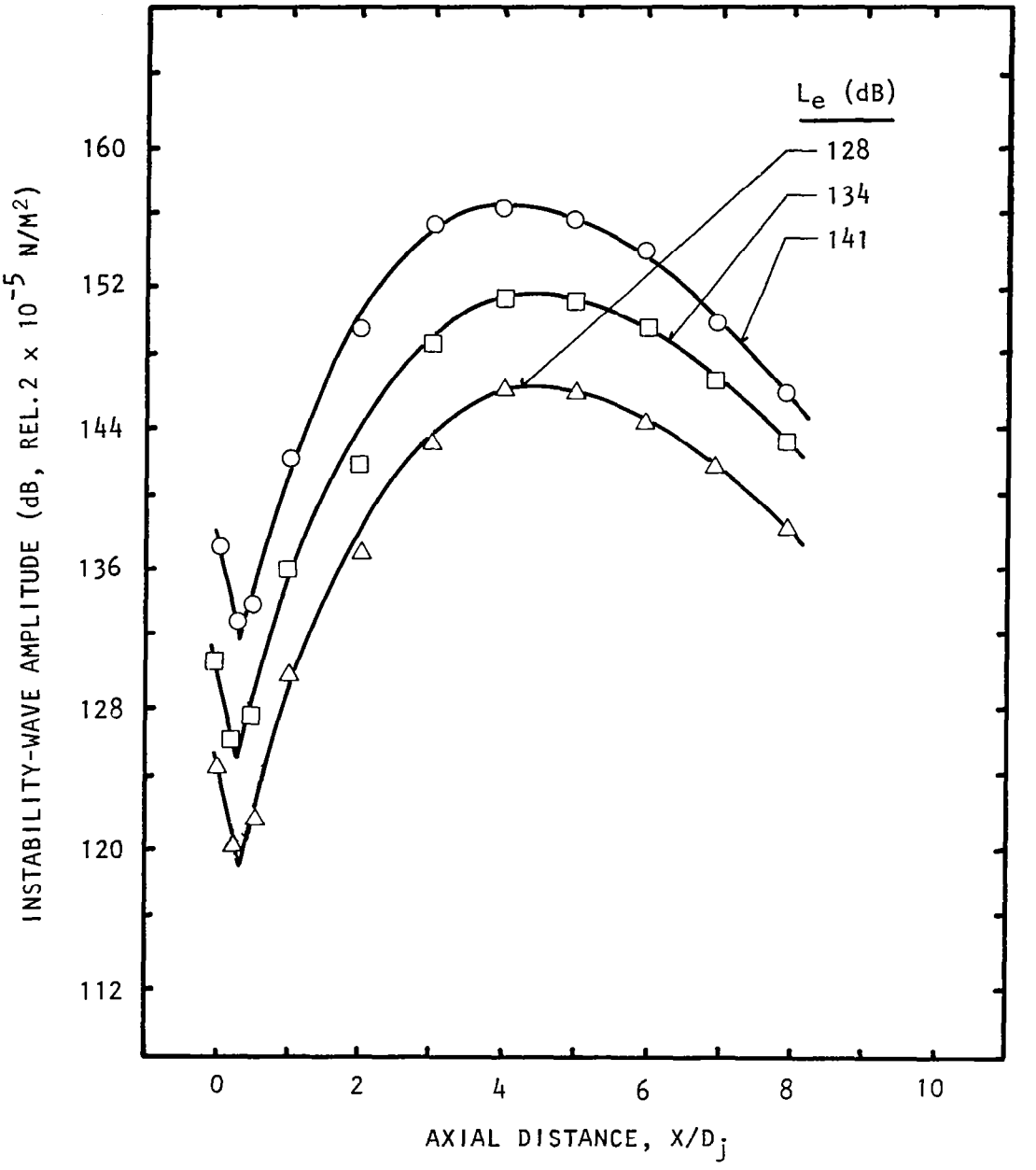

Figure 5.4 Centerline variation of instability-wave pressure amplitude at various excitation levels. M_j = 0.78, U_j = 255 m/s, Unheated, Static, S_e = 0.4, (0,0) Mode.

It should be noted that, up to the tip of the potential core of the jet, the effect of the excited instability wave of the large-scale structure is felt throughout the jet, and the maximum amplitude of the instability-wave pressure occurs close to the lip, as shown in pressure-magnitude profile plots of figure 5.5. Similar conclusions can be drawn by comparing the lip line and the centerline distribution of the instability-wave amplitude as shown in figure 5.6.

Other results of importance were the phase-velocity measurements. Phases of the pressures, measured by a nose-cone microphone, along the centerline of the jet were measured with respect to the electronic signal fed to the electro-acoustic drivers. This method of phase measurement was similar to that used by Bechert and Pfizenmaier (ref. 29) and Moore (ref. 6). Typical results are shown in figure 5.7. Based upon these phase measurements, the phase velocity of the jet operated at $M_j = 0.58$ ($V_j = 190$ m/s) was found to be 170 m/s which was significantly different from the speed of sound. These results, together with the fact that beyond about one jet diameter instability-wave pressure amplitude were significantly higher than those of the acoustic wave (as shown in figure 5.2), confirm that the measured pressures were indeed the instability-wave pressures for axial distances larger than one jet diameter.

The modifications of the flow structure due to the presence of the excited instability waves will now be discussed.

5.2 EXCITATION LEVEL EFFECTS

The results of the acoustic experiments described later in section 6.0 indicated that maximum amplification in the broadband jet noise due to discrete-tone excitation was obtained at an excitation Strouhal number, S_e, between 0.4 and 0.63. The majority of the detailed turbulence measurements were, therefore, made at the intermediate excitation Strouhal number, $S_e = 0.5$. These detailed measurements at $S_e = 0.5$ included the variation of turbulence-intensity and mean-velocity profiles with axial distance, both with and without upstream excitation. For other Strouhal numbers, only the centerline distributions of the mean velocities and turbulence intensities were measured.

The effect of excitation level on centerline and the lip-line distribution of the mean velocities as well as turbulence intensities are shown in figure 5.8. Here the data for $M_j = 0.58$, $S_e = 0.5$, and the jet excited by plane-wave mode at excitation level $L_e = 128$, 136, and 141 dB are compared with the corresponding values for the unexcited conditions. The rapid decay of the mean-velocity with downstream distance clearly shows that, as the excitation level is increased, the potential core is reduced in length. This effect is further seen in figure 5.8 in the plots of centerline distribution of turbulence intensities, where it is found that the turbulence intensities increase as a result of increased upstream excitation level. It is to be noted that, at high levels of excitation, the turbulence-intensity distribution has a hump between two and three diameters downstream. This is because these plots are for the total fluctuating-velocity intensity, which

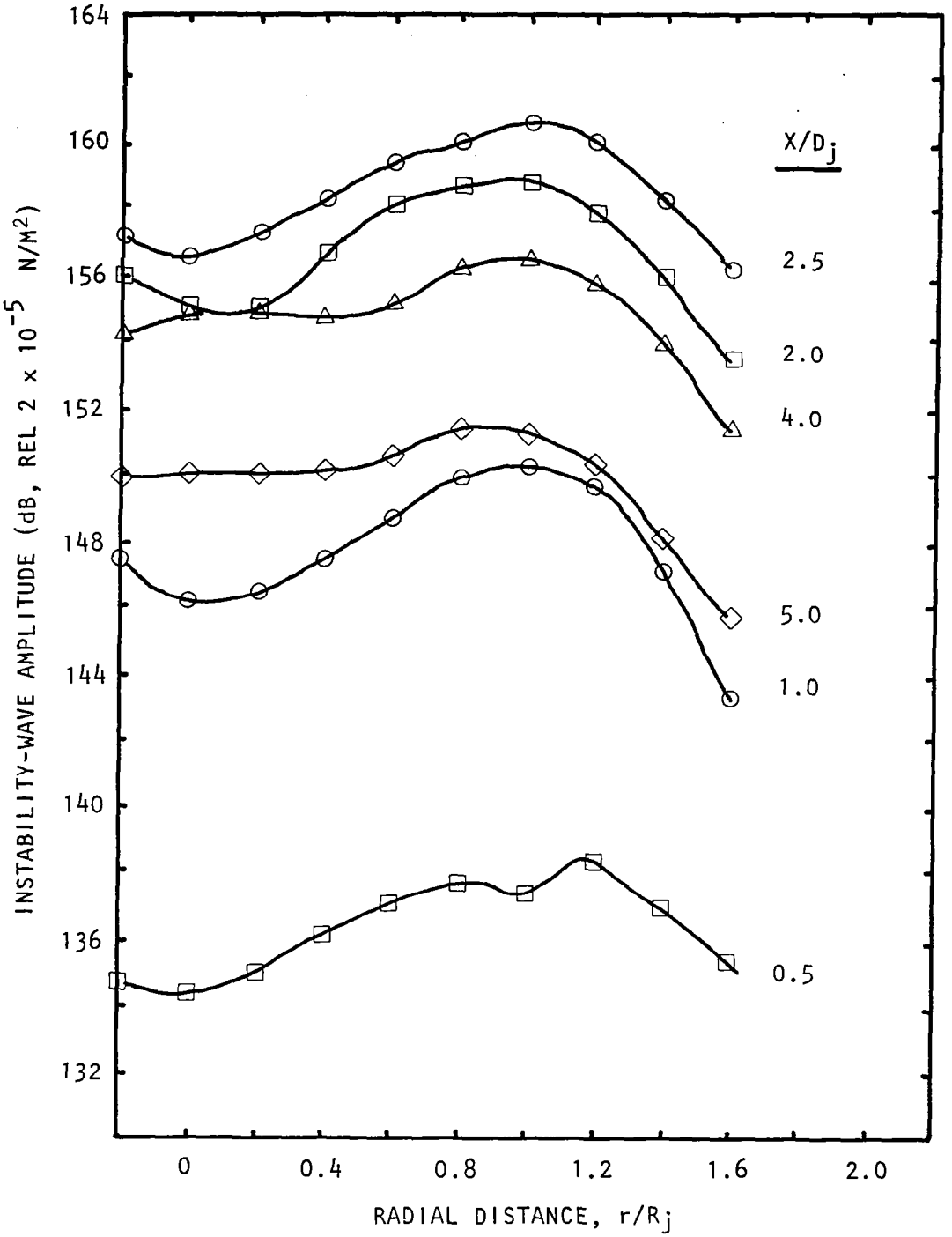

Figure 5.5 Instability-wave pressure profiles at various axial distances. M_j = 0.58, U_j = 195 m/s, Unheated, Static, S_e = 0.5, L_e = 141 dB, (0,0) Mode.

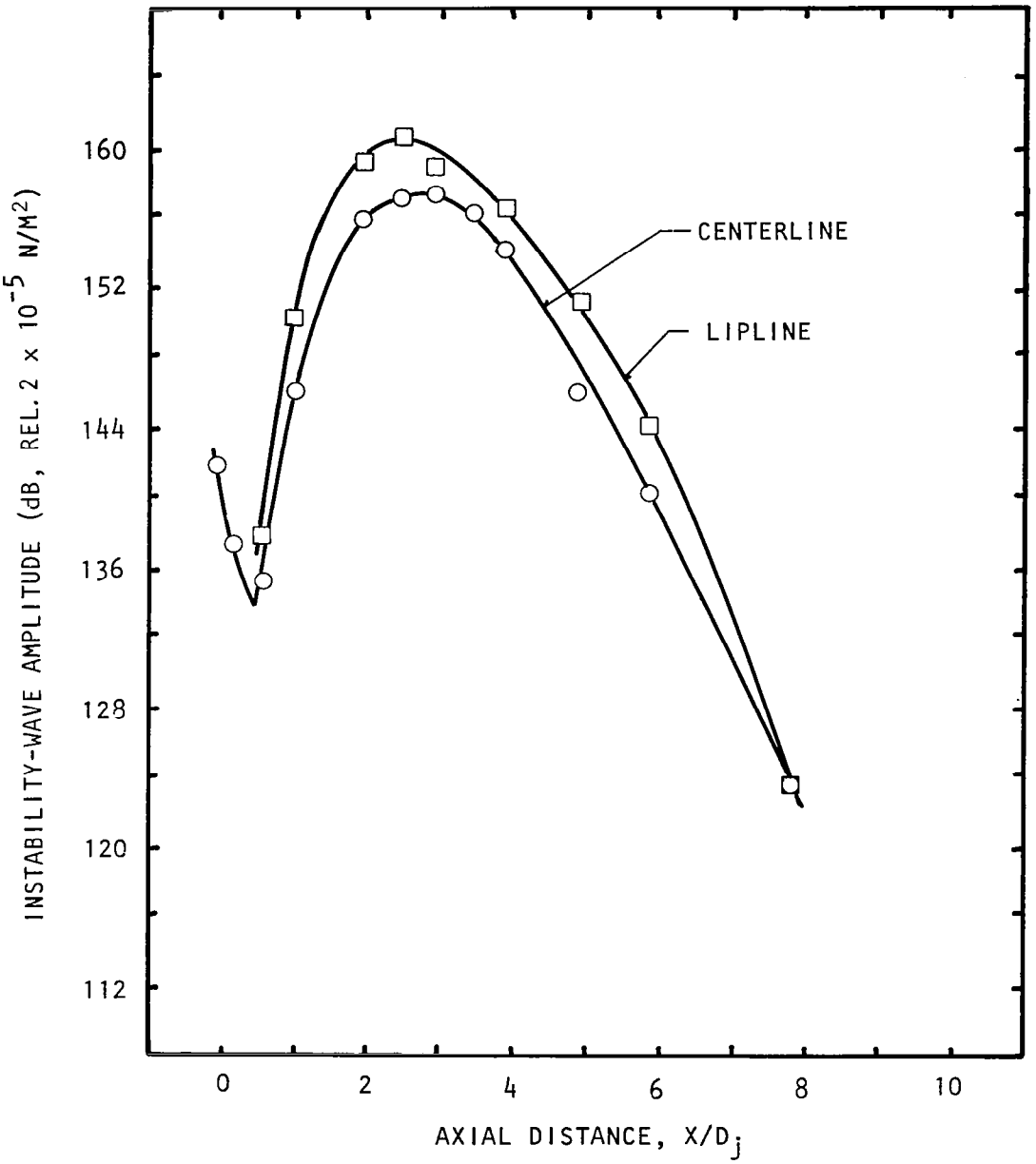

Figure 5.6 Comparison between the centerline and the lipline distribution of the instability-wave pressure amplitude.
M_j = 0.58, U_j = 195 m/s, Unheated, Static, S_e = 0.5, L_e = 141 dB, (0,0) Mode.

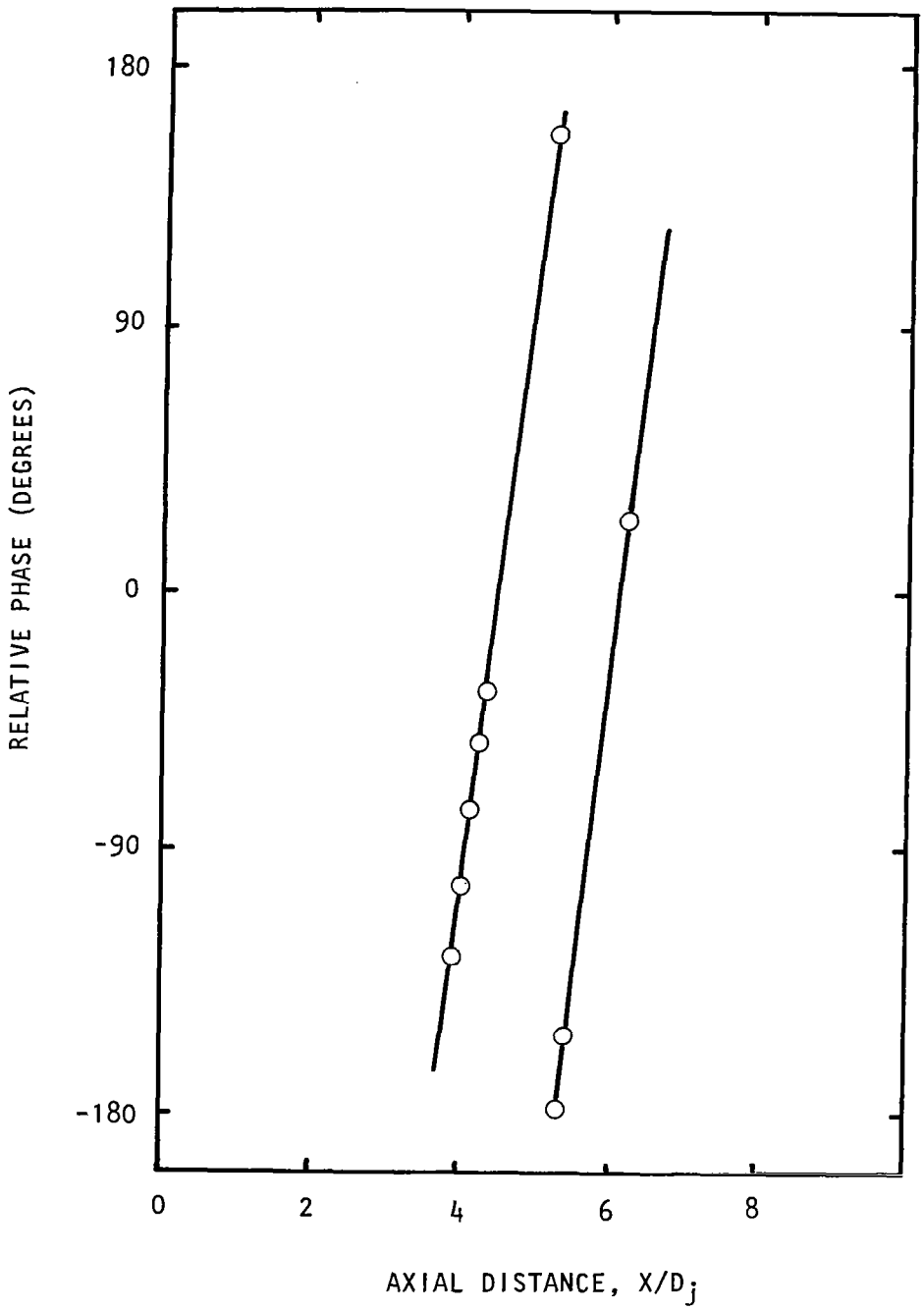

Figure 5.7 Instability-wave phase distribution.
M_j = 0.58, U_j = 195 m/s, Unheated, Static, S_e = 0.5,
L_e = 136 dB, (0,0) Mode.

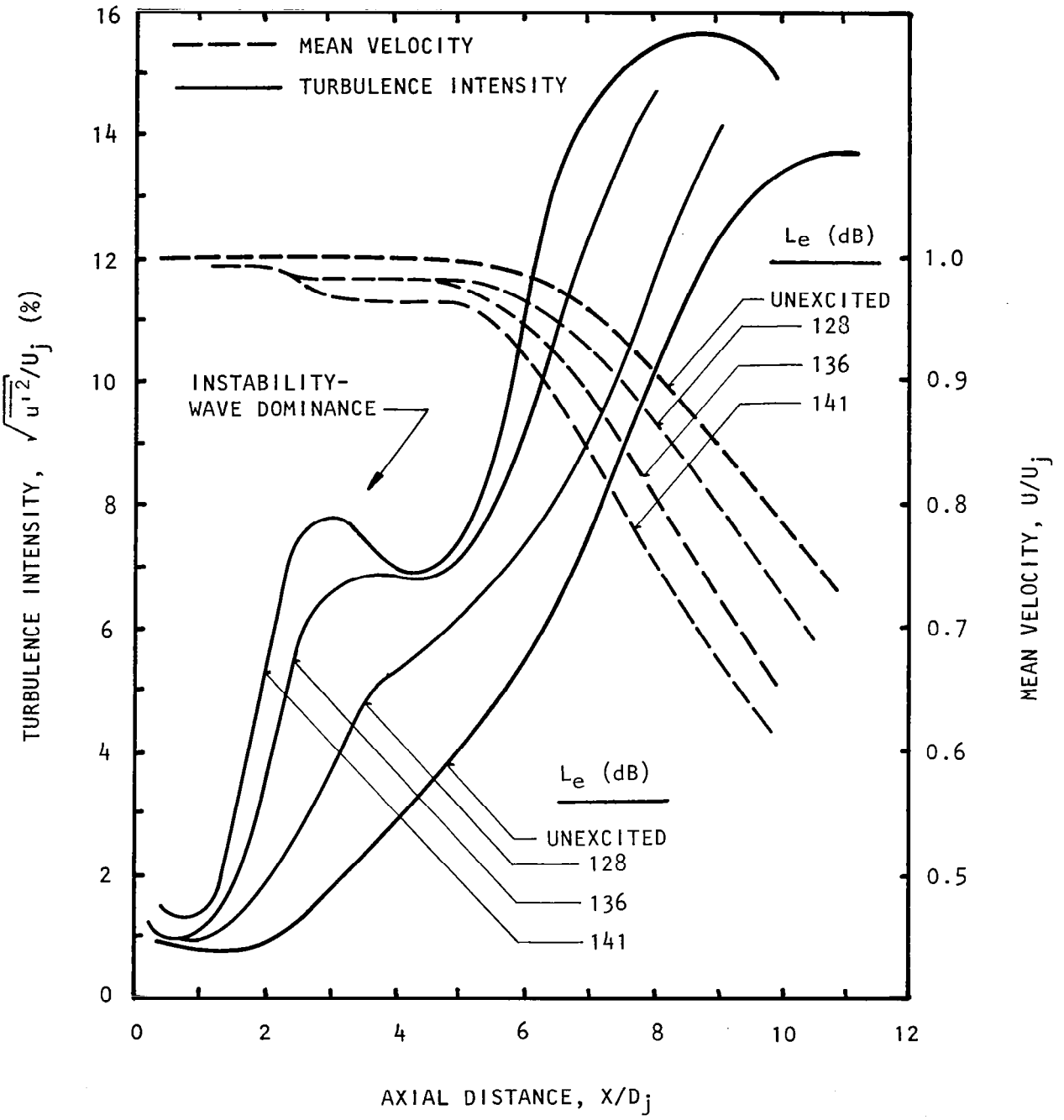

Figure 5.8 Excitation-level effects on centerline distributions. Mj = 0.58, U_j = 195 m/s, Unheated, Static, S_e = 0.5, (0,0) Mode.

(See figures D.1(a) and D.1(b) for actual measurement points.)

includes the components from the small-scale as well as the large-scale turbulence. However, beyond about five to six diameters, the contribution from the large-scale turbulence is insignificant and most of the changes in turbulence intensity are those due to the small-scale turbulence alone.

To see how the velocities are changed along various radial locations, contours of $U/U_j = 1$ and 0.5 are plotted in figure 5.9. This figure shows clearly that, at an excitation level of $L_e = 141$ dB and Strouhal number $S_e = 0.5$, the potential-core length has decreased from almost 5.75 diameters to about 3 diameters. Similarly, the half-velocity contour has shifted outward, indicating an overall opening-up of the jet plume, and thus an increased mixing and entrainment of ambient air.

Similar results were obtained at other Mach numbers, for example, see figure 5.10 for $M_j = 0.78$; and at other excitation Strouhal numbers, for example, see figures 5.11 and 5.12 for $S_e = 0.4$ and 0.6 respectively.

For the sake of completeness, contours of mean velocity and turbulence intensity acquired in this study are shown in figure 5.13 for both the unexcited and the excited conditions. A close inspection of these contours leaves no doubt in establishing that the effect of upstream excitation is to widen the jet plume, and increase the large-scale as well as the small-scale turbulence considerably. This is further seen in the radial profiles of the mean velocities, and axial components of turbulence intensities at various axial locations shown in figure 5.14.

Published literature on the effects of upstream excitation on the jet flows is seriously lacking in detailed flow-data. In the present study, in addition to mean velocity and axial turbulence data, some radial-turbulence intensity data were also acquired. Typical results showing the changes in the radial components of turbulence intensity are shown in figures 5.15 and 5.16. Clearly, the radial component of turbulence intensity is also increased considerably in the dominant jet-noise producing region of the jet (up to $X/D_j \simeq 10$) as a result of upstream excitation.

Finally, the typical results showing the effects of increasing upstream-excitation levels on the spectral characteristics are presented in figure 5.17. These results clearly show that the effect of discrete-tone excitation is to raise the level of turbulence at all frequencies.

The flow results presented above and the instability-wave pressure results presented in subsection 5.1 basically describe the global features of an excited jet. Experimental results showing effects of other factors on the flow structure of the excited jets will now be presented.

5.3 STROUHAL-NUMBER EFFECTS

Strouhal-number effects were studied only at three Strouhal numbers: 0.4, 0.5, and 0.6. Typical mean-velocity and axial turbulence-intensity

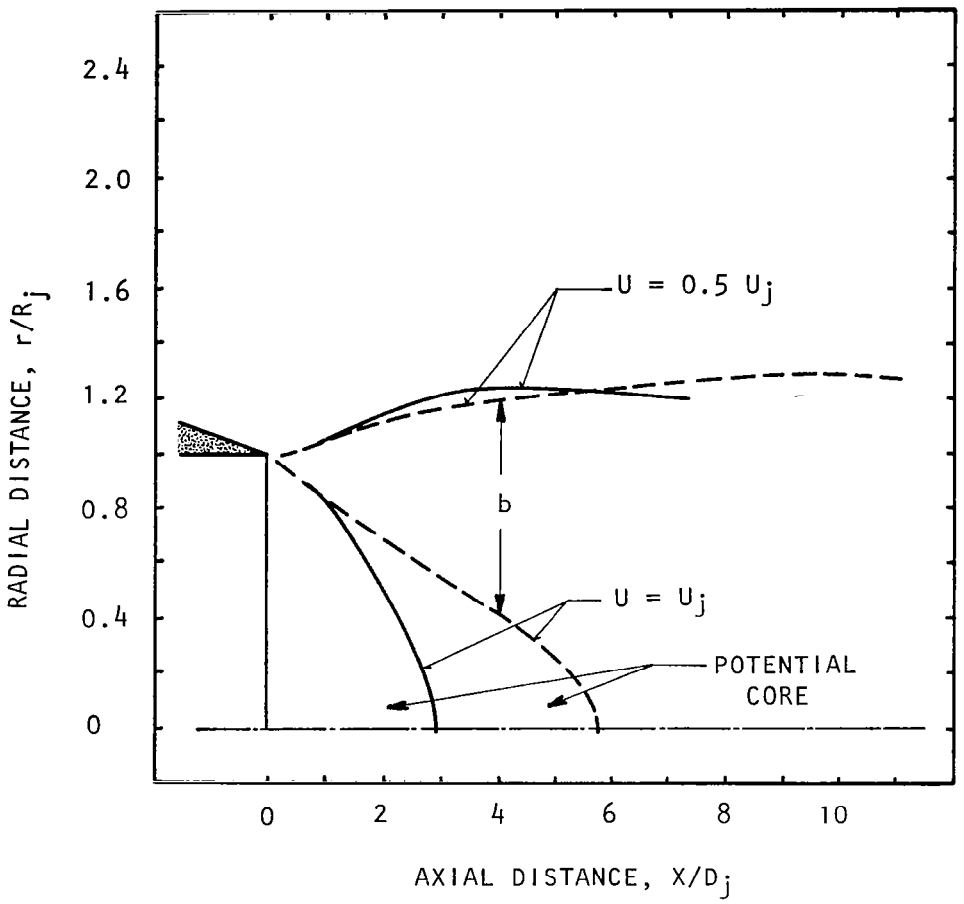

Figure 5.9 Effect of acoustic excitation on contours of axial mean velocity.
M_j = 0.58, U_j = 195 m/s, Unheated, Static,
S_e = 0.5, L_e = 141 dB, (0,0) Mode.
— — — — , Unexcited; ————, Excited

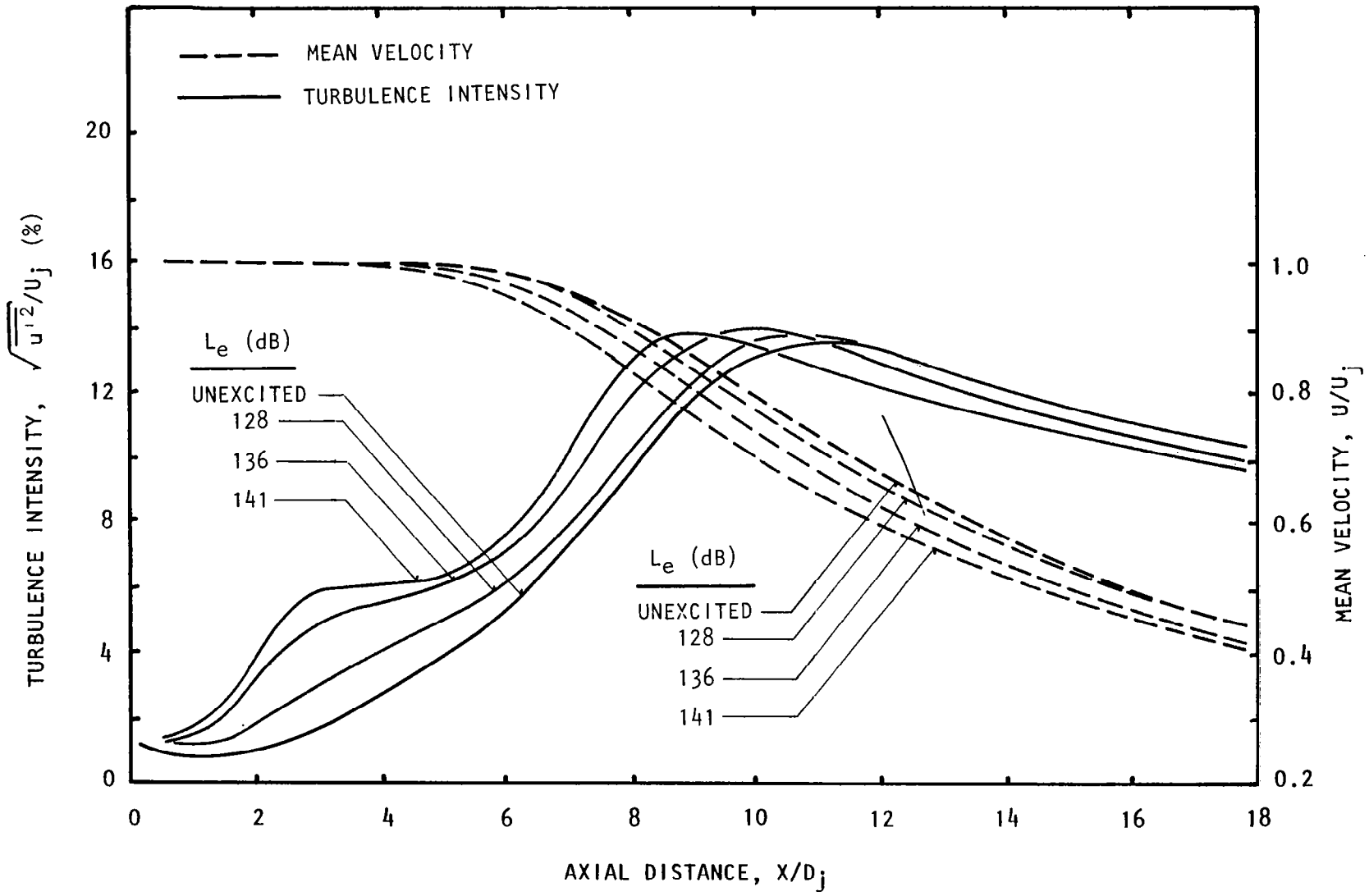

Figure 5.10 Excitation-level effects on centerline distributions.
M_j = 0.78, U_j = 255 m/s, Unheated, Static; S_e = 0.5, (0,0) Mode

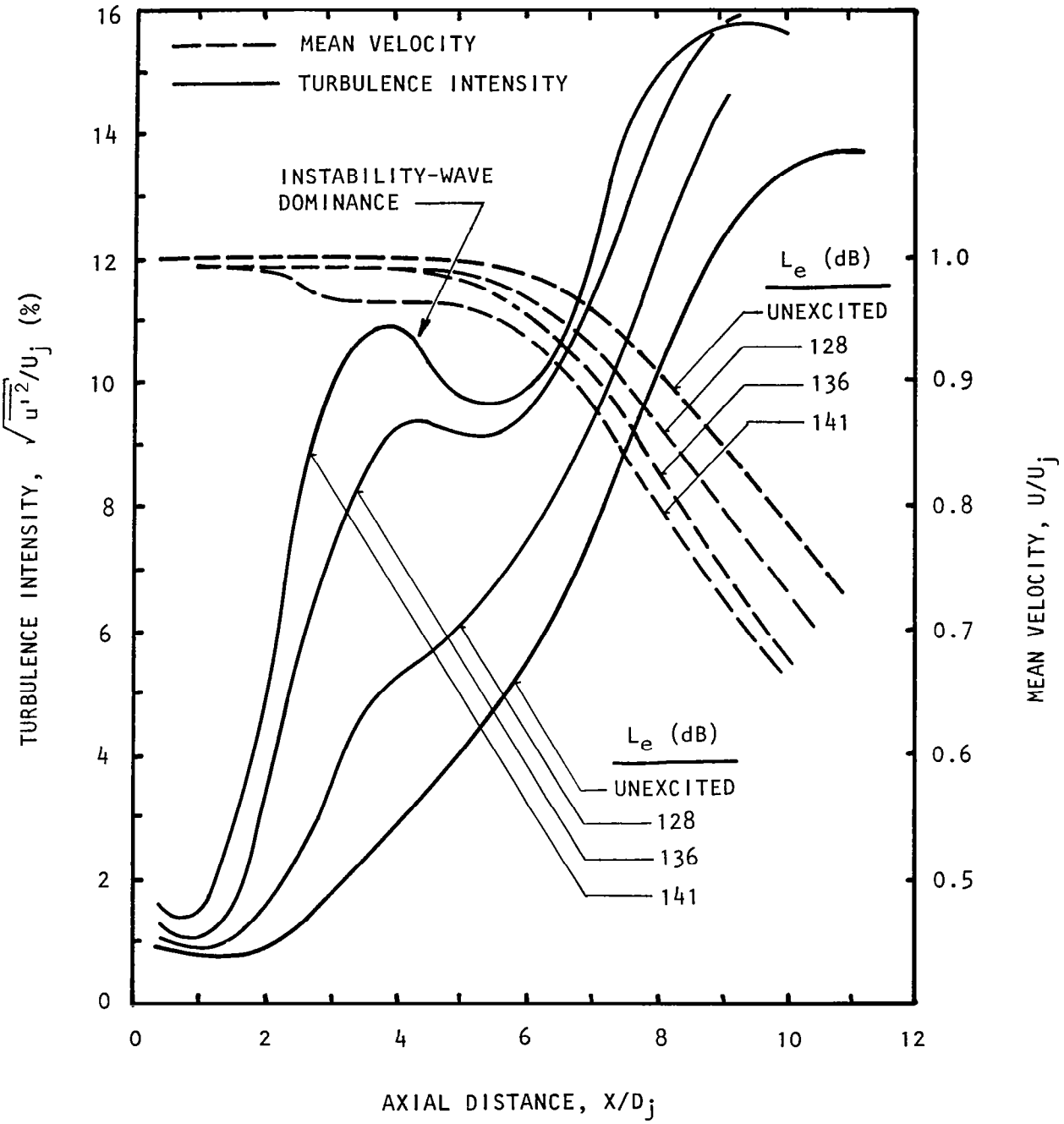

Figure 5.11 Excitation-level effects on centerline distributions.
M_j = 0.58, U_j = 195 m/s, Unheated, Static, S_e = 0.4, (0,0) Mode.

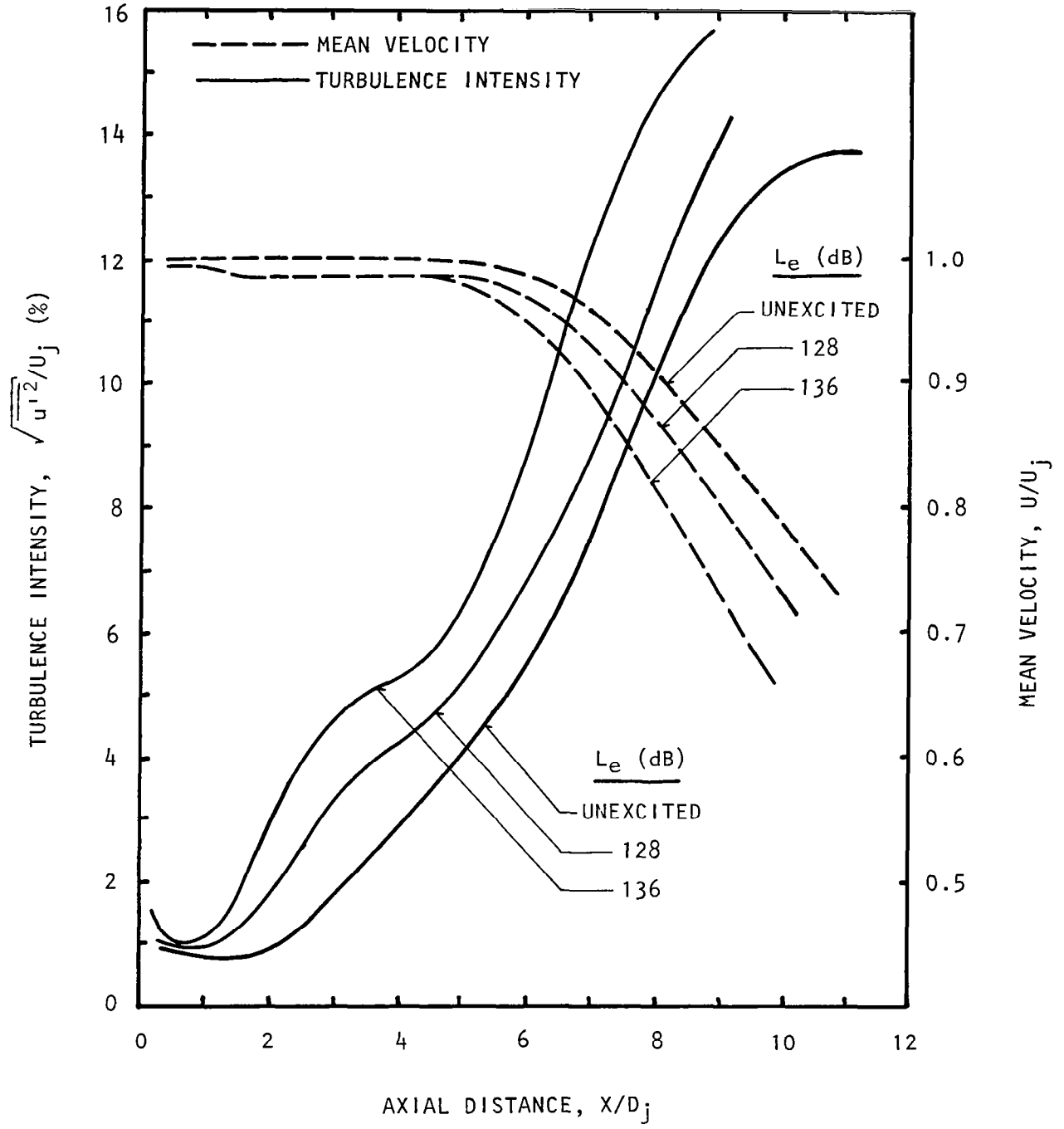

Figure 5.12 Excitation-level effects on centerline distributions. $M_j = 0.58$, $U_j = 195$ m/s, Unheated, Static, $S_e = 0.6$, (0,0) Mode

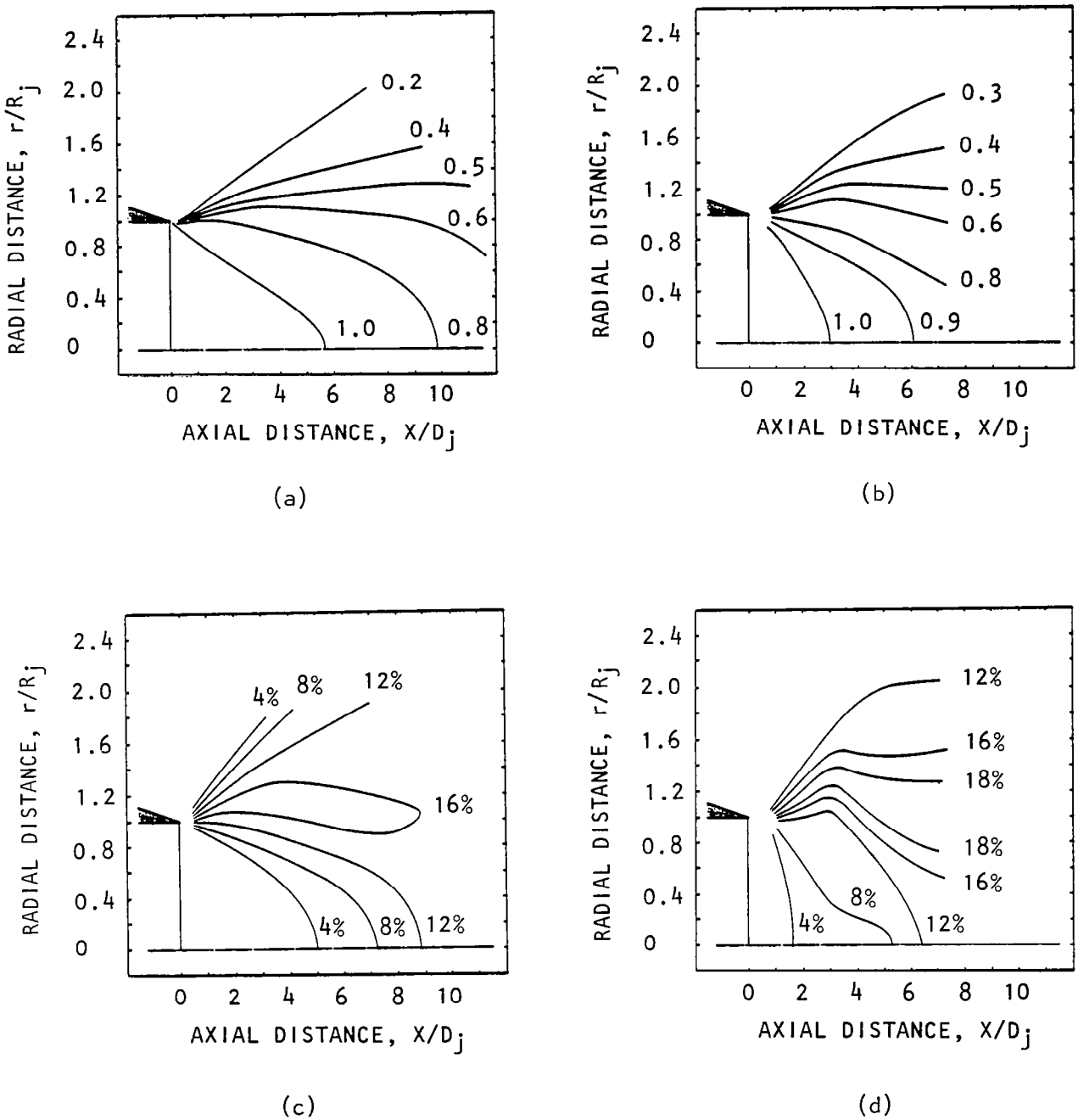

Figure 5.13 Contours of mean velocities - (a) unexcited, (b) excited; and turbulence intensities - (c) unexcited, (d) excited. M_j = 0.58, 195 m/s, Unheated, Static, S_e = 0.5, L_e = 141 dB, (0,0) Mode.

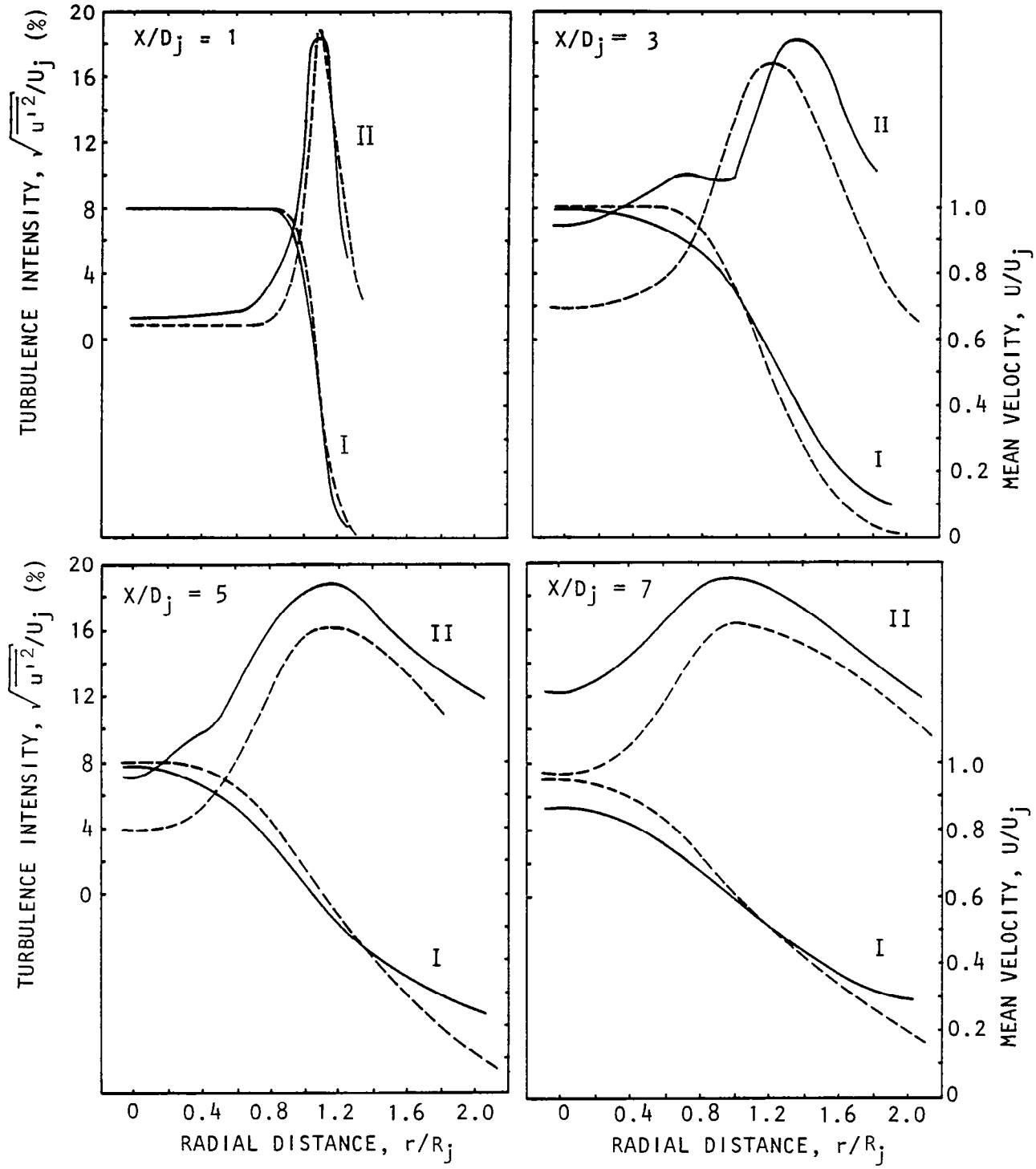

Figure 5.14 Excitation effects on radial distribution of axial components of mean velocity (I) and turbulence intensity (II) at different axial locations. M_j = 0.58, U_j = 195 m/s, Unheated, Static, L_e = 141 dB, S_e = 0.5, — — — —, Unexcited; ————, Excited.

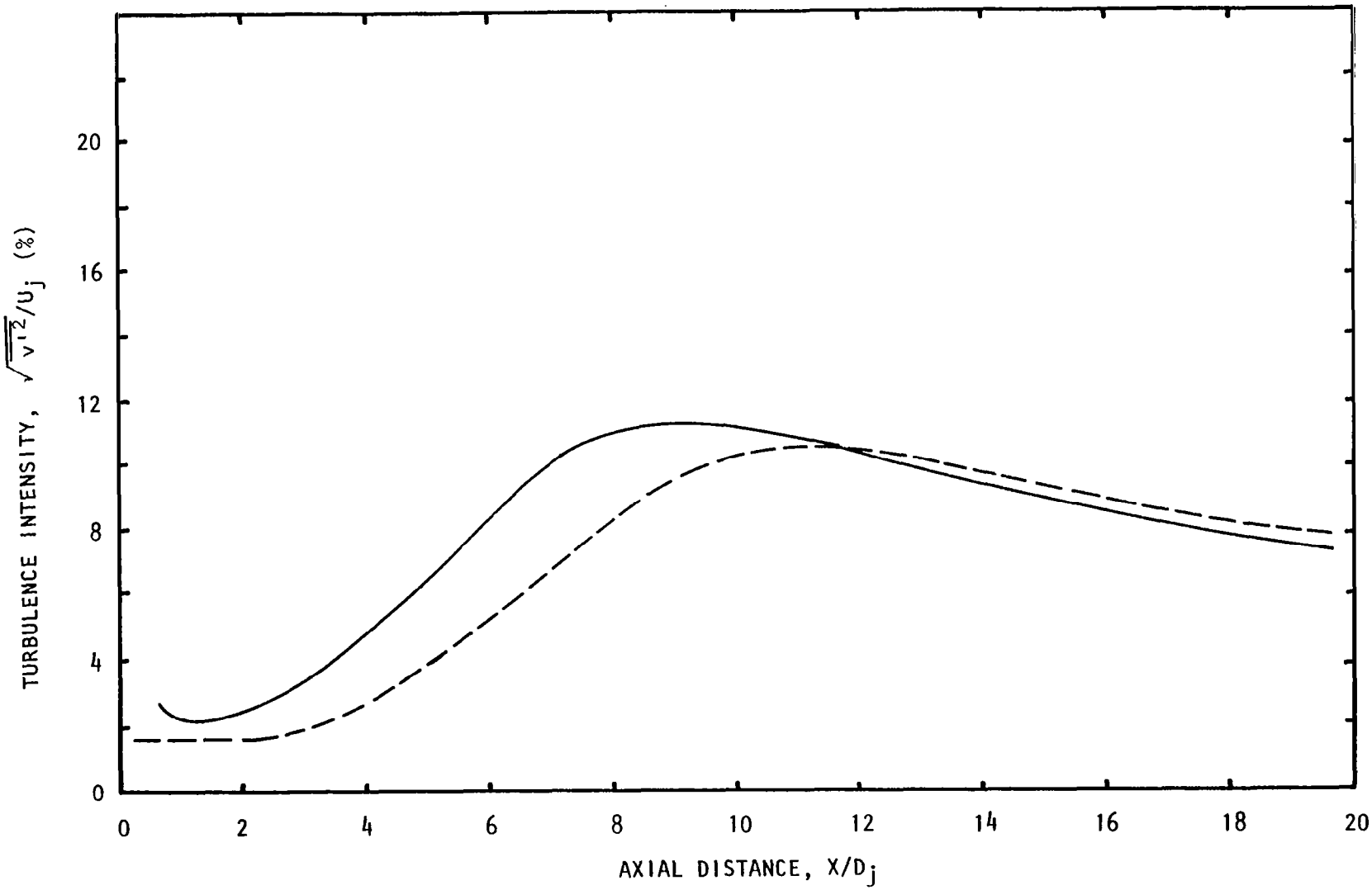

Figure 5.15 Excitation effects on centerline distribution.
$M_j = 0.58$, $U_j = 195$ m/s, Unheated, Static, $S_e = 0.5$,
$L_e = 141$ dB, (0,0) Mode.
– – – –, Unexcited, ———, Excited

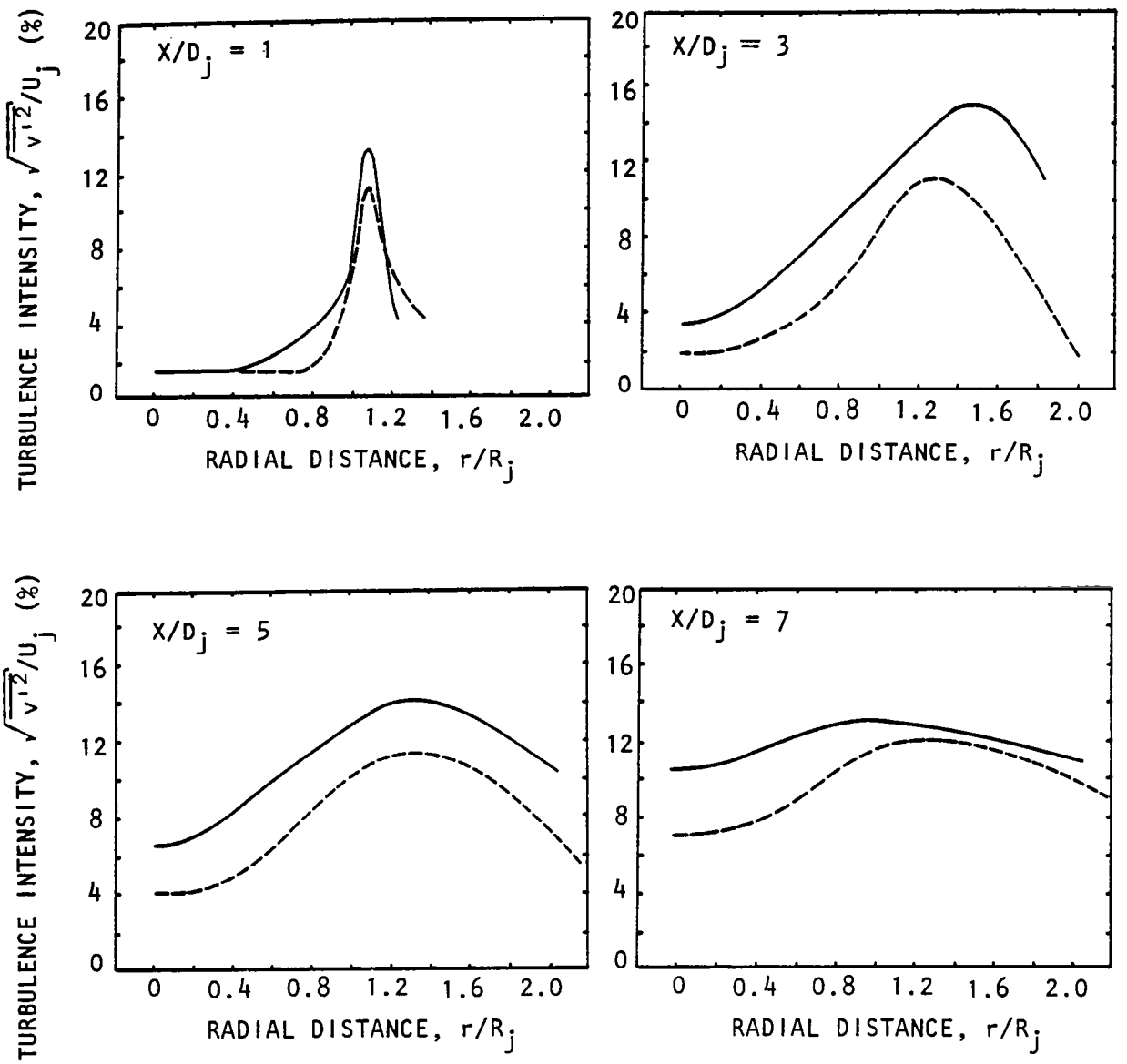

Figure 5.16 Excitation effects on radial distribution of radial component of turbulence intensity at different axial locations.
M_j = 0.58, U_j = 195 m/s, Unheated, Static, S_e = 0.5, L_e = 141 dB, (0,0) Mode.
— — — Unexcited, ———, Excited
(See figure D.3 for actual measurement points.)

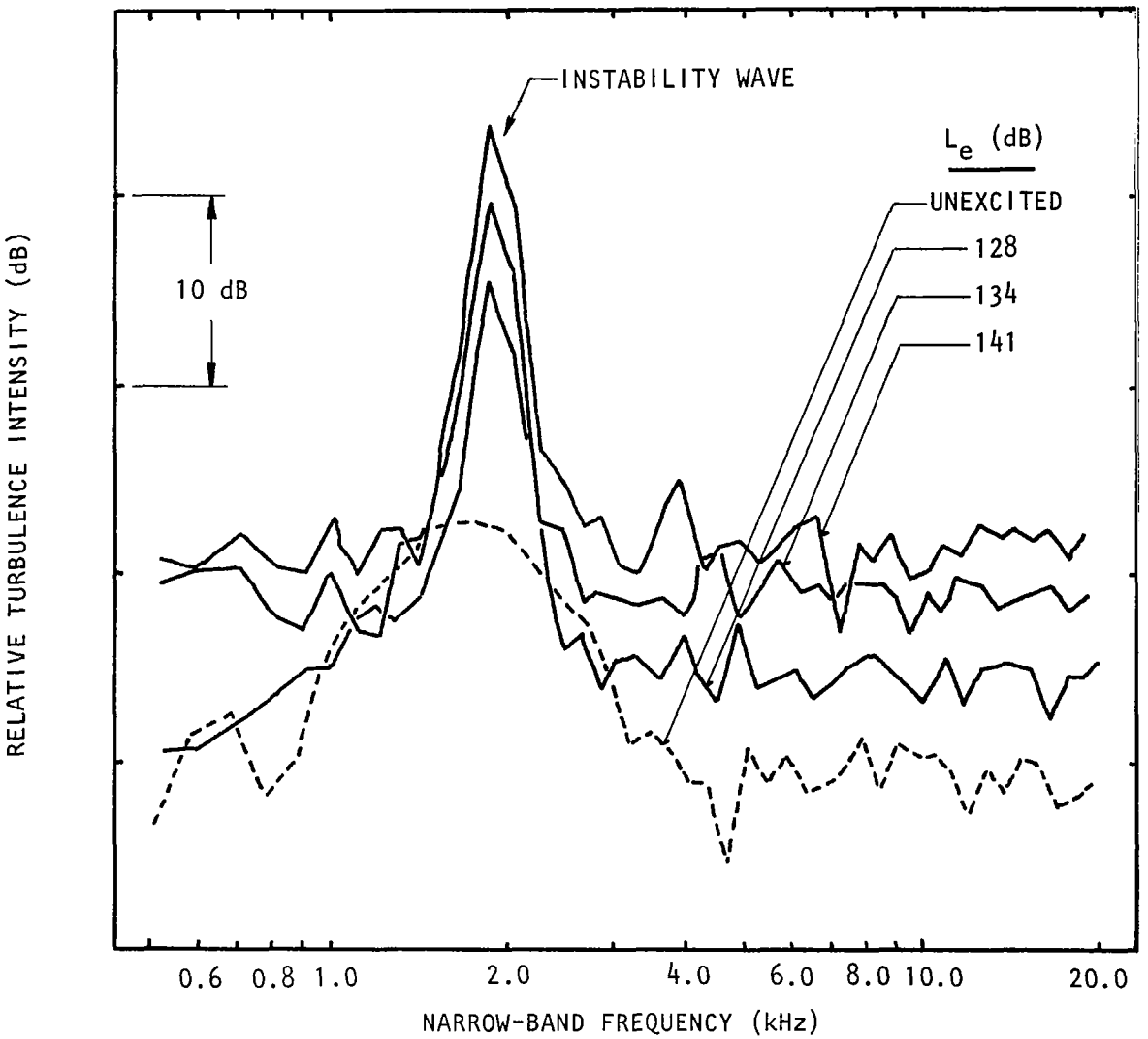

Figure 5.17 Turbulence spectra on centerline at $X/D_j = 3$. $M_j = 0.58$, $U_j = 195$ m/s, Unheated, Static, $S_e = 0.5$, (0,0) Mode, analysis bandwidth $\Delta f = 100$ Hz.
(Note that the instability wave was most dominant in the vicinity of the location of these measurements, i.e. $x/D_j = 3$.)

distributions for three Strouhal numbers are shown in figure 5.18 for excitation level L_e = 128 dB, in figure 5.19 for L_e = 136 dB, and in figure 5.20 for L_e = 141 dB. In each figure, the humps close to X/D_j = 3 are because of the dominance of the large-scale turbulence over the small-scale turbulence, as pointed out earlier. At larger distances, where the small-scale turbulence is dominant, each of the three Strouhal numbers appears to have the same effect on the flow structure, at least for low excitation levels (up to L_e = 136 dB). This is also evident in the mean-velocity distributions shown in figures 5.18 and 5.19.

At the highest excitation level of 141 dB, however, the magnitudes of the changes in small-scale turbulence intensity and the mean velocity depend upon the value of the excitation Strouhal number. This is shown in figure 5.20. Here, data for only two Strouhal numbers, S_e = 0.4 and 0.5, are compared with those for the unexcited condition. (Because of the low acoustic efficiency of the acoustic drivers at high frequencies, the highest level of 141 dB could not be produced at S_e = 0.6.) At this excitation level, the two Strouhal numbers appear to have different effects on turbulence-intensity distribution in the region where the small-scale turbulence is dominant. The effects of Strouhal number in the region of large-scale turbulence, corresponding to the humps at about X/D_j = 3, are similar and consistent with the effects at lower levels of upstream excitation, but in the region of small-scale turbulence, the peak of the turbulence intensity is apparently shifted closer to the nozzle exit. Thus the turbulence intensity for X/D_j = 4 to 8 is higher for S_e = 0.5 than for S_e = 0.4, but further downstream, beyond X/D_j = 8, the trend appears to be reversed, and the turbulence intensities at S_e = 0.4 seem to have higher values. The reason for this behavior is not quite clear.

Mean-velocity data, presented in figure 5.20, however, produce a more clear-cut picture of the effect of the excitation Strouhal numbers on flow structure at the highest excitation level of 141 dB. Mean velocities for S_e = 0.5 appear to decay faster than those for S_e = 0.4. This indicates that, in an overall sense, S_e = 0.5 is more effective in converting mean kinetic energy of the jet into turbulence than S_e = 0.4, and that our choice of S_e = 0.5 for detailed flow measurements is perhaps the right choice.

5.4 MACH-NUMBER EFFECTS

Figures 5.21 and 5.22 show the changes in the centerline distribution of the mean velocities and the axial-turbulence intensities respectively of an excited jet at two Mach numbers: 0.58 and 0.78. Both the mean velocity and the turbulence intensity data indicate that, for a fixed excitation level, the changes in these flow quantities are larger at lower Mach numbers.

Data of figure 5.22 are plotted in a different way in figure 5.23, where the ratios of the turbulence intensities for the excited jet to those for

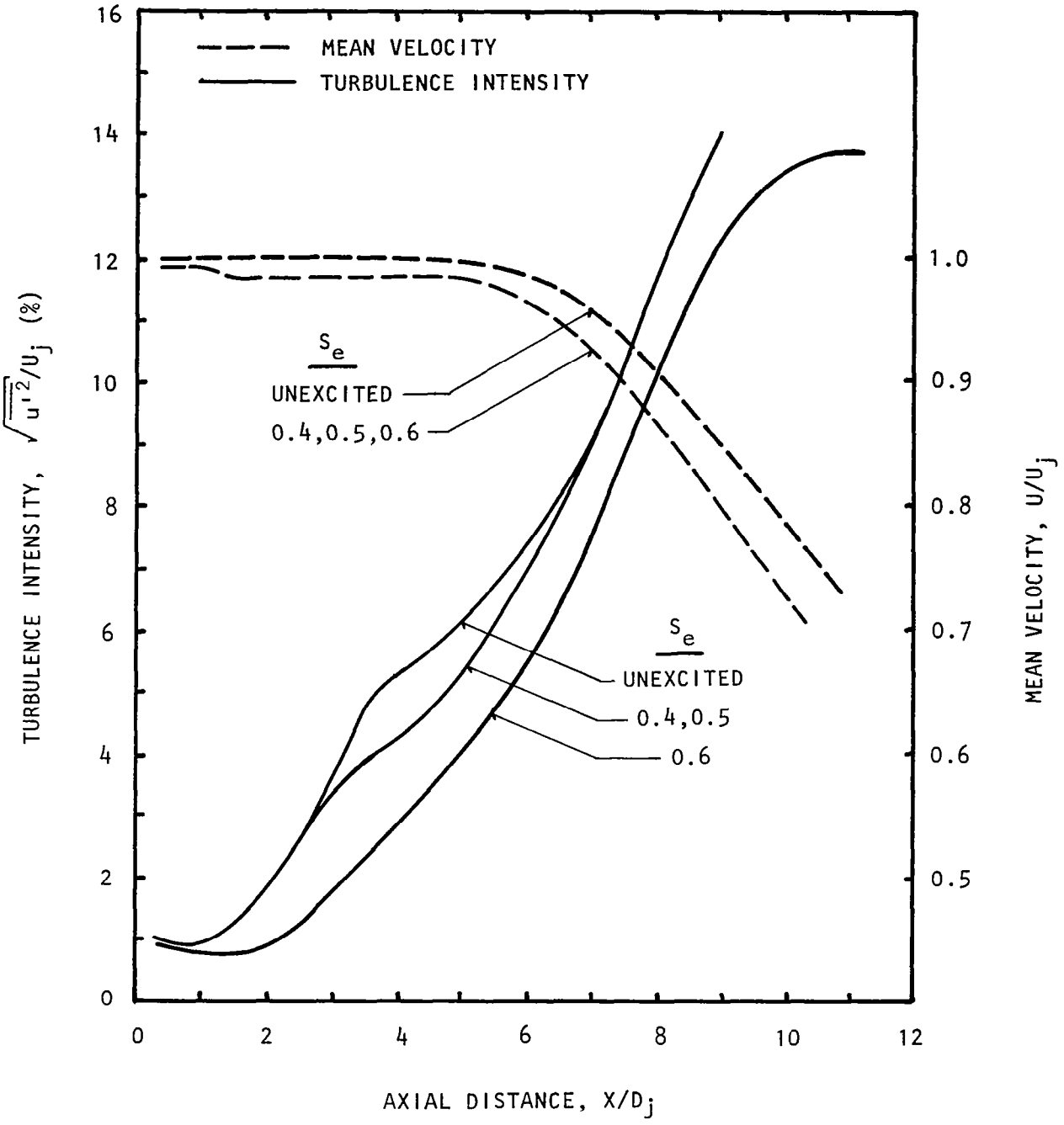

Figure 5.18 Strouhal-number effects on centerline distributions. M_j = 0.58, U_j = 195 m/s, Unheated, Static, L_e = 128 dB, (0,0) Mode.

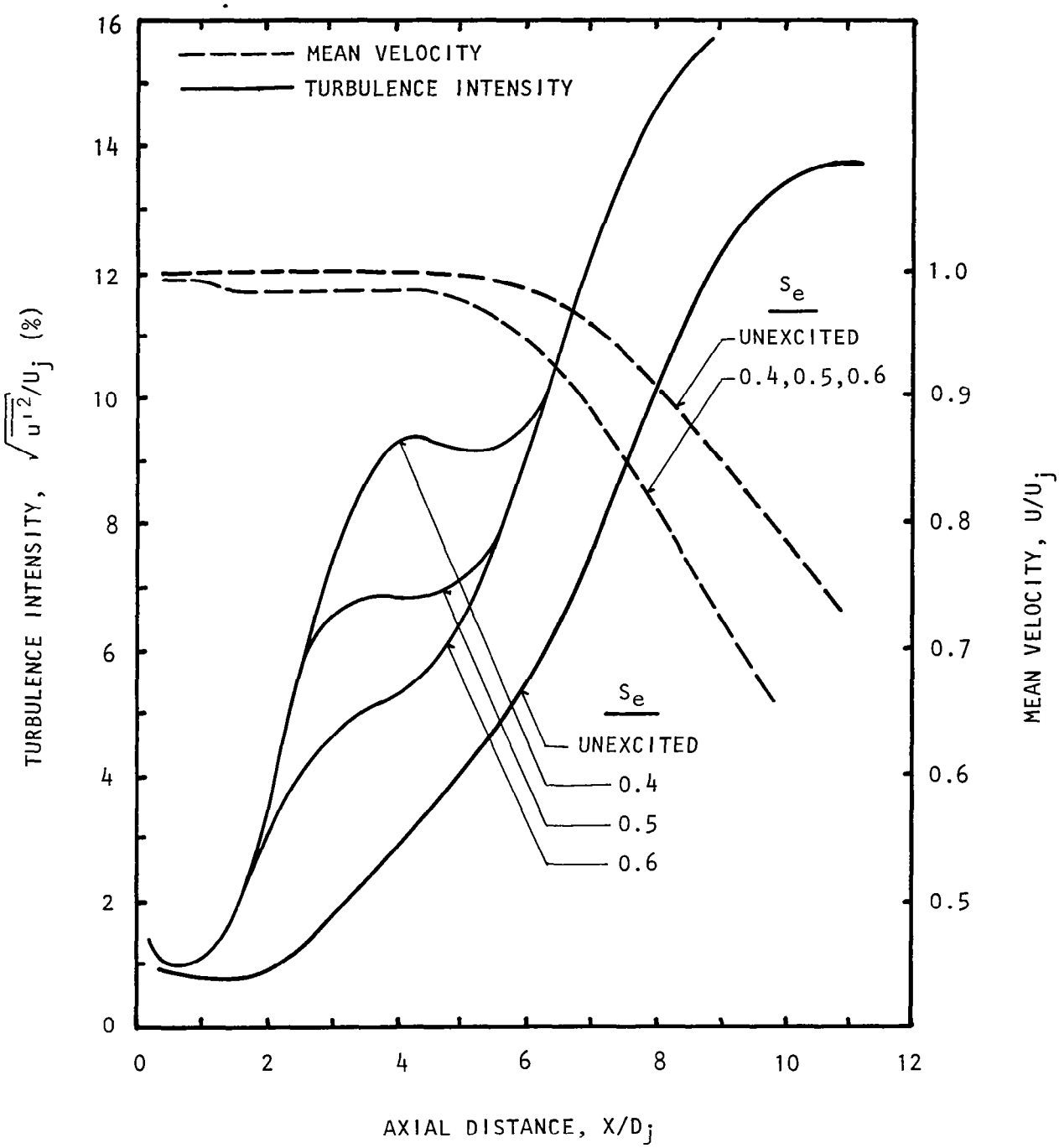

Figure 5.19 Strouhal-number effects on centerline distributions. M_j = 0.58, U_j = 195 m/s, Unheated, Static, L_e = 136 dB, (0,0) Mode.

(See figures D4(a) and D.4(b) for actual measurement points.)

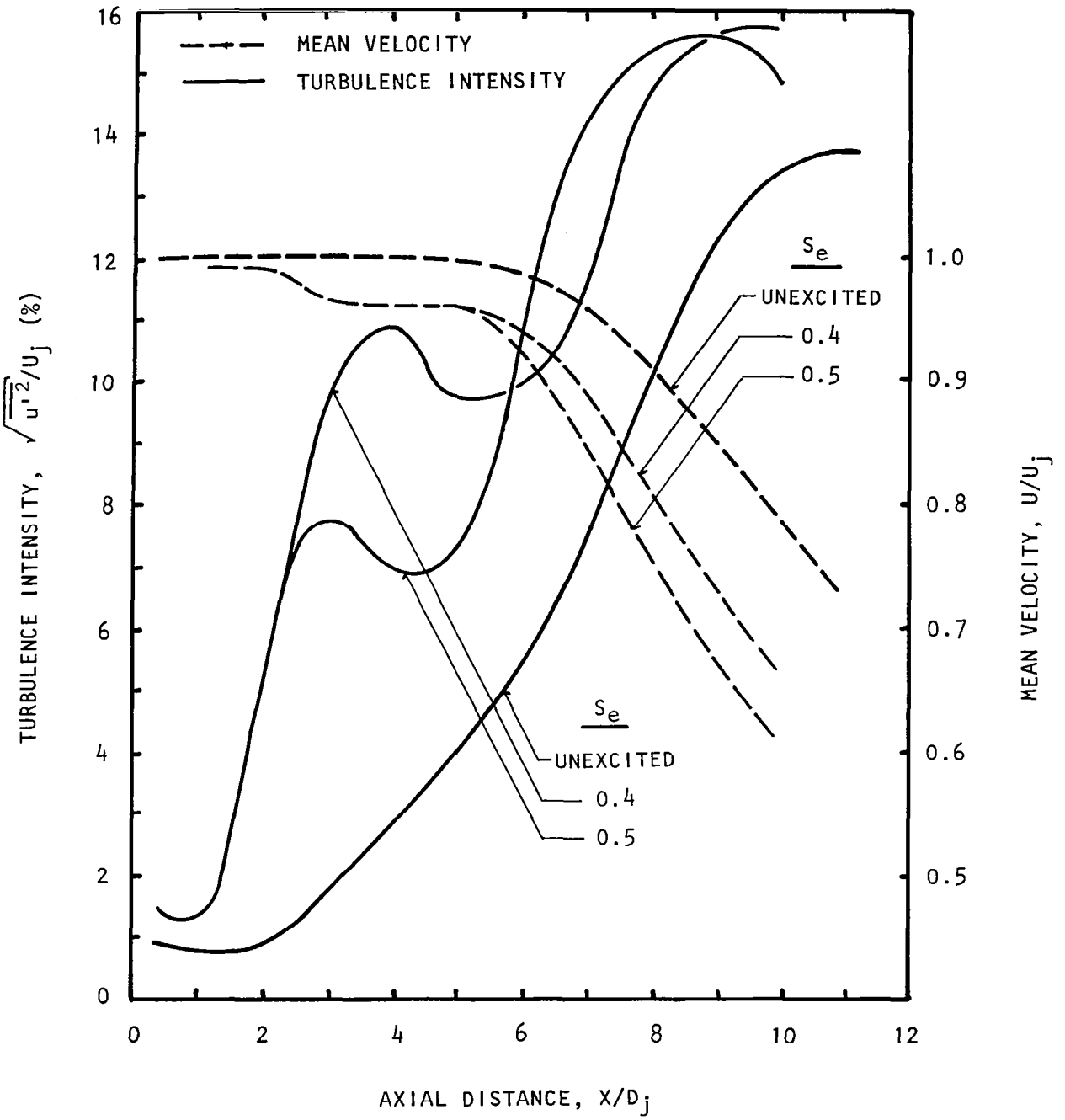

Figure 5.20 Strouhal-number effects on centerline distributions. M_j = 0.58, U_j = 195 m/s, Unheated, Static, L_e = 141 dB, (0,0) Mode.

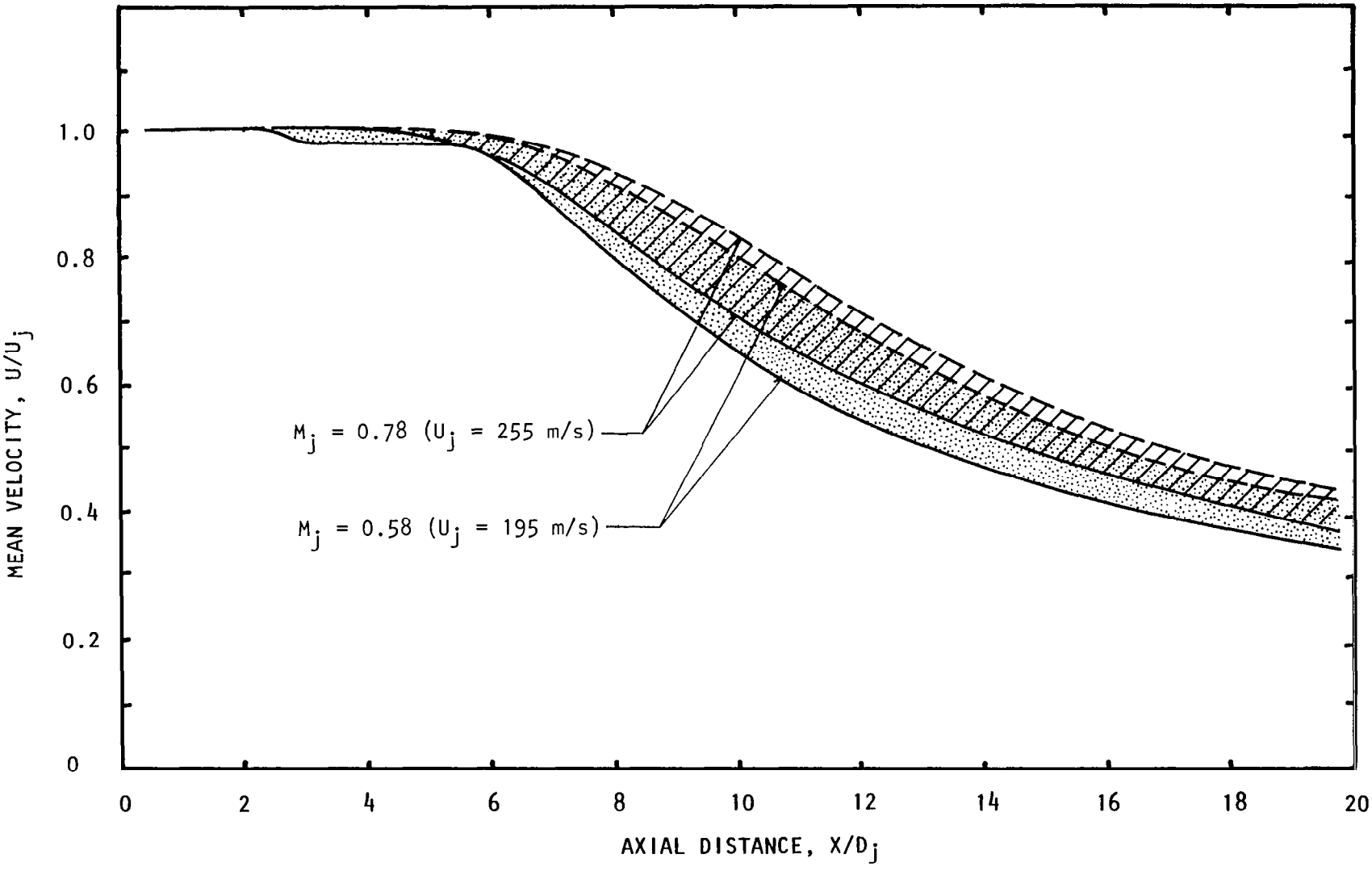

Figure 5.21 Mach-number effects on centerline distributions.
Static, Unheated, S_e = 0.5, L_e = 141 dB, (0,0) Mode.
– – – –, Unexcited; ———, Excited

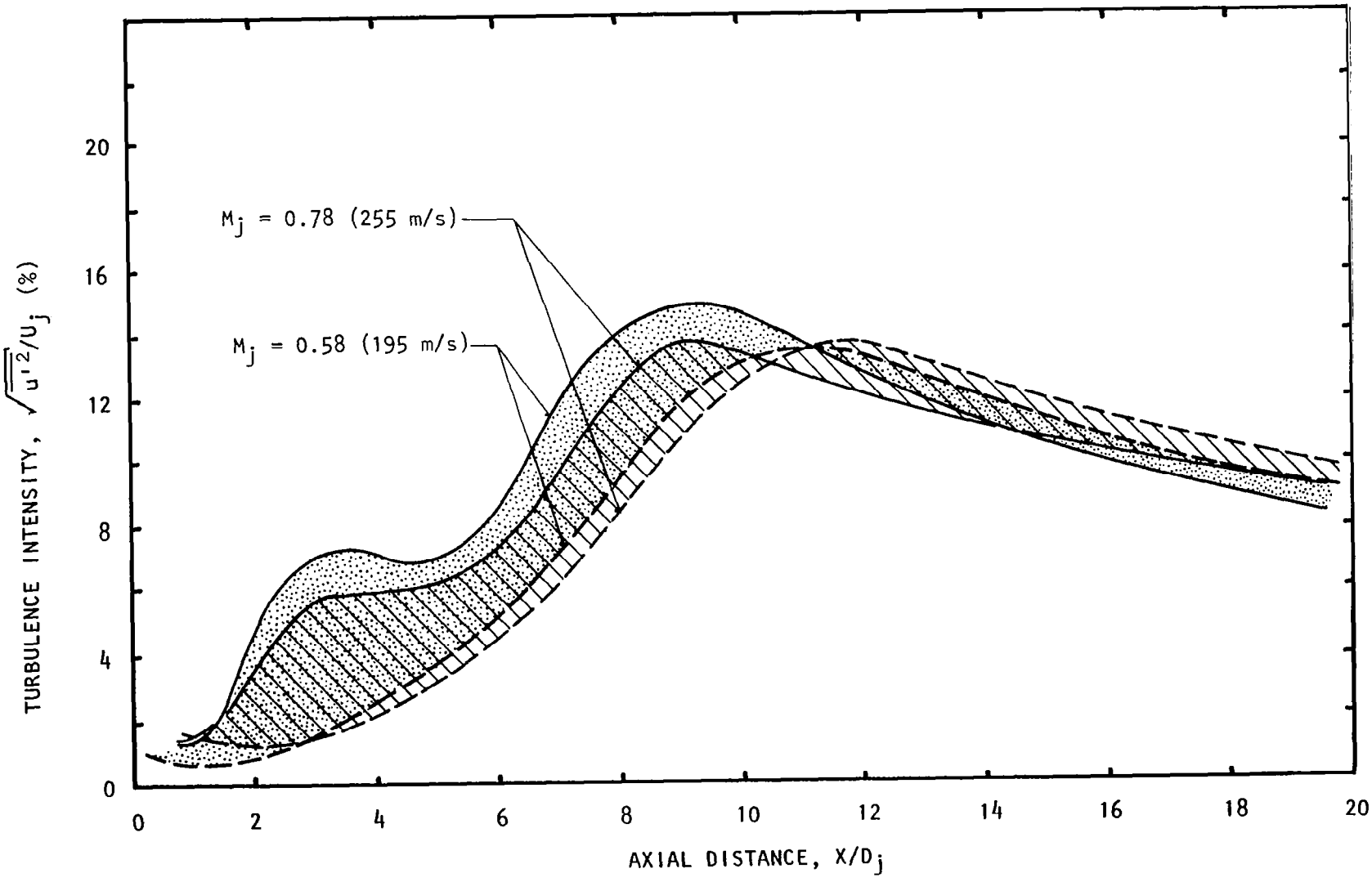

Figure 5.22 Mach-number effects on centerline distributions.
Static, Unheated, S_e = 0.5, L_e = 141 dB, (0,0) Mode.
— — — , Unexcited; ——— , Excited

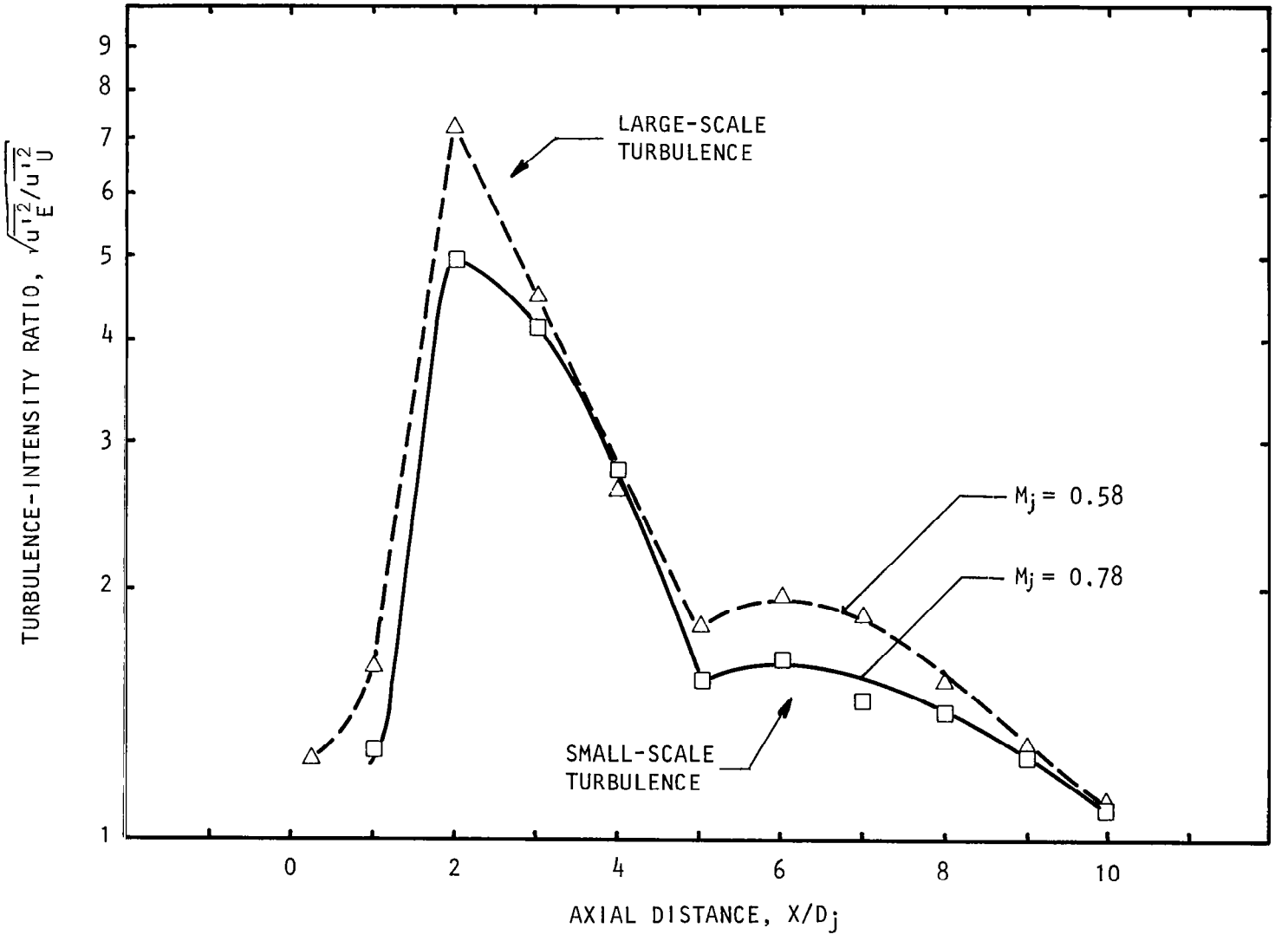

Figure 5.23 Mach-number effects on center distributions of turbulence-intensity ratios.
Unheated, Static, $S_e = 0.5$, $L_e = 141$ dB, (0,0) Mode .

the unexcited jets are presented for two Mach numbers: 0.58 and 0.78. Clearly, the higher the Mach number, the lower is the enhancement of turbulence intensity. This applies to both,large-scale turbulence (near $X/D_j = 3$) and small-scale turbulence intensities.

This is consistent with the theoretical results presented in chapter 7.0, where it is shown that the threshold of excitation level, beyond which noticeable changes in jet-flow turbulence take place, is a function of jet Mach number. Higher excitation levels are needed to observe changes in the higher Mach number jets. Correspondingly, the higher the jet Mach number, the higher is the required excitation level to produce a given change in the small-scale turbulence intensity of the jet.

The acoustic results given in section 6.0 also support the above observations, where it is found that, for a fixed value of S_e and L_e, the higher the jet Mach number, the lower the jet-noise amplification.

5.5 MODE-ORDER EFFECTS

Before presenting detailed results on the effect of mode order on the jet-flow structure, the radial variation of acoustic field at the nozzle exit will be presented for the first-order spinning mode (i.e., the helical (1,0) mode). This is shown in figure 5.24. Here the measured radial distribution of acoustic amplitudes at the nozzle exit, as measured for a jet operated at $M_j = 0.58$ and excited at $L_e = 136$ dB and $S_e = 1.0$, are compared with those predicted. for a (1,0) mode at the duct exit, by classical duct acoustics (ref. 30). The agreement between the measured and predicted values is excellent indicating that a (1,0) mode was indeed generated in isolation.

Clearly, for a pure (1,0) mode, the acoustic pressure at the center of the duct exit should ideally be zero, and a maximum along the lip line. The excitation levels for the helical (1,0) mode are, therefore, defined as the maximum amplitudes of the exciting acoustic wave at the lip line.

Similar to the (0,0) mode, the instability-wave pressures for the (1,0) mode were also measured by a 0.635-cm diameter B&K microphone fitted with a nose cone. While the measurements for the (0,0) mode were made along the centerline, those for the (1,0) mode were made along the lip line. Typical instability-wave pressure distributions for three excitation levels: 122 dB, 128 dB, and 136 dB, and for $S_e = 1.0$,are presented in figure 5.25. Basic characteristics of these curves are similar to those for the (0,0) mode presented in figure 5.2, except that the peak pressures appear to occur at $X/D_j = 1.0$ for each excitation level.

For the (1,0) mode, the excitation-level effects on the lip-line distribution of the mean velocities and turbulence intensities are shown in figures 5.26(a) and 5.26(b) respectively. As found for the 0,0 mode,

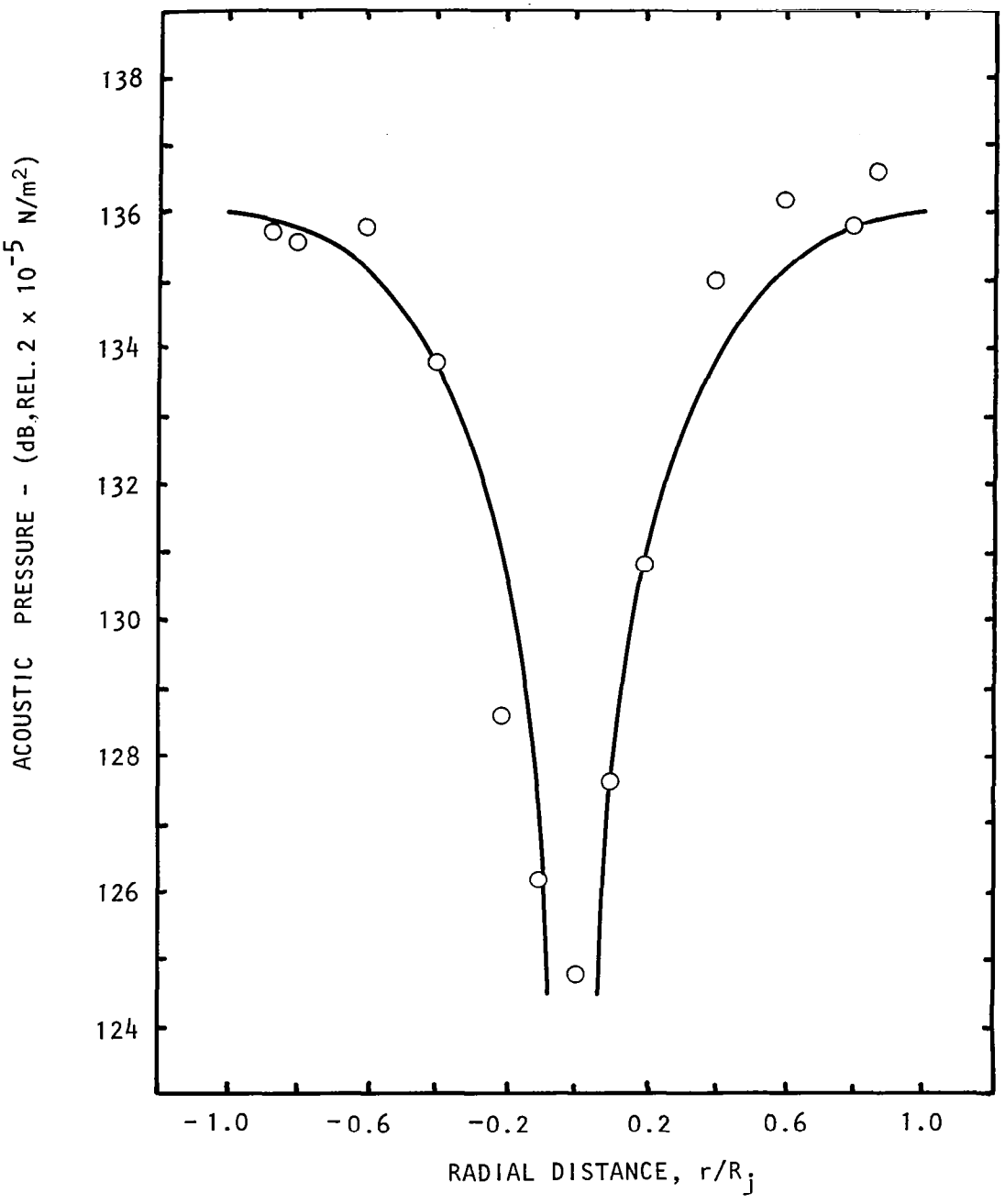

Figure 5.24 Comparison between measured (O) and predicted (——) acoustic pressures at the nozzle exit for the (1,0) mode.
M_j = 0.58, U_j = 195 m/s, Unheated, Static,
S_e = 1.0, L_e = 136 dB.

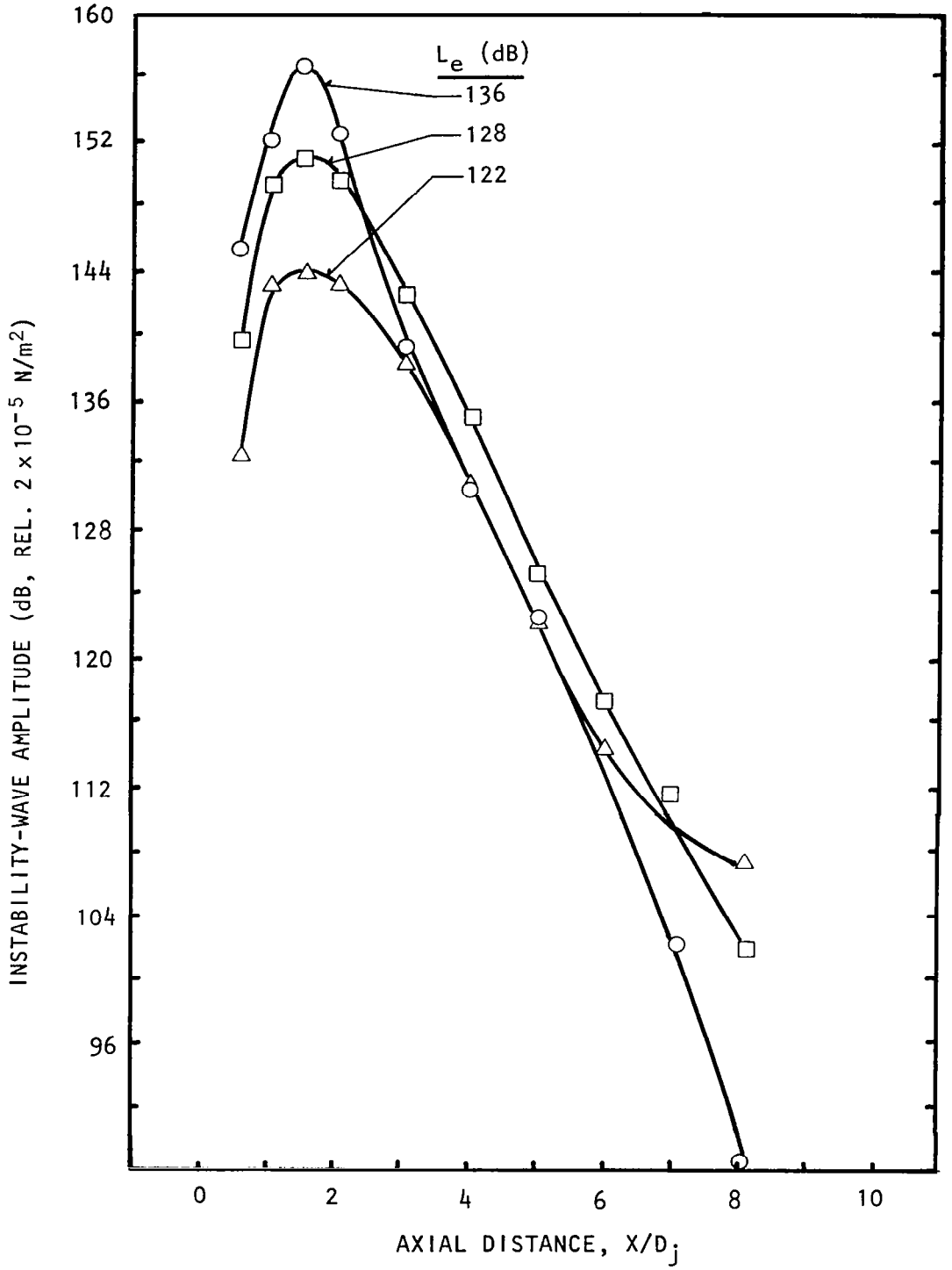

Figure 5.25 Lip-line variation of instability-wave pressure at various excitation levels.
M_j = 0.58, U_j = 195 m/s, Static, Unheated,
S_e = 1·0, (1,0) Mode.

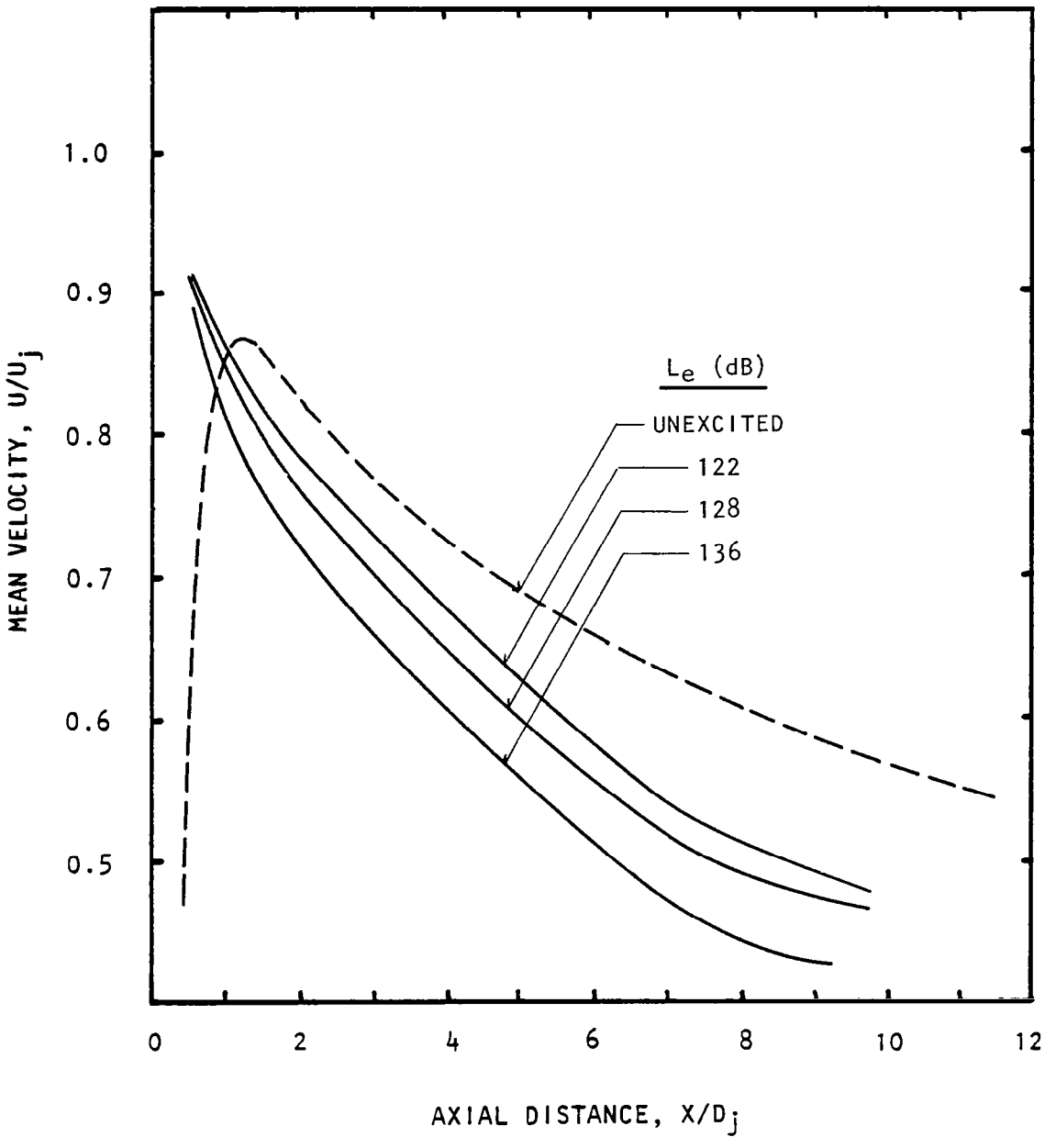

Figure 5.26(a) Excitation-level effects on the lip-line distribution of mean velocities.
M_j = 0.58, U_j = 195 m/s, Unheated, Static,
S_e = 1.0, (1,0) Mode .

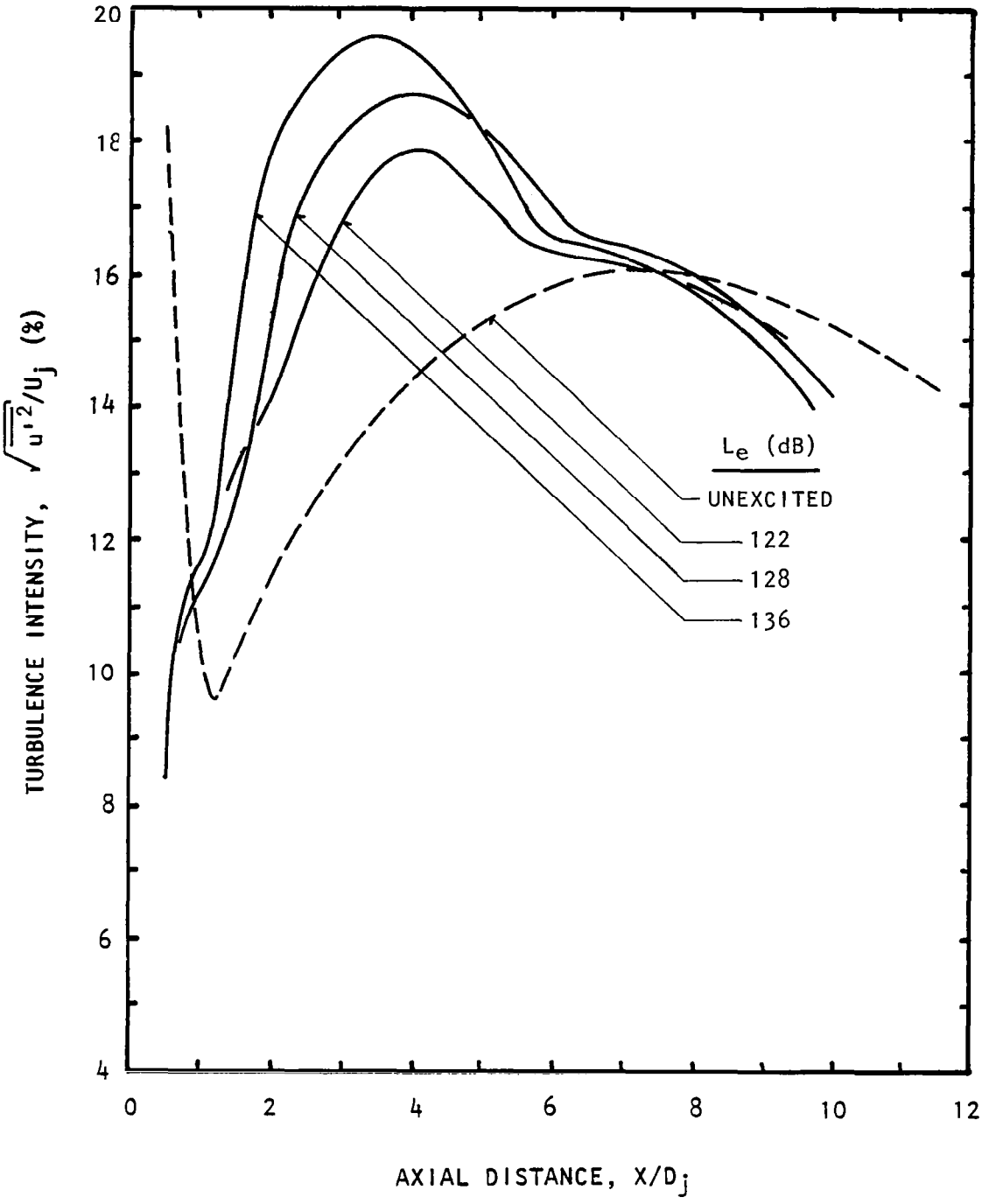

Figure 5.26(b) Excitation-level effects on the lip-line distribution of turbulence intensities.
M_j = 0.58, U_j = 195 m/s, Unheated, Static,
S_e = 1.0, (1,0) Mode.
(See figure D.5 for actual measurement points.)

for (1,0) mode also, the mean velocities decay rapidly with increasing excitation level. This effect is reflected as a corresponding increase in the small-scale turbulence.

It should be noted that we do not have $S_e = 1.0$ data for the (0,0) mode, and therefore, a one-to-one comparison between (1,0)-and (0,0)-mode data is not possible. The lip-line measurements of (0,0)-mode mean velocities and turbulence intensities at $S_e = 0.5$, however, produced results very similar to those presented above for the (1,0) mode at $S_e = 1.0$. These data for the (0,0) mode are shown in figures 5.27(a) and (b).

It should be clarified here that the humps in the turbulence intensity plots of figure 5.26(b) for the excited conditions are, in all likelihood, those due to small-scale turbulence, and not due to the dominance of the large-scale turbulence as shown earlier in figure 5.8. The reasons for believing this are twofold. First, the peak in the instability curves for the (1,0) mode shown in figure 5.25 occur close to $X/D_j = 1.0$, and, therefore, if the measured turbulence intensities are dominated by the large-scale turbulence levels, the humps should occur close to $X/D_j = 1.0$, and not around $X/D_j = 3.0$, as they do. Second, a closer inspection of the effect of forward velocity on the lip-line distribution indeed suggests that these humps are dominated by small-scale turbulence. This is shown in figures 5.28(a) and (b). As seen here, the mean-velocity decay rate is considerably reduced as a result of forward velocity. This effect should show up as a reduction in small-scale turbulence as it indeed does, both in the region of the above-mentioned hump and on its both sides. The only region, where the effects are insignificant, is around $X/D_j = 1.0$ where the instability wave is dominant. As shown in section 7.0, this is to be expected from theory.

In summary, therefore, the effect of (1,0)-mode excitation on the jet flow structure is similar to that of the (0,0) mode. Due to the lack of sufficient test points for higher-order mode measurements, however, it is difficult to draw firm conclusions.

This completes the presentation of all unheated- and static-jet data. Effect of flight velocity on the excited jet flows will now be presented.

5.6 FLIGHT EFFECTS

To show the effect of forward velocity on jet-noise amplification, it is best to present data for unexcited jets first. Figure 5.29 shows the effect of forward velocity on both the mean velocities and the turbulence intensities. Clearly, as the forward velocity is increased, the potential-core length increases, and the turbulence intensities decrease. These effects are quite drastic. For example, the turbulence intensity at $X/D_j = 8$, due to the forward velocity of 34 m/s, has decreased from about 10% to 3.5%. Similar results were obtained for the higher jet Mach number of $M_j = 0.78$ (see figure 5.30).

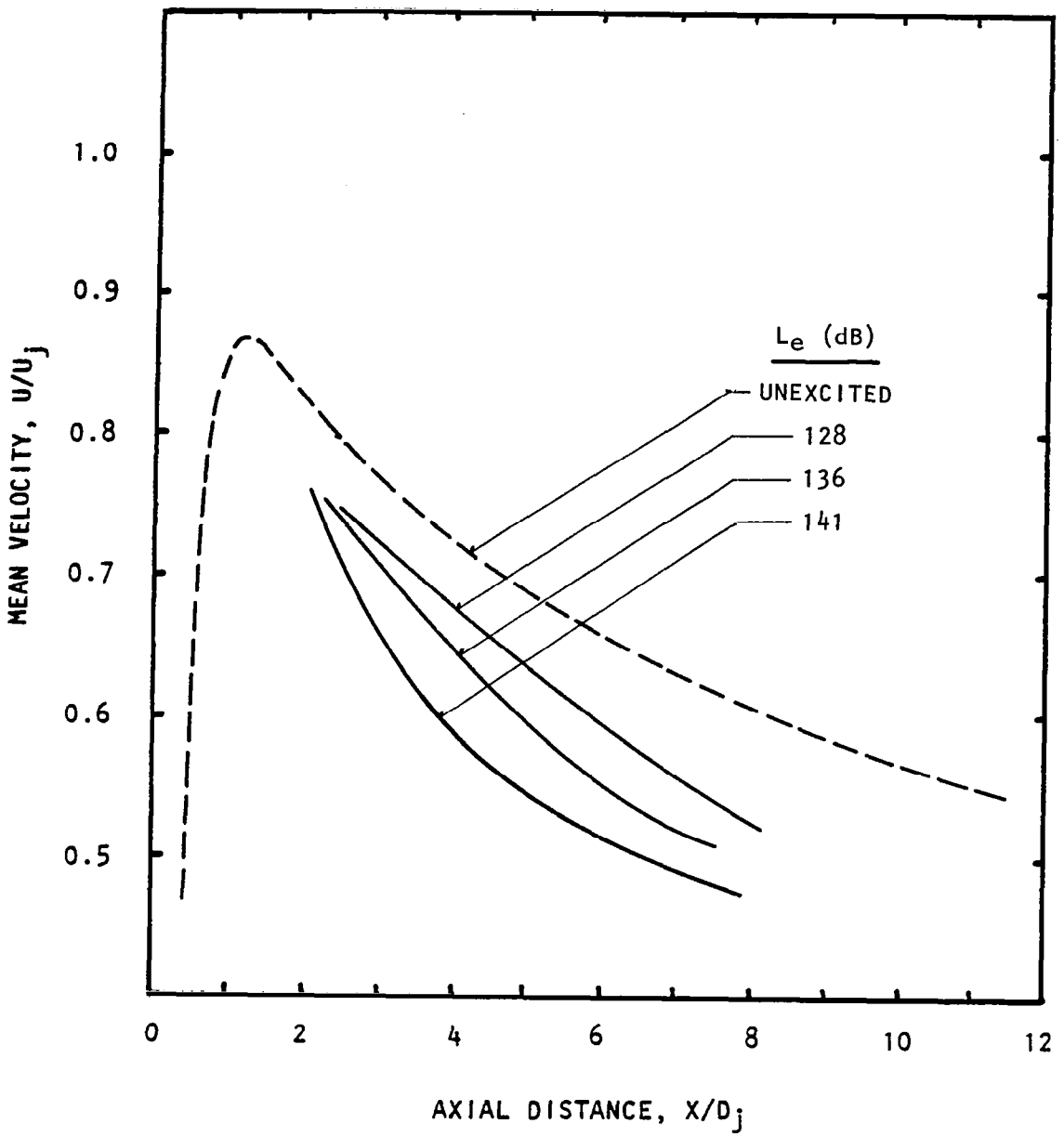

Figure 5.27(a) Excitation-level effects on the lip-line distribution of mean velocities.
M_j = 0.58, U_j = 195 m/s, Unheated, Static,
S_e = 0.5, (0,0) Mode.

(See figure D.6 for actual measurement points.)

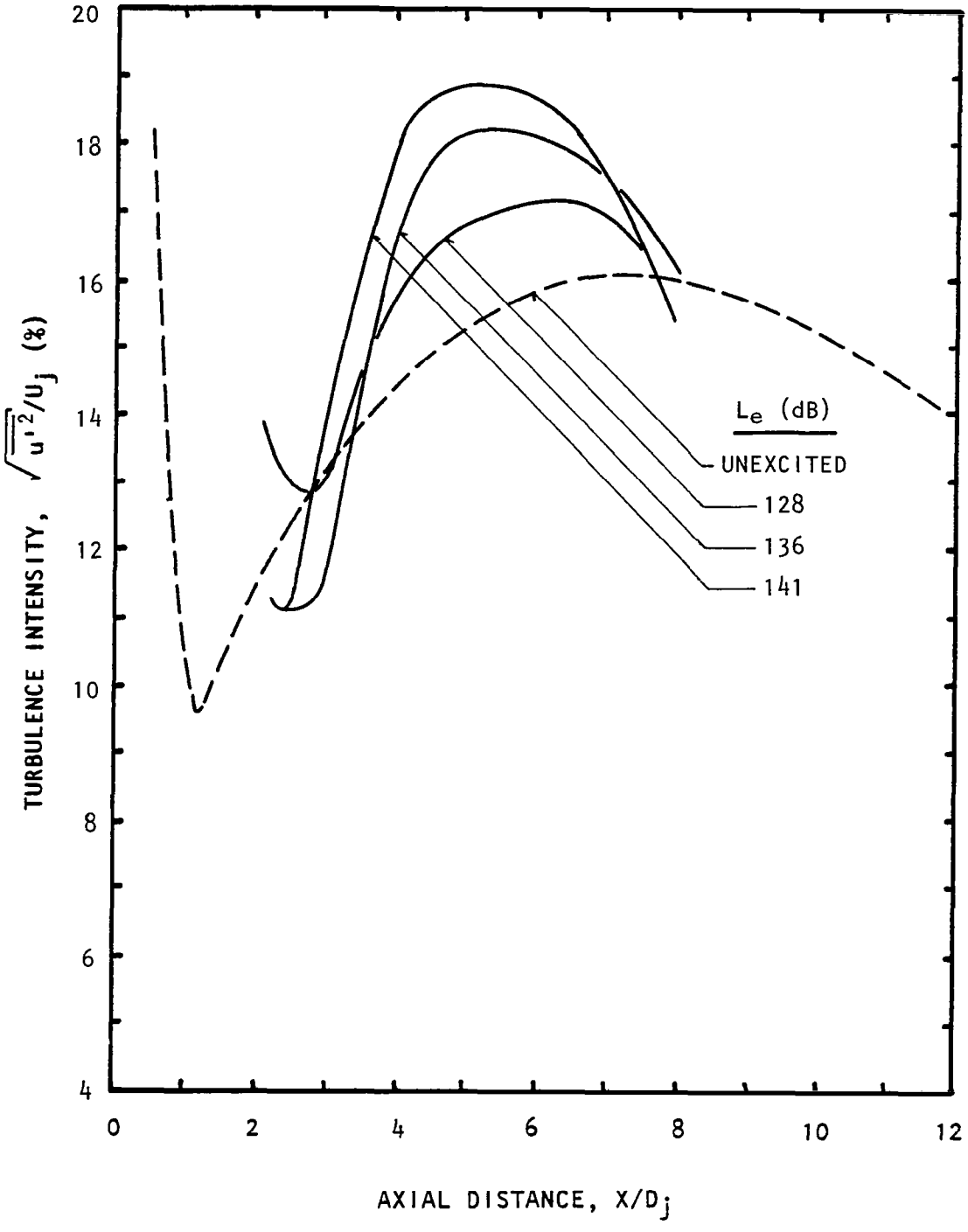

Figure 5.27(b) Excitation-level effects on the lip-line distribution of turbulence intensities.
$M_j = 0.58$, $U_j = 195$ m/s, Unheated, Static,
$S_e^j = 0.5$, (0,0) Mode .

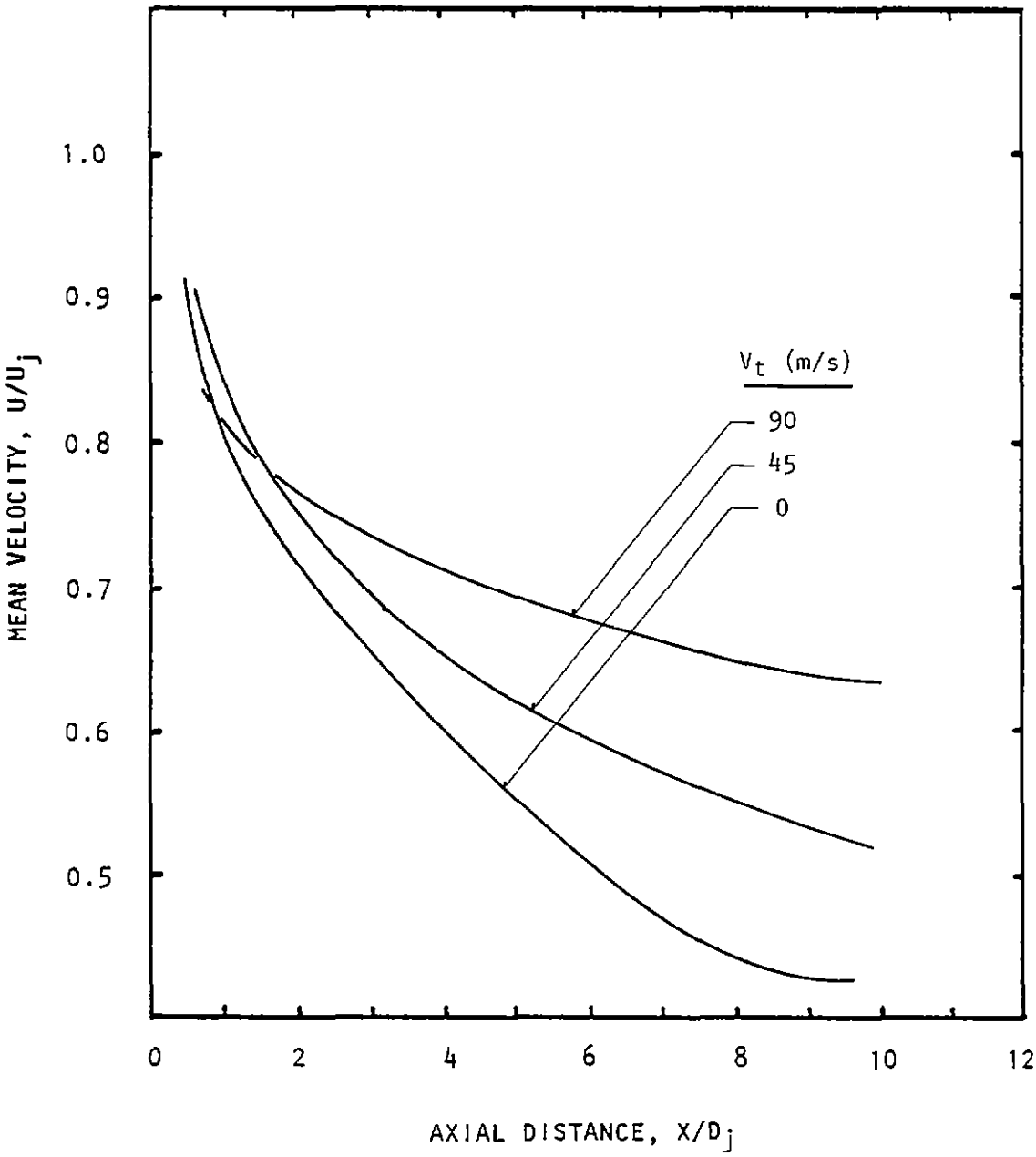

Figure 5.28(a) Flight-velocity effects on lip-line distribution of mean velocities.
M_j = 0.58, U_j = 195 m/s, Unheated, Static,
L_e = 136 dB, S_e = 1.0, (1,0) Mode.
(See figure D.7 for actual measurement points.)

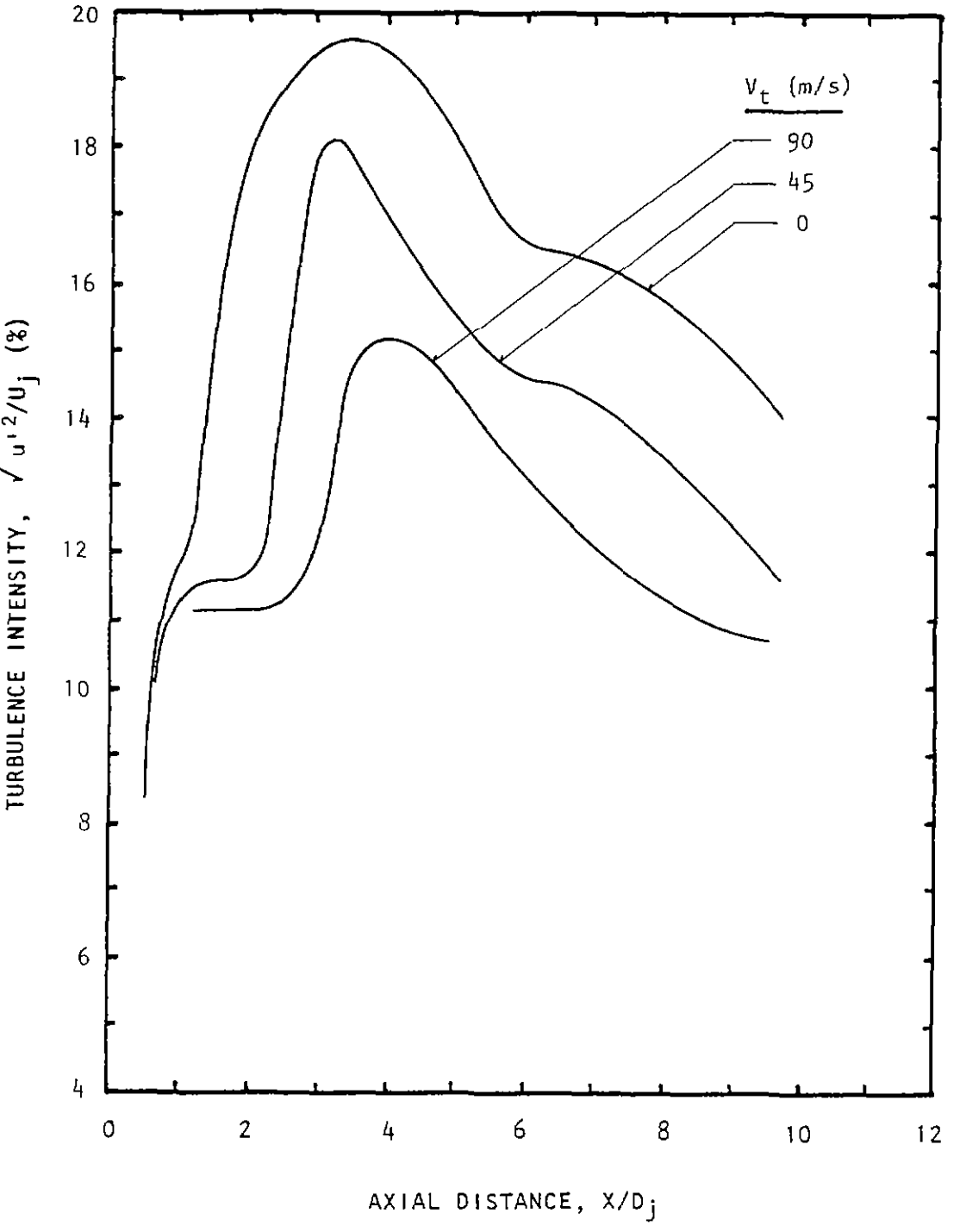

Figure 5.28(b) Flight-velocity effects on lip-line distribution of turbulence intensities.
M_j = 0.58, U_j = 195 m/s, Unheated, Static,
L_e = 136 dB, S_e = 1.0, (1,0) Mode.

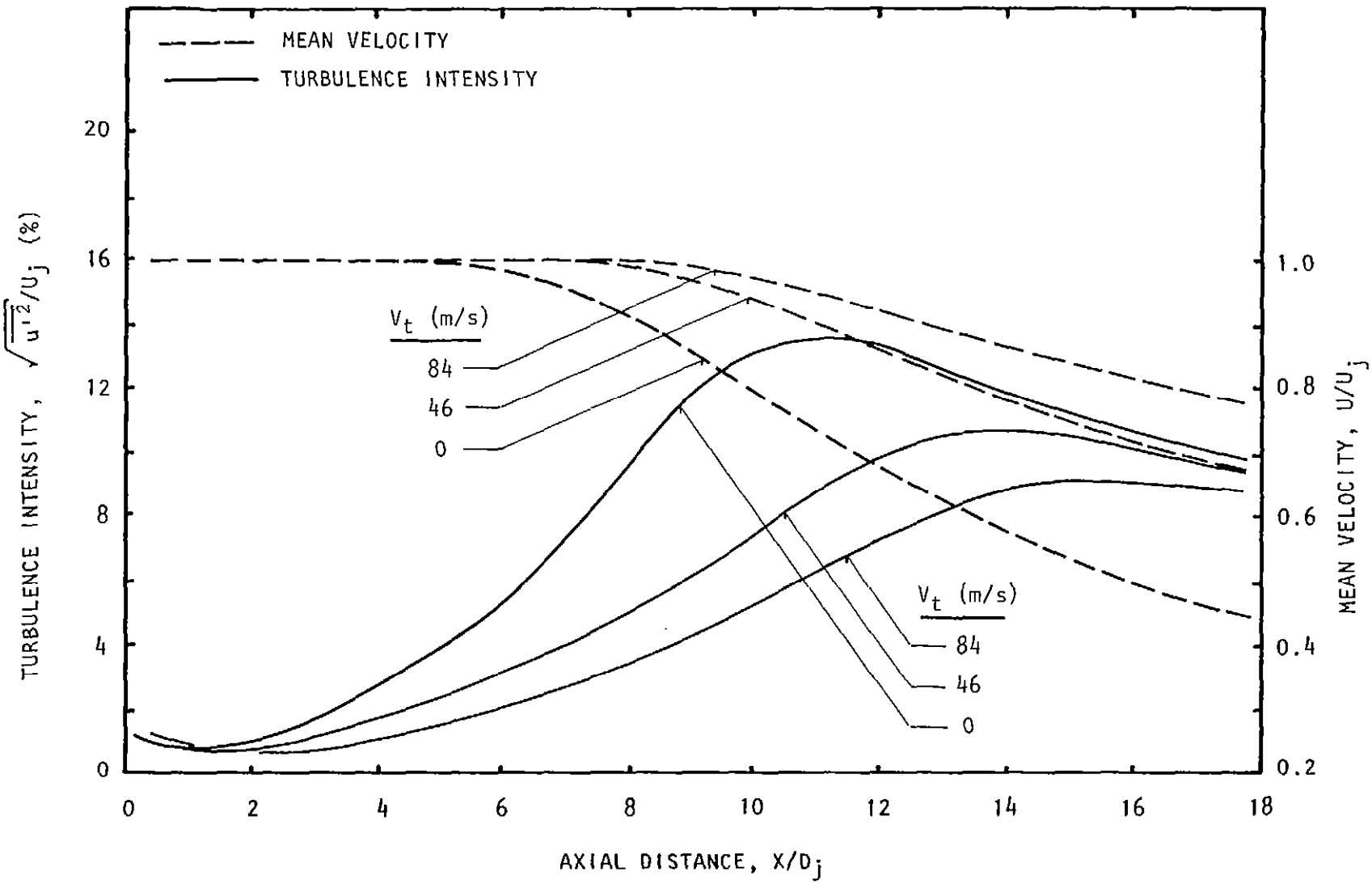

Figure 5.29 Flight-velocity effects on centerline distribution of an unexcited jet.
M_j = 0.58, U_j = 195 m/s, Unheated .

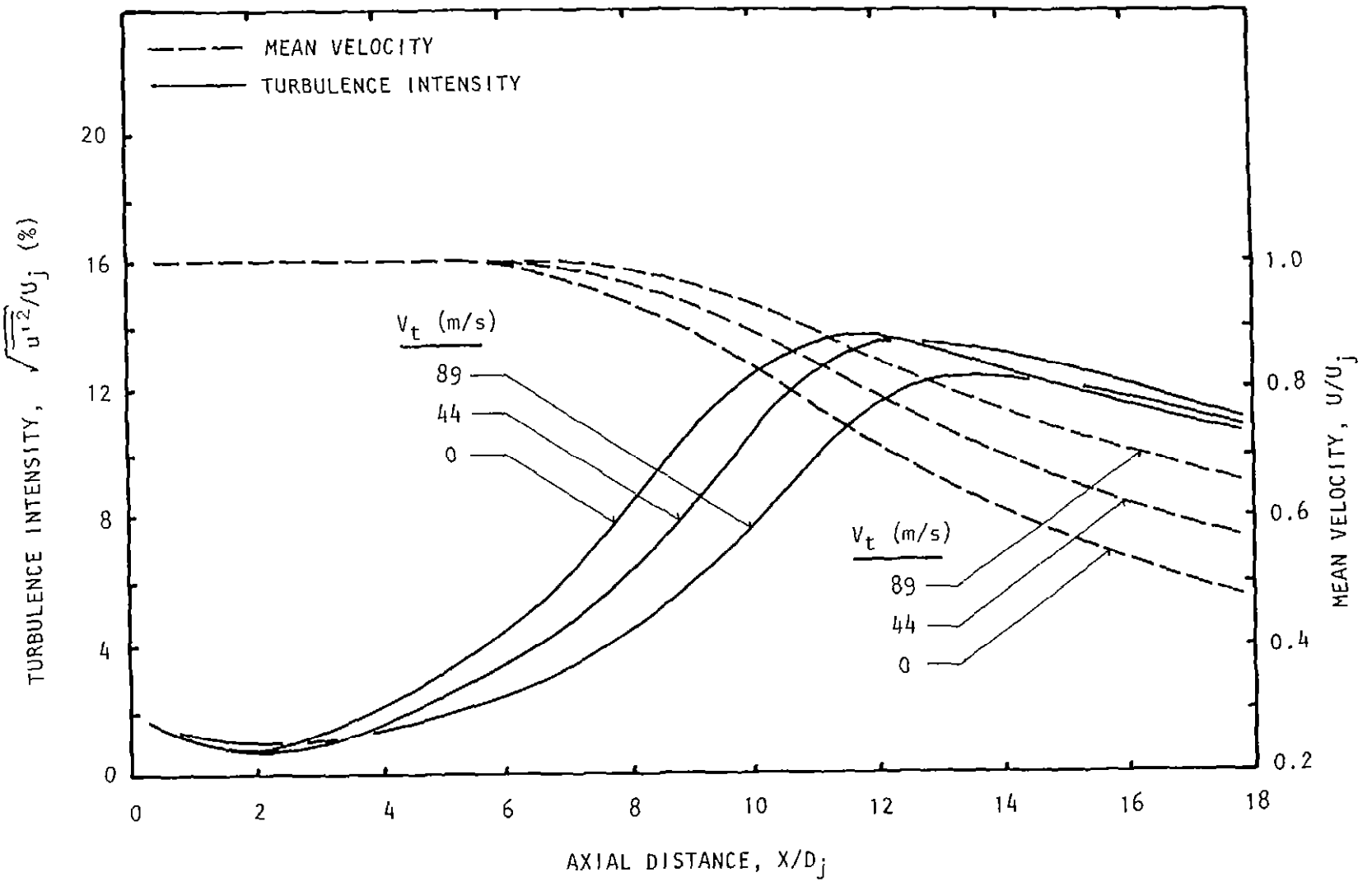

Figure 5.30 Flight velocity effects on centerline distribution of an unexcited jet.
M_j = 0.78, U_j = 255 m/s, Unheated.

When the jet is excited, and a forward velocity is superimposed, the results appear to be very similar to those for the static case. Typical results are presented in figure 5.31 for M_j = 0.58. As for the static case (figure 5.8), the potential core is reduced as a result of excitation. Similarly, the turbulence intensities are reduced at all axial stations up to ten exit diameters. Similar results were obtained for the higher jet Mach number of 0.78 (see figure 5.32).

It is to be noted that, in the centerline distribution of the turbulence intensities shown in figure 5.31, the magnitudes of the first hump in each forward-velocity condition has not changed significantly. Since, as mentioned earlier, the hump is dominated by the turbulence intensity associated with the large-scale turbulence structure, it is reasonable to assume that the large-scale structures grow to about the same amplitude in both the flight and the static case. As shown in section 7.3, this very conclusion is reached based upon the theoretical arguments.

The presence of an external flow reduces the average velocity shear gradient across the mixing layer of the jet. As a result, the growth rates of the excited large-scale instability waves are expected to be reduced. It follows, therefore, that the rate of mixing is also reduced, resulting in a longer jet-core region over which the instability wave can grow. Thus, although the effect of flight decreases the spatial-growth rate of the excited large-scale instability waves, they can grow over a longer distance. Also, as argued in section 7.3, the initial amplitude of the instability wave is, for all intents and purposes, independent of the flight speed. The net result of these effects is that the large-scale instability waves, represented by the humps in figure 5.31, grow to about the same amplitude, both in flight and in static case, even though they achieve the final amplitude at different axial locations.

The above arguments are best substantiated by comparing the shear-layer thicknesses for both the unexcited and excited conditions with and without forward velocity. This is shown in figure 5.33, where the shear-layer thickness, b, is defined as the distance between the potential-core contour and the half-velocity contour, as shown in figure 5.9. Clearly, there is little change in the plume width, whether the forward velocity is included or not.

Finally, the effects of increasing excitation level on the mean velocities and turbulence intensities, for the flight case, were similar to those for the static case, both for the axial distribution (see figure 5.34, 5.35, 5.36 and 5.37), and also for the corresponding radial profiles (see figure 5.38). The results of flight simulation on the (0,0) mode (figure 5.29 thru 5.36) and the (1,0) mode (figure 5.28) were similar, and the arguments given above apply to the results for both modes of acoustic excitation.

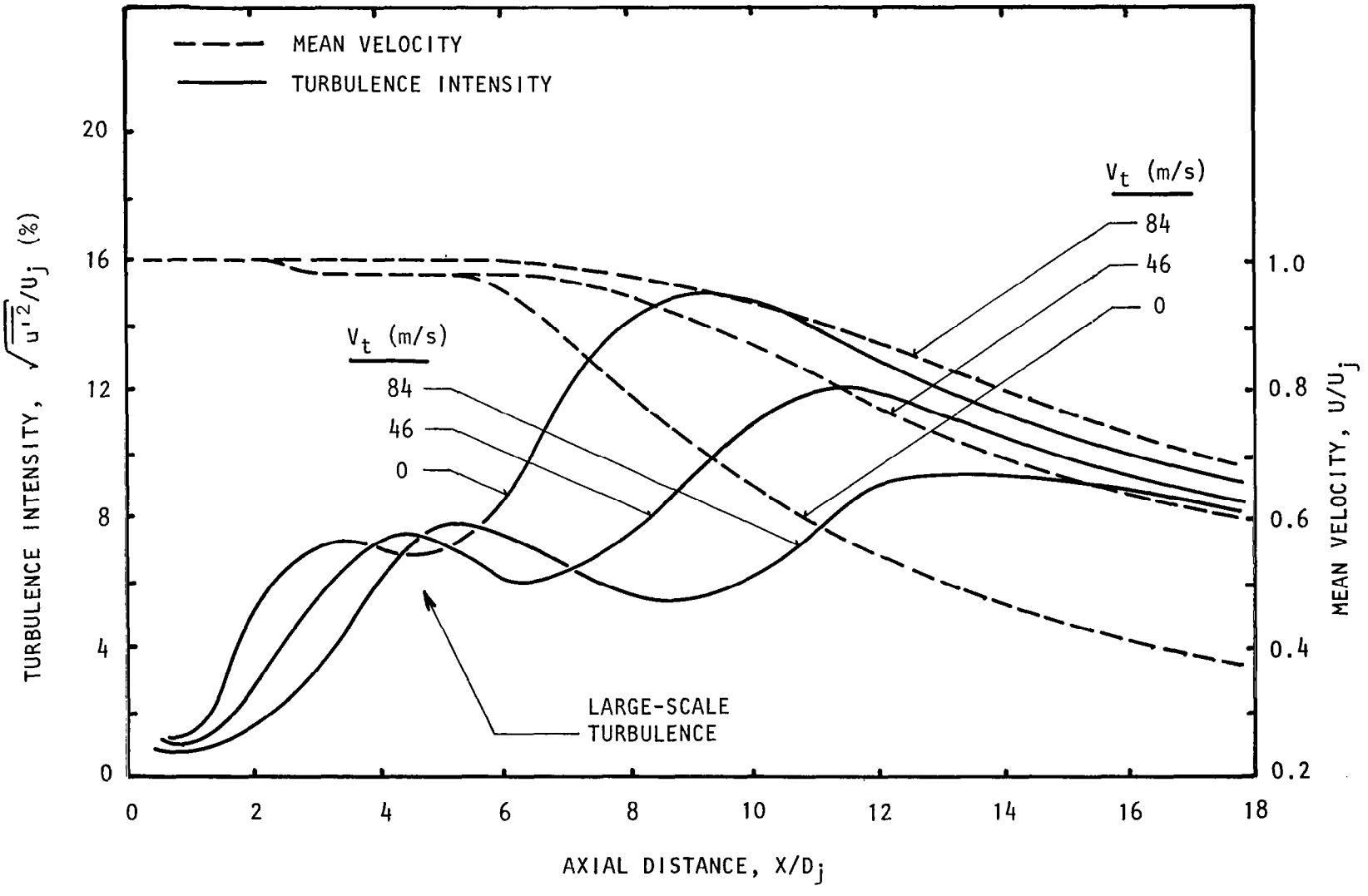

Figure 5.31 Flight velocity effects on centerline distributions.
M_j = 0.58, U_j = 195 m/s, Unheated, S_e = 0.5
L_e = 141 dB, (0,0) Mode.

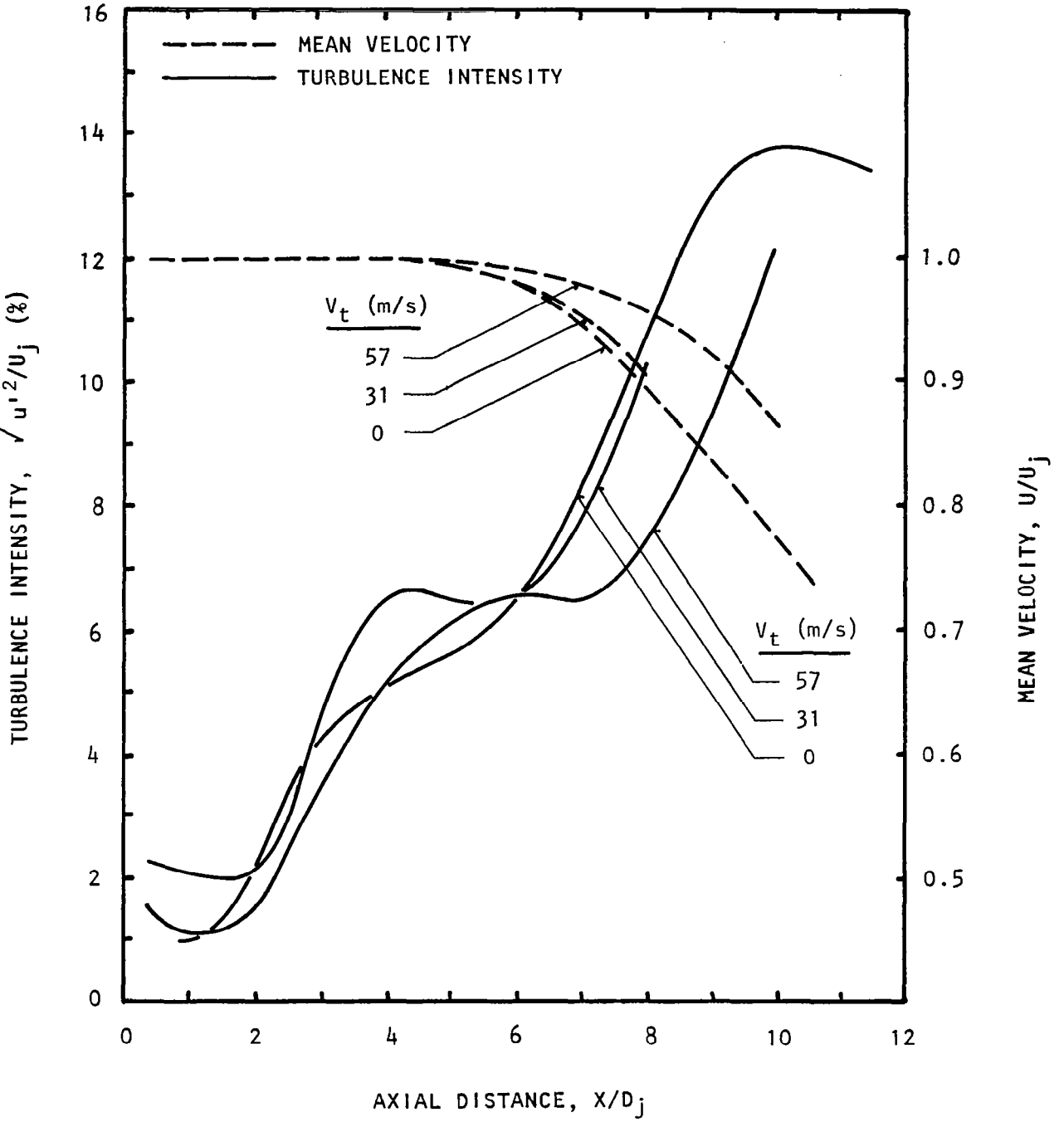

Figure 5.32 Flight-velocity effects on centerline distributions.
M_j = 0.78, U_j = 255 m/s, Unheated,
L_e = 136 dB, S_e = 0.5, (0,0) Mode.

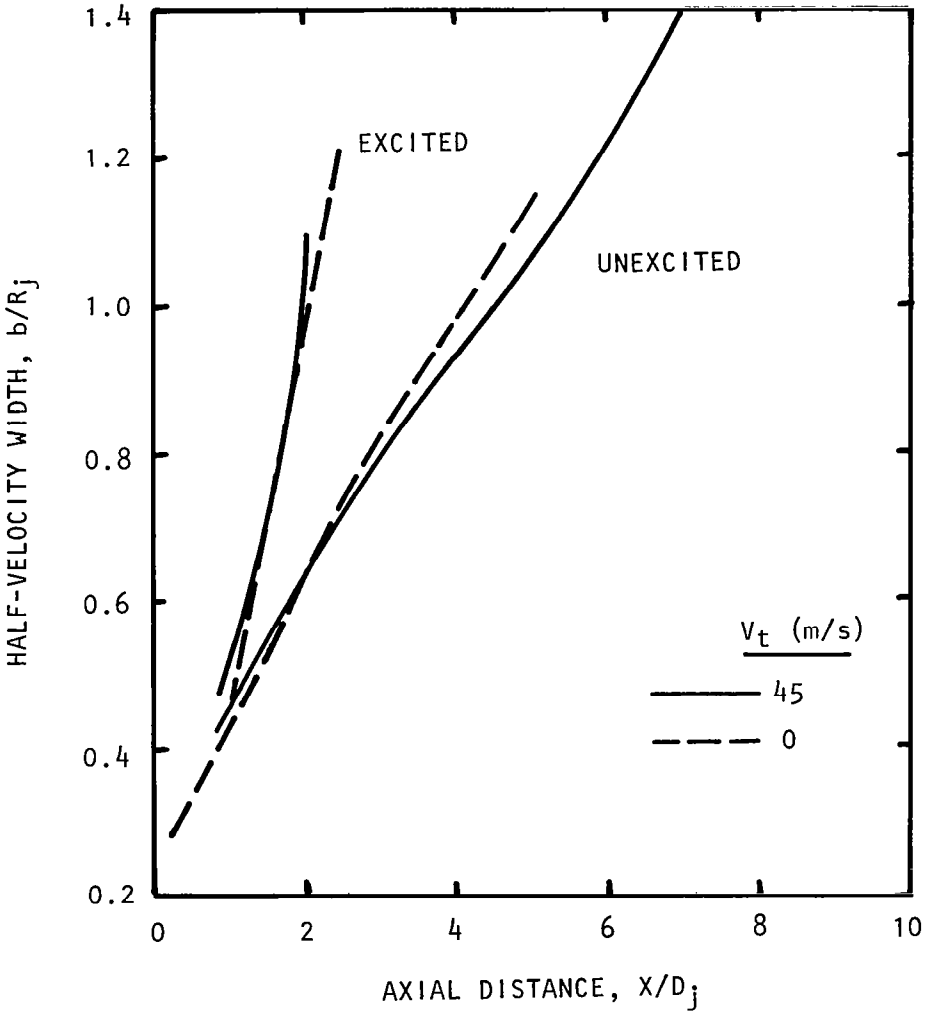

Figure 5.33 Excitation effects on axial distribution of dimensionless half-velocity shear-layer width with and without flight velocity.
M_j = 0.58, U_j = 195 m/s, Unheated, S_e = 0.5, L_e = 141 dB, (0,0) Mode.

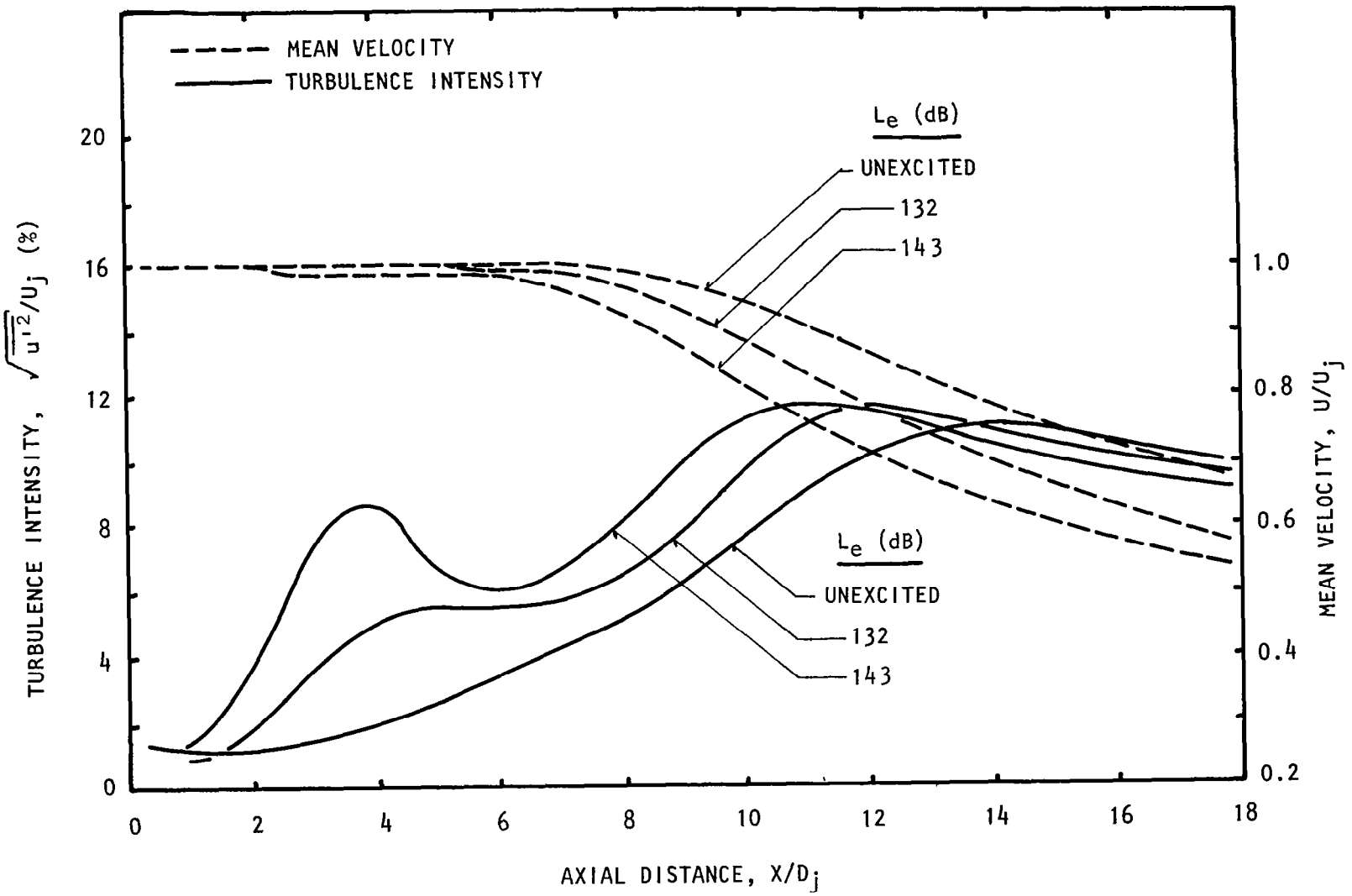

Figure 5.34 Excitation-level effects on centerline distributions of jet under flight simulation.
M_j = 0.58, U_j = 195 m/s, Unheated,
V_t = 45 m/s, S_e = 0.5, (0,0) Mode.

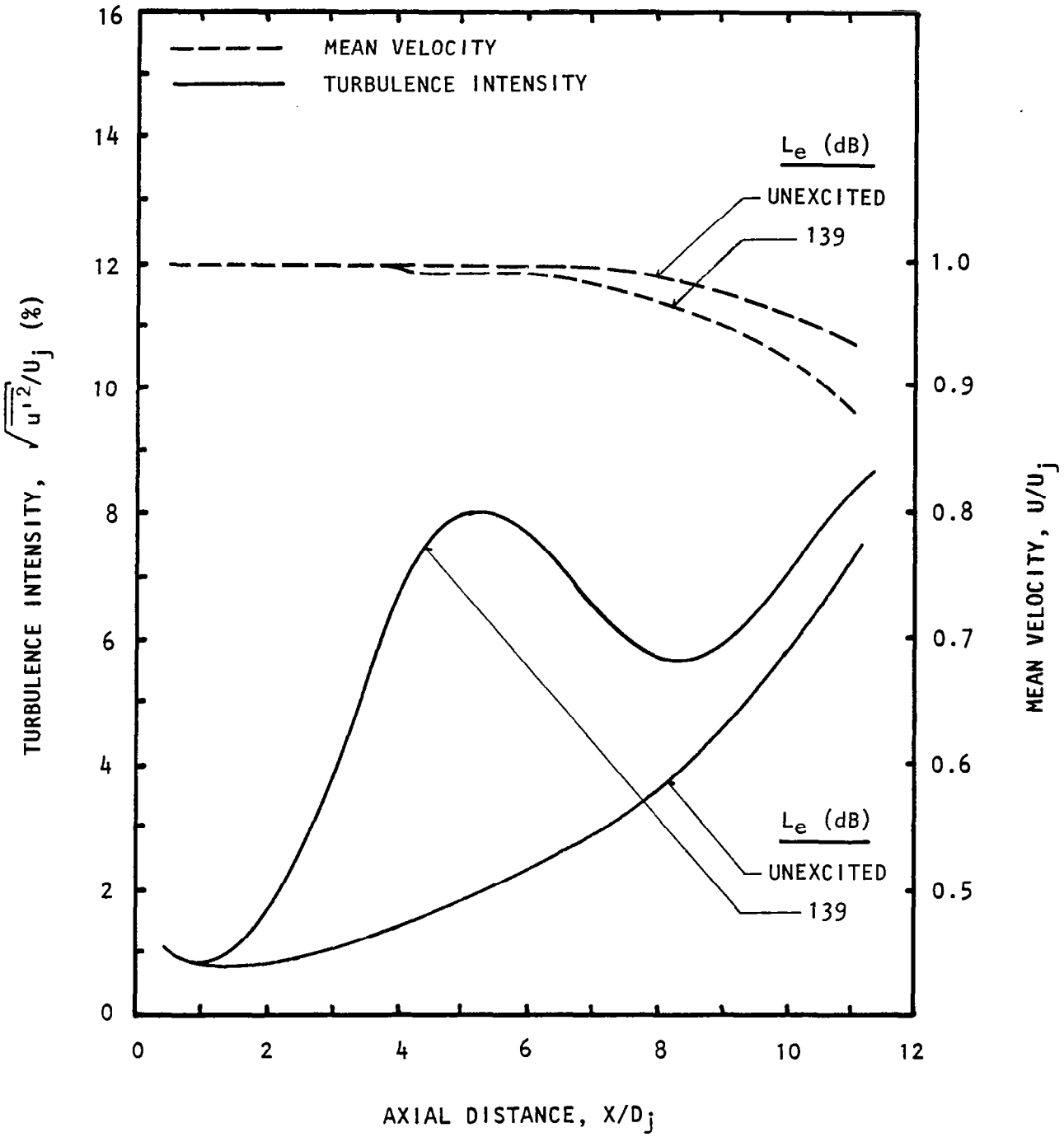

Figure 5.35 Excitation-level effects on centerline distributions of jet under flight simulation.
M_j = 0.58, U_j = 195 m/s, Unheated,
V_t = 84 m/s, S_e = 0.5, (0,0) Mode.

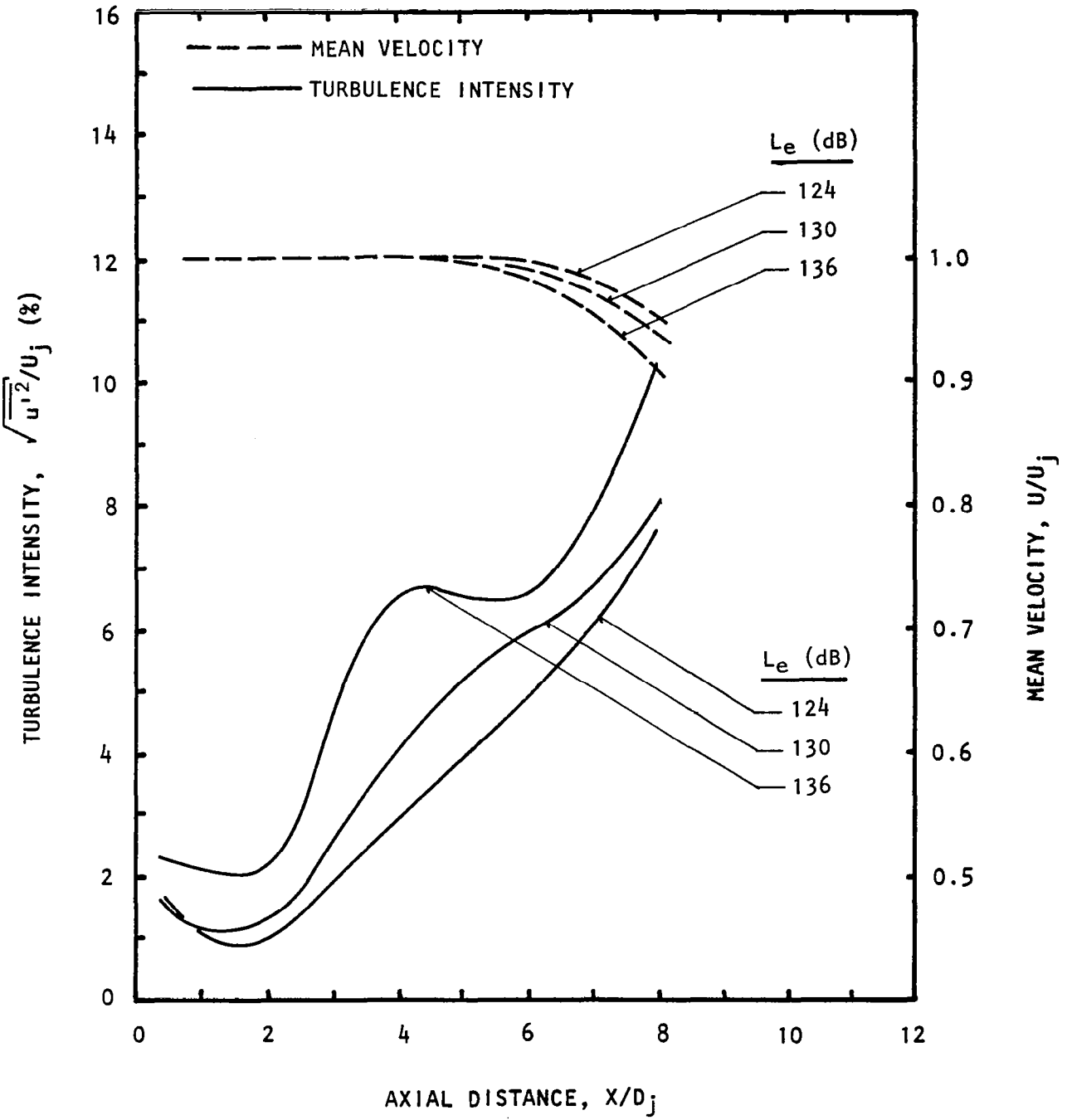

Figure 5.36 Excitation-level effects on centerline distributions of jet under flight simulation.
M_j = 0.78, U_j = 255 m/s, Unheated,
V_t = 31 m/s, S_e = 0.5, (0,0) Mode.

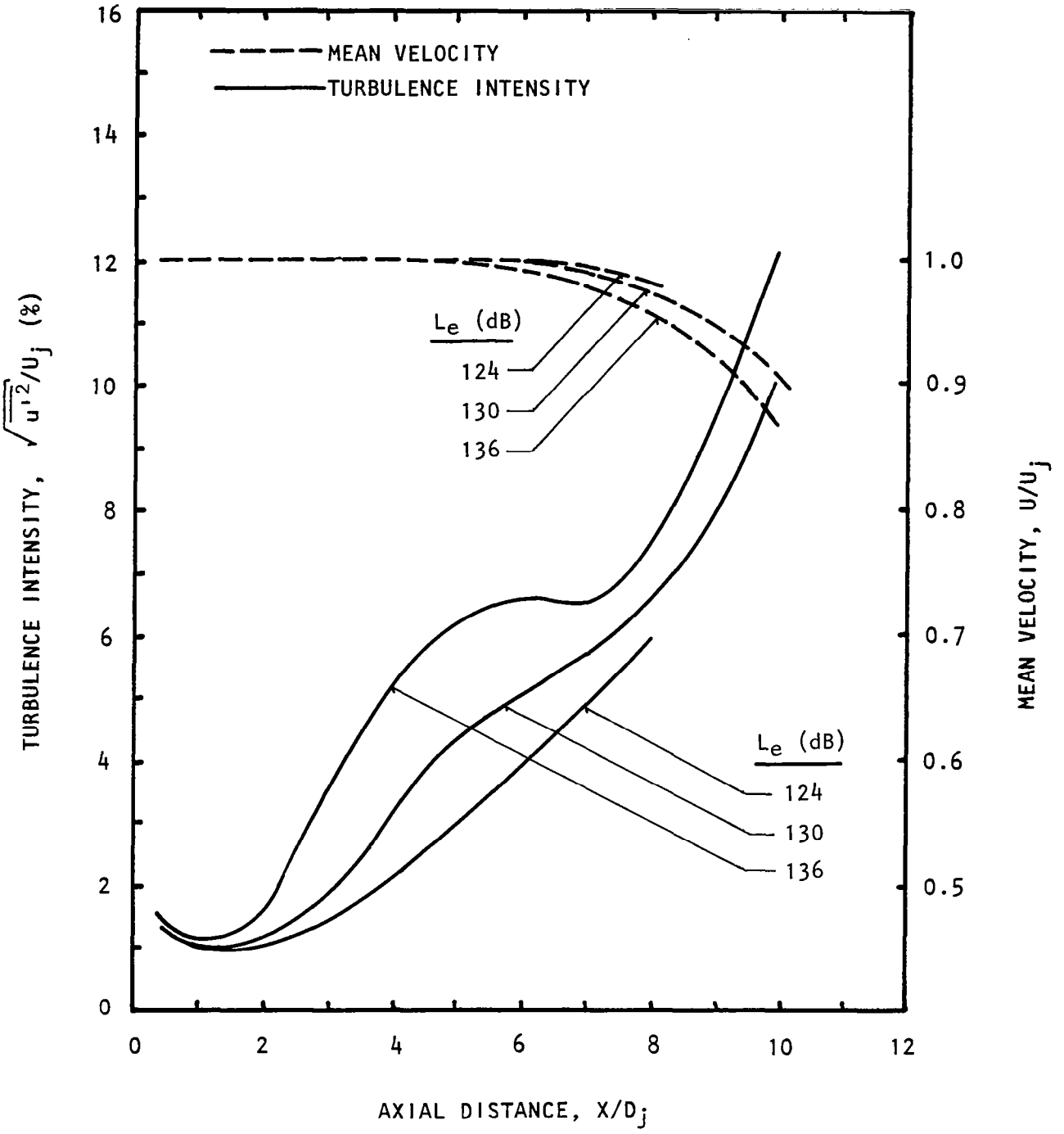

Figure 5.37 Excitation-level effects on centerline distributions of jet under flight simulation.
M_j = 0.78, U_j = 255 m/s, Unheated
V_t = 57 m/s, S_e = 0.5, (0,0) Mode .

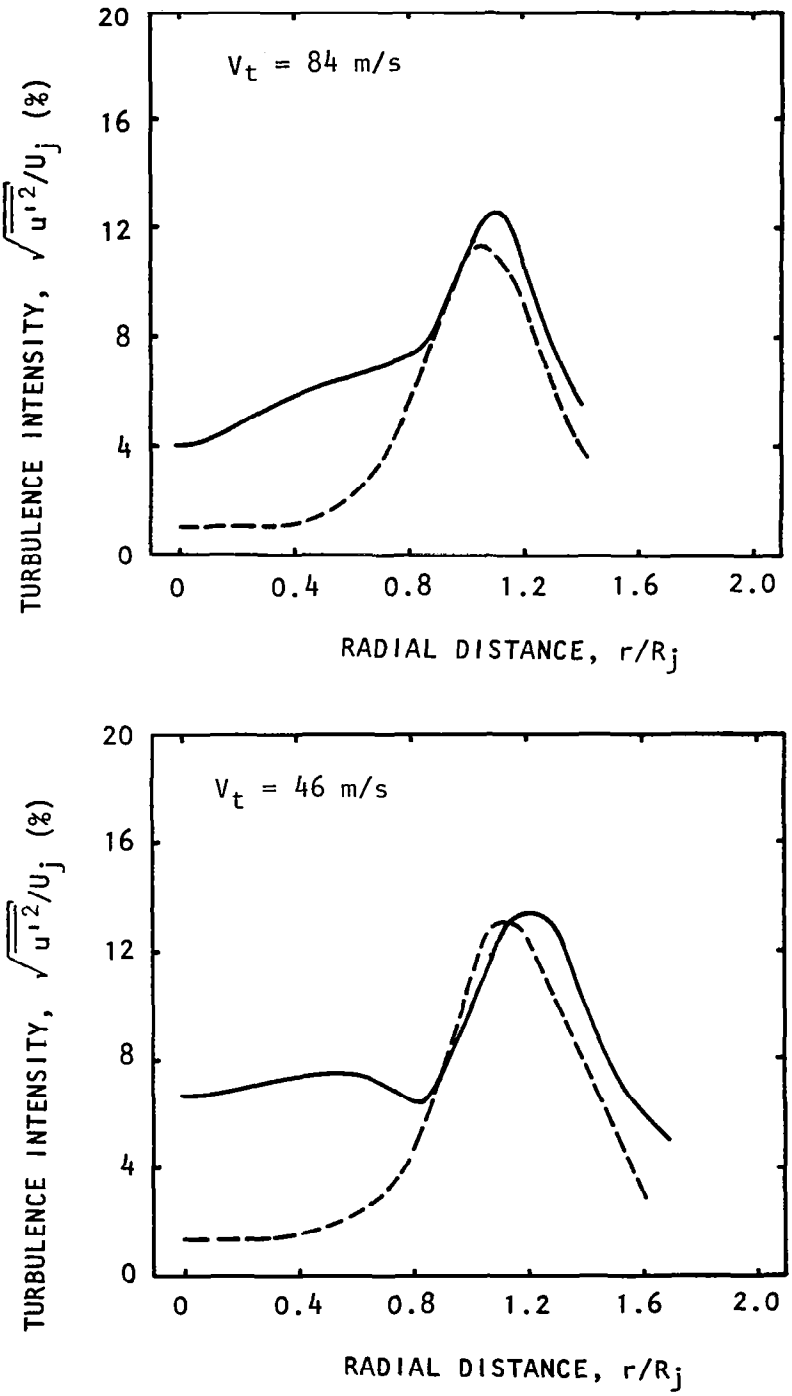

Figure 5.38 Turbulence-intensity profiles at X/D_j = 3 under flight simulation. M_j = 0.58, U_j = 195 m/s, Unheated, S_e = 0.5, L_e = 141 dB.
— — — , Unexcited, ——— Excited

5.7 TEMPERATURE EFFECTS

Only a limited amount of data was acquired for the heated jets. The effects of upstream excitation for heated jets was studied only at one Strouhal number: $S_e = 0.5$, and one excitation level: $L_e = 141$ dB. As will become clear below, the results appear to be unusual in that they contradict the theoretical predictions presented in section 7.0. However, since these results were consistent, major experimental errors were ruled out as the cause of the observed anomaly.

The mean-velocity and turbulence-intensity distributions along the centerline for the unexcited heated jet ($t_r = 800K$) are first presented in figure 5.39. Effect of heating is to increase the turbulence intensity and widen the jet plume, up to $X/D_j \simeq 10$. At axial locations, farther than 10 D_j, the turbulence intensity is increased. This trend is in agreement with that observed by Lau (ref. 31) and Ahuja (ref. 32).

When a fixed Mach-number ($M_j = 0.78$) heated jet is excited, the results shown in figure 5.40 were obtained. Here it is seen that the effect of excitation is to decelerate the mean-velocity decay rate of the jet, and also correspondingly decrease the turbulence intensities up to $X/D_j = 7$. Beyond $X/D_j = 7$, an increase in turbulence intensities is observed. These results are somewhat perplexing, since the theoretical results presented in section 7.0 suggest an increase in total kinetic energy associated with the small-scale turbulence as a result of the upstream excitation, both for the unheated as well as heated jets.

To establish if the excited, heated jets behave any differently from the excited unheated jets, described in the previous section, the effects of forward velocity on the mean-velocity and the turbulence-intensity distributions were examined for three flight velocities. This is shown in figure 5.41. The effect of forward velocity is to reduce the mean velocity-decay rate and also the turbulence intensities. Effects of flight velocity for the excited heated jet are, thus, quite similar to those for the excited unheated jet.

Further work is clearly needed to assess the effects of upstream excitation on heated jets. No firm conclusion can, therefore, be drawn from the results discussed above.

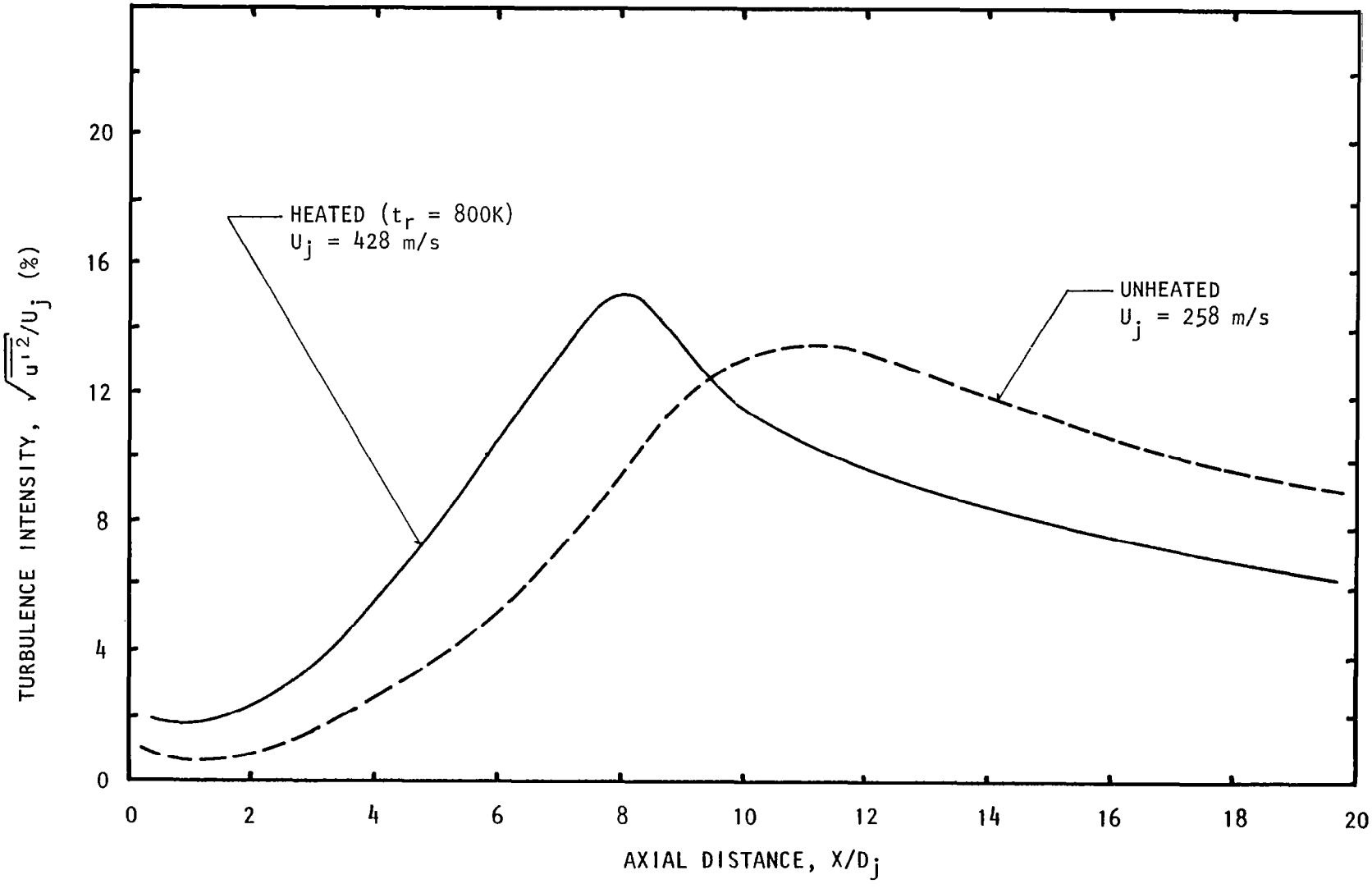

Figure 5.39(a) Reservoir-temperature effects on centerline distribution of turbulence intensity.
M_j = 0.78, Static, Unexcited .

(See figure D.8(a) for actual measurement points.)

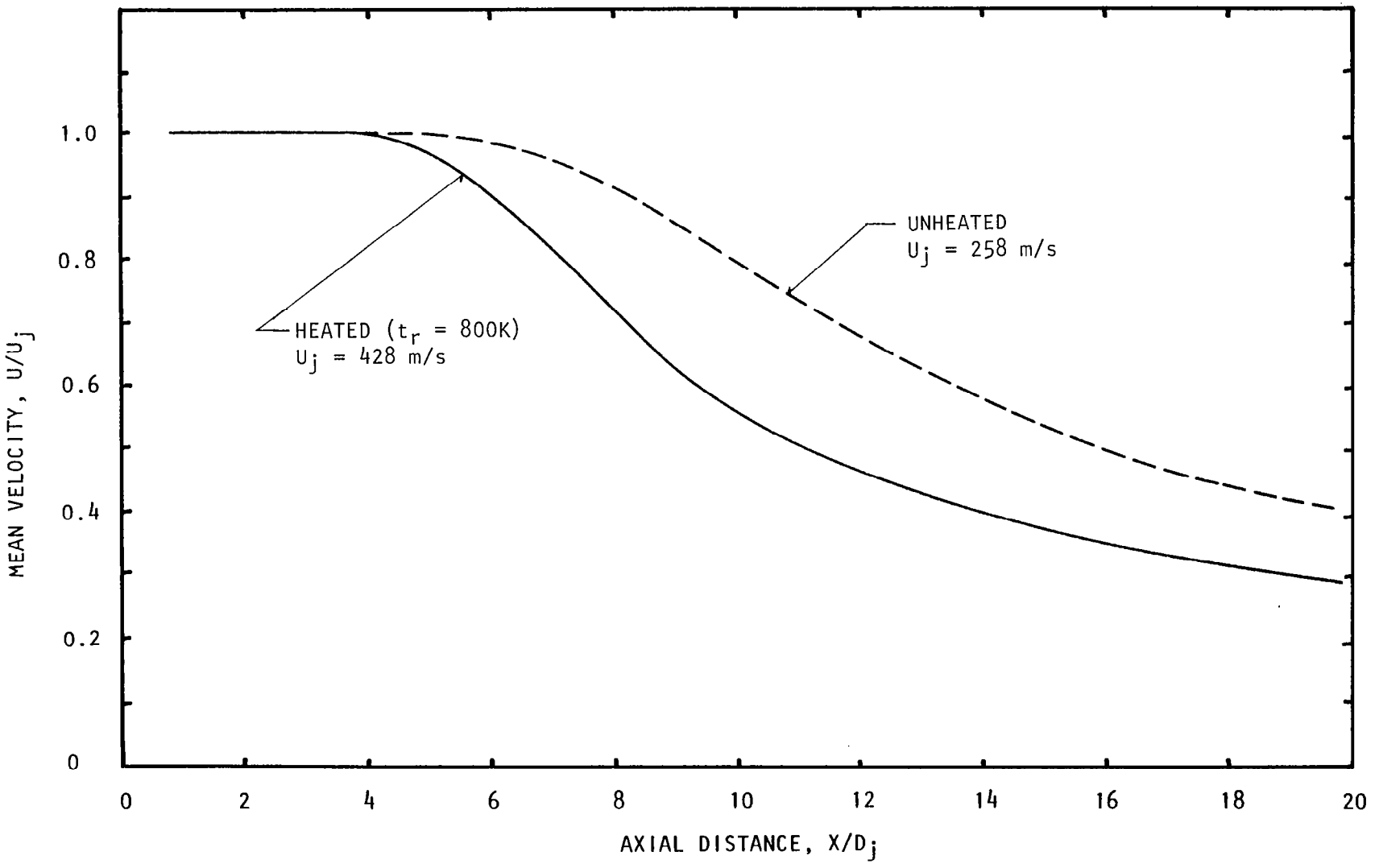

Figure 5.39(b) Reservoir-temperature effects on centerline distribution of mean velocity.
M_j = 0.78, Static, Unexcited.

(See figure D.8(b) for actual measurement points.)

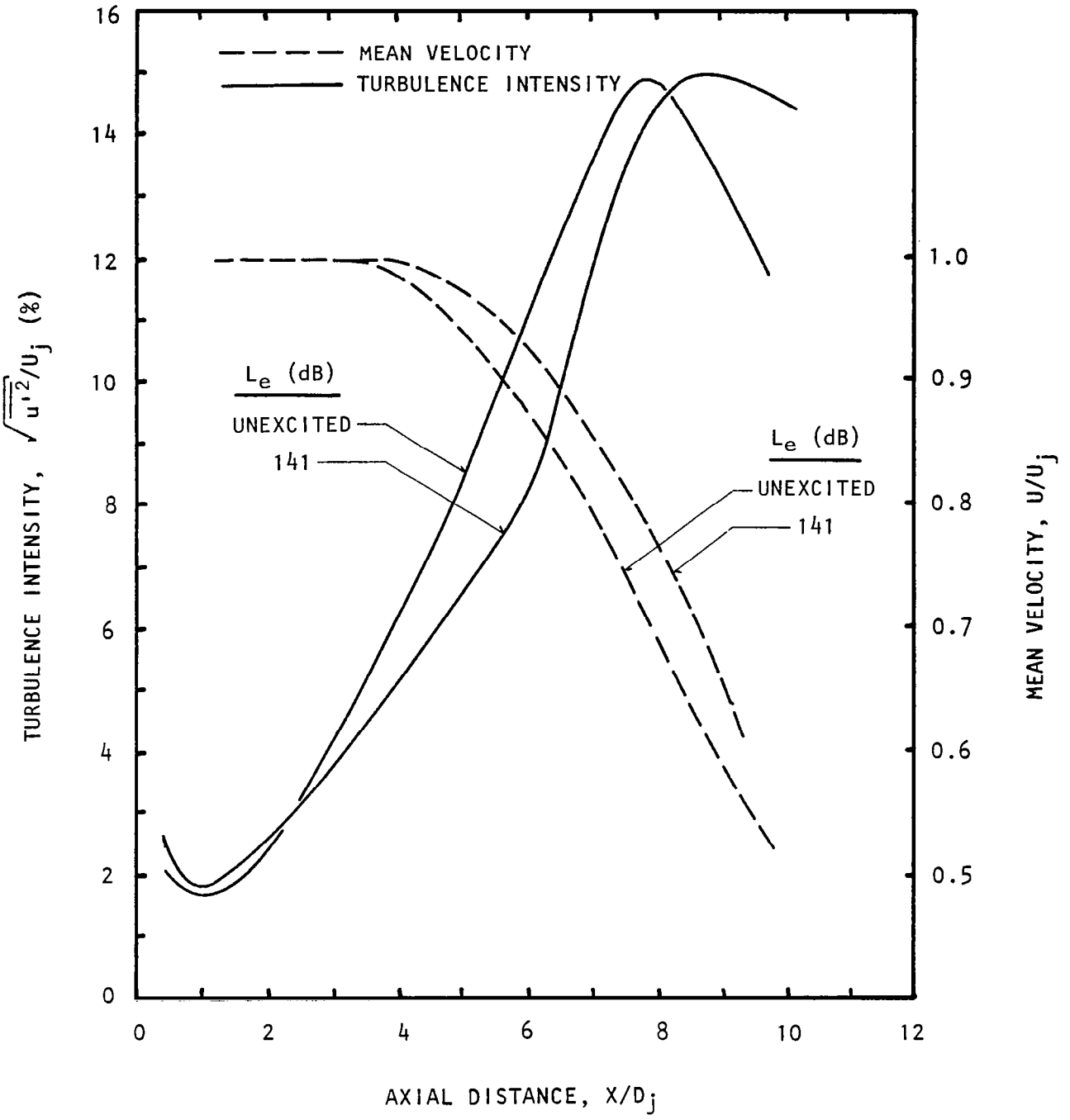

Figure 5.40 Effects of upstream excitation on the centerline distributions of the heated jet. M_j = 0.78, U_j = 428 m/s, t_r = 800K, Static, S_e = 0.5, (0,0) Mode.

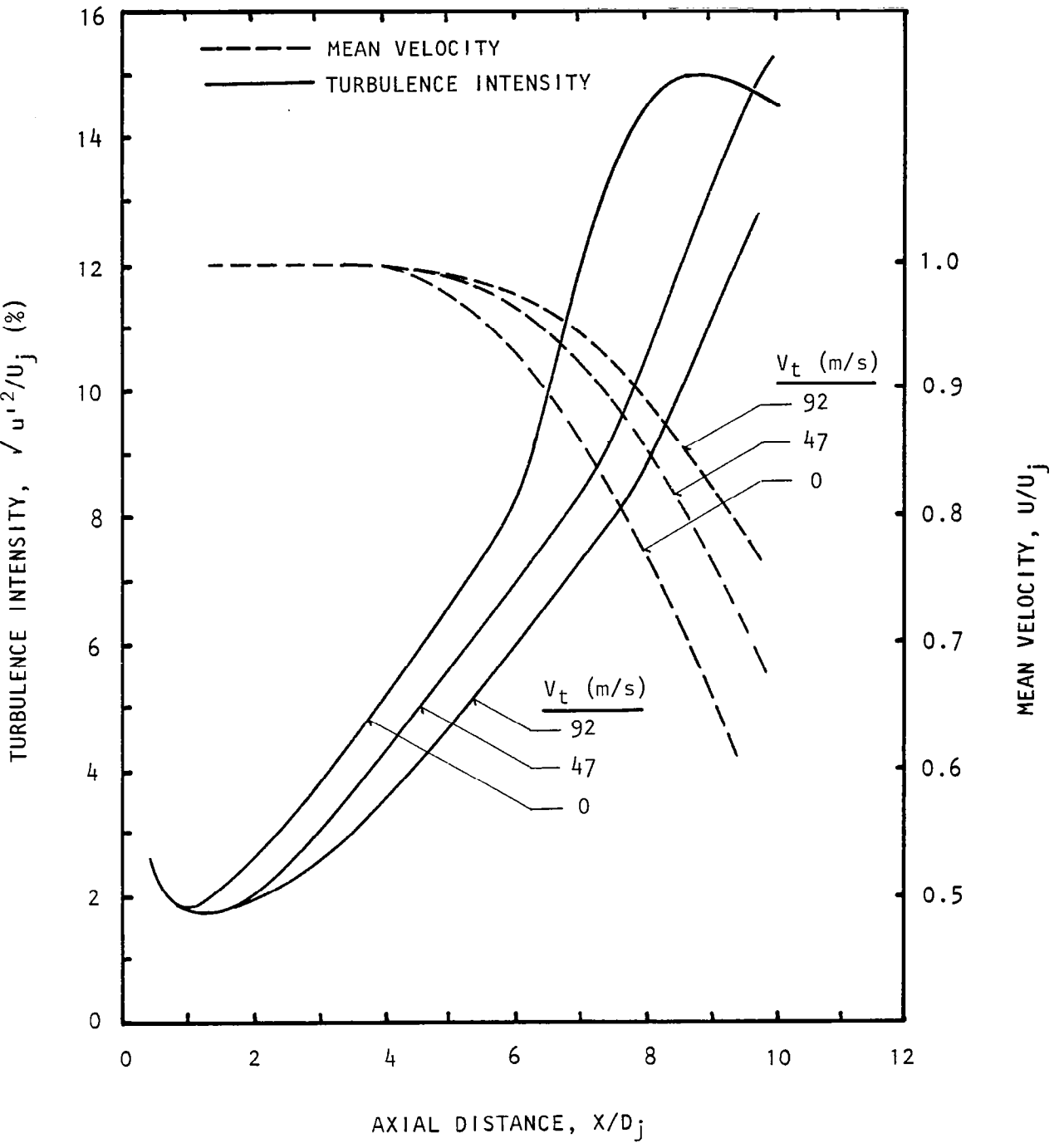

Figure 5.41 Flight-velocity effects on centerline distributions of the heated jet. M_j = 0.78, U_j = 428 m/s, t_r = 800K, S_e = 0.5, L_e = 141 dB, (0,0) Mode .

5.8 A NOTE ON UNEXCITED-JET SPECTRA

A typical turbulence spectrum of an unexcited jet was presented in figure 5.17 for one axial location, where it was compared with the spectra for excited jet for three excitation levels. It is seen in figure 5.17 that the peak in the unexcited-jet turbulence spectrum is at a Strouhal number of 0.5. Further analysis of the turbulence spectra of the unexcited jet at other various axial locations and for two jet Mach numbers: 0.58 and 0.78 indeed showed that the unexcited jet itself has a natural frequency of about fD_j/U_j = 0.5. This is shown in figure 5.42(a) for M_j = 0.58, where the axial-turbulence intensity spectra, measured along the centerline, are presented for seven axial locations: X/D_j = 1,2,3,4,5,7, and 9. Clearly, within the region of the potential core, well-defined peaks are observed at frequencies corresponding to a Strouhal number of $\simeq$ 0.5. Similar results were obtained for the higher jet Mach number of 0.78, as seen in figure 5.42(b).

The above mentioned humps can be attributed to the naturally occurring large-scale turbulence structure of the unexcited jet. As the measurement point is moved outside the potential core, higher levels of small-scale turbulence, particularly at low frequencies, dominate the large-scale turbulence. It is for this reason that, in figure 5.42, well defined peaks can not be seen at X/D_j greater than 5. This is also found to be true for the spectra measured along the lip-line for both Mach numbers, as shown in figure 5.43. It is our contention that if a conditional sampling technique were used in these latter measurements, thus minimizing the contribution of the small-scale turbulence, the spectral contribution of the naturally occurring large-scale turbulence would have also become apparent.

The important observation to be made here is that, since the natural frequency of the large-scale turbulence peaks at $fD_j/U_j \simeq 0.5$, the jet would be most receptive to external excitation at this Strouhal number, as indeed it does.

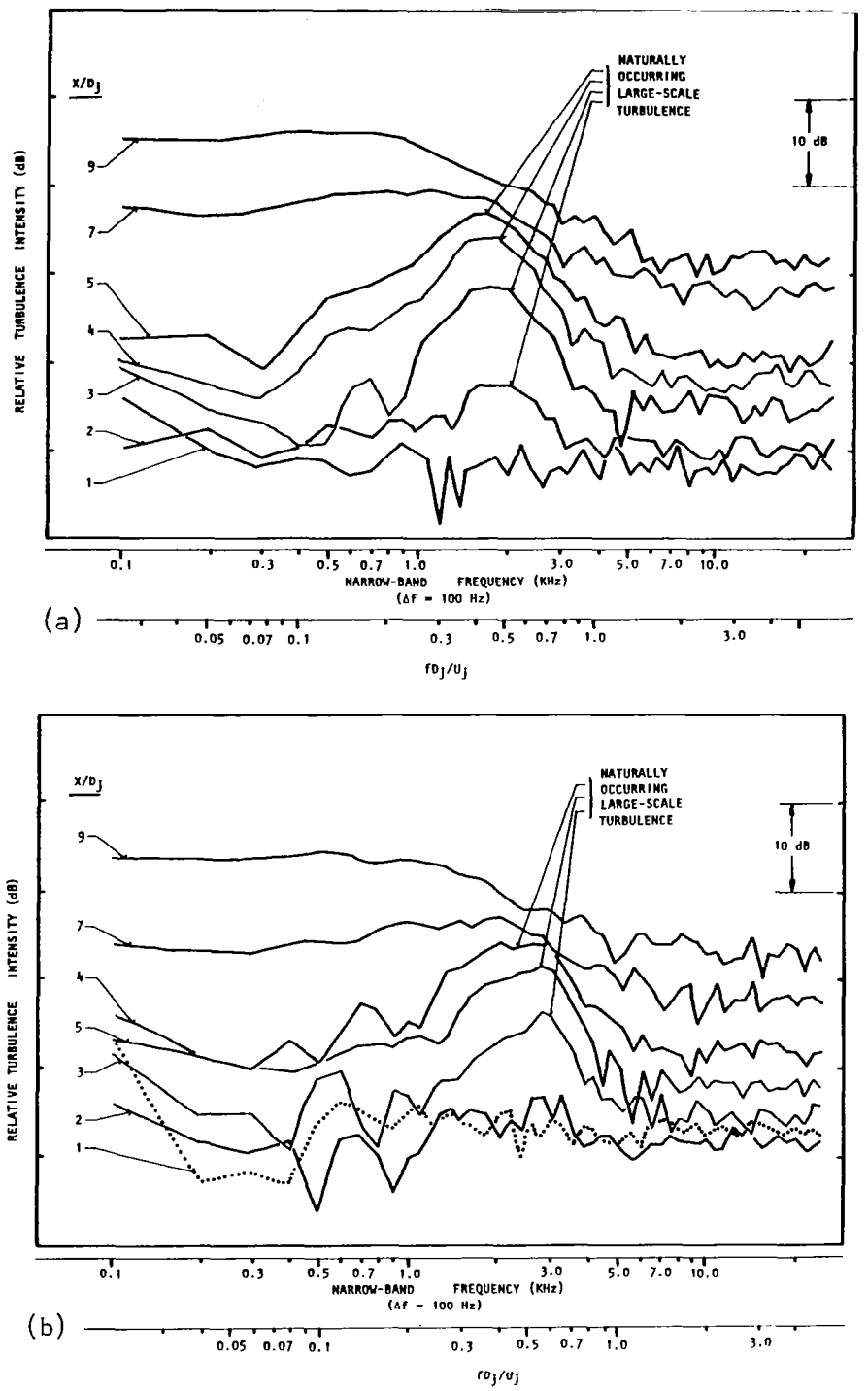

Figure 5.42 Centerline distribution of the turbulence spectra for an unheated and unexcited jet at (a) M_j = 0.58 and (b) M_j = 0.78.

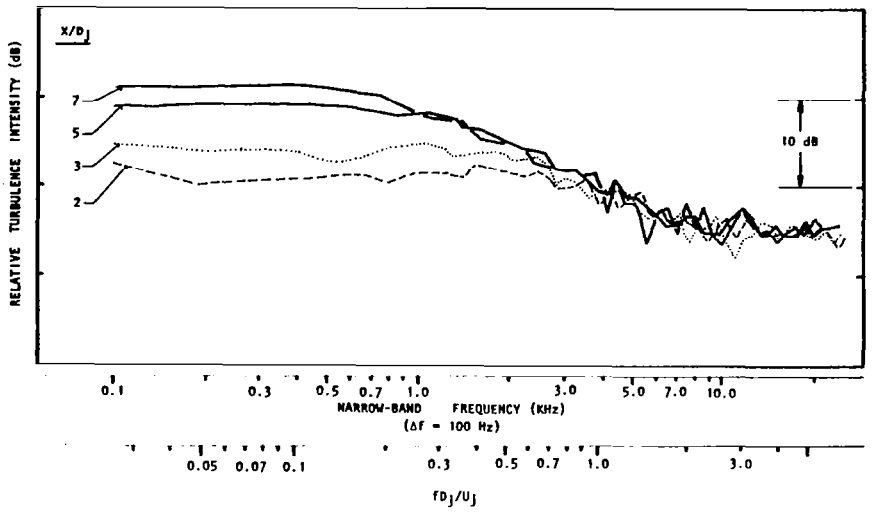

(a)

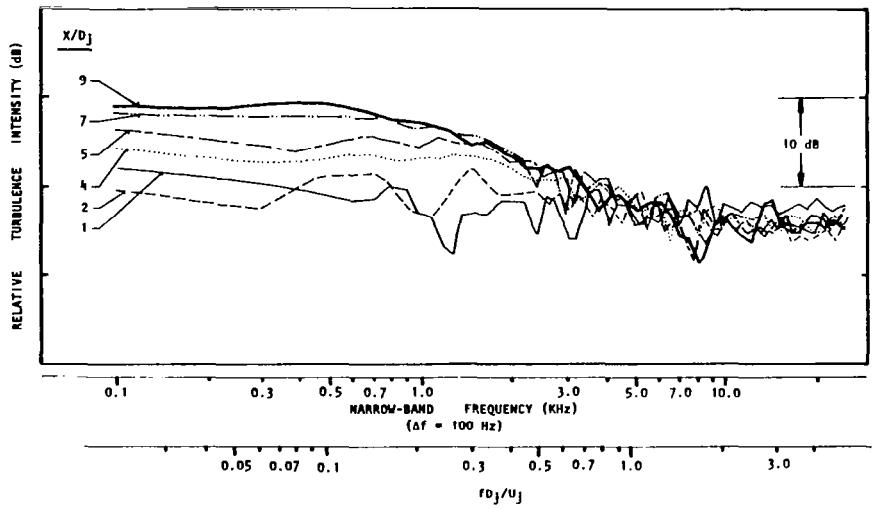

(b)

Figure 5.43 Lipline distribution of the turbulence spectra for an unheated and unexcited jet at (a) M_j = 0.58 and (b) M_j = 0.78.

6.0 ACOUSTIC RESULTS

Even though the results of the acoustic experiments were acquired before conducting the jet-flow measurements described in the preceding section, it was decided to present the jet-flow results prior to presenting the acoustic results, to render the understanding of the acoustic results presented here, easier. Similar to the turbulence results, the effects of excitation Strouhal number, excitation level, mode order, jet temperature, jet Mach number, and flight velocity on far-field jet-noise amplification are described in separate subsections.

Throughout this section, the excitation levels, L_e, and the sound pressure levels, SPL, are referred to 2×10^{-5} N/m^2, whereas the acoustic powers, PWLs, are referred to 10^{-12} watts.

As mentioned before, all acoustic measurements were made in the anechoic open-jet wind-tunnel. In fact, even for the static case, there was a low velocity flow through the open jet because of the ejector effect. All one-third octave data presented here have, therefore, been corrected to ideal wind-tunnel (IWT) conditions using the procedure described in reference 3, and extrapolated to 100 nozzle-exit diameters.

6.1 STROUHAL-NUMBER EFFECTS

Typical 1/3-octave band PWLs, with and without upstream excitation, at (0,0) mode are shown in figures 6.1(a) thru 6.1(g) at S_e = 0.2, 0.315, 0.40, 0.45, 0.48, 0.63, and 1.0 respectively for an unheated jet excited at excitation level L_e = 134 dB and operated at M_j = 0.58. As the excitation Strouhal number approaches S_e = 0.48, a peak amplification in the broadband noise is noticed. This is consistent with the instability-wave pressure amplitude measurements made for the above conditions in the acoustic facility, as shown in figure 6.2. Here the instability wave pressures at x/D_j = 3.0 were measured for the fixed excitation level, L_e = 134 dB, but for a range of excitation Strouhal numbers. Clearly, the maximum amplitude of the instability wave is reached at S_e = 0.48. And as explained in section 7.2.2, the conditions under which the excited instability wave or the large turbulent structures reach the greatest amplitude coincide with the largest changes in the mean flow and small-scale turbulence development. One should, therefore, expect maximum amplification in the radiated jet noise at about S_e = 0.48.

In general, for a given excitation level, the maximum jet-noise amplification was found to lie between S_e = 0.4 and 1.0, depending upon whether the amplification at a given frequency was considered or whether the OASPL data, after subjectively subtracting the contribution of the excitation from the

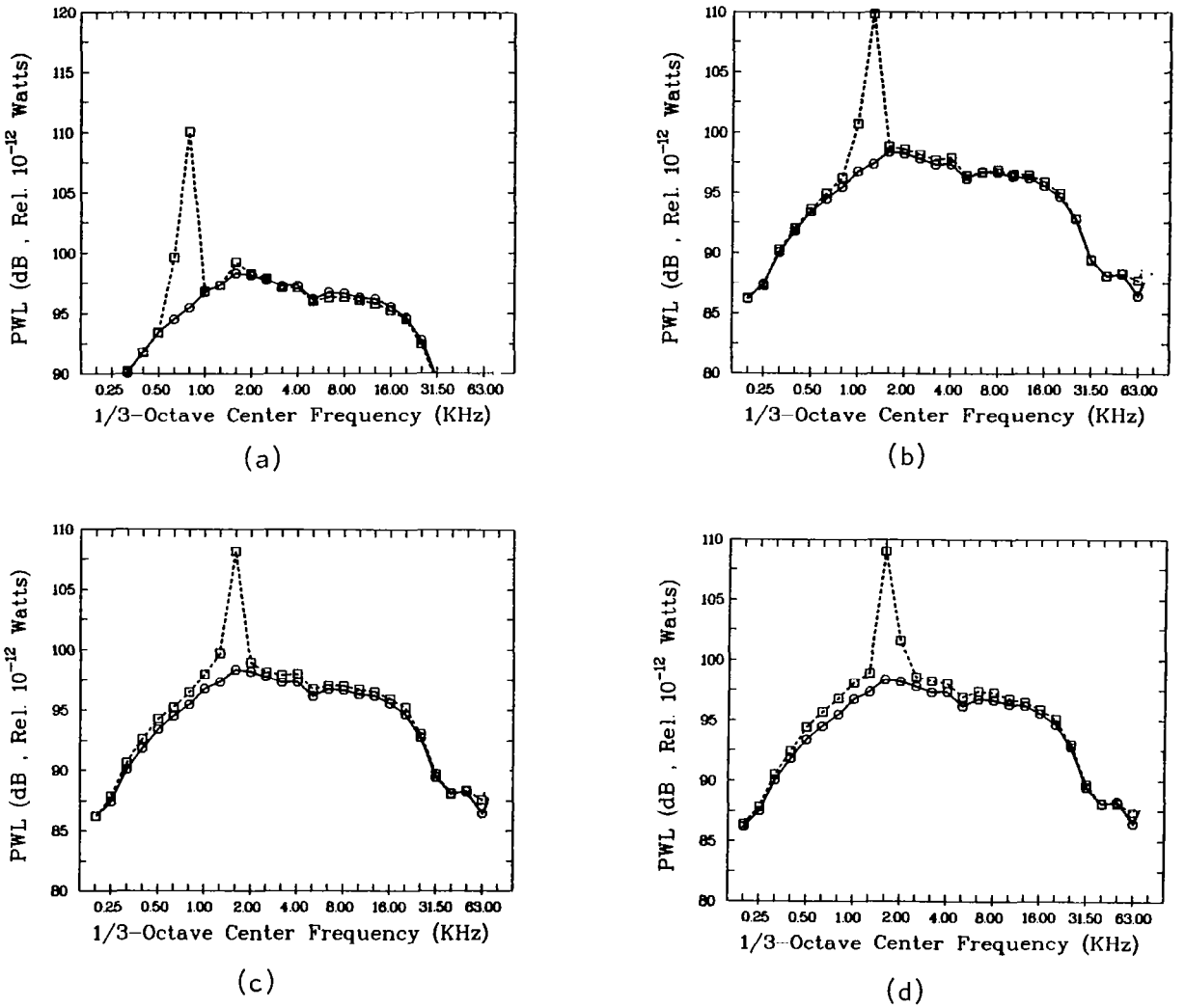

Figure 6.1a,b,c,d Comparison between 1/3-octave PWLs for the unexcited jet (○) and the excited jet (□) at various excitation Strouhal numbers, S_e: (a) 0.20, (b) 0.315, (c) 0.40, and (d) 0.45. M_j = 0.58, Uj = 190 m/s , Unheated, Static, L_e = 134 dB, (0,0) Mode.

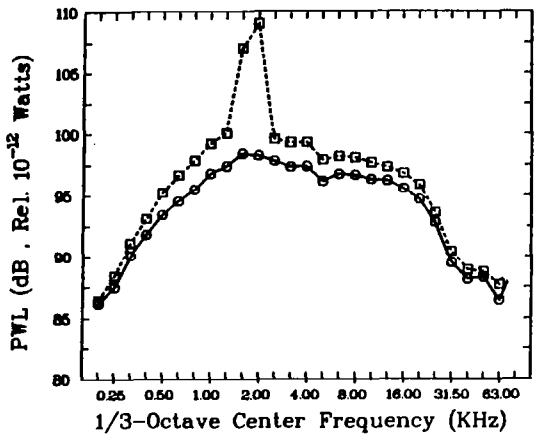

(e)

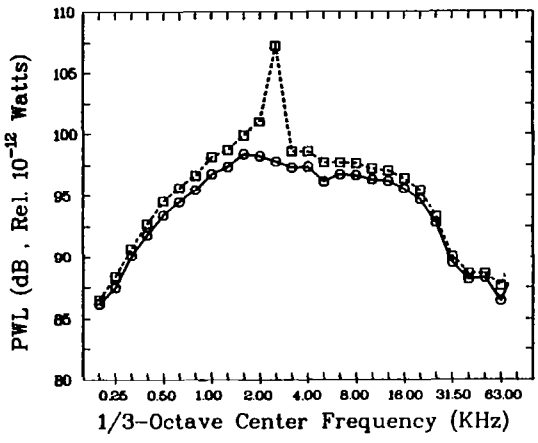

(f)

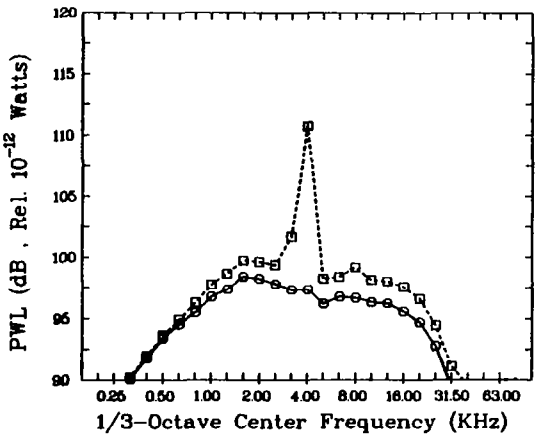

(g)

Figure 6.1e,f,g Comparison between 1/3-octave PWLs for the unexcited jet (○) and the excited jet (□) at various excitation Strouhal numbers, S_e: (e) 0.48, (f) 0.63, and (g) 1.0. M_j = 0.58, U_j = 190 m/s, Unheated, Static, L_e = 134 dB, (0,0) Mode.

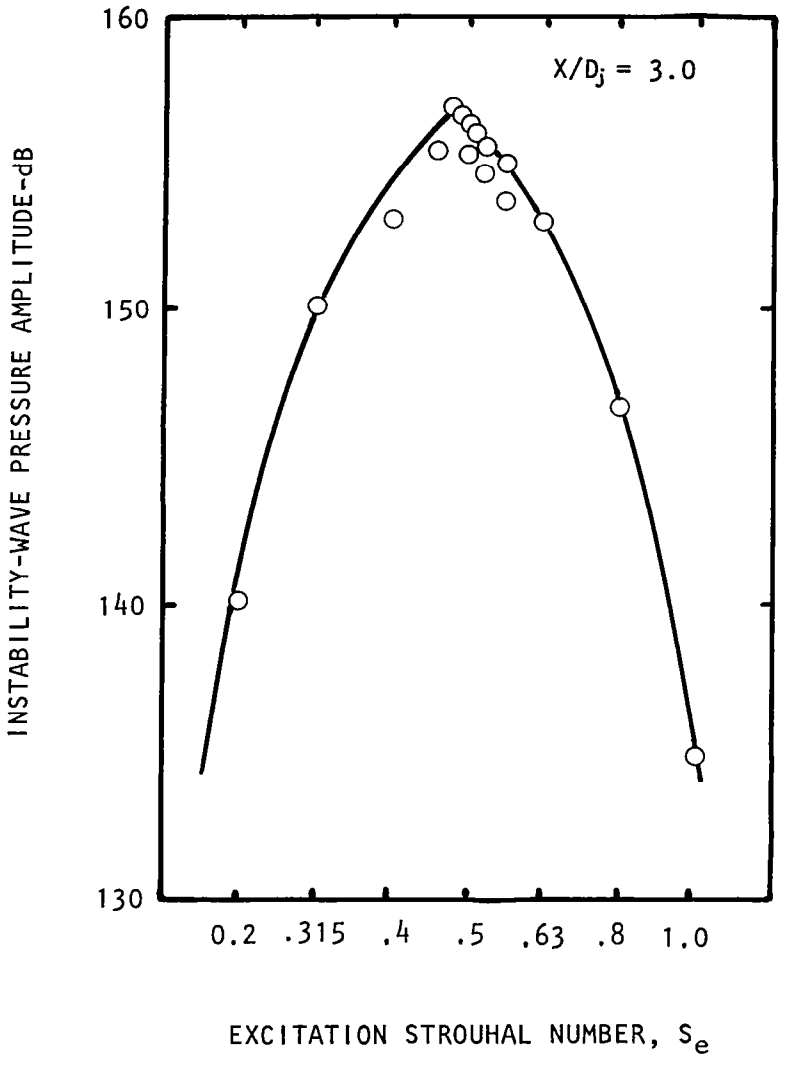

Figure 6.2 Variation of centerline instability-wave pressure amplitude at $X/D_j = 3.0$ with excitation Strouhal number. $M_j = 0.58$, $U_j = 190$ m/s, Unheated, Static, $L_e = 134$ dB, (0,0) mode.

discrete tone, were examined. On the other hand, outcome was somewhat different if the amplification in the far-field acoustic power was considered.

Published literature on this subject is inconsistent with respect to the effect of excitation Strouhal number on far-field acoustic radiation. For example, Moore (ref. 6) has considered only the OASPLs at a selected angle,while Jubelin (ref. 9) has considered overall acoustic powers. In the present investigation, in addition to SPL spectra and OASPLs, the 1/3-octave acoustic power spectra and overall power levels (OAPWLs) are also calculated. The OASPLs and OAPWLs are calculated by removing the discrete tones from the corresponding spectral plots.

As reported by others (refs. 5,6,9), it was found that exciting the jet by discrete-tone sound amplified jet-mixing noise at all frequencies at certain excitation Strouhal numbers and above certain excitation levels.

Data presented in figure 6.1 were for the lower Mach number of 0.58. Similar results were obtained for the higher Mach number of 0.78. These results are plotted as the amplification spectra for a range of excitation Strouhal numbers in figure 6.3. Here the excitation discrete tone, and its harmonics, if present, have been removed, and the curves have been smoothed to ±0.25 dB. Clearly, different amplification is observed at different frequencies in the spectrum. At certain jet-noise frequencies and low excitation Strouhal numbers, a minor reduction is also noticed.

Data of figure 6.3 are plotted in figure 6.4 in a different form. Here the amplifications in the 1/3-octave PWLs at various frequencies of the spectrum are plotted as a function of the excitation Strouhal number. These results show that for all jet-noise frequencies, there is a preferential excitation Strouhal number at which the largest amplification in jet noise is observed. This peak value of S_e is a function of the jet-noise frequency, and lies between $S_e = 0.5$ and 0.63 for most of the frequencies.

The overall sound power levels, after being corrected for the excitation discrete tones and harmonics (if and when present), are presented in figure 6.5 for $M_j = 0.78$ in the form of amplification versus emission angle with the jet axis for various excitation Strouhal numbers. These results indicate that the angles affected most by jet-noise amplification lie between 40° and 90° with the downstream jet axis. Outside this range of angles, the amplifications reduce sharply and, in fact, for the lower Strouhal numbers, an attenuation in jet noise may be obtained, particularly in the forward arc.

The results for the tone-corrected OAPWLs display a rather interesting trend with S_e as shown in figure 6.6. The OAPWL amplification varies as $S_e^{\frac{1}{4}}$ until it reaches a peak at $S_e = 0.63$. Thereafter, it starts to decrease as $S_e^{-\frac{1}{2}}$. Data in this form have not been studied or documented before in the published literature, and no clear-cut answers are available to explain this trend.

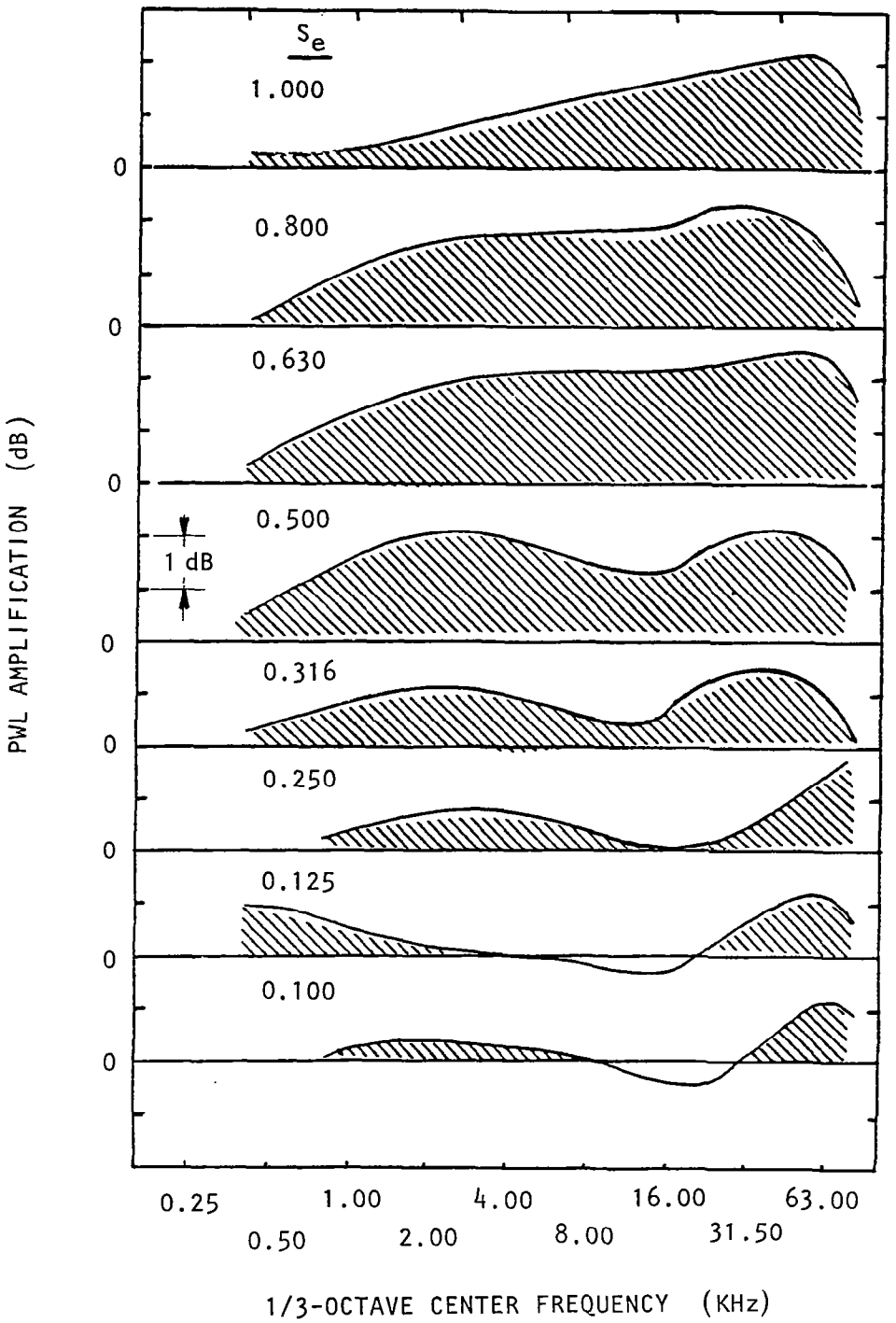

Figure 6.3 PWL-amplification spectra for various excitation Strouhal numbers. M_j = 0.78, U_j = 251 m/s, Unheated, Static, L_e = 136 dB, (0,0) Mode.

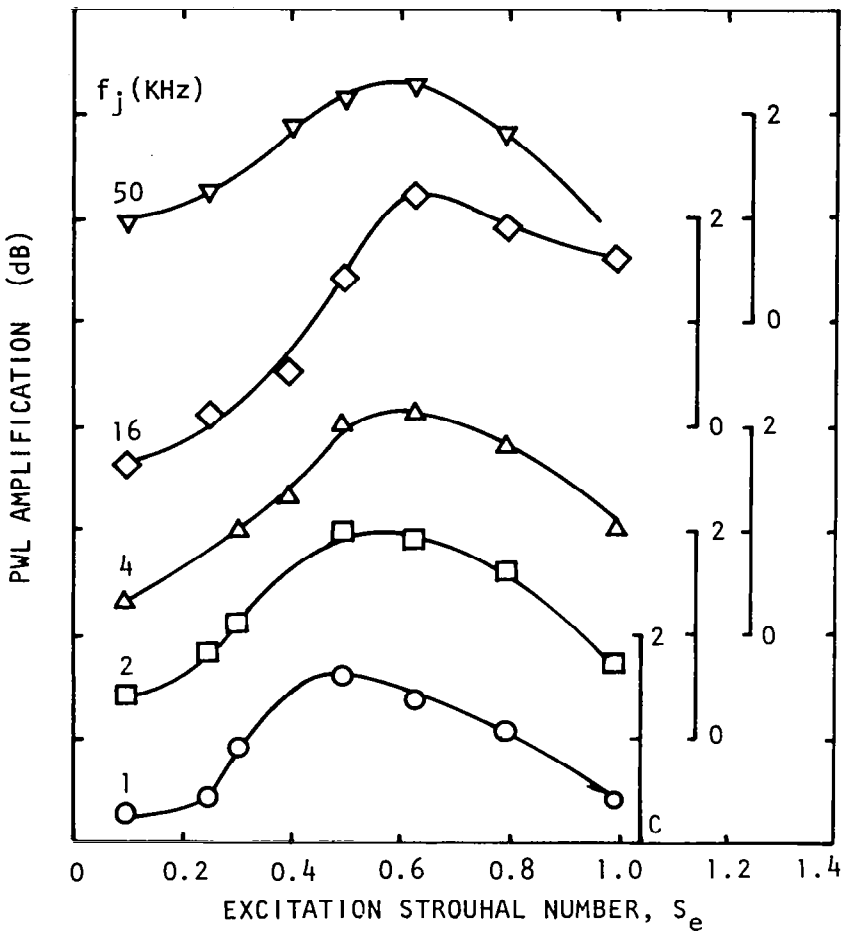

Figure 6.4 Variation of jet noise power amplification with excitation Strouhal number at various jet noise frequencies, f_j.
M_j = 0.78, U_j = 251 m/s, Unheated, Static,
L_e = 136 dB, (0,0) Mode.

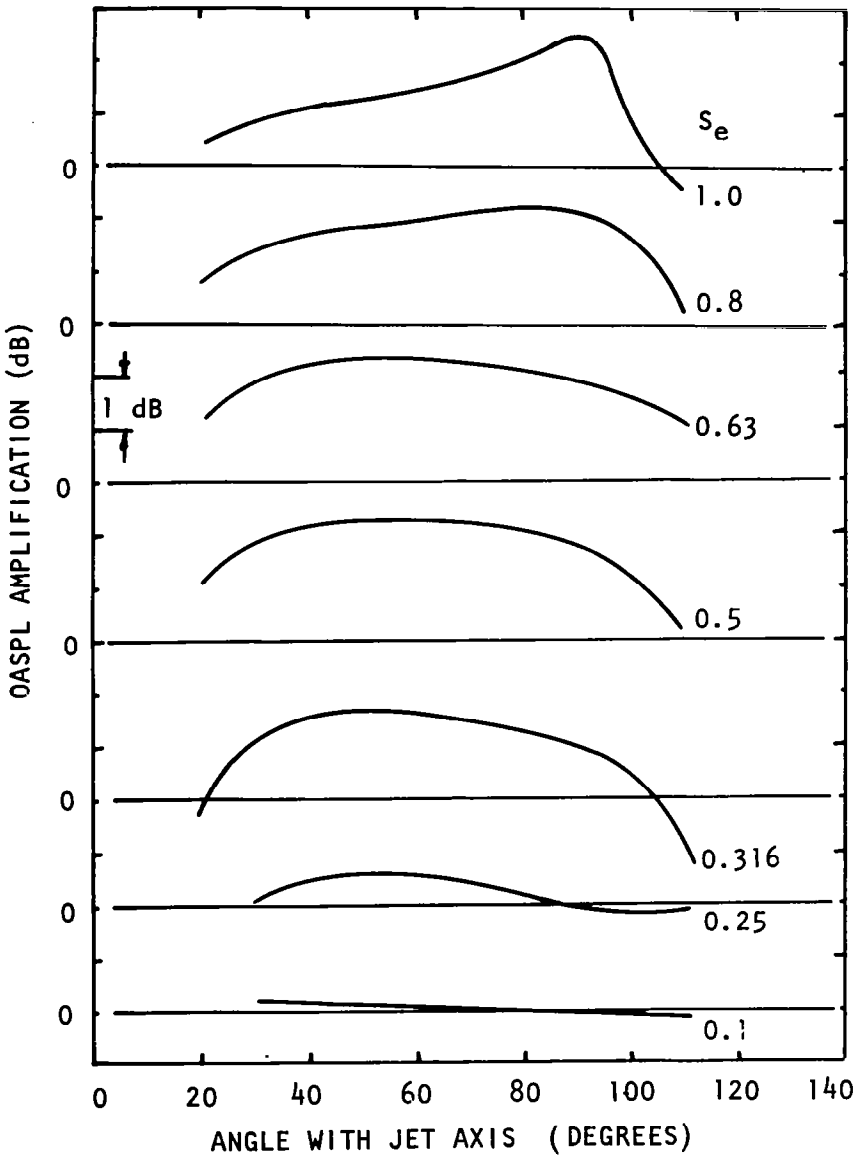

Figure 6.5 Variation of jet noise OASPL-amplification directivity with excitation Strouhal number, S_e. $M_j = 0.78$, $U_j = 251$ m/s, Unheated, Static, $L_e = 136$ dB, (0,0) Mode.

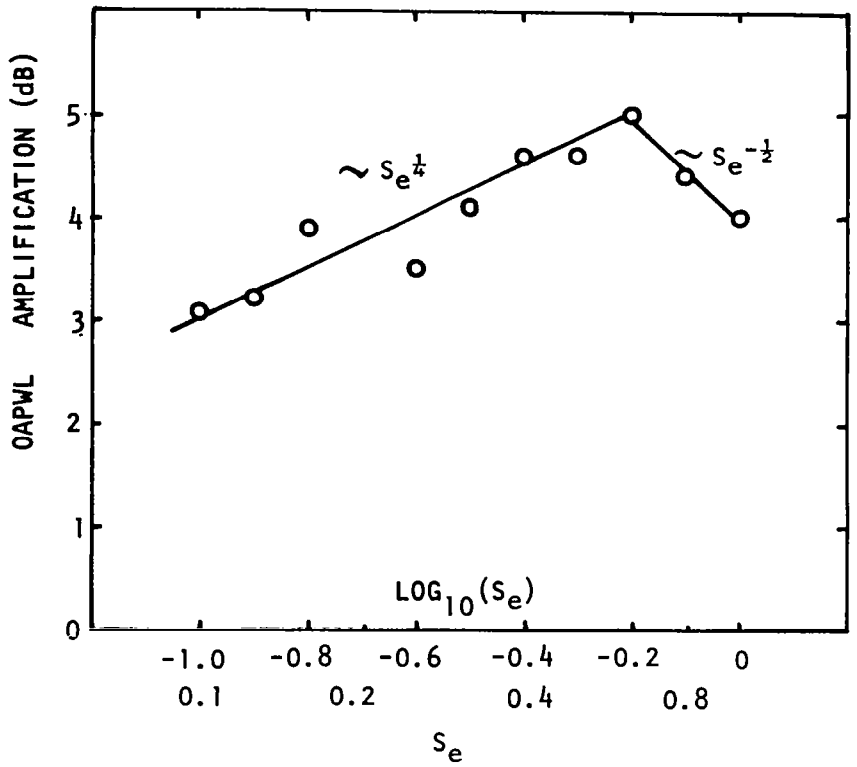

Figure 6.6 Variation of OAPWL amplification with excitation Strouhal number. M_j = 0.78, U_j = 251 m/s, Unheated, Static, L_e = 136 dB, (0,0) Mode.

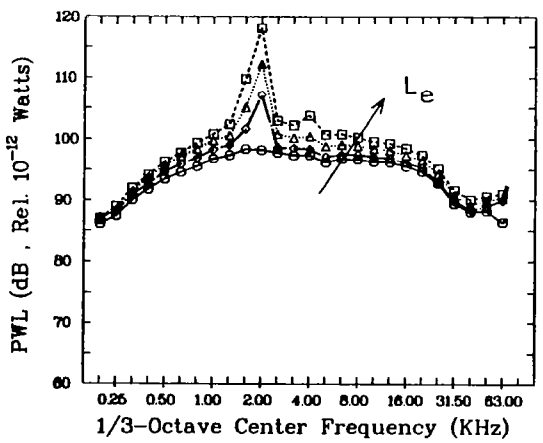

Figure 6.7 1/3-octave PWLs at various excitation levels:
○ , unexcited, ◇ , 130 dB, △ , 136 dB;
□ , 141 dB. M_j = 0.58, U_j = 190 m/s, Unheated, Static, S_e = 0.5, (0,0) mode.

Clearly, it is difficult to single out a value of excitation Strouhal number at which maximum amplification is obtained in 1/3-octave SPLs and PWLs, OASPLs and OAPWLs. However, based upon these measurements, and those of others (refs. 6,9), the general trend is that the maximum amplification takes place between $S_e = 0.4$ and 0.63. To assess the effects of other excitation parameters, it was decided, therefore, to consider $S_e = 0.5$ as a typical peak Strouhal number.

6.2 EXCITATION-LEVEL EFFECTS

The effects of increasing the magnitude of the upstream excitation tones on far-field acoustic power are shown in figure 6.7. Far-field acoustic-power spectra are compared for four different excitation levels: unexcited, 130 dB, 136 dB, and 141 dB. Clearly, as the excitation level is increased, further amplification is obtained at all frequencies. At $L_e = 141$ dB, an amplification of up to 5 dB in the radiated acoustic power is obtained. This amplification in PWL is a cumulative effect of amplification at all angles to the jet axis. The effect of increasing the excitation level is indeed found to increase the far-field broadband jet noise at all angles as shown in figure 6.8.

The data presented in figures 6.7 and 6.8 were for an excitation Strouhal number, $S_e = 0.5$ and jet Mach number, $M_j = 0.58$. Effect of increasing excitation levels were the same at $S_e = 0.63$ (see figure 6.9) and also at higher jet Mach number, $M_j = 0.78$ (see figure 6.10).

Instead of presenting a number of PWL spectra or SPL spectra at various angles for the test conditions studied, the excitation-level effects can be best summarized by presenting the tone-corrected amplifications in the OASPLs and OAPWLs as a function of the excitation levels. This is done in figure 6.11, where the tone-corrected OAPWLs and also the OASPLs at $\theta = 30°$ and 90° are presented for two jet Mach numbers: $M_j = 0.58$ and 0.78. Clearly, there appears to be a threshold below which there is no amplification, but above which the amplification increases linearly with excitation level.

The precise value of the threshold level can only be estimated from these plots within $\pm$ 1/2 dB of amplification. Based upon the measurements of Moore (ref. 6) and our own theoretical analysis given in section 7.0, the threshold level should be 0.08% of the dynamic head of the jet. Appropriate calculations indicate that the corresponding threshold level for the lower Mach number, $M_j = 0.58$, is 119 dB, and that for the higher Mach number, $M_j = 0.78$, is 124.5 dB. By allowing for the errors in amplifications of $\pm$ 1/2 dB, it is possible to arrive at these threshold levels for the present measurements also, thus confirming the validity of threshold level being about 0.08% of the jet dynamic head.

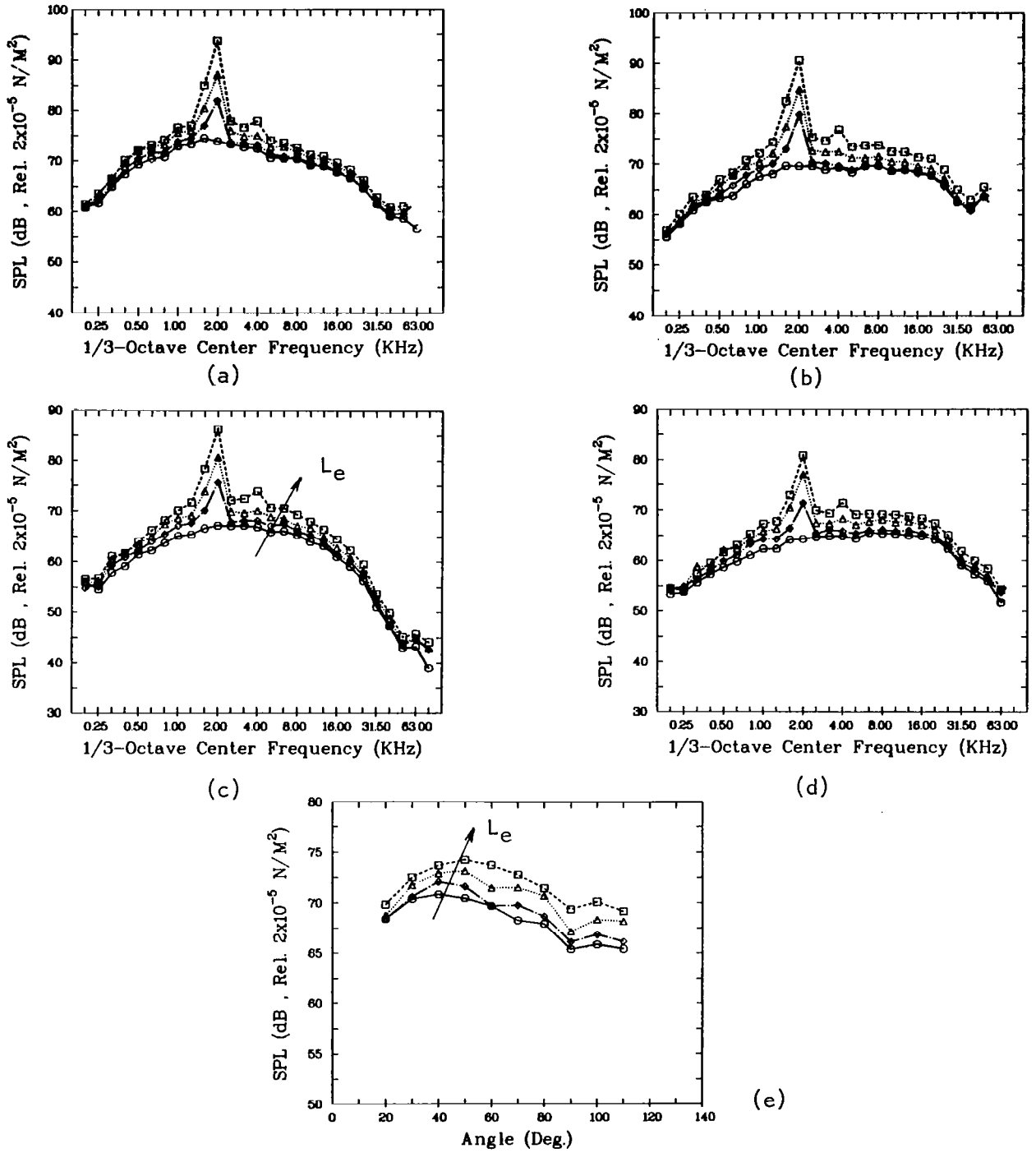

Figure 6.8 Variation of 1/3-octave SPLs with excitation levels, L_e at various emission angles, θ: (a) 30°, (b) 60°, (c) 90°, (d) 110°, and (e) a typical directivity of $f_j = 8$ kHz. L_e: ○ , Unexcited; ◇ , 130 dB, △ , 136 dB; □ , 141 dB. $M_j = 0.58$, $U_j = 190$ m/s, Unheated, Static, $S_e = 0.5$, (0,0) Mode.

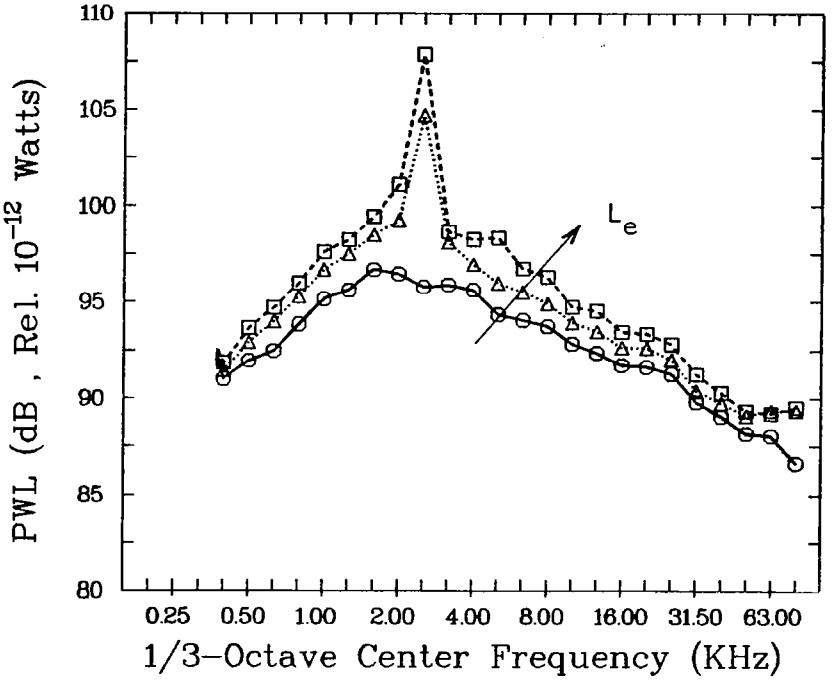

Figure 6.9 1/3-octave PWLs at various excitation levels:
○ , Unexcited; △ , 131 dB; □, 136 dB.
M_j = 0.58, U_j = 190 m/s, Unheated, Static, S_e = 0.63,
(0,0) Mode.

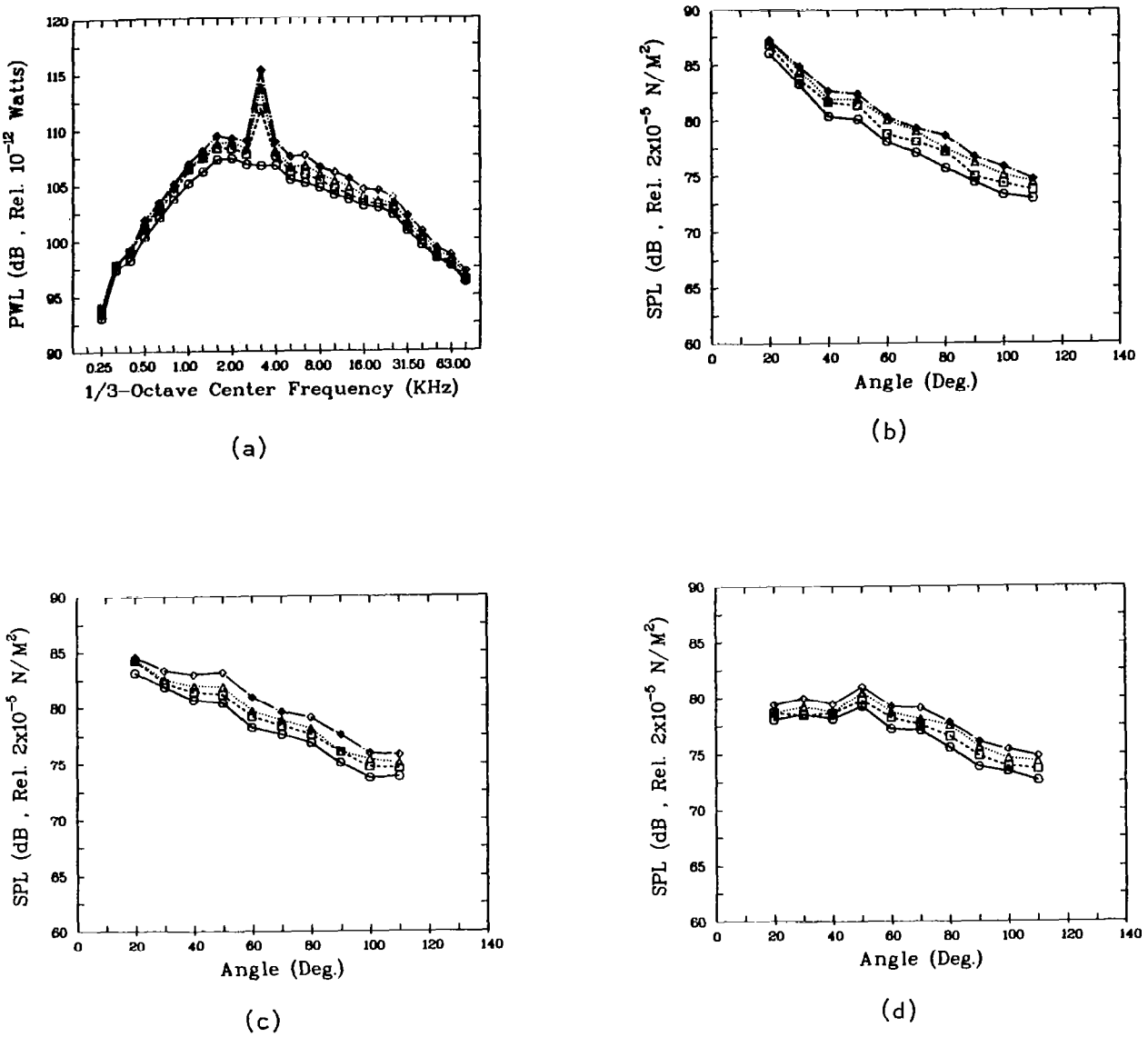

Figure 6.10 Effect of excitation levels on (a) 1/3-octave PWLs and directivities at different jet-noise frequencies, f_j (kHz): (b) 2.0, (c) 4.0, and (d) 8.0. L_e: ○ , Unexcited; △ , 132 dB; □ , 134 dB; ◇ 136 dB. M_j = 0.78, U_j = 252 m/s, Unheated, Static, S_e = 0.63, (0,0) Mode.

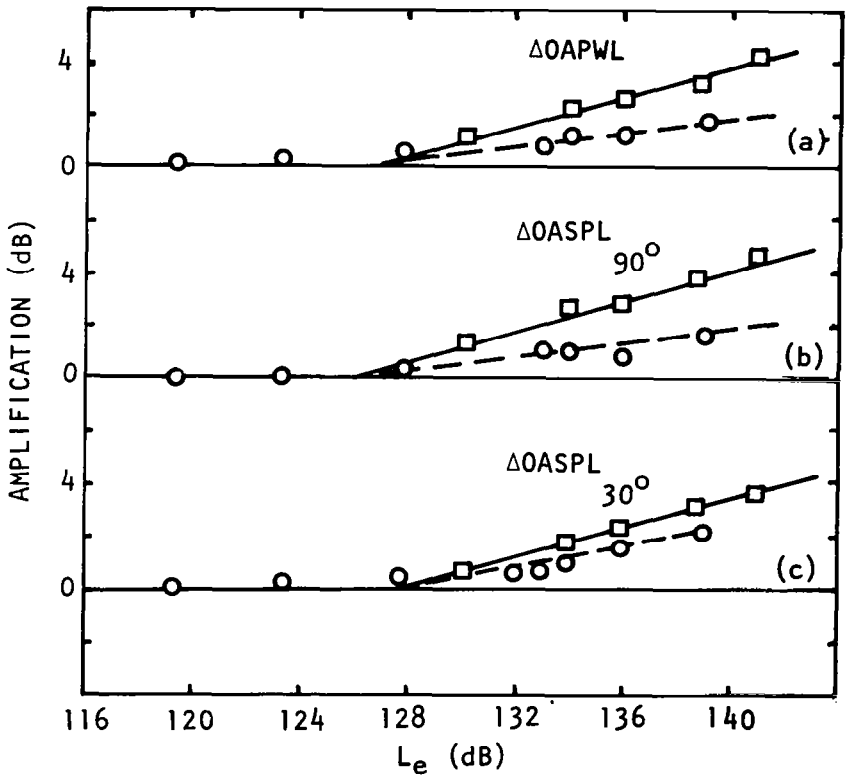

Figure 6.11 Variation of OAPWLs and OASPLs with excitation level and Mach number. M_j: □ , 0.58; ○ , M_j = 0.78, U_j = 190 m/s, Unheated, Static, S_e = 0.5, (0,0) Mode.

6.3 MACH-NUMBER EFFECTS

The results shown in figure 6.11 and discussed above, in relation to the excitation level effects, also allude to the Mach-number effects. These results clearly show that, for a given excitation level, the higher the jet Mach number, the lower the jet-noise amplification. This is consistent with the turbulence results of figures 5.21 thru 5.23, where it was shown that, as a result of a given upstream excitation, the turbulence intensities increased more for the lower Mach numbers.

On a spectral basis, the Mach number effects can best be seen by comparing the 1/3-octave PWL's for different Mach numbers, as shown in figures 6.12(a) thru 6.12(d) for M_j = 0.34, 0.58, 0.78, and 0.96, respectively. The excitation parameters are: L_e = 134 dB and S_e = 0.5. Comments made above appear to apply to the whole frequency range, and not just to the corrected overall levels. That this effect is applicable at all angles is shown in figure 6.12(e) where the directivities at a typical frequency in the spectra, in this case 4 KHz, are plotted for the same four Mach numbers at which the far-field noise spectra shown in figure 6.12(a) thru (d) were acquired. This data, shows clearly that, for fixed excitation parameters, the effect of increasing the jet Mach number is to reduce the magnitude of jet-noise amplification at all angles.

It is for these reasons that a systematic study for broadband amplification of supersonic jets could not be carried out, even though such a study was initially planned. To observe significant amplification in supersonic jet noise, it would have required excitation levels, L_e, in excess of 150 dB, which could not be generated with the source-section used in this study. Limited data for a convergent-divergent nozzle, operated at its design Mach number, M_j = 1.37, however, indicated that broadband jet noise amplification may be important for supersonic jets also. Typical results for this nozzle, operated at design Mach number, are shown as PWL-amplification spectra in figure 6.14 for L_e = 139 dB, and S_e = 0.25, 0.4, 0.45, 0.5,and 0.63. The amplification appears to be dominant only at limited frequency range between 1 KHz to 16 KHz, but more importantly, this is the region of the peak levels in the jet-noise spectra. It is conceivable that higher amplifications could have been obtained if the excitation levels were much higher.

Further work, with a more efficient upstream noise source, is needed to study the broadband jet-noise amplification phenomenon as applicable to supersonic jets.

6.4 MODE-ORDER EFFECTS

As mentioned in section 2.0, only two mode-orders were set up in these experiments: (0,0) plane-wave mode and the (1,0) helical mode. Before

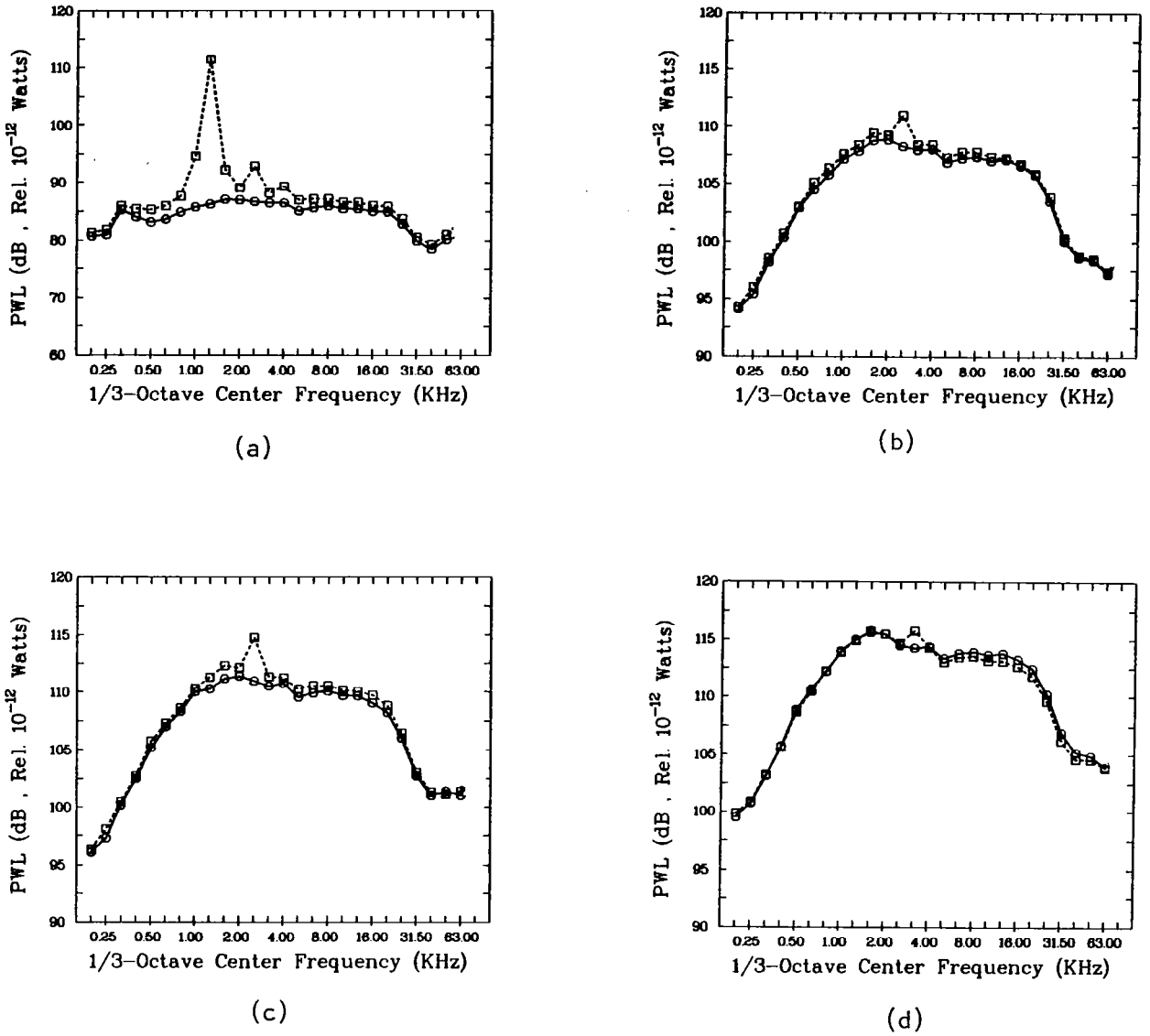

(e) See the next page.

Figure 6.12 Effect of jet Mach numbers on (a) thru (d) 1/3-octave PWLs and (e) far-field directivities at f_j = 4.0 KHz. Mj (U_j, m/s): (a) 0.34 (117), (b) 0.58 (251), (c) 0.79 (270), (d) 0.96 (300) Unheated, Static, S_e = 0.5, L_e = 134 dB, (0,0) Mode.

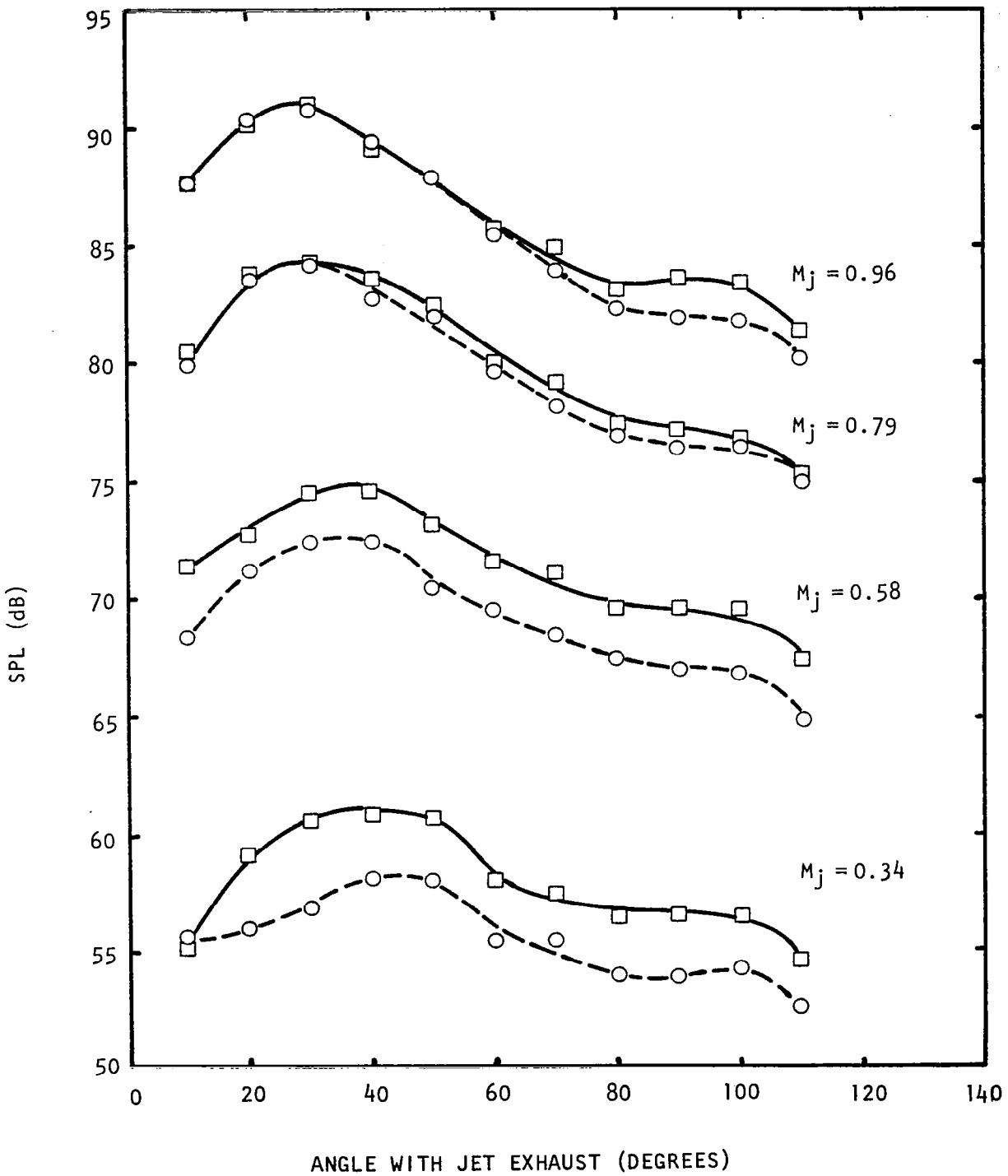
95
90
85
80
75
70
65
60
55
50
SPL (dB)
0
20
40
60
80
100
120
140
ANGLE WITH JET EXHAUST (DEGREES)
Mj = 0.96
Mj = 0.79
Mj = 0.58
Mj = 0.34

Figure 6.12(e)

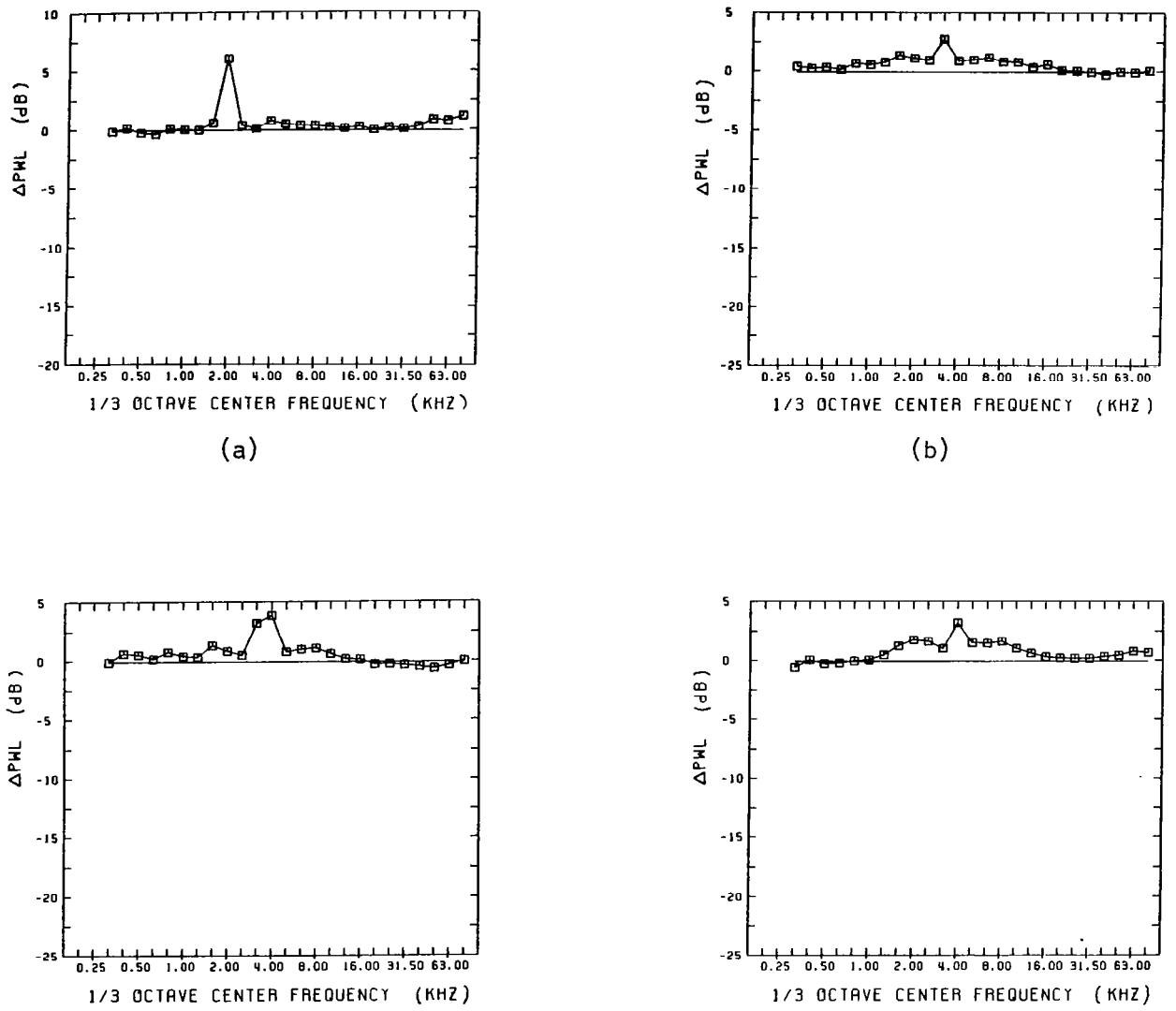

Figure 6.13 Broadband PWL-amplification spectra for M_j = 1.37 supersonic jet at various excitation Strouhal numbers, S_e: (a) 0.29, (b) 0.4, (c) 0.45, (d) 0.5. Unheated, Static, L_e = 139 dB, (0,0) Mode.

presenting a comparison of jet noise amplification for the two modes, a short discussion on the capability of a given duct system in sustaining the higher order modes is given below.

The wave number k, and thus the frequency above which the (1,0) helical mode is cut on in a duct, is given by

$$k = \frac{1.8413}{R_j} (1-M^2)^{\frac{1}{2}} \qquad (6\text{-}1)$$

where M is the Mach number in the duct. In the 10.16-cm diameter supply duct, therefore, the (1,0) mode can be cut on only above certain frequencies given by curve A in figure 6.14. However, since the diameter of the nozzle attached to the 10.16-cm duct is different (5.08 cm), and the Mach number at the exit is also different from that within the duct, the frequency requirement of the (1,0) mode to exist at the nozzle exit is different from that for the upstream duct section, and as shown in figure 6.14, the cut-on frequencies follow curve B. The combined effect of the supply duct and the nozzle system is, thus, to restrict the existence of the (1,0) mode only in the shaded region of this figure.

For the reasons given above, it was not possible to establish the effects of excitation Strouhal number on jet-noise amplification for the (1,0) mode. For Strouhal numbers lower than 0.63, the (1,0) mode could not be generated, and at higher Strouhal numbers the acoustic driver could not generate high enough sound levels. Majority of this subsection is, therefore, devoted to results for $S_e = 0.63$ and $M_j = 0.78$.

Typical 1/3-octave PWL spectra for the (1,0) mode excitation are shown in figure 6.15 for four excitation levels: L_e = unexcited, 135 dB, 138 dB and 139 dB. These spectra are very similar to those for the (0,0) mode, in that as excitation level increases so does the broadband amplification.

To see how the effects of (1,0) mode differ from the (0,0) mode of excitation, the PWL amplifications at two typical frequencies (f_j = 4 KHz and 8 KHz) in the jet noise spectra are plotted as a function of excitation level for $S_e = 0.63$, and compared with the corresponding data for the (0,0) mode in figure 6.16. These curves are very similar to those presented earlier in figure 6.11, and indicate that the jet noise amplification takes place after a threshold level is reached for the excitation amplitude, L_e. Beyond the threshold level, the amplifications increase monotonically with increasing excitation levels. There is a tendency for the (0,0) mode to produce up to 1.5 dB higher amplification than that produced by the (1,0) mode. This observation is consistent with the theoretical findings described in section 7.0 where it is shown that compared to (1,0) mode, (0,0) mode of excitation has more drastic effect on the flow structure that is responsible for jet noise production. The threshold level for both modes can be taken to lie anywhere between 120 dB and 129 dB. (As mentioned before in subsection 6.2, this threshold level should be 124.5 dB for it to be 0.08% of the dynamic head.)

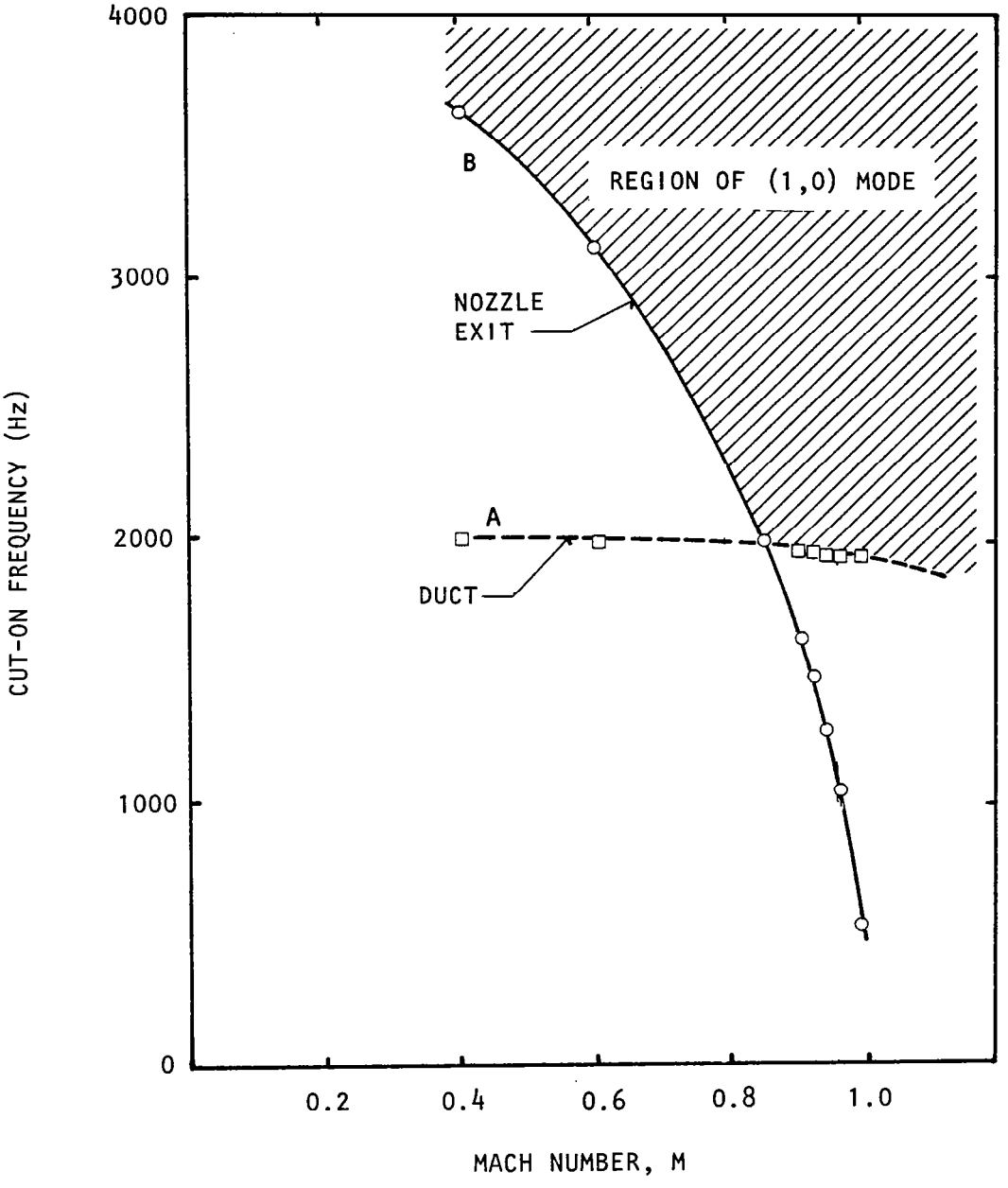

Figure 6.14 Variation of (1,0)-mode-cut-on frequency with Mach number within the 10.16 cm diameter duct (□) and at the 5.08 cm diameter nozzle exit.

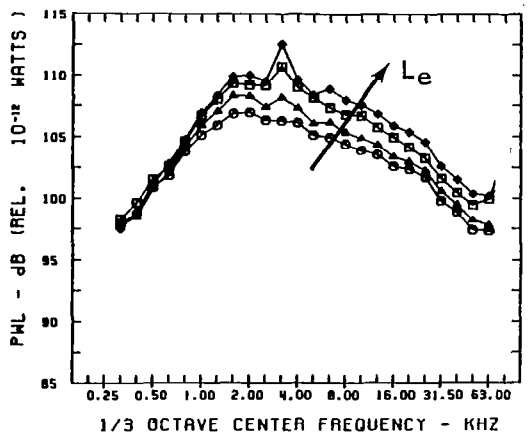

Figure 6.15 Variation of 1/3-octave PWL spectra with excitation level for the (1,0) mode. L_e: ○, Unexcited; △, 135 dB; □, 138 dB; ◇, 140 dB.
M_j = 0.78, U_j = 250 m/s, Unheated, Static, S_e = 0.63.

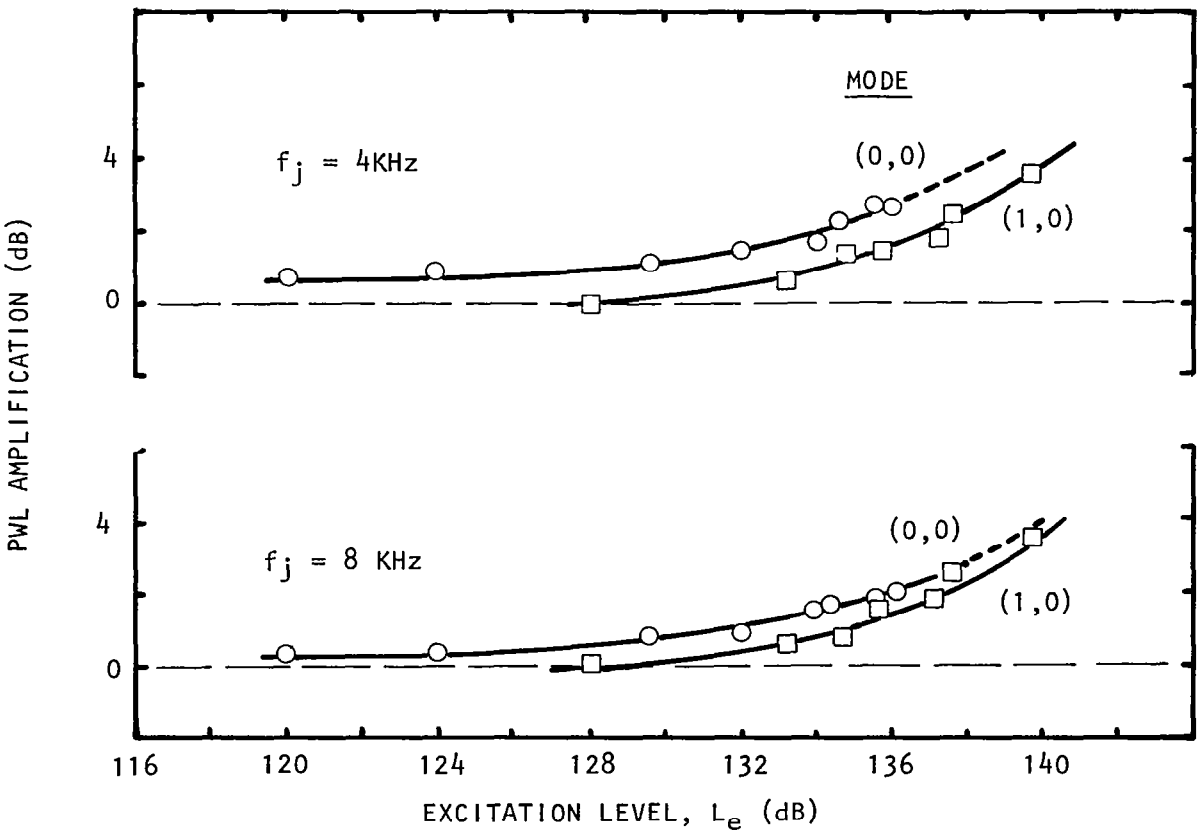

Figure 6.16 Variation in the PWL amplification with excitation level--(0,0) mode (○) versus (1,0) mode (□). M_j = 0.78, U_j = 250 m/s, Unheated, Static, S_e = 0.63.

The effect of the two modes of excitation on a spectral basis are further shown by comparing the 1/3-octave spectra of the PWLs in figure 6.17, and SPLs at θ = 30°, 60°, and 90° in figures 6.18(a) thru (c) respectively.

A very important observation to be made about the (1,0) mode spectra of figures 6.17 and 6.18 is that, unlike the (0,0) mode, the high-level discrete tone for the (1,0) mode generated at the exit is not discernible in the far-field, but yet an amplification in the broadband jet noise is observed. Another example of this behavior is shown in figure 6.19, where the data for S_e = 1.0 is presented. Here, in an attempt to set up a (1,0) mode, it was found, from the mode decomposition program, that a (2,0) mode was more dominant. At the jet exit, the (1,0) mode amplitude was only 118 dB as opposed to L_e = 128 dB for the (2,0) component. Thus, discrete tones at the higher-order modes also produce jet-noise amplification, even though their presence may not be felt directly in the far-field jet-noise spectra.

6.5 FLIGHT EFFECTS

Before describing the effects of flight on the noise generated by tone-excited jets, it is instructive to present some results on the effects of flight on the unexcited jets. Typical results of forward velocity on an unheated jet are shown in figure 6.20. Clearly, as the forward velocity is increased, the jet-noise levels are reduced at all frequencies. This is a direct result of a reduction in the shear-velocity which correspondingly reduces the turbulence intensities in the jet, as already discussed in section 5.0. Unless the noise levels generated by the flight simulator free-jet are high, reduced jet-noise levels are always obtained. This effect is found to hold for both the unheated and also the heated jets as shown in figure 6.21 for a t_r = 800k jet.

Turning now to the tone-excited jets under flight simulation, figures 6.22(a) thru (d) show a comparison between the unexcited and the excited jet-noise spectra for flight velocity V_t = 45 m/sec at three emission angles: θ = 30°, 60°, and 90°, respectively. Corresponding 1/3-octave PWL spectra, encompassing integrated effect of all the angles, are shown in figure 6.22(d). These figures show that an amplification in broadband jet noise is obtained even under the flight condition

To quantify the jet-noise amplifications under flight and compare them with those under static conditions, typical amplifications under both conditions are shown in figure 6.23. In this figure, the region with vertical lines indicates the amplification for the static case, and the dotted region indicates the amplification for the flight case. Clearly, even though the unexcited jet noise has decreased at all frequencies as a result of the forward velocity, the result of excitation is to provide approximately the same amount of amplification as obtained for the static case. Actually there is a tendency for the flight-case amplifications to be somewhat lower than those for the static case. This statement is further confirmed when

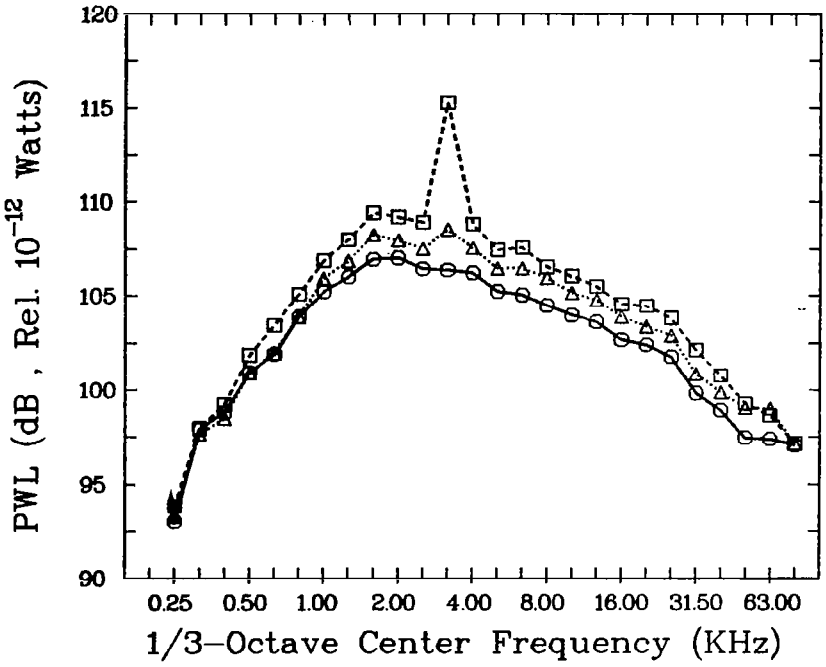

Figure 6.17 (0,0) mode (□) Versus (1,0) mode (△), and the unexcited jet (○).
M_j = 0.78, U_j = 250 m/s, Unheated, Static, S_e = 0.63, L_e = 136 dB.

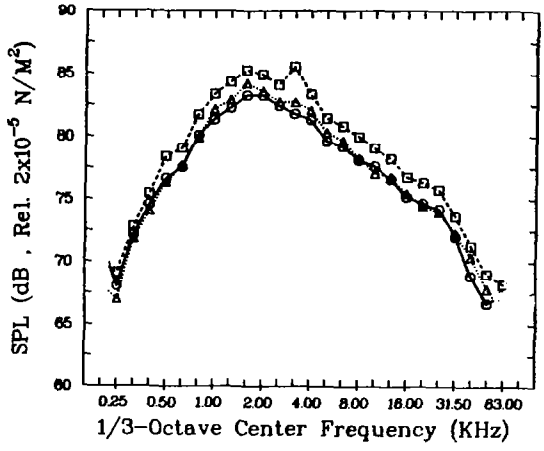

(a)

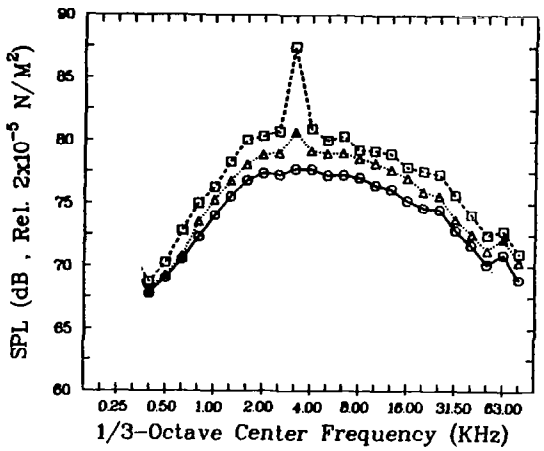

(b)

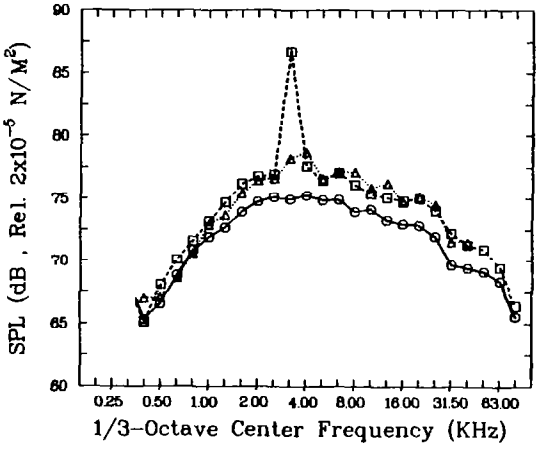

(c)

Figure 6.18 Data of figure 6.17 at various emission angles, θ: (a) 30°, (b) 60°, (c) 90°.

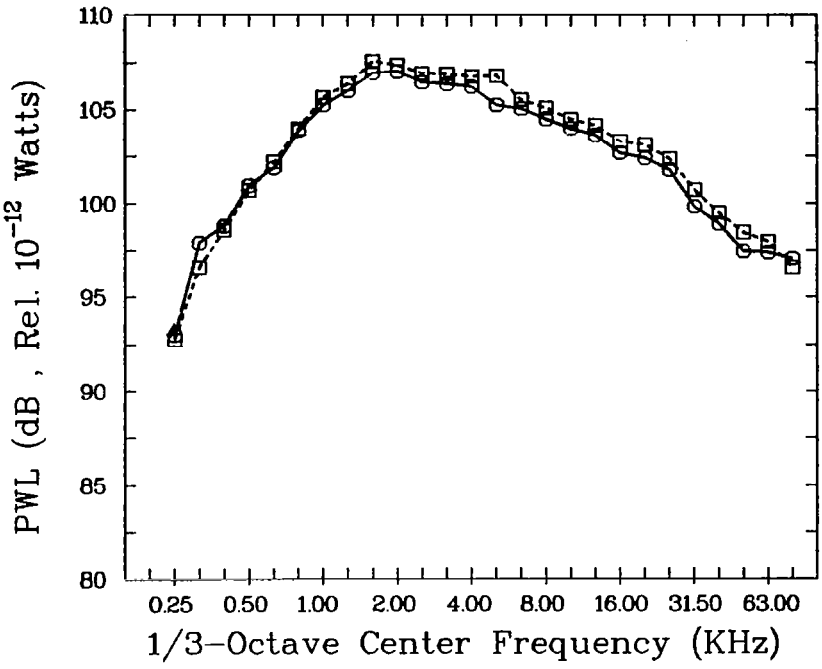

Figure 6.19 Effect of excitation with (2,0) mode.
M_j = 0.78, U_j = 251 m/s, Unheated, Static,
S_e = 1.0,

L_e: O , Unexcited; □ , Excited

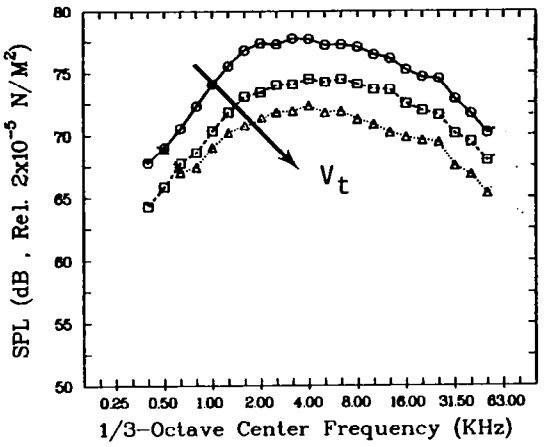

Figure 6.20 Effect of forward velocity on the 1/3-octave SPLs of an unexcited jet. M_j = 0.78, U_j = 251 m/s, Unheated. V_t: ○ , static;□ , 45 m/s; △, 90 m/s.

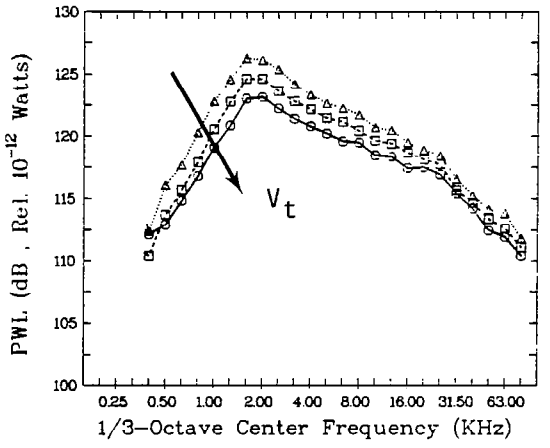

Figure 6.21 Effect of forward velocity on the 1/3-octave PWLs of an unexcited jet. M_j = 0.78, U_j = 445 m/s, Heated (t_r = 800 K). V_t: ○ , static; □, 45 m/s; △, 90 m/s.

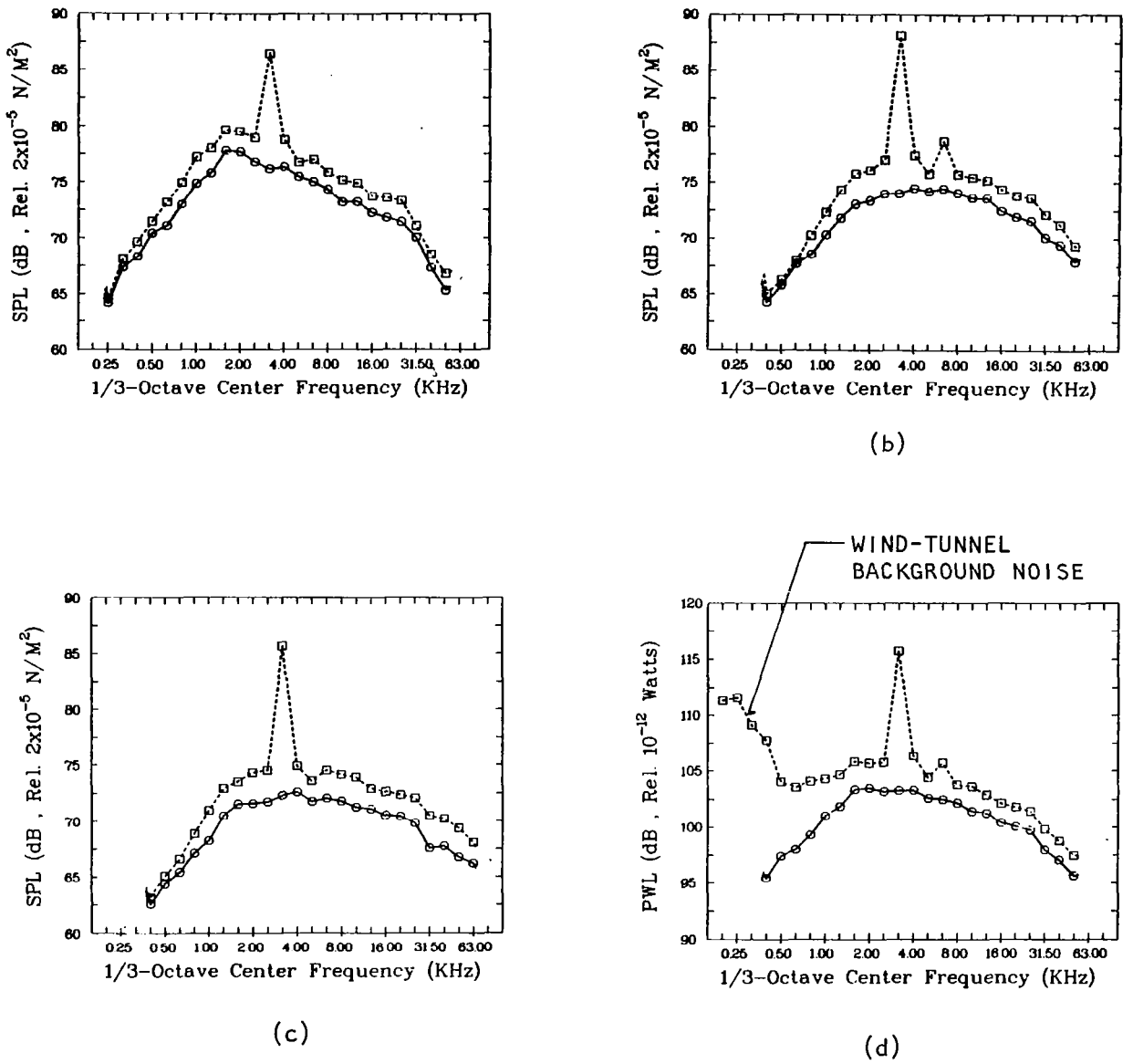

Figure 6.22 Broadband amplification of SPLs at θ: (a) 30°, (b) 60°, and (c) 90°; and of (d) PWLs under flight simulation, V_t = 45 m/s. M_j = 0.78, U_j = 251 m/s, Unheated, S_e = 0.63, (0,0) mode.
L_e: ○, Unexcited; □, 136 dB.

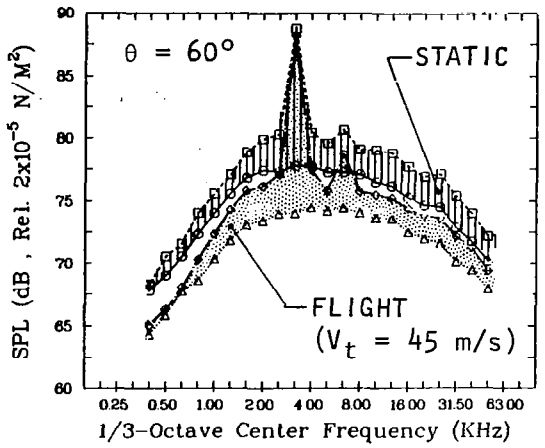

Figure 6.23 Comparison of broadband jet-noise amplification for the static ( ) and the flight-simulation ( ) case of $V_t = 45$ m/s. $M_j = 0.78$, $U_j = 251$ m/s, Unheated, $S_e = 0.63$, (0,0) mode.
L_e: ○,△, Unexcited; □,◇, 136 dB.

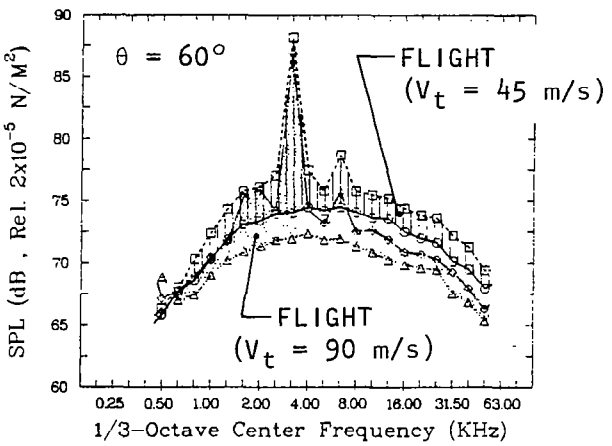

Figure 6.24 Comparison of broadband jet-noise amplification for two flight cases: $V_t = 45$ m/s ( ) and $V_t = 90$ m/s ( ). $M_j = 0.78$, $U_j = 251$ m/s, Unheated, $S_e = 0.63$, (0,0) mode.
L_e: ○ ,△, Unexcited; □ ,◇, 136 dB.

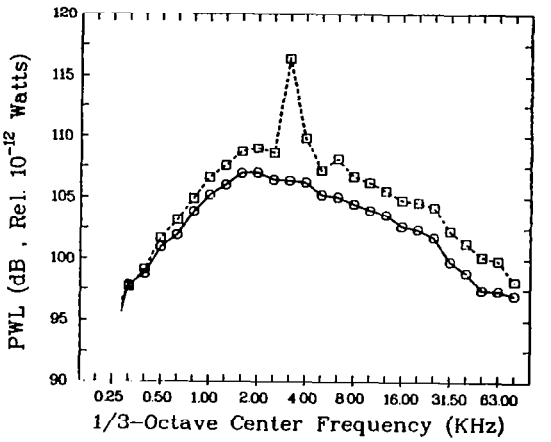

(a)

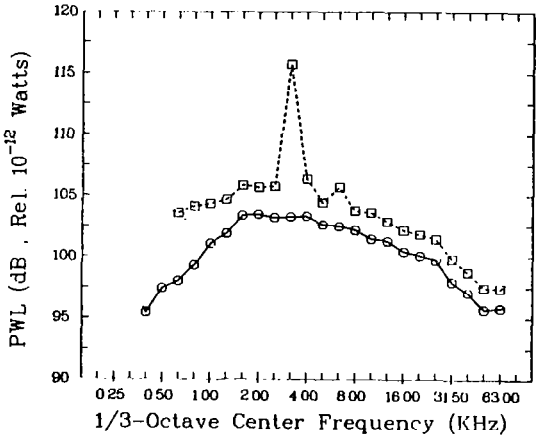

(b)

Figure 6.25 Effect of upstream excitation on 1/3-octave PWLs for the (a) static case and (b) flight-simulation case, V_t = 45 m/s. M_j = 0.78, U_j = 251 m/s, S_e = 0.63, (0,0) mode. L_e: O , Unexcited; □, 136 dB.

one compares the spectra for the flight velocity, V_t = 45 m/sec with those for the higher flight velocity V_t = 90 m/sec as shown in figure 6.24. Based upon the results of figures 6.22 thru 6.24 and others inspected but not presented here, it appears that, for all intents and purposes, the amplification for a jet operated at various flight velocities is the same -- remembering that in each flight case the reference jet noise is lower than the noise from the static jet.

The above arguments apply not only to the SPLs at a given angle, but also to the PWLs as seen by comparing the PWL spectra in figure 6.25 for the static case with those for the flight case (V_t = 45 m/s). It is seen that approximately equal amount of amplification is obtained at all frequencies for both cases, except at low frequencies for the excited data of flight simulation case. Here, an increased low frequency noise is obtained which can be attributed to the increased background noise (of the free jet) as sensed by the microphones close to the nozzle exit. It is conceivable that the widening of the primary jet by upstream excitation has also widened the free-jet, and the microphones close to the jet axis are now being affected by the increased low frequency hydrodynamic noise. Precise reason for this behavior is, however, not quite clear.

The jet-noise amplification under flight simulation was obtained for both the (0,0) mode and the (1,0) mode. A typical comparison between flight spectra, with and without upstream excitation, for the (1,0) mode is presented in figure 6.26. Similar to the (0,0) mode, broadband jet-noise amplification is obtained for the (1,0) mode at all frequencies. To compare the behavior of the (1,0) mode excitation under flight simulation with that of the (0,0) mode, typical results are shown in the form of relative amplification versus excitation level for both (0,0) mode and (1,0) mode, in figure 6.27. By 'relative amplification' is meant the difference between the flight amplification and the static amplification. Thus a zero value of relative amplification means identical amplification, and a positive value implies a higher amplification for the flight case. Data in figure 6.27 are at a typical frequency in the noise spectrum, in this case 5 KHz. Within a decibel, the (0,0) mode and the (1,0) mode provide the same amplification, both statically and under flight simulation, at all excitation levels studied.

Finally, for the flight simulation case, the effects of excitation levels at all frequencies in the jet-noise spectra were similar to those obtained for the static jets. With increasing excitation levels, the jet-noise amplifications increased. Typical results showing this effect are presented in figure 6.28. These results should be compared for their remarkable similarity with those for the static case presented earlier in figure 6.15. As regards the effects of excitation Strouhal numbers there was a tendency for the peak Strouhal number in the flight case to lie between 0.63 and 0.8.

Most of the experimental results discussed above are consistent with the changes observed in the flow behavior of excited jets under the influence of flight (as discussed in section 5.0). They are also consistent with the theoretical trends predicted in the next section, where it is pointed out that the large-scale instability waves grow to about the same

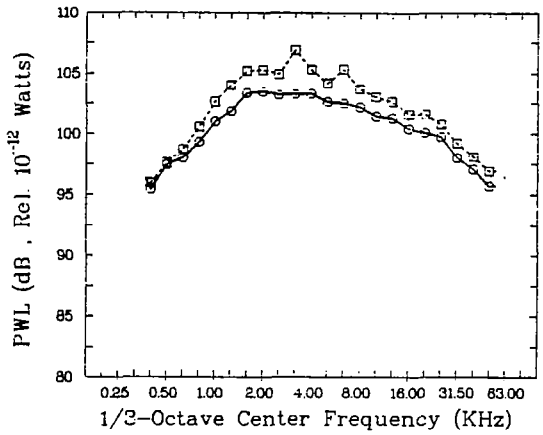

Figure 6.26 Broadband jet-noise amplification for (1,0) mode excitation under flight simulation (V_t = 45 m/s). M_j = 0.78, U_j = 251 m/s, Unheated.
L_e: ○ , Unexcited; □ , 132 dB.

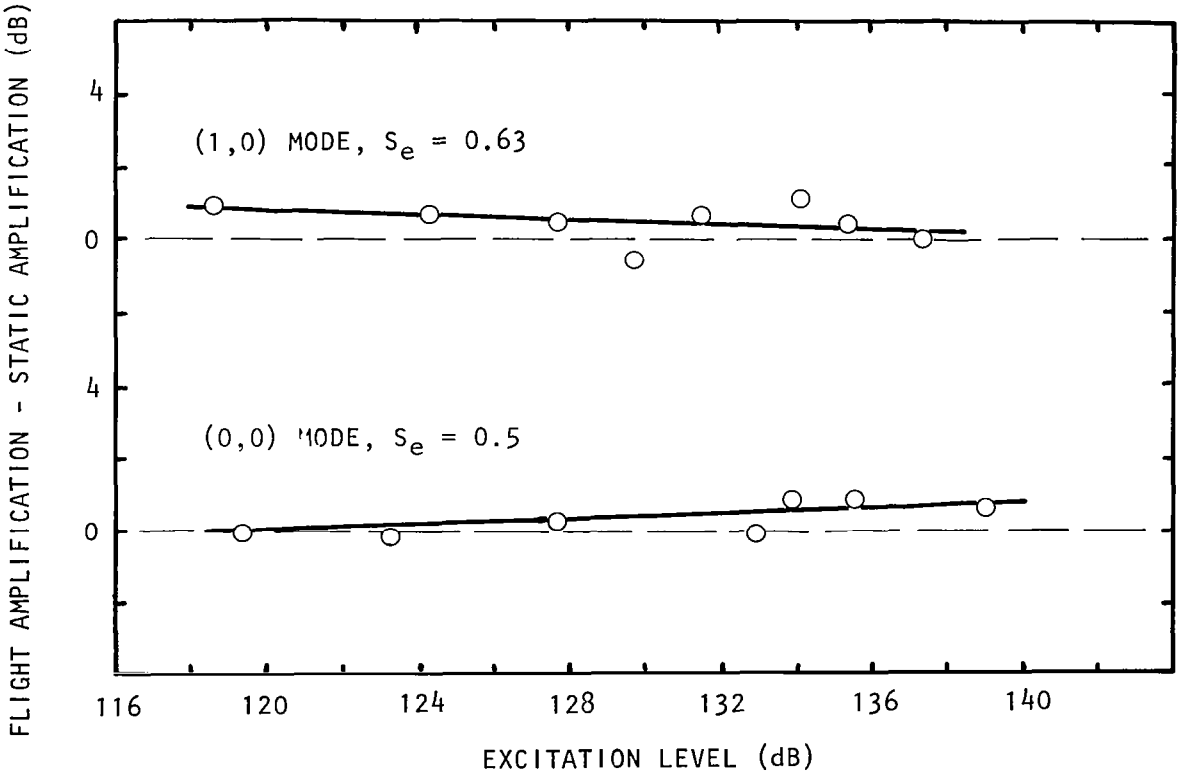

Figure 6.27 Relative jet-noise amplification under flight simulation at f_j = 5KHz and θ = 90°. M_j = 0.78, Unheated, V_t = 45 m/s.

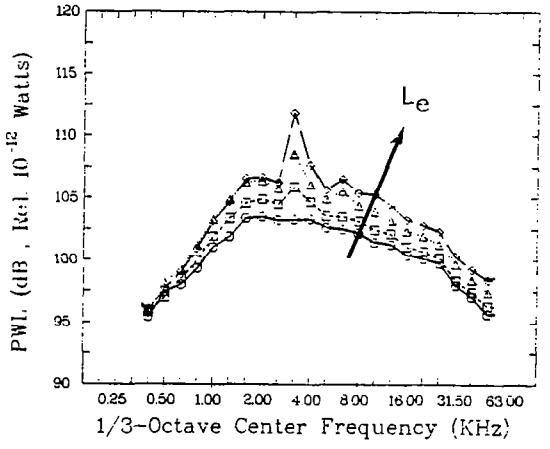

Figure 6.28 Effect of excitation level on broadband jet-noise amplification under flight simulation (V_t = 45 m/s) and (1,0) mode excitation. M_j = 0.78, U_j = 251 m/s, Unheated.
L_e: ○, Unexcited; □, 135 dB; △, 138 dB; ◇, 140 dB.

amplitude in both the flight and the static case. Because of this, it is expected that the increase in fine-scale turbulence would also most likely be about the same in both cases. By implication, therefore, the total increase of broadband jet noise due to upstream-tone excitation is nearly independent of flight velocity.

6.6 TEMPERATURE EFFECTS

The jet-noise amplifications for majority of the heated-jet test conditions, studied here, were found to be insignificant. Typical results for a jet-reservoir temperature of 800K and jet Mach number of 0.58 are shown in figure 6.29. The far-field acoustic-power spectrum for the unexcited jet is compared with that for the jet excited at $S_e = 0.5$, $L_e = 142$ dB, and at (0,0) mode. Similar results were obtained at other Strouhal numbers, for example, see figure 6.30 for $S_e = 0.63$. Flight simulation data also displayed less than one decibel of amplification; for example see the PWL-spectra comparison for $M_j = 0.58$ in figures 6.31 and 6.32, with the jet excited at $S_e = 0.5$ and 0.63, respectively. Similar results were obtained for the higher jet Mach number, $M_j = 0.78$ (see figure 6.33). These comments apply not only to the PWL spectra as presented here but also to the SPL spectra, at various angles, which were analysed and plotted, but are not presented here, since they look very much like the PWL spectra.

These results for the heated jets are in contradiction with the acoustic results presented by Jubelin (ref. 9). They also appear to disagree with the theoretical predictions given in section 7.0. But yet, and most importantly, the acoustic data presented here and the turbulence data for the heated jets presented in section 5.0, appear to be quite consistent for both the static as well as the flight case. This is so, in spite of the fact that the acoustic and the turbulence data were acquired in two completely different facilities. It should be recalled that the effect of upstream excitation on the heated jets was to reduce the turbulence and extend the potential core-- an effect opposite of that observed for the unheated jets. Some of the acoustic results actually showed a tendency for the jet noise to reduce at certain frequencies, although only by marginal amount (e.g., see figures 6.31 and 6.33).

The study for the heated jets here was actually not as exhaustive as it was for the unheated jets. Due to the limited range of flow and excitation conditions for the heated jets in the present study, therefore, it is dangerous to draw firm conclusions about jet noise amplification for the heated jets. Further study with a range of reservoir temperatures, jet Mach numbers, excitation Strouhal numbers, excitation levels and mode orders is, therefore, warranted.

This concludes the presentation of all experimental results. A theory to predict the effects of upstream excitation on jet flows, and thus on the far-field jet noise is developed in the next section. Where possible, comparison between theory and measurements is also made.

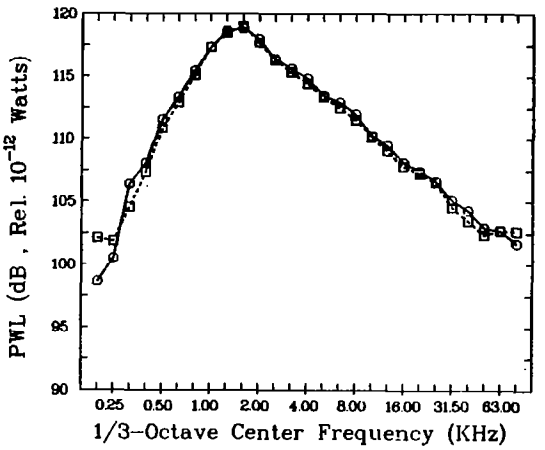

Figure 6.29 Effect of upstream excitation on a heated jet. M_j = 0.58, U_j = 321 m/s, t_r = 800 K, Static, S_e = 0.5, (0.0) mode. L_e: ○ , Unexcited; □, 142 dB.

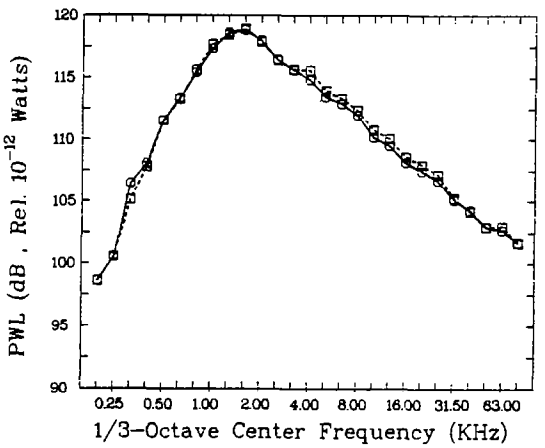

Figure 6.30 Effect of upstream excitation on a heated jet. M_j = 0.58, U_j = 321 m/s, t_r = 800 K, Static, S_e = 0.63, (0,0) mode. L_e: ○ , Unexcited; □, 138 dB.

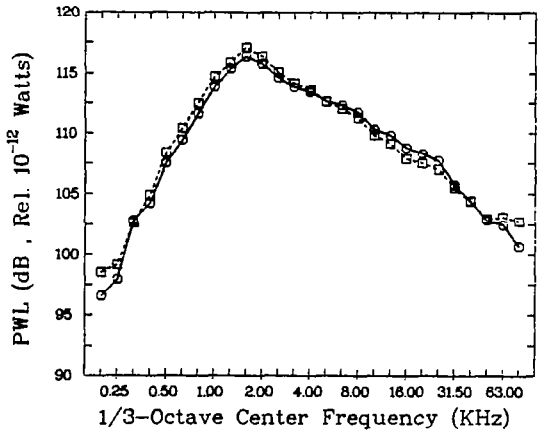

Figure 6.31 Effect of upstream excitation on a heated jet under flight simulation (V_t = 45 m/s). M_j = 0.58, U_j = 321 m/s, t_r = 800 K, S_e = 0.5, (0,0) mode.
L_e: ○ , Unexcited; □, 142 dB.

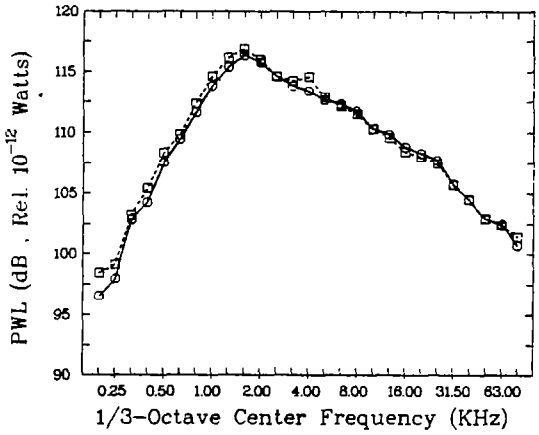

Figure 6.32 Effect of upstream excitation on a heated jet under flight simulation (V_t = 45 m/s). M_j = 0.58, U_j = 321 m/s, t_r = 800 K, S_e = 0.63, (0,0) mode.
L_e: ○ , Unexcited; □, 138 dB.

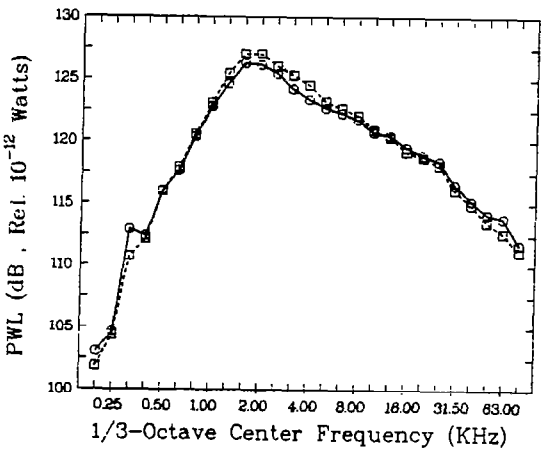

Figure 6.33 Effect of upstream excitation on a heated jet. M_j = 0.78, U_j = 428 m/s, t_r = 800 K, S_e = 0.5, (0,0) mode.
L_e: ○, Unexcited; □, 141 dB.

7.0 THEORY AND COMPARISON WITH EXPERIMENTS

The physical processes that lead to broadband-noise amplification by upstream tones are believed to consist of three essential parts. The first link of the complete chain of events involved is the excitation of the large-scale turbulence structures by the pressure and velocity fluctuations associated with the excitation-sound tones. These large-scale turbulence structures are basically the intrinsic instability waves of the jet flow. To avoid confusion, it is appropriate to state at this time that throughout the remaining part of this report the terms 'instability waves' and 'large-scale turbulence structures' will be used interchangeably to refer to the same physical entities. The process of acoustic excitation, which is often referred to as the receptivity problem, takes place as the sound waves emerging from the nozzle exit traverse the shear layer of the jet. It is well known that jet flows are inherently unstable in the initial mixing region. The instability waves or the large-scale turbulence structures, once excited, will, therefore, grow rapidly as they propagate downstream. The interaction of the instability waves or the large-scale turbulence structures, and the mean flow of the jet together with the enhancement of fine-scale turbulence forms the second link of the overall process. Within the Strouhal number range of 0.1 to 1.0, for which the jet is most sensitive to excitation, the growth and decay of the instability wave would usually be completed within one to one-and-a-half jet-core length. However, because of the effect of mean-flow convection, the enhancement of fine-scale turbulence, extends well beyond this axial distance downstream. In a subsonic jet, broadband noise is generated by fine-scale turbulence. The enhancement of fine-scale turbulence as a result of the interaction of the mean flow and the excited large-scale instability waves or turbulence structures, therefore, immediately leads to broadband-noise amplification. This noise radiation process is the third link of the physical phenomenon under consideration.

The primary objective of the present theoretical effort is to develop a mathematical model of these processes. Since turbulence and noise generation are complicated problems on their own, it is beyond the scope of this work to provide a detailed modeling of their characteristics. Instead, only the salient and necessary dynamical properties of turbulence in an excited jet flow will be incorporated in the model. Of the three parts involved in the broadband noise-amplification processes, the first two are intimately related to each other. The third part deals with the noise radiation by the fine-scale turbulence.

It is well established that in a turbulent jet the back reaction of the radiated sound on the flow and turbulence of the jet is negligibly small. Thus the noise problem may be considered independently after the flow and turbulence problems are solved. This strategy will be followed in this section.

Although the process of excitation of the large-scale instability waves of a jet by upstream tones takes place over an extended axial length of the jet mixing layer, it is most effective in the region immediately downstream of the nozzle exit. There are two basic reasons for this. Firstly, in this region the mixing layer is thin. As a result, the spatial growth rates of the instability waves are the largest there. Once a wave is excited, it can, therefore, quickly grow to an appreciable amplitude. Secondly, as the upstream sound wave emerges from the confines of the nozzle, its intensity decreases rapidly in the axial direction because of lateral spreading. Thus the pressure and velocity oscillations, necessary to excite the jet, are strongest and most effective near the trailing edge of the nozzle. In this work, the theory of Tam (refs. 16, 33 and 18) will be followed in formulating the receptivity of large-scale jet-instability waves to upstream tone excitation. A locally-parallel flow model will be used to determine the local coupling coefficients between the upstream sound waves and excited instability waves. The gradual change of these coefficients and the instability wave characteristics in the flow direction, which is an extremely important aspect of the physical phenomenon, is then accounted for by allowing the wave-amplitude equation to have variable coefficients.

In a jet, the growth rates of instability waves are rather large. Thus the excited wave usually acquires an amplitude large enough to affect the mean flow and fine-scale turbulence intensity. The interaction of these three types of fluid motion is definitely nonlinear, and must be modeled accordingly. However, the nonlinear self-interaction of the excited large-scale instability wave is believed to be of minor importance. This contention is supported by the success of a similar quasi-linear model of the large-scale turbulent structures in a two-dimensional mixing layer developed by Tam and Chen (ref. 34). Recently the same model has been applied by Plaschko (ref. 35) to the study of large turbulence structures of a jet with equal success.

In subsection 7.1, a quasi-linear model will be developed for a jet under acoustic forcing. The predicted results of this model are then compared with measurements in section 7.2. The effect of forward flight on the phenomenon of broadband noise amplification by upstream tones will be examined theoretically in section 7.3. Time constraints on the present project has not allowed the development of a comprehensive mathematical model on flight effects similar to that for the static case. However, the changes brought about by the presence of the external flow on the mean-velocity profile of the jet, the spatial-growth rate of the excited instability waves and the receptivity of these waves to upstream tone excitation is analyzed separately. The combined effects of all these changes are discussed.

7.1 A QUASI-LINEAR THEORY

As mentioned above, attempts will not be made to give a detailed modeling of the flow and turbulence. Instead, the three different kinds of fluid motion, namely, the mean flow, the coherent large turbulent motion, and the fine-scale turbulence in an excited jet will be characterized by a few averaged variables. That this approach is feasible and meaningful,hinges on the existence of "disparate time scales" between the large turbulence structures and the fine-scale turbulence of the flow. In the problem under consideration, the time scale for the fine-scale turbulence to adjust itself to some sort of dynamical equilibrium state is very short. Thus, within the pertinent time scale of the large turbulence structures, the fine-scale turbulence can be regarded as responding to any large-scale changes with some average characteristics. Within this same framework of reasoning, the fine-scale turbulence would also be able to smooth out the mean flow so that it would attain a dynamical equilibrium profile. If indeed this is approximately true, then it follows that the turbulence-intensity distribution as well as the mean-flow velocity profile of the jet would probably have nearly the same shape with or without acoustic forcing.

In an unexcited jet it is well known that the mean-velocity profile can be well approximated by a Gaussian function. Specifically the axial velocity in the core part of the jet can be approximated by

$$\frac{u}{u_j} = \begin{cases} 1 & r \le h \\ \exp\left[-\ell n(2)\left(\frac{r-h}{b}\right)^2\right] & r \ge h \end{cases} \qquad (7\text{-}1)$$

(see fig. 7.1) where u_j is the jet-exit velocity, h is the radius of the jet core, and (b + h) is the radius of the half-velocity point of the jet. In equation (7-1), the velocity profile is characterized by two parameters, namely, h and b. To test the "disparate time scales" hypothesis, equation (7-1) has been used to fit the mean-velocity profiles of an excited jet by choosing h and b appropriately. Figure 7.2 shows the measured mean-velocity profiles of an $M_j = 0.58$ unheated jet, excited by mode (0,0) sound at Strouhal number $S_e = 0.5$ and excitation level $L_e = 141$ dB at three axial locations. The fitted Gaussian velocity profiles are also shown. As is readily seen, the Gaussian profiles do approximate the measured data reasonably well. With this justification, it will be assumed that the mean-velocity profile of equation (7-1) is also applicable to jets excited by upstream tones.

To characterize the distribution of fine-scale turbulence intensity in the jet flow, the recent work of Lau (ref. 36) has been found to be most useful. Lau measured and analyzed the intensity of the axial-velocity fluctuations of unexcited jets over an extended range of jet operating conditions. By correlating a large set of data, he demonstrated that the root-mean-square axial turbulence velocity had a radial distribution which could be satisfactorily represented by the function

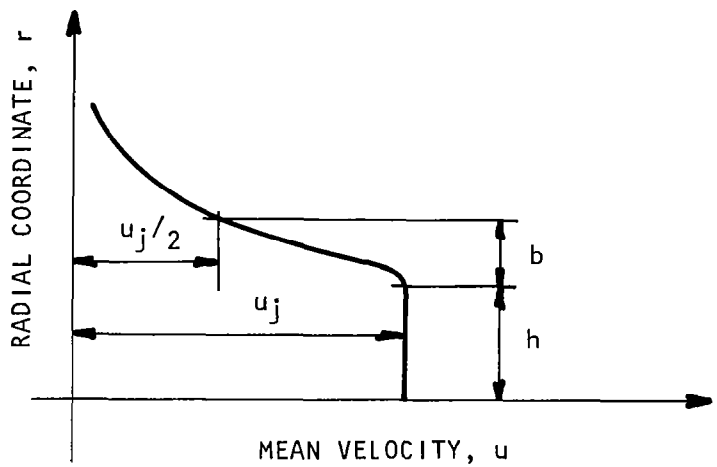

Figure 7.1 Mean-velocity profile in the core region of a round jet.

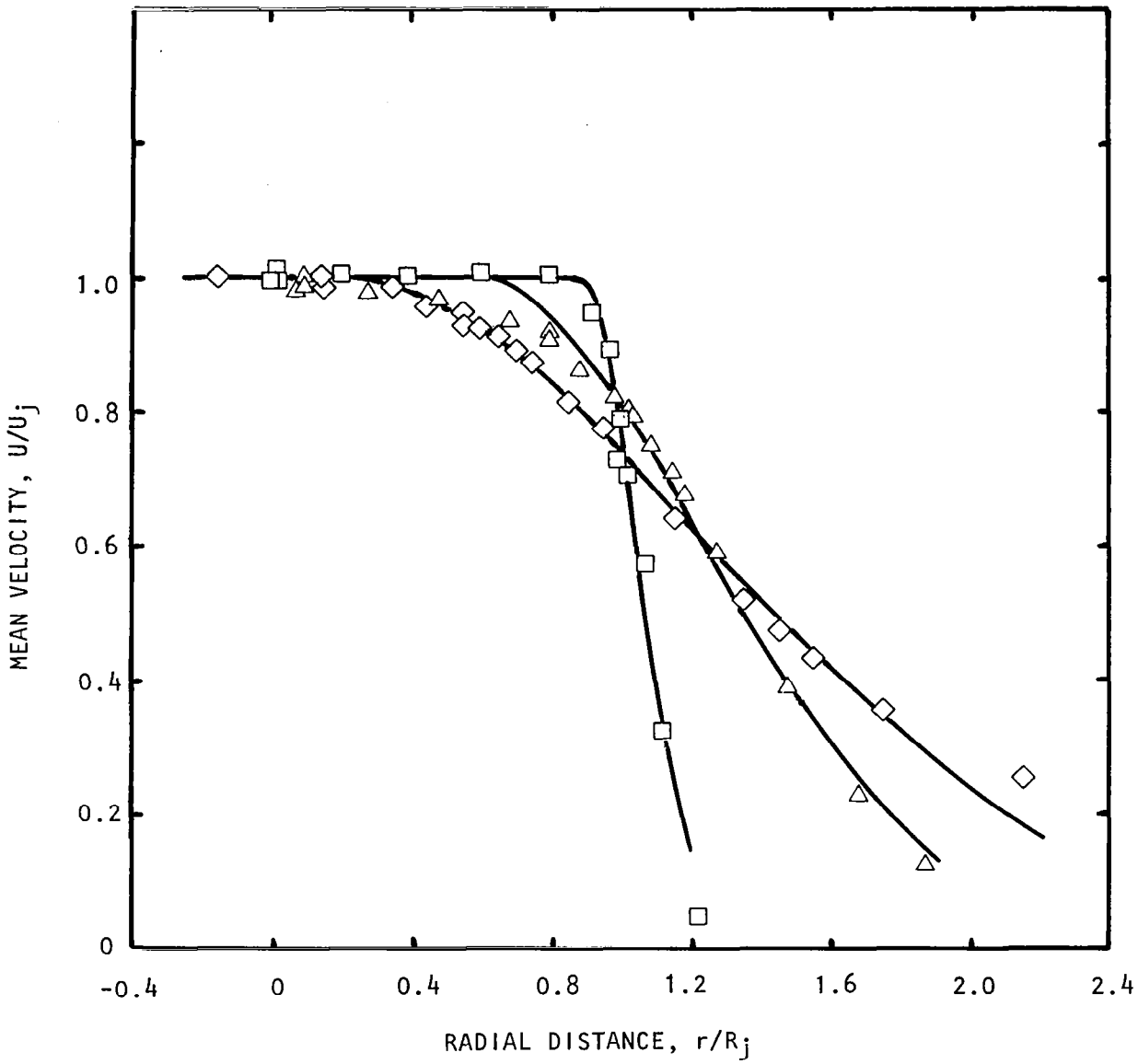

Figure 7.2 Comparison of mean-velocity profile of excited jet and Gaussian profile.
M_j = 0.575, S_e = 0.5, L_e = 141 dB, t_r/t_o = 1.0 .
———— , fitted Gaussian profile;
Measured data: □ , x/D_j = 1.0; △ , x/D_j = 3.0;
◇ , x/D_j = 5.0.

$$\frac{u'}{u_r'} = \exp\ [-0.56\ (\sigma_n^*)^2] \qquad (7\text{-}2)$$

where $\sigma_n^* = 1.2658\ (r-r_{0.5})/b$; $r_{0.5}$ being the radius at which the mean axial velocity is $0.5\ u_j$, and u_r' is the peak axial turbulence intensity. If the fine-scale turbulence is locally isotropic then the turbulent kinetic energy $q = \frac{1}{2}(u'^2 + v'^2 + w'^2)$ would have a radial distribution equal to the square of the right hand side of equation (7-2). By means of equation (7-1), the turbulent kinetic energy distribution may, therefore, be approximated by

$$\frac{q}{\bar{q}} = \exp\ [-1.7945\ (\frac{r-h-b}{b})^2] \qquad (7\text{-}3)$$

in the core region of the jet, where $\bar{q}(x)$ is the peak turbulent kinetic energy at the particular cross section of the jet. By the "disparate fine scales" hypothesis, equation (7-3) will be assumed to be applicable to acoustically excited jets as well. At present, it is not possible to test the validity of this assumption. This is because the contributions of the large turbulence structures in a forced jet must be educed out from single point measurements to obtain q, the fine-scale turbulence intensity. Such a process is laborious, and has not been carried out. Under these circumstances, the validity of equation (7-3) must be judged by comparison of the predicted results of the present quasi-linear theory with experiments.

The dynamical characteristics of the large turbulence structures of a jet are very complicated. However, if interest is confined to a gross description of these structures in some statistical average sense, they can be predicted with remarkable accuracy by regarding them as instability waves of the mean-flow profile. The works of Chan (ref. 37), Moore (ref. 6), Tam and Chen (ref. 34), and more recently Plaschko (ref. 35) strongly support this contention. In this section, in keeping with the proposed characterization of the mean flow and fine-scale turbulence by a few profile parameters, these excited large turbulence structures will be described by an amplitude function and a spatial growth or decay rate which is a function of the mean flow parameters and frequency. The growth and decay rates are to be calculated in accordance with locally-parallel hydrodynamic stability theory. As will be shown later, this relatively simple theory is capable of offering extraordinarily good results.

7.1.1 Receptivity

To facilitate the formulation of a quantitative description of the receptivity process by which the intrinsic instability waves of a jet are excited by upstream tones, the following assumptions will be adopted.

1. The shear layer in the core part of the jet will be assumed to be locally parallel, characterized by a uniform core of radius h(x) and a shear layer half-width b(x) as shown in figure 7.1.

2. The instability waves of the shear layer are excited by the upstream acoustic disturbances as these disturbances traverse the shear layer. This is illustrated in figure 7.3.

Let the subscript i denote the physical variables associated with the upstream tones. As these sound waves pass through the shear layer of the jet, disturbances will be generated both inside the shear layer as well as in the core of the jet. Subscripts s and c will be used to designate corresponding physical variables associated with the disturbances in the shear layer and the core of the jet respectively. On invoking the usual locally parallel flow assumption, the dimensionless governing equations for the density, ρ, pressure, p, and velocity, $\vec{v}$, of the disturbances are :

For $r \geq h$

$$\frac{\partial \rho_s}{\partial t} + \bar{u} \frac{\partial \rho_s}{\partial x} + \nabla \cdot (\bar{\rho} \vec{v}) = 0$$

$$\bar{\rho} \left[\frac{\partial \vec{v}_s}{\partial t} + \bar{u} \frac{\partial \vec{v}_s}{\partial x} + v_s \frac{\partial \bar{u}}{\partial r} \hat{e}_x \right] = -\nabla p_s \qquad (7\text{-}4)$$

$$\frac{\partial p_s}{\partial t} + \bar{u} \frac{\partial p_s}{\partial x} + \gamma \bar{p} \nabla \cdot \vec{v}_s = 0$$

$\hat{e}_x$ = unit vector in the x-direction

For $r \leq h$

$$\frac{\partial \rho_c}{\partial t} + \frac{\partial \rho_c}{\partial x} + \nabla \cdot \vec{v}_c = 0$$

$$\frac{\partial \vec{v}_c}{\partial t} + \frac{\partial \vec{v}_c}{\partial x} = -\nabla p_c \qquad (7\text{-}5)$$

$$\frac{\partial p_c}{\partial t} + \frac{\partial p_c}{\partial x} + \gamma \bar{p} \nabla \cdot \vec{v}_c = 0$$

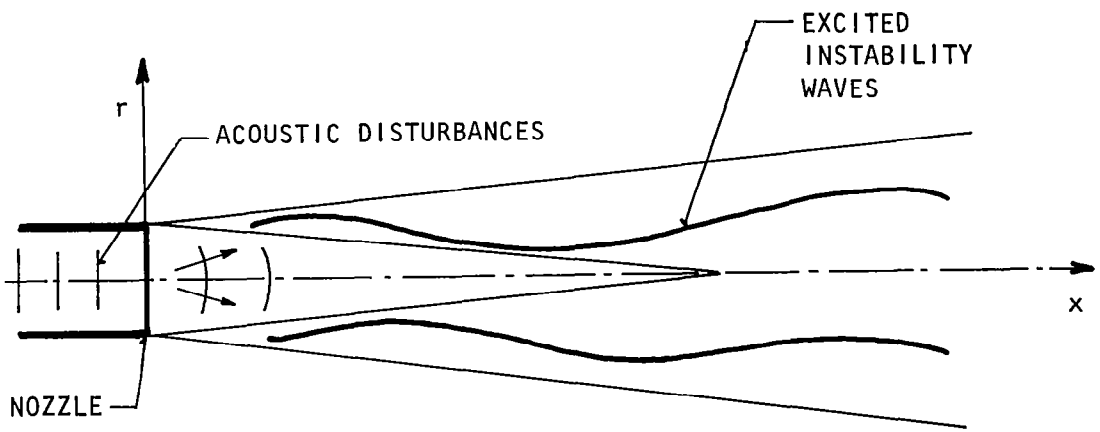

Figure 7.3 Excitation of instability waves by upstream tones.

where a bar denotes the mean flow quantity. The scales of length, velocity, time, density, and pressure are R_j (the radius of the jet), u_j (the jet exit velocity), R_j/u_j, ρ_j (the jet exit density), and $\rho_j u_j^2$. Equations (7-4) and (7-5) are the linearized continuity, momentum and energy equations of a compressible inviscid fluid. If the fluid is viscous (i.e. where an eddy-viscosity model may be used to model the effect of fine-scale turbulence), the same analysis as outlined below can easily be carried out. However, for the purpose of determining the coupling coefficients between the upstream tones and the excited instability waves, an inviscid model is considered sufficient. A cylindrical coordinate system (r,θ,x), centered at the nozzle exit, has been used. The velocity components in the (r,θ,x) directions are represented by (v,w,u) respectively. Within the locally-parallel flow approximation, $h(x)$ and $b(x)$ of the mean flow are regarded as constants, and $\bar{p}$ is equal to the ambient pressure (by the boundary layer approximation). The appropriate boundary conditions are,

at $r = h$

$$p_i(h,\theta,x,t) + p_c = p_s \tag{7-6a}$$

$$v_i(h,\theta,x,t) + v_c = v_s \tag{7-6b}$$

Here as,

$$r \to o \quad p_c \text{ and } \vec{v}_c \text{ are bounded, and as} \tag{7-7}$$

$$v \to \infty \quad p_s \text{ and } \vec{v}_s \text{ are bounded or satisfy the outgoing wave condition .}$$

Equation (7-6) is simply a statement of continuity of pressure and velocity at the edge of the core of the jet. In this equation, $p_i(h,\theta,x,t)$ and $v_i(h,\theta,x,t)$ are considered as known functions. They are to be determined from the known upstream tone. Without loss of generality, these quantities can be decomposed into Fourier components in θ and t. It will suffice to consider only the nth Fourier component. The general solution is simply a linear superposition of all such solutions. Thus p_i and v_i of the inhomogeneous boundary condition given by equation (7-6) will be replaced by:

$$p_i = \hat{p}_n(x) \exp\,[i(n\theta-\Omega t)] \tag{7-8}$$

$$v_i = \hat{v}_n(x) \exp\,[i(n\theta-\Omega t)] \tag{7-9}$$

Equations (7-4) to (7-9) form an inhomogeneous boundary value problem. For arbitrary values of $\hat{p}_n(x)$ and $\hat{v}_n(x)$, the problem can be solved by the local Green's function technique developed in references 16, 18 and 33. The method consists of replacing $\hat{p}_n$ and $\hat{v}_n$ by delta function $\delta(x-\xi)$; that

is at r = h

$$\alpha\ \delta(x-\xi)\ \exp\ [i(n\theta - \Omega t)] + p_c = p_s \tag{7-10a}$$

$$\beta\ \delta(x-\xi)\ \exp\ [i(n\theta - \Omega t)] + v_c = v_s \tag{7-10b}$$

The solution of this special problem provides the necessary Green's functions which can be used to construct the general solution. Let $(u_{pn}, v_{pn}, w_{pn}, p_{pn}, \rho_{pn})$ be the special solution with $\alpha = 1$ and $\beta = 0$ in equation (7-10), and $(u_{vn}, v_{vn}, w_{vn}, p_{vn}, \rho_{vn})$ be the special solution with $\alpha = 0$ and $\beta = 1$; then it is easy to show that the general solution for arbitrary $\hat{p}_n(x)$ and $\hat{v}_n(x)$ is

$$p(r,\theta,x,t) = \int_{-\infty}^{\infty} p_{pn}\ (r,\theta,x,t;\xi)\ \hat{p}_n(\xi)d\xi + \int_{-\infty}^{\infty} p_{rn}\ (r,\theta,x,t;\xi)\ \hat{v}_n(\xi)\ d\xi \tag{7-11}$$

Similar expressions as in equation (7-11) give the values of u, v, w and ρ.

To construct the Green's functions, the method of Fourier transforms can be used. Since the problem is linear, it is clear that all the physical variables should have an exp [inθ] dependence which can easily be factored out from the problem. By applying the Fourier transform in x and t to equations (7-4) to (7-8) and (7-10), the problem is reduced to that of solving an ordinary differential equation with inhomogeneous boundary conditions. The solution can be constructed in a straightforward manner. Now the Green's functions are found by evaluating the Fourier inverse transform of this solution. The proper procedure in performing the contour integrals has been elaborated in (refs. 16 and 18). Essentially, proper contour deformation in compliance with the casuality condition is required. On following the steps outlined there, and restricting consideration to the excited instability wave of the mean flow alone, it is easy to find

$$\begin{bmatrix} p_{pn} \\ p_{vn} \end{bmatrix} = \begin{bmatrix} C_{pn} \\ C_{vn} \end{bmatrix} \cdot \exp\ [ik_n(x-\xi) + i(n\theta - \Omega t)]\hat{p}(r,\Omega,k_n)H(x-\xi) \tag{7-12}$$

where k_n is the eigenvalue of the instability wave corresponding to frequency Ω. $\hat{p}(r,\Omega,k_n)$ is the pressure eigenfunction. $H(x-\xi)$ is the unit step function. The coefficients C_{pn} and C_{vn} are

$$C_{pn} = \frac{i\sqrt{(\Omega-k_n)^2M_j^2-k_n^2}\; J_n'\left(\sqrt{(\Omega-k_n)^2M_j^2-k_n^2}\; h\right)}{\left(\frac{\partial\Delta}{\partial k}\right)_{k_n}}$$

$$C_{vn} = \frac{(\Omega-k_n)\; J_n\left(\sqrt{(\Omega-k_n)^2M_j^2-k_n^2}\; h\right)}{\left(\frac{\partial\Delta}{\partial k}\right)_{k_n}} \qquad (7\text{-}13)$$

where M_j is the jet Mach number, $J_n(z)$ is the Bessel function of order n, and $J_n'(z) = \frac{d}{dz} J_n(z)$.

The function $\Delta(k)$ is equal to

$$\Delta = \sqrt{(\Omega-k)^2M_j^2-k^2}\; J_n'\left(\sqrt{(\Omega-k)^2M_j^2-k^2}\; h\right) \quad \phi(r,\Omega,k)$$
$$-J_n\left(\sqrt{(\Omega-k)^2M_j^2-k^2}\; h\right) \quad \frac{d\phi(r,\Omega,k)}{dr} \qquad (7\text{-}14)$$

in which $\phi(r,\Omega,k)$ is the solution of

$$\frac{d^2\phi}{dr^2} + \left[\frac{1}{r} - \frac{1}{\bar{\rho}}\frac{d\bar{\rho}}{dr} + \frac{2k}{\Omega-\bar{u}k}\frac{d\bar{u}}{dr}\right]\frac{d\phi}{dr} + \left[\frac{(\Omega-\bar{u}k)^2}{\bar{a}^2} - \frac{n^2}{r^2} - k^2\right]\phi = 0 \qquad (7\text{-}15)$$

Satisfying $\phi \to \lambda H_n^{(1)}\left(\sqrt{\Omega^2/\bar{a}_o^2 - k^2}\; r\right)$ as $r \to \infty$ (7-16)

It should be noted that equation (7-15), for spatially damped waves, must be integrated along a deformed contour in the complex r-plane as discussed by Tam and Morris (ref. 38).

In equations (7-15) and (7-16), $\bar{a}$ is the nondimensional speed of sound, and $\bar{a}_o$ is the ambient value of $\bar{a}$. $H_n^{(1)}(z)$ is the nth order Hankel function of the first kind. The real constant λ is the normalization constant of the eigenfunctions. Here λ will be chosen such that the eigenfunctions $(\hat{u},\hat{v},\hat{w},\hat{p})$ satisfy the following normalization condition:

$$\int_0^\infty \left[\frac{1}{4}\bar{\rho}\bar{u}\left(|\hat{u}|^2+|\hat{v}|^2+|\hat{w}|^2\right)+\frac{\bar{u}|\hat{p}|^2}{4\gamma\bar{p}}+\frac{1}{2}R_e\left(\hat{p}\hat{u}^*\right)\right] r\,dr = 1 \qquad (7\text{-}17)$$

where * denotes the complex conjugate. The significance of the normalization condition (7-17) is that, as normalized, the growth rate of the wave is related to its energy flux. This is so even when the effect of eddy viscosity is included as discussed in reference 22. It is to be noted that for spatially damped waves, the inviscid eigenfunctions are not completely defined along the real r-axis. In this case, a small amount of eddy viscosity must be added to the governing equations in determining the eigenfunction and λ.

Now let A(x) be the complex amplitude of the excited instability wave defined by

$$\begin{bmatrix} u \\ v \\ w \\ p \end{bmatrix} = A(x) \begin{bmatrix} \hat{u} \\ \hat{v} \\ \hat{w} \\ \hat{p} \end{bmatrix} \exp\left[i(n\theta - \Omega t)\right] \qquad (7\text{-}18)$$

substitution of equations (7-18), (7-12), and similar expressions for u_{pn}, u_{vn}, v_{pn}, v_{vn} etc. into (7-11), it is easy to find that

$$A(x) = \int_{-\infty}^{x} C_{pn} e^{ik_n(x-\xi)} \hat{p}_n(\xi)\,d\xi + \int_{-\infty}^{x} C_{vn} e^{ik_n(x-\xi)} \hat{v}_n(\xi)\,d\xi \qquad (7\text{-}19)$$

By differentiating equation (7-19) with respect to x, the following equation for A is derived.

$$\frac{dA}{dx} = ik_n A + C_{pn}\hat{p}_n(x) + C_{vn}\hat{v}_n(x) \qquad (7\text{-}20)$$

In equation (7-20), parameters k_n, C_{pn}, and C_{vn} are functions of the mean flow parameters b and h. To account for the slow variation of b and h in the axial direction of the jet, this equation will now be considered as one with variable coefficients in x. The solution of this complex wave-amplitude equation together with equation (7-18) provides a complete mathematical description of the excited instability wave of the jet.

7.1.2 Conservation Equations

As mentioned before, no attempt will be made here to describe the turbulent fluid motion of an excited jet in detail. Instead, the mean flow, the fine-scale turbulence, and the excited instability waves or large

turbulence structures will be characterized by the gross parameters b, h, $\bar{q}$, and A as given in equations (7-1), (7-3), and (7-18). These parameters, as functions of x, are related nonlinearly through a set of conservation equations. The use of conservation equations to predict the nonlinear development of a wave is not new. Models of this kind with different degrees of sophistication have been employed by Ko et al (ref. 21), Tam (ref. 22), Chan (ref. 23), and Morris (ref. 25) in the past. The present analysis can, therefore, be considered as an extension of these previous analyses.

The equations of motion for a viscous compressible fluid in dimensionless form are

$$\frac{\partial \rho}{\partial t} + \nabla\cdot(\rho\vec{v}) = 0$$

$$\rho\left[\frac{\partial \vec{v}}{\partial t} + \vec{v}\cdot\nabla\vec{v}\right] = -\nabla p + \frac{1}{R_e}\nabla^2\vec{v} \qquad (7\text{-}21)$$

$$\frac{\partial p}{\partial t} + \nabla\cdot(p\vec{v}) + (\gamma - 1)\, p\nabla\cdot\vec{v} = 0$$

where R_e is the Reynolds number based on the radius of the jet. The physical variables will be split into three parts corresponding to the mean flow, the large-scale instability wave, and the fine-scale turbulence motion, as follows,

$$\begin{aligned} \vec{v} &= \bar{\vec{v}} + \tilde{\vec{v}} + \vec{v}' \\ p &= \bar{p} + \tilde{p} + p' \\ \rho &= \bar{\rho} + \tilde{\rho} + \rho' \end{aligned} \qquad (7\text{-}22)$$

The mean flow equations are derived by first taking the phase average, indicated by a ~, and then the time average indicated by a -, of the equations of motion (7-21). The equations for the wave components are then obtained by subtracting the mean-flow equations from the phase-averaged equations. Finally, the equations for the fine-scale turbulent motion are obtained by subtracting the phase-averaged equations from the original equations of motion. The process of phase averaging was discussed by Hussain and Reynolds (ref. 39) and applied very effectively by Chan (ref. 23) to incompressible jet flows. These three sets of equations written in cylindrical coordinates are given in Appendix C.

Now, by multiplying equation (C-2) of Appendix C by (rdr), and integrating from r = 0 to r = ∞, the equation of conservation of mean axial-momentum flux is obtained. To the order of $1/R_e$, the equation can be written as

$$\frac{d}{dx}\int_0^\infty [\bar{\rho}\bar{u}^2 + \bar{\rho}\overline{\tilde{u}\tilde{v}} + \bar{\rho}\,\overline{u'v'} + 2\overline{\tilde{\rho}\tilde{u}}\bar{u} - \bar{p}-p_o]\ r dr = 0$$

or after integrating over x,

$$\int_0^\infty [\bar{\rho}\bar{u}^2 + \bar{\rho}\,\overline{\tilde{u}\tilde{v}} + \bar{\rho}\overline{u'v'} + 2\overline{\tilde{\rho}\tilde{u}}\bar{u} + \bar{p}-p_o]\ r dr = \text{constant}$$

In most cases, the inequalities $\bar{u}^2 >> \overline{\tilde{u}^2}$ etc. hold. Therefore, to a first approximation, the statement of conservation of mean axial-momentum flux is

$$\int_0^\infty \bar{\rho}\bar{u}^2\ r dr \simeq \frac{1}{2} \tag{7-23}$$

The equation of conservation of mean kinetic energy is equivalent to the integral of the first moment of equation (C-2). The product of equation (C-2) and $\bar{u}$, after simplification by using equation (C-1), can be written as

$$\frac{\bar{\rho}\bar{v}}{2}\frac{\partial \bar{u}^2}{\partial r} + \frac{\bar{\rho}\bar{u}}{2}\frac{\partial \bar{u}^2}{\partial x} = \bar{\rho}\,(\overline{\tilde{u}\tilde{v}} + \overline{u'v'})\ \frac{\partial \bar{u}}{\partial r} - \frac{1}{r}\frac{\partial}{\partial r}[\bar{\rho}(\overline{\tilde{u}\tilde{v}} + \overline{u'v'})\ r]$$

$$- \frac{\overline{\tilde{\rho}\tilde{v}}}{2}\frac{\partial \bar{u}^2}{\partial r} - \frac{\bar{u}}{r}\frac{\partial}{\partial r}(\overline{\tilde{\rho}\tilde{u}\tilde{v}}r) - \bar{u}\frac{\partial}{\partial x}(\bar{\rho}(\overline{\tilde{u}^2} + \overline{\tilde{v}^2}))$$

$$- \bar{u}\frac{\partial}{\partial x}(\overline{\tilde{\rho}\tilde{u}\tilde{u}}) - \frac{\overline{\tilde{\rho}\tilde{u}}}{2}\frac{\partial \bar{u}^2}{\partial x} - \bar{u}\frac{\partial \bar{p}}{\partial x} + \frac{\bar{u}}{R_e}\left[\frac{\partial^2 \bar{u}}{\partial x^2} + \frac{1}{r}\frac{\partial}{\partial r}\left(r\frac{\partial \bar{u}}{\partial r}\right)\right]$$

This equation can be further simplified by applying the boundary-layer approximation to the terms on the right hand side. On multiplying by rdr and integrating over all r, the integral mean kinetic-energy flux equation is obtained:

$$\frac{d}{dx}\int_0^\infty \left(\frac{1}{2}\bar{\rho}\bar{u}^3\right) r dr = \int_0^\infty \bar{\rho}\,\overline{\tilde{u}\tilde{v}}\frac{\partial \bar{u}}{\partial r}\, r dr + \int_0^\infty \bar{\rho}\,(\overline{u'v'})\frac{\partial \bar{u}}{\partial r}\, r dr \tag{7-24}$$

Earlier it was mentioned that the fine-scale turbulence-intensity distribution would be approximated by equation (7.3), which is characterized by the peak turbulence intensity $\bar{q}(x)$. To determine $\bar{q}$, use will be made of the turbulence kinetic-energy equation. This equation can be obtained by first multiplying equations (C-8), (C-9), and (C-10) by u', v', and w', respectively; and then taking the phase and the time average. By applying the boundary layer approximation to the sum of these equations and neglecting the terms representing the convection of q by the wave, as compared to the convection by the mean flow, it is straightforward to derive the following equation for the turbulence intensity $\left[q = \frac{1}{2} \overline{(u'^2 + v'^2 + w'^2)} \right]$.

$$\bar{\rho}\bar{v} \frac{\partial q}{\partial r} + \bar{\rho}\bar{u} \frac{\partial q}{\partial x} = -\frac{1}{r} \frac{\partial}{\partial r} \overline{\langle v'(p' + \bar{\rho}q') \rangle} - \bar{\rho} \overline{\langle u'v' \rangle} \frac{\partial \bar{u}}{\partial r} + \phi - \varepsilon \qquad (7\text{-}25)$$

where $\langle \ \rangle$ = phase average

$$q' = \frac{1}{2} (u'^2 + v'^2 + w'^2)$$

and

$$\begin{aligned} \phi = -\bar{\rho} \Bigg[& \overline{\langle u'^2 \rangle \frac{\partial \tilde{u}}{\partial x}} + \overline{\langle u'v' \rangle \frac{\partial \tilde{v}}{\partial x}} + \overline{\langle u'w' \rangle \frac{\partial \tilde{w}}{\partial x}} \\ & + \overline{\langle u'v' \rangle \frac{\partial \tilde{u}}{\partial r}} + \overline{\langle v'^2 \rangle \frac{\partial \tilde{v}}{\partial r}} + \overline{\langle v'w' \rangle \frac{\partial \tilde{w}}{\partial r}} \\ & + \overline{\frac{\langle u'w' \rangle}{r} \frac{\partial \tilde{u}}{\partial \theta}} + \overline{\frac{\langle v'w' \rangle}{r} \frac{\partial \tilde{v}}{\partial \theta}} + \overline{\frac{\langle w'^2 \rangle}{r} \frac{\partial \tilde{w}}{\partial \theta}} \\ & + \overline{\frac{\langle w'^2 \rangle \tilde{v}}{r}} - \overline{\frac{\langle v'w' \rangle \tilde{w}}{r}} \Bigg] \end{aligned} \qquad (7\text{-}26)$$

It should be noted that, here, ϕ represents the rate of dissipation of wave energy to fine-scale turbulence, and ε contains all the viscosity terms, and represents the viscous dissipation of turbulence energy. The integral of equation (7-25) gives the turbulence kinetic-energy equation:

$$\frac{d}{dx}\int_0^\infty (\bar{\rho}\bar{u}q)\ r\,dr = -\int_0^\infty \bar{\rho}\,\overline{\langle u'v'\rangle}\,\frac{\partial \bar{u}}{\partial r}\,r\,dr + \int_0^\infty \phi\ r\,dr - \int_0^\infty \varepsilon\ r\,dr \qquad (7\text{-}27)$$

So far, the energy equations for the mean flow and the fine-scale turbulence have been derived. To be consistent, it appears that an energy equation for the large-scale coherent wave motion should also be included in the set of conservation equations. It is important to point out at this stage that amplitude equation (7-20) has been formulated for the instability wave. Thus, what is required is to show that equation (7-20) is equivalent to the wave-energy equation.

The equation for the wave-energy flux can be found in the same way as the turbulence kinetic-energy equation. However, for a compressible flow, the energy density consists of a potential energy component as well as the usual kinetic-energy density. By multiplying equations (C-4), (C-5), and (C-6) by $\tilde{u}$, $\tilde{v}$, and $\tilde{w}$, respectively, and then taking the time average of the sum of these equations, one obtains the wave-energy equation:

$$\bar{\rho}\bar{v}\frac{\partial Q}{\partial r} + \bar{\rho}\bar{u}\frac{\partial Q}{\partial x} = -\left[\frac{\partial}{\partial x}\overline{(\tilde{p}\tilde{u})} + \frac{1}{r}\frac{\partial}{\partial r}\overline{(r\tilde{p}\tilde{v})}\right]$$

$$+ \overline{\tilde{p}\left[\frac{\partial \tilde{u}}{\partial x} + \frac{1}{r}\frac{\partial}{\partial r}(r\tilde{v}) + \frac{1}{r}\frac{\partial \tilde{w}}{\partial \theta}\right]} - \bar{\rho}\,\overline{\tilde{u}\tilde{v}}\frac{\partial \bar{u}}{\partial r}$$

$$+ \frac{1}{r}\frac{\partial}{\partial r}\left[\overline{\bar{\rho}\,(\tilde{u}\langle u'v'\rangle + \tilde{v}\langle v'^2\rangle + \tilde{w}\langle v'w'\rangle)r}\right] - \phi$$

$$+ \text{viscous terms} \qquad (7\text{-}28)$$

where $Q = 1/2\ \overline{(\tilde{u}^2 + \tilde{v}^2 + \tilde{w}^2)}$ is the wave kinetic-energy density. In equation (7-28), only the lowest-order terms under the usual boundary-layer approximation are retained. In addition, for a sinusoidal wave, triple-order terms average to zero, and fourth-order terms are small in magnitude. These terms, therefore, have been neglected in obtaining equation (7-28). For large Reynolds-number flow, the molecular-viscosity effects are unimportant for the large-scale wave motion, and will be omitted in all subsequent consideration. The integral of equation (7-27), weighted by r, gives

$$\frac{d}{dx}\int_0^\infty (\bar{\rho}\bar{u}Q + \overline{\tilde{p}\tilde{u}})\,r\,dr = \int_0^\infty \overline{\tilde{p}\left[\frac{\partial \tilde{u}}{\partial x} + \frac{1}{r}\frac{\partial}{\partial r}(r\tilde{v}) + \frac{1}{r}\frac{\partial \tilde{w}}{\partial \theta}\right]}\,r\,dr$$

$$- \int_0^\infty \bar{\rho}\,\overline{\tilde{u}\tilde{v}}\,\frac{\partial \bar{u}}{\partial r}\,r\,dr - \int_0^\infty \phi\,r\,dr \qquad (7\text{-}29)$$

which is the integral wave-energy equation in the absence of external forcing. In part II of Appendix C, it is shown that this equation is satisfied if the wave variables are represented by those of an instability wave, calculated according to the locally parallel-flow approximation and subjected to normalization condition given by equation (7-17). Thus, in the following, it will not be necessary to consider this equation further.

In summary, three conservation equations, (7-23), (7-24), and (7-27), involving momentum and energy fluxes, have now been derived. These equations, together with the wave-amplitude equation (7-20), form the principal set of governing equations of the present model. However, in their present form, they do not provide a closed system of equations. In the next subsection, they will be supplemented by closure models.

7.1.3 Closure Models

The conservation equations obtained above do not form a closed system of equations. There are more unknowns than equations. To complete the present quasi-linear theory, closure-model relations will be introduced below. Because of the disparate time and length scales between the fine-scale turbulence and the mean flow or the large-scale wave motion, it is customary to model the turbulent Reynolds stresses by a Newtonian eddy-viscosity closure scheme. Here, this approach will be followed, and the following closure relationship will be assumed.

$$\langle u'u' \rangle = -2\,\varepsilon_t\left(\frac{\partial \bar{u}}{\partial x} + \frac{\partial \tilde{u}}{\partial x}\right);\quad \overline{u'u'} = -2\,\varepsilon_t\frac{\partial \bar{u}}{\partial x}$$

$$\langle u'v' \rangle = -\varepsilon_t\left[\frac{\partial \bar{u}}{\partial r} + \frac{\partial \bar{v}}{\partial x} + \frac{\partial \tilde{u}}{\partial r} + \frac{\partial \tilde{v}}{\partial x}\right];\quad \overline{u'v'} = -\varepsilon_t\left(\frac{\partial \bar{u}}{\partial r} + \frac{\partial \bar{v}}{\partial x}\right)$$

$$\langle u'w' \rangle = -\varepsilon_t\left[\frac{1}{r}\frac{\partial \bar{u}}{\partial \theta} + \frac{\partial \bar{w}}{\partial x} + \frac{1}{r}\frac{\partial \tilde{u}}{\partial \theta} + \frac{\partial \tilde{w}}{\partial x}\right];\quad \overline{u'w'} = -\varepsilon_t\left(\frac{1}{r}\frac{\partial \bar{u}}{\partial \theta} + \frac{\partial \bar{w}}{\partial x}\right)$$

$$\langle v'v' \rangle = -2\,\varepsilon_t \left[\frac{\partial \bar{v}}{\partial r} + \frac{\partial \tilde{v}}{\partial r}\right] \; ; \; \overline{v'v'} = -2\varepsilon_t \frac{\partial \bar{v}}{\partial r}$$

$$\langle v'w' \rangle = -\,\varepsilon_t \left[r\frac{\partial}{\partial r}\left(\frac{\bar{w}}{r}\right) + \frac{1}{r}\frac{\partial \bar{v}}{\partial \theta} + r\frac{\partial}{\partial r}\left(\frac{\tilde{w}}{r}\right) + \frac{1}{r}\frac{\partial \tilde{v}}{\partial \theta}\right]; \; \overline{v'w'} = -\varepsilon_t\left[r\frac{\partial}{\partial r}\left(\frac{\bar{w}}{r}\right) + \frac{1}{r}\frac{\partial \bar{v}}{\partial \theta}\right]$$

$$\langle w'w' \rangle = -\,2\varepsilon_t \left[\frac{1}{r}\frac{\partial \bar{w}}{\partial \theta} + \frac{\bar{v}}{r} + \frac{1}{r}\frac{\partial \tilde{w}}{\partial \theta} + \frac{\tilde{v}}{r}\right] \; ; \; \overline{w'w'} = -2\varepsilon_t \left[\frac{1}{r}\frac{\partial \bar{w}}{\partial \theta} + \frac{\bar{v}}{r}\right] \qquad (7\text{-}30)$$

where ε_t is the kinematic turbulent-eddy viscosity. On substituting the above Reynolds-stresses relation in equations (C-4) and (C-7) of Appendix C, it is easy to find that the linearized equations of motion for the large-scale instability waves are given by equations (C-11). In addition, the integral

$$-\int_0^\infty \bar{\rho}\,\overline{u'v'}\,\frac{\partial \bar{u}}{\partial r}\,r\,dr,$$

which appears both in the mean kinetic-energy equation and the turbulence kinetic-energy equation, is now given by

$$-\int_0^\infty \bar{\rho}\,\varepsilon_t \left(\frac{\partial \bar{u}}{\partial r}\right)^2 r\,dr \qquad (7\text{-}31)$$

Launder et al (ref. 40) and Chan (ref. 23) have found the model formulas for the kinematic eddy viscosity, ε_t, and viscous-dissipation function, ε, given by

$$\varepsilon_t = C_1\, q^{\frac{1}{2}}\, \ell \qquad (7\text{-}32)$$

$$\varepsilon = C_2\, \frac{q^{3/2}}{\ell} \qquad (7\text{-}33)$$

to be satisfactory. In these formulas, C_1 and C_2 are empirical constants, and ℓ is the distance between the two points in the shear layer of the jet, where $\bar{u}$ is equal to 0.9 and 0.1, respectively. The motivation of these closure models has been discussed by these and other authors, and will not be repeated here.

In principle, the turbulence-dissipation function ϕ of the turbulence kinetic-energy equation can be calculated if the eigenfunctions of the instability waves are known. However, these eigenfunctions are quite sensitive

to the numerical scheme by which they are computed. Further, it is questionable whether the computed linear eigenfunctions can indeed provide good detailed representations of the large-scale turbulence structures, especially near the critical points. These considerations suggest that it would be more advantageous to adopt a closure model for the function ϕ as well. It is noted that

$$\phi \propto \varepsilon_w \overline{\left(\frac{\partial \tilde{u}}{\partial r}\right)^2} + \text{----}$$

Hence one finds (approximately) that in the core part of the jet

$$\phi \propto \varepsilon_w \frac{1}{\ell^2} \cdot \frac{2|A|^2}{\left[(h+b)^2 - h^2\right]}$$

It seems reasonable to assume ε_w to have the same functional form as ε_t. This leads to the reation

$$\phi = C_3 \frac{q^{\frac{1}{2}} |A|^2}{\ell[(h+b)^2 - h^2]} \tag{7-34}$$

where C_3 is left as an unknown empirical constant.

Equations (7-30) to (7-34) are the closure model relations of the present quasi-linear theory. Except for equation (7-34), they have been widely used in turbulent-flow calculations. Their validity, in the case of an excited turbulent jet, will be tested, and confirmed in a later section of this report.

7.1.4 Governing Equations and Parameters of the Quasi-Linear Theory

The governing equations of the present quasi-linear theory can now be found by substituting the closure-model relations given by equation (7-31) to (7-34) into the conservation equations (7-23), (7-24), and (7-27). They are,

Mean axial-momentum equation

$$\int_0^\infty \bar{\rho}\, \bar{u}^2\, r dr = \frac{1}{2} \tag{7-35a}$$

Mean kinetic-energy equation

$$\frac{d}{dx}\int_0^\infty \left(\frac{1}{2}\bar{\rho}\,\bar{u}^3\right) rdr = 2\,k_i|A|^2 - \frac{C_3|A|^2}{\ell[(h+b)^2-h^2]}\int_0^\infty q^{\frac{1}{2}}\,rdr$$

$$- C_1\,\ell\int_0^\infty \bar{\rho}\,q^{\frac{1}{2}}\left(\frac{\partial\bar{u}}{\partial r}\right)^2 rdr \qquad (7\text{-}35b)$$

Turbulence-energy equation

$$\frac{d}{dx}\int_0^\infty (\bar{\rho}\,\bar{u}\,q)\,rdr = C_1\,\ell\int_0^\infty \bar{\rho}\,q^{\frac{1}{2}}\left(\frac{\partial\bar{u}}{\partial r}\right)^2 rdr +$$

$$\frac{C_3|A|^2}{\ell[(h+b)^2-h^2]}\int_0^\infty q^{\frac{1}{2}}\,rdr - \frac{C_2}{\ell}\int_0^\infty q^{3/2}\,rdr \qquad (7\text{-}35c)$$

In addition, the amplitude function A is the solution of the wave-amplitude equation (7-20), i.e.,

$$\frac{dA}{dx} = ik_n A + C_{pn}\hat{p}_n(x) + C_{vn}\hat{V}_n(x) \qquad (7\text{-}35d)$$

In deriving equation (7-35b), equation (C-20) of Appendix C has been used. In the above equations, $\bar{u}$ and q are given by equations (7-1) and (7-3). Also from equation (7-1), it is easy to find that the characteristic length ℓ is related to b by

$$\ell = 1.43274\,b \qquad (7\text{-}36)$$

The mean density $\bar{\rho}$ is a function of the mean flow velocity if the turbulent Prandtl number is unity, which is assumed here. A straightforward application of Crocco's relation yields the following relation:

$$\bar{\rho} = [\frac{\gamma - 1}{2} \bar{u} (1 - \bar{u}) M_j^2 + \bar{u} + \frac{t_o}{t_r} (1 + \frac{\gamma - 1}{2} M_j^2) (1 - \bar{u})] \qquad (7\text{-}37)$$

where t_o/t_r is the ratio of ambient-to-reservoir temperatures, and M_j is the jet Mach number.

Equations (7-35a) to (7-35d) consist of 4 coupled equations for the 4 unknowns: b, and h for the mean flow, $\bar{q}(x)$ of the peak turbulence intensity, and A-the complex wave amplitude. To start the solution, the initial values of these unknowns at the nozzle exit must be given. Here it will be assumed that $b(o) = b_o$ is provided. Physically, b_o is determined by the boundary-layer thickness at the nozzle exit, and is, therefore, a property of the nozzle design and operating conditions. Once b_o is known, h(o) is to be found by solving the mean axial-momentum flux equation (7-35a). At the nozzle exit, the level of excited turbulence intensity is usually quite low. It is found that any small initial value for $\bar{q}$ at x = 0 provides the same solution for the jet development. When the jet flow emerges from the nozzle exit, the mixing layer has a profile that is more typical of a boundary layer than that of a free shear layer. Actually, the mean flow is quite stable against waves with frequencies in the typical unstable frequency range of the jet-mixing layer slightly downstream. Therefore, it appears that the shear-layer instability waves would start to develop only in a region somewhat downstream of the nozzle exit. This consideration suggests strongly that a good, approximate, initial condition for A(x) is that it is equal to zero at x = 0. To sum up, the initial conditions at x = 0 are:

$$b_o \rightarrow \text{to be provided from measurements} \qquad (7\text{-}38a)$$

$$\bar{q}(0) \text{ a small value } (3.75 \times 10^{-5}) \qquad (7\text{-}38b)$$

$$A(0) = 0 \qquad (7\text{-}38c)$$

In the present model, there are 3 closure constants, namely, C_1, C_2 and C_3. They are to be determined empirically. A simple procedure by which these constants can be found is described in section 7.2. The inhomogeneous terms of the system of equations are $\hat{p}_n(x)$ and $\hat{v}_n(x)$ for a given tone, with a known sound pressure level at the nozzle exit, is to use the Born approximation. That is, $\hat{p}_n(x)$ and $\hat{v}_n(x)$ are given by the duct mode of the nozzle. As has been pointed out before, the coupling between the upstream tones and the excited instability waves is most effective near the nozzle exit. Thus, although the Born approximation would seriously overestimate the values of $\hat{p}_n(x)$ and $\hat{v}_n(x)$ downstream of the first two jet diameters, the error would not affect the predicted results of the model severely.

The main advantage of the Born approximation is its simplicity. For low to moderate subsonic Mach number jets, it is known that the presence of the flow does not greatly affect the distribution of the sound intensity downstream of the nozzle exit. Therefore, an alternate way of prescribing $\hat{p}_n(x)$ and $\hat{v}_n(x)$ for these jets is to use the calculated or measured values of $\hat{p}_n(x)$ and $\hat{v}_n(x)$, in the absence of flow. This procedure, which accounts for the decrease of sound intensity in the streamwise direction due to lateral spreading, should provide slightly better predicted results. These two ways of imposing the forcing terms will be further discussed later.

Finally, the mean flow, instability wave, and turbulence characteristics and intensity, as predicted by the present model, are affected by five input parameters. They are: S_e (the Strouhal number of the upstream tone), L_e (the level of the tone excitation at the nozzle exit), m (the mode number), t_r/t_o (the temperature ratio of the jet), and b_o (the initial thickness of the mixing layer). Thus once the model has been adequately tested by comparison with experiment, and its validity established, it would provide an extremely useful analytical tool for a systematic parametric study of the effect of upstream-tone excitation. Such a study would provide a valuable complement to the experimental data which covers only a very limited region of the five-dimensional parameter space. This is especially true for heated jets and high mode-number tones. In these cases, experimental measurements are extremely difficult to carry out.

7.2 COMPARISON BETWEEN THEORY AND EXPERIMENT

As described in section 7.1.3, the development of the unexcited jet and the interaction between the large structures and the fine-scale turbulence is controlled by three empirical coefficients C_1, C_2, and C_3. In the initial part of the numerical study, the values of these coefficients will be fixed on the basis of a chosen set of experimental data. The turbulent mixing of the unexcited jet is determined by the coefficients C_1 and C_2 alone. The former controls the amount of turbulence production at a given axial location, and the latter fixes the amount of viscous dissipation. The balance between these two components of the turbulence determines the integrated flux of mean flow energy which, in turn, governs the rate of spread of the jet in the annular mixing region.

The value of C_2 was fixed at its commonly used value of 1.5 (ref. 23, 40), and the value of the production coefficient C_1 was varied until the predicted rate of spread of the jet matched the measured values. As discussed in section 7.1.4, the calculations require initial values of the jet half-width, b and the maximum turbulent kinetic energy, $\bar{q}$ at the jet exit. The small, initial value of $\bar{q}$ is taken to be 0.0000375, which corresponds, for isotropic turbulence, to an initial turbulence intensity of 0.5 percent. The jet development has been found to be insensitive to changes in this initial value, and the value of $\bar{q}$ has been found to reach rapidly a nearly constant value, many orders of magnitude higher. The initial thickness of

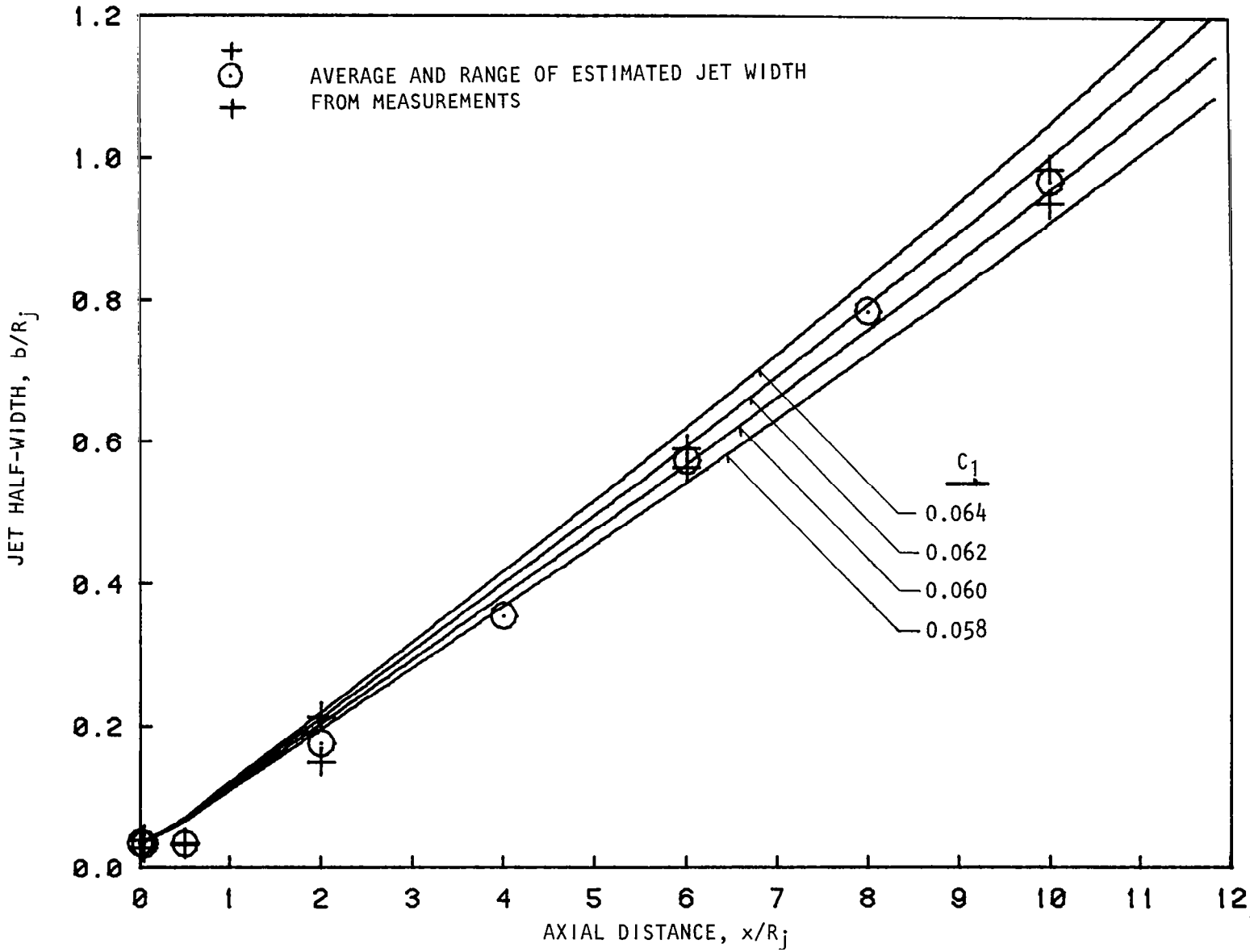

Figure 7.4 Variation of predicted jet growth for several values of C_1. $\xi = 1.25$, $t_r/t_o = 1.0$ (unheated)

the mixing layer, however, is found to be an important parameter particularly for the excited-jet cases. Its value is taken from the experimental data.

It is important to note that the shape of the mean velocity profile at the jet exit is of a turbulent boundary-layer type, though it rapidly develops the half-Gaussian shape used in the present analysis and given in equation (7-1). However, the initial value of b is taken as the half-width of this boundary-layer profile. The measured value has been found to be $0.035R_j$. The variation of b and $\bar{q}$ with axial distance is found by solving equation (7-35) with $|A|^2$ set to zero. The calculated variation of half-width b with axial distance is shown in figure 7.4 for several values of C_1. As the value of C_1, hence the fine-scale turbulence production, increases, the rate of spread of the jet also increases. The measured values of b for $M_j = 0.58$ and $t_r/t_o = 1.0$ (unheated) are also shown as symbols.

The value of b is difficult to determine directly from the measured mean-velocity profiles, since the radial location at which the velocity reaches its centerline value (i.e. the edge of the potential core) is hard to locate accurately. In this study, the value of b was found by assuming a half-Gaussian shape for the mean-velocity profiles and determining the radial distance between points with specified values of mean velocity. The values were taken as $0.9U_j$, $0.8U_j$, $0.5U_j$, and $0.2U_j$. For example, when $U/U_j = 0.9$, $n = 0.389876$ etc. It can be readily shown that one estimate of b is,

$$b = (r_{0.5} - r_{0.9}) \times 1.639011 \qquad (7\text{-}39)$$

where $r_{0.5}$ and $r_{0.9}$ are the values of radius at which $U/U_j = 0.5$ and 0.9, respectively. The spread in the estimated values of b at each axial measurement location is shown in figure 7.4. On the basis of this comparison, the value of C_1 was fixed at 0.060.

7.2.1 Excited-Jet Calculations

Before describing the results of the calculations for the effects of upstream excitation on the jet development, a brief description will be given of the computer program. A highly simplified block diagram is shown in figure 7.5. The jet operating conditions, the pressure ratio, and the total temperature ratio, ξ and t_r/t_o, are the first input parameters. The second input block describes the excitation level, Strouhal number, and mode number of the excitation tone. All other empirical coefficients or parameters required for the numerical solution are contained within the program, making it very straightforward to execute. The next section of the program calculates the coupling coefficients, wave number, and growth rate of the excited instability wave as a function of the local jet half-width, b. The associated analysis is described in section 7.1.1 and references 16 and 18. The values of b at which the calculations are made are closely spaced for small values of b (near the jet exit), and more widely spaced at larger values (towards the end of the potential core).

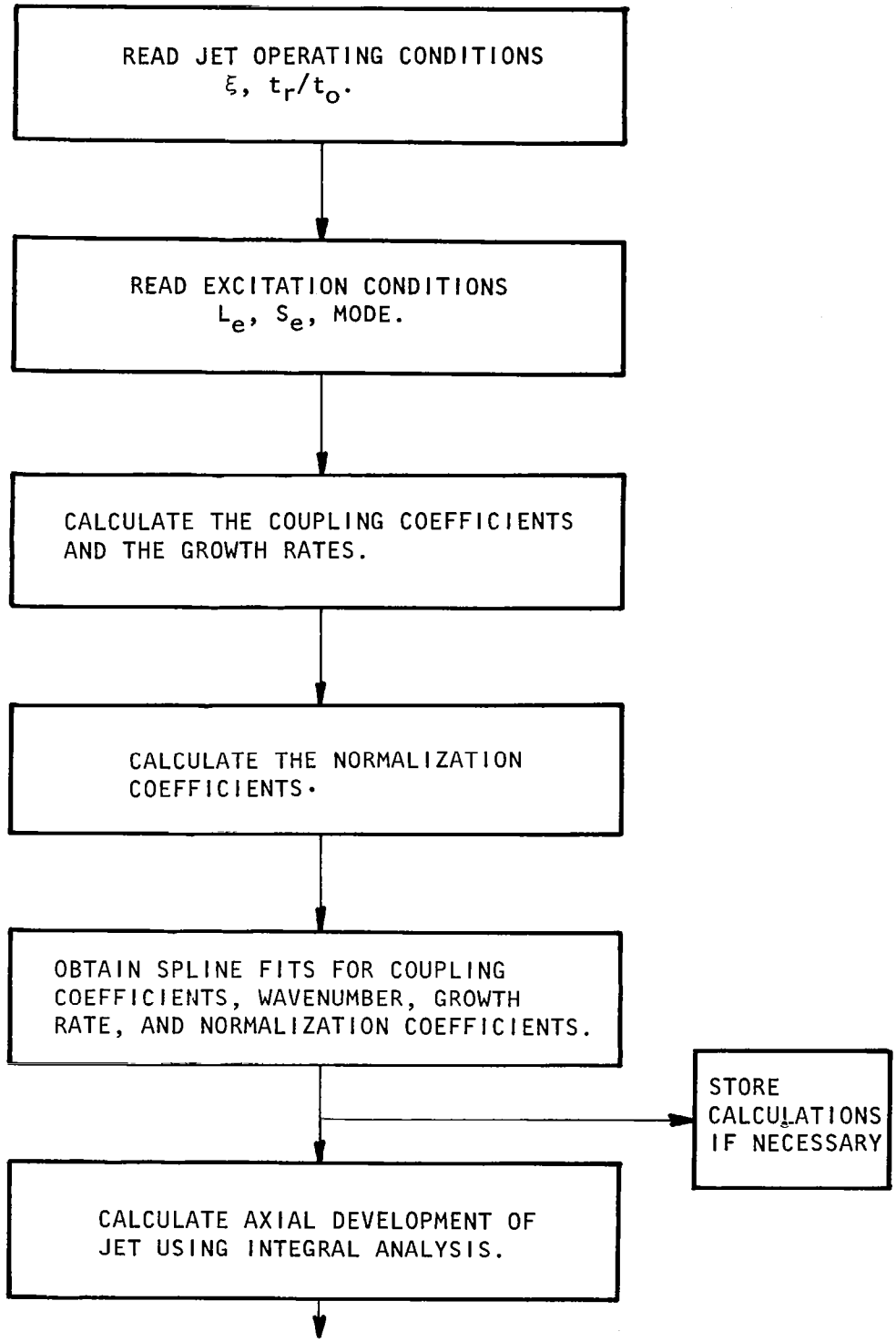

Figure 7.5 Block diagram of prediction program

As discussed in section 7.1.1 it is necessary to appropriately normalize the eigensolutions to the linear stability equations that are used to describe the instability wave. The inviscid solution only provides a valid solution on the real radial axis for unstable or growing waves. In order to obtain a description of the solutions for both growing and decaying waves for all real radial locations, it is necessary to solve the viscous stability or Orr-Sommerfeld equation. The Reynolds number used in this calculation is based on an eddy viscosity which is dependent of radius. Based on the measurements of Wygnanski and Fiedler (ref. 42) and the calculations of Tam and Chen (ref. 34), the numerical value of the Reynolds number is taken to be 500. At this value of the Reynolds number, the eigensolutions closely approach their inviscid values.

The viscous stability calculations are performed in the next section of the program. The calculation procedure is described in references 43 and 44. The normalization coefficients are then calculated such that equation (7-17) is satisfied. In order to obtain a smooth approximation to the values of the coupling coefficients, wave numbers, growth rates, and normalization coefficients at intermediate values of jet half-width, a cubic-spline fit is performed in the next section of the program. Since all of the calculations performed to this stage are independent of the excitation level, the calculations may be stored at this point. This is particularly useful if calculations are to be made at a series of levels yet to be determined. This is because the vast majority of the program execution time is consumed in the prior calculations, and the calculation of the jet development at different levels of excitation is relatively rapid. The final section of the program calculates the development of the jet half-width, the maximum turbulent kinetic energy, and the level of the excited instability wave or large-scale turbulent structures using the integral conservation equations given in section 7.1.4. The output also includes the axial variation of the centerline instability pressure and velocity, the axial phase velocity, and radial distributions of the mean velocity, the turbulent kinetic energy, and instability wave pressure, and velocity at selected axial locations.

As discussed in section 7.1.4, it is necessary to specify the value of the excitation pressure and radial velocity at the edge of the potential core. The Born approximation would be adequate for prediction purposes alone, but since the important empirical coefficient C_3 has yet to be fixed, some of the more unusual features of the excited jet flow, such as the interference between the excited instability wave and the excitation wave, would be missed. No analysis for the axial decay of the excitation wave has been performed. Instead, a simple empirical fit has been made to the measured data for the zero flow case. Since the chosen measurements are for a given frequency and mode number, the fit may not be exact for all excitation cases. However, the improvement over the Born approximation is felt to be physically, though not necessarily quantitatively, significant. The axial behavior is most easily expressed using a decibel scale for the excitation pressure which is given by

$$(p_i)_{dB} = \{L_e - 7.0\ x/R_j\} \exp\ [iM_j\omega x/(1+M_j)R_j]:\ 0<x/R_j\leq 1.0 \qquad (7\text{-}40a)$$

$$(p_i)_{dB} = \{L_e - 7.0)x^{-0.059}\} \exp\ [iM_j\omega x/(1+M_j)R_j]\colon\ x/R_j>1.0 \qquad (7\text{-}40b)$$

These expressions apply to the axisymmetric or plane excitation mode for which the pressure is independent of radius, and the radial velocity is zero. For the helical (1,0) mode, the axial variation is assumed to take the same form, but the pressure and radial velocity at the edge of the potential core are weighted by the appropriate Bessel functions, and their radial shape is given by

$$p_i(r) \sim J_1\ (\mu_{10}r/R_j) \qquad (7\text{-}41a)$$

$$v_i(r) \sim i\ \{\mu_{10}J_o(\mu_{10}r/R_j) - J_1(\mu_{10}r/R_j)/(r/R_j)\}/\{\omega(1-M_j)\} \qquad (7\text{-}41b)$$

$$\text{where } \mu_{10} = 1.84118 \qquad (7\text{-}41c)$$

The relationship between the nondimensional pressure and its decibel value depends on the nondimensionalizing scales. For the present calculations, this relationship may be written in two identical ways:

$$(p_i)_{dB} = 20\ \log_{10}(p_i) + 20\ \log_{10}(\rho_j u_j^2) + 90.969 \qquad (7\text{-}42a)$$

$$(p_i)_{dB} = 20\ \log_{10}(p_i) + 20\ \log_{10}(\rho_o a_o^2 M_j^2) + 90.969 \qquad (7\text{-}42b)$$

With the tone excitation described, it is possible to determine the value of the coefficient C_3. Its value is obtained by comparing the measured rate of spread of the jet at a given excitation condition with the predicted values for several values of C_3. The comparison is shown in figure 7.6. The measured values shown are the average of the estimates of the half-width using the method described above. In all cases the predicted growth of the jet is more rapid than the measured. However, it should be recalled that the predictions assume a mixing-layer profile at the jet exit that is more receptive to the tone excitation than the actual boundary-layer profile. If the apparent location of the jet exit for the calculations is shifted a small distance downstream, about $0.4R_j$, to account for this effect, very good agreement is obtained for $C_3 = 1.0$. This value has been used in all subsequent calculations, but no correction for the shift in the apparent jet exit has been made. This implies that the predictions will also show the effects of the excited instability wave occurring slightly closer to the jet exit than the measured values.

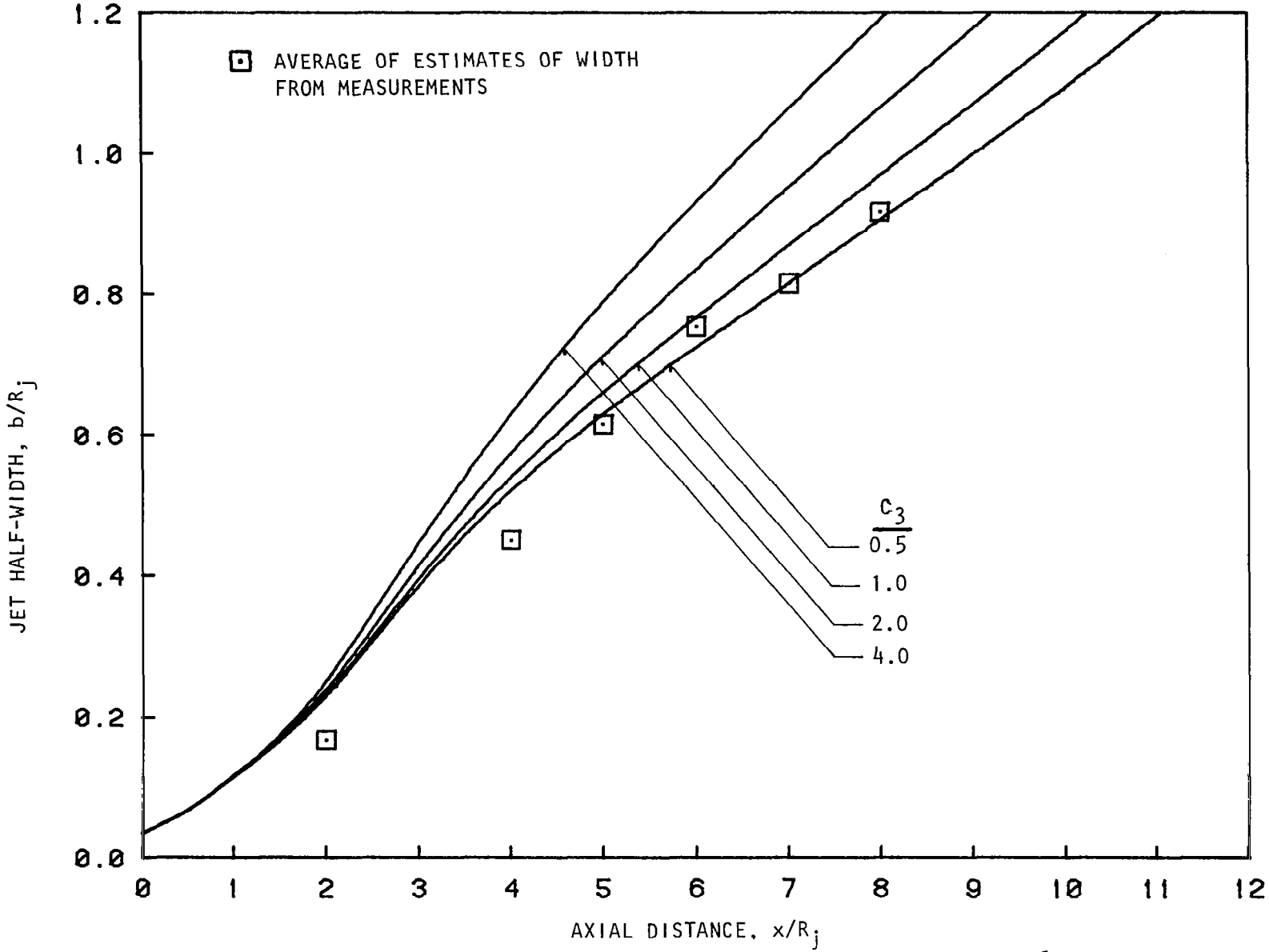

Figure 7.6 Variation of predicted excited jet growth for several values of $C_3:C_1 = 0.060$
$\xi = 1.25$; $t_r/t_o = 1.0$; $L_e = 141$ dB; $S_e = 0.5$, (0,0) Mode.

With all the empirical coefficients and the excitation tone parameters described, it is possible to examine the predicted effects of changes in the flow and excitation values. In subsequent sections, the predicted effects of excitation level, Strouhal number, mode number, and the effects of jet pressure and temperature ratio are examined.

7.2.2 Excitation Level Effects

As a first example, we will consider the effect of change of excitation level at a fixed Strouhal and mode number, and constant jet-operating conditions. To correspond with the experimental test points, the jet pressure, ξ and temperature ratio, t_r/t_o are set at 1.25 and 1.0 (unheated), respectively, and the excitation is taken to be an axisymmetric (0,0) mode with Strouhal number 0.5. The most obvious effect of increasing the excitation level is the change in the rate of jet spreading and the associated increase in the entrainment of the ambient fluid. This may be seen in figure 7.7, where the jet half-width is shown as a function of axial distance for several excitation levels. The jet is initially unaffected by the excitation until about one diameter downstream of the jet exit. Subsequently, the jet spreads more rapidly than in the unexcited case, the jet width then increases, at a given axial location, with increasing excitation level.

It will be shown later that there is a threshold level of excitation below which there are no observable changes in the jet mean flow or the fine-scale turbulence levels. The three excitation levels used in the calculations for figure 7.7 are clearly above this threshold level. The change in the rate of spread of the jet may be associated with the excited instability wave or large turbulent structures reaching a finite amplitude. By finite amplitude, it is meant that the stresses associated with the instability wave play an appreciable role in the overall energy balance for the flow, and are not negligible terms in the mean momentum and energy equations.

The growth of the instability wave or large turbulent structures is shown in figure 7.8, where the amplitude of the instability-wave pressure on the jet centerline is shown as a function of axial distance. It should be noted that this figure shows the pressure in absolute not relative units, and does not represent the ratio of the centerline pressure to its initial value, in this case zero, which has been obtained in previous calculations (refs. 22 and 23). Also shown in figure 7.8 is the form chosen for the centerline decay of the exciting acoustic wave and its measured values for the zero flow case. The excited instability wave starts with zero amplitude at the jet exit. At this location the tone excitation begins to trigger the instability wave growth as described in section 7.1.1. Once excited, the instability wave or large turbulent structure grows very rapidly according to linear hydrodynamic stability theory. However, it should be emphasized that the acoustic excitation continues to stimulate the instability wave away from the exit of the jet. This is confirmed by calculations, not included here, that compare the growth of the instability wave using the Born approximation, and using the present decaying acoustic

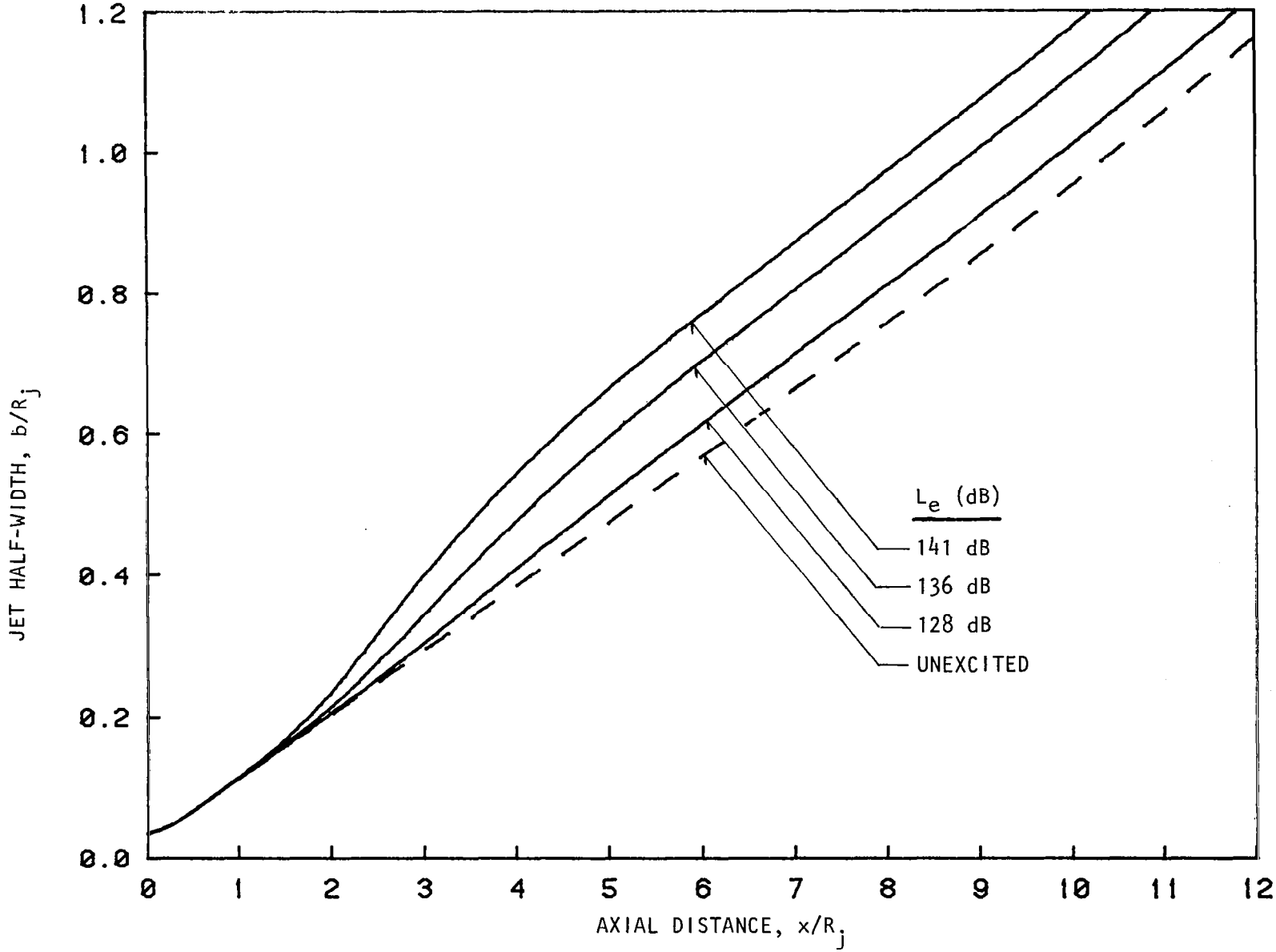

Figure 7.7 Effect of excitation level on the jet spreading rate as predicted by present theory.
$\xi = 1.25$, $t_r/t_o = 1.0$, $S_e = 0.5$, (0,0) Mode.

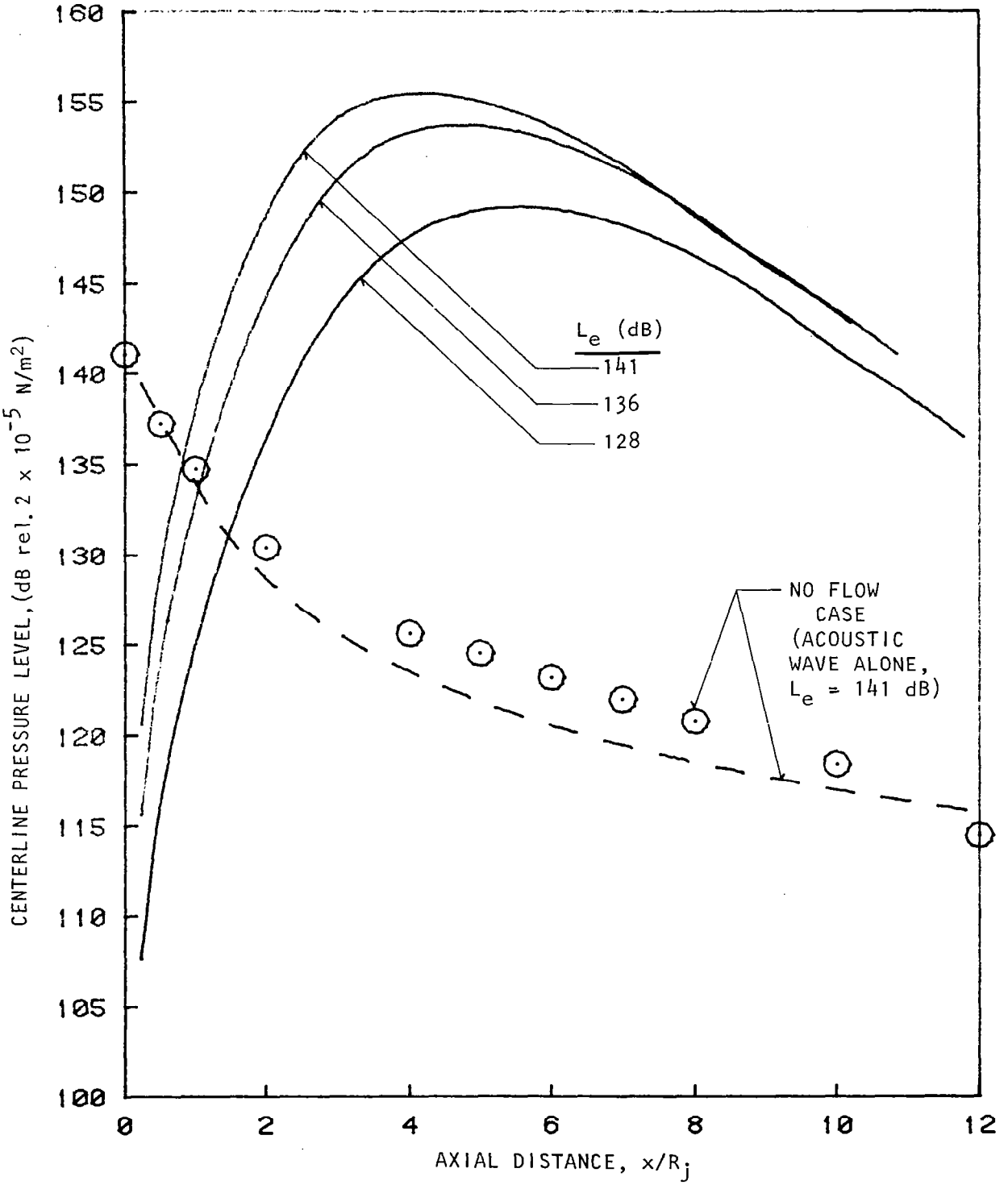

Figure 7.8 Axial variation of instability-wave centerline-pressure for various excitation levels. ξ = 1.25, t_r/t_o = 1.0, S_e = 0.5, (0,0) Mode.

———, and — — — —, Theory; ⊙, Measurement

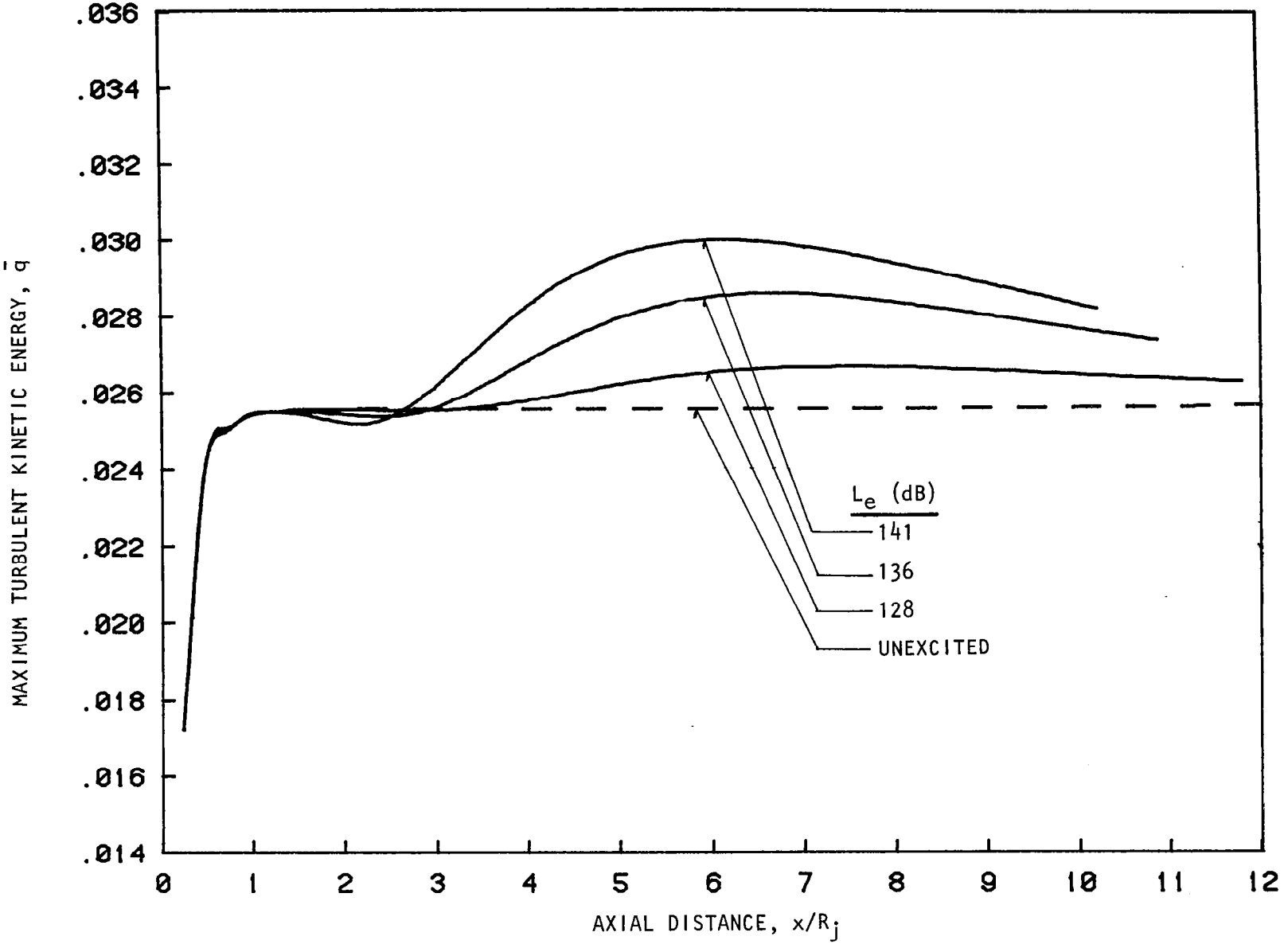

Figure 7.9 Predicted axial variation of maximum turbulent kinetic energy for several excitation levels.
ξ = 1.25, t_r/t_o = 1.0, S_e = 0.5, (0,0) Mode.

wave. The maximum level reached by the instability wave was greater for the Born approximation even though the excitation level at the jet exit was the same.

Clearly, the triggering of the instability wave is not isolated at the jet exit but is a distributed effect. Figure 7.8 shows how the large turbulent structures grow, reach a maximum amplitude about two diameters downstream, and then decay. Comparison with the measured data for the same conditions, shown in figure 5.2, shows that the location of the axial peak is predicted to occur too close to the jet exit, though the absolute peak level reached is very well predicted. No satisfactory explanation for the discrepancy has been found. From figure 8.7, it may be seen that, as the excitation level increases, the location of the maximum level moves towards the jet exit. This agrees with the measurements. It can also be seen that the peak level does not increase linearly with excitation level. This nonlinear behavior is discussed below.

From equation(7-35c), it can be seen that the axial variation of the fine-scale turbulent kinetic-energy flux is controlled by the balance of three source terms. The first is the transfer of energy from the mean flow. The second is the transfer of energy from the periodic-flow component corresponding to the excited instability wave or large turbulent structures. The final term represents the dissipation of energy due to viscous action. In the absence of excitation, the level reached by the fine-scale turbulence is controlled by the rate at which viscous effects dissipate the energy transferred from the mean flow. With excitation, additional energy is fed to the fine-scale turbulence. From equation(7-35c) it can be seen that the additional energy depends on the amplitude of the excited instability wave or large-scale turbulent structures.

The effect of the excitation level on the maximum turbulent kinetic energy is shown in figure 7.9. As the excitation level and hence the instability wave amplitude increases so the maximum fine-scale turbulence levels increase. As the excitation level increases, the fine-scale turbulence also begins to increase closer to the jet exit. This is consistent with the instability-wave amplitudes shown in figure 7.8. For the case of an excitation Strouhal number of 0.5, it can be seen in figure 7.8 that the amplitude of the large turbulent structures has decayed by about 15 dB from its maximum value by the end of the potential core. Since the only effect that can reduce the maximum turbulent kinetic energy, as can be seen from equation(7-35c), is the viscous dissipation, it is clear that the slow decrease in fine-scale turbulence levels seen in figure 7.9 is due to an increase in viscous dissipation and a decrease in the energy fed from the large turbulent structures to the fine-scale turbulence.

7.2.3 Strouhal Number Effects

From the preceding section, it is clear that the conditions under which the excited instability wave or large turbulent structures reach the greatest amplitude coincide with the largest changes in the mean flow and fine-scale turbulence development. To consider the effect of the excitation

Strouhal number on the growth of the instability wave, the excitation level was fixed at a value well in excess of the threshold level for a Strouhal number of 0.5, and the jet operating conditions were kept the same as in the preceding section: $\xi = 1.25$, $t_r/t_o = 1.0$. The axisymmetric (0,0) mode was considered. The effect of the excitation Strouhal number on the growth of the instability wave is shown in figure 7.10, where the centerline pressure is calculated as a function of axial distance. For an excitation Strouhal number of 0.1, the level of the excited wave does not exceed that of the acoustic excitation, shown by the dashed line, until five jet radii from the exit. Its maximum level never exceeds the excitation level at the jet exit, and falls far below the maximum levels achieved at higher Strouhal numbers.

As the excitation Strouhal number increases, so does the maximum amplitude of the excited large turbulent structures until S_e reaches 0.4. Increasing the excitation Strouhal number beyond this value results in a lowering of the peak amplitude. As the value of S_e increases from 0.1, the axial location at which the excited instability wave reaches its maximum value moves towards the jet exit.

From these calculations, it is clear that the maximum changes in the jet development should occur for an excitation Strouhal number of about 0.4. This is clearly seen to be the case in figure 7.11, which shows the axial variation of the jet width for several excitation Strouhal numbers. For the value of S_e of 0.1, there is no discernable change in the jet spread rate from the unexcited case. For the other three values of S_e shown, changes do occur with the greatest increase in jet half-width occuring for $S_e = 0.5$. As the excitation Strouhal number increases, the change in the jet width begins closer to the jet exit.

A similar trend is observed when the fine-scale turbulence levels are considered. Figure 7.12 shows the axial variation in the maximum turbulent kinetic energy for the same range of excitation Strouhal numbers. Once again, there is no change in the turbulent kinetic energy for an excitation Strouhal number of 0.1. For the other values of S_e shown, the value of $\bar{q}$ increases with the maximum increase for $S_e = 0.5$. As the value of S_e increases, the location of the axial peak in the value of $\bar{q}$ moves closer to the jet exit. From these calculations, it is clear that the value of S_e is important in determining the change in the jet development. The threshold level, above which discernible changes occur in the jet development, depends on the excitation Strouhal number. It appears that this threshold level increases as the excitation Strouhal number decreases. Because of the excessive computer times involved, sufficient calculations could not be performed to quantify this effect.

Before considering the effects of changes in other operating or excitation conditions, the phase velocity of the excited instability wave or large turbulent structures may be examined. In the calculations, the phase velocity, according to the locally-parallel flow approximation, is simply the ratio of the frequency of the wave to the real part of its wavenumber. It should be noted that, since the actual jet flow is diverging

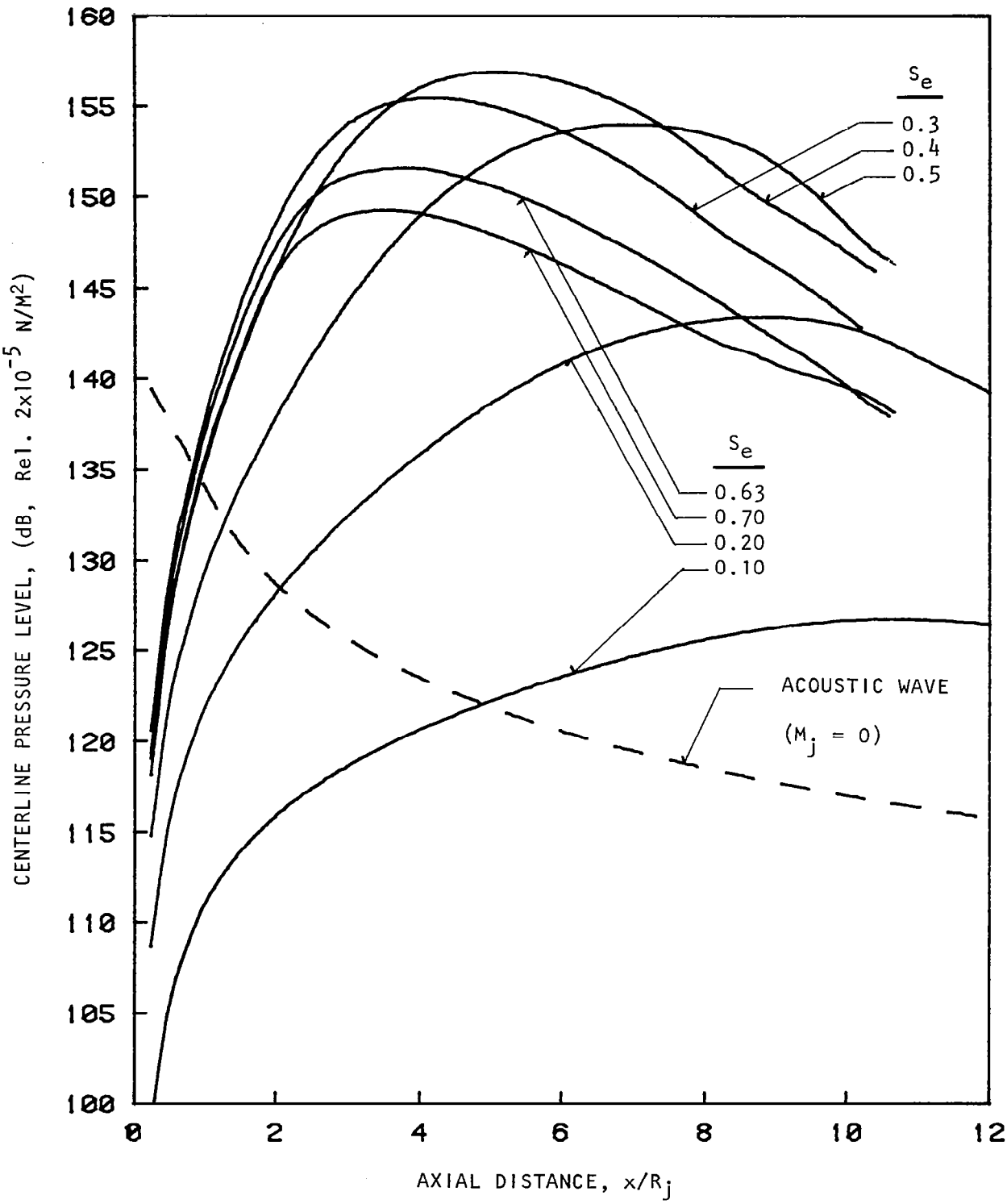

Figure 7.10 Predicted axial variation of centerline pressure level with excitation Strouhal number.
ξ = 1.25, t_r/t_o = 1.0 (unheated) (0,0) Mode, L_e = 141 dB.

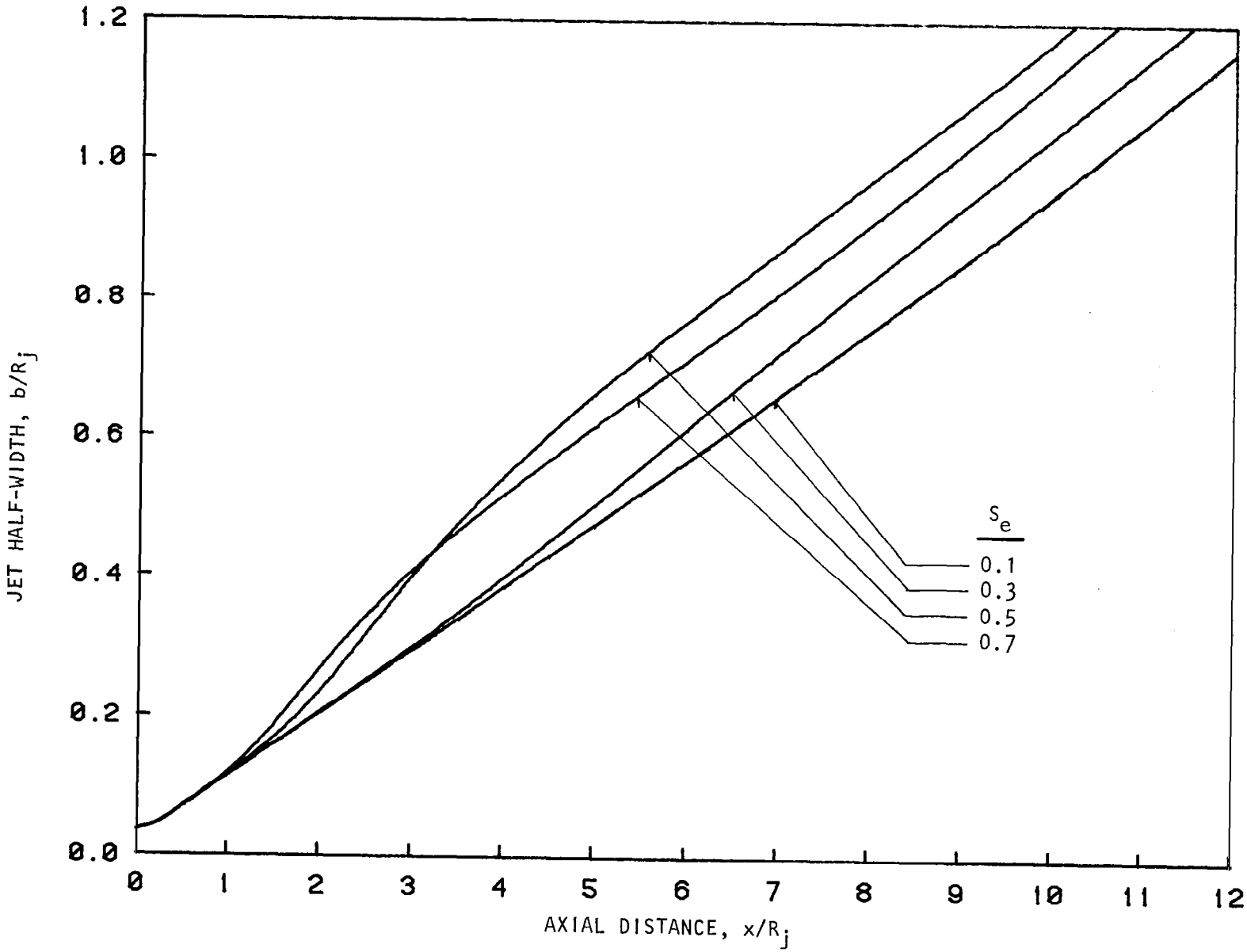

Figure 7.11 Predicted axial variation of jet half-width with excitation Strouhal number
ξ = 1.25, t_r/t_p = 1.0 (unheated), (0,0) Mode, L_e = 141 dB.

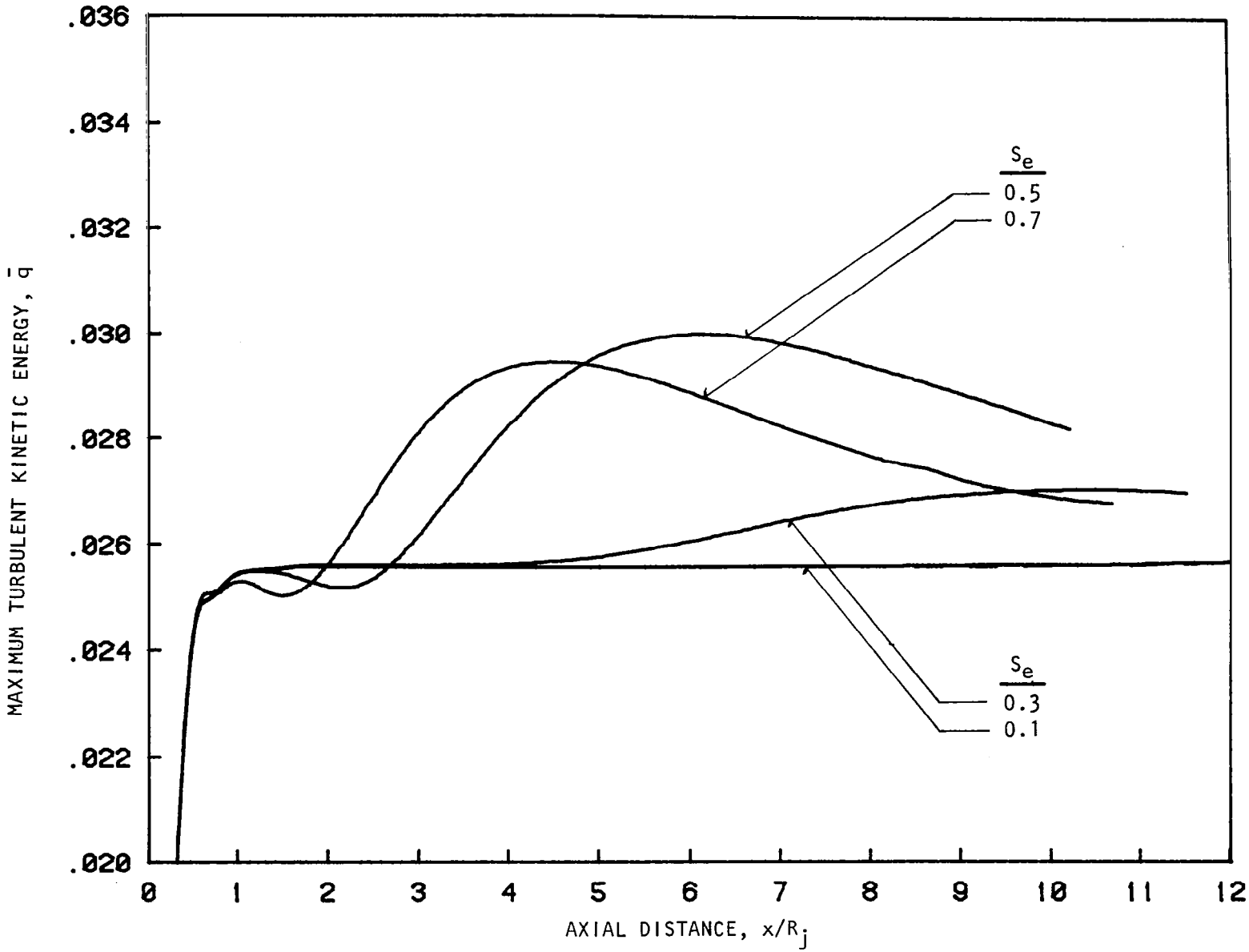

Figure 7.12 Predicted axial variation of maximum turbulent kinetic energy with excitation Strouhal number.
ξ = 1.25, t_r/t_o = 1.0 (unheated), (0,0) Mode, L_e = 141 dB.

slowly, the phase velocity, as measured, depends on the relative phase or radial distribution of the excited instability wave. This, in turn, is a function of the flow variable considered: velocity component or pressure, and the radial position. This effect is relatively small when the phase velocity is computed, but may be more significant if a calculated local growth rate is compared with its measured value. The variation of the phase velocity with axial distance for several values of S_e is shown in figure 7.13. The phase velocity initially decreases with axial distance, decreasing most rapidly at the highest excitation Strouhal number. Further downstream, the phase velocity begins to increase. This corresponds to the region in which the instability wave is decaying. It is important to note that at each axial location the variation of the phase velocity with S_e is different; though, in the initial mixing region of the jet, the trend is for a reduction in phase velocity with an increase in the value of S_e. Armstrong (ref. 45) found that in an unexcited jet this trend was reversed. He therefore argued that "the results of linear stability theory are perhaps better applicable to the turbulence structure of an (internally) acoustically forced jet than to that of an unforced jet." However if the arguments of Tam and Chen (ref. 34) are applied to the jet, one would expect the unforced structure to be dominated by the locally most-amplified normal modes. Though there are apparent differences between the forced and unforced jet's turbulence structure, further calculations are required before the relevance of linear stability theory to the naturally occurring turbulence may be determined.

7.2.4 Mach Number Effects

As the pressure ratio of the jet, for a fixed excitation level, increases, the ratio of the energy associated with the excitation to the mechanical energy of the jet decreases. In a nondimensional sense, the value of p_j decreases. Thus, even without a detailed knowledge of the receptivity of the jet or the growth rate of instability waves at higher Mach numbers, the effect of a fixed excitation level on the jet development might be expected to decrease as the pressure ratio is increased. This observation was confirmed in the present experiments and also those of Moore (ref. 6).

Figure 7.14 shows, by predicting the peak centerline pressure as a function of excitation level for several values of jet-pressure ratio, how the growth of an instability wave or large turbulent structure is influenced by the jet-pressure ratio. At a given excitation level, the peak centerline pressure decreases with increasing jet Mach number. This is a reflection of the reduced relative excitation level and a decrease in the rate of growth of the large turbulent structures as the pressure ratio increases. At a given jet-pressure ratio, the peak centerline pressure increases linearly with excitation level. Associated with this linear behavior are no observed changes in the jet development. As the excitation level increases, a departure from a linear response occurs. This nonlinear behavior is a result of an increase in the fine-scale turbulence levels, due to a transfer of energy from the finite-amplitude large turbulent structures, which leads to more rapid mixing and spreading of the jet, with a resulting decrease in the growth rate of the large turbulent structures.

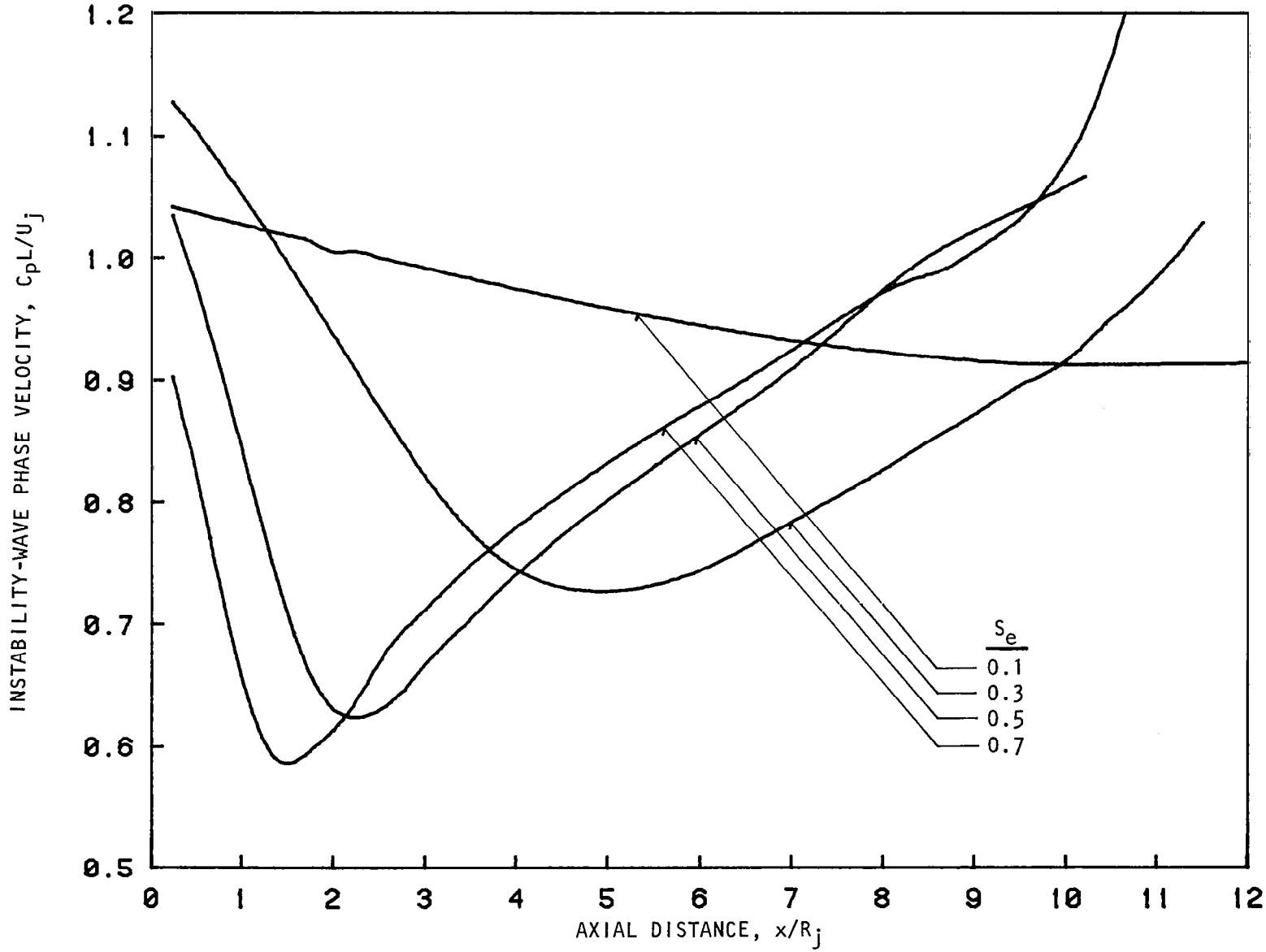

Figure 7.13 Axial variation of instability wave phase velocity with excitation Strouhal number.
ξ = 1.25, t_r/t_o = 1.0 (Unheated), (0,0) Mode, L_e = 141 dB.

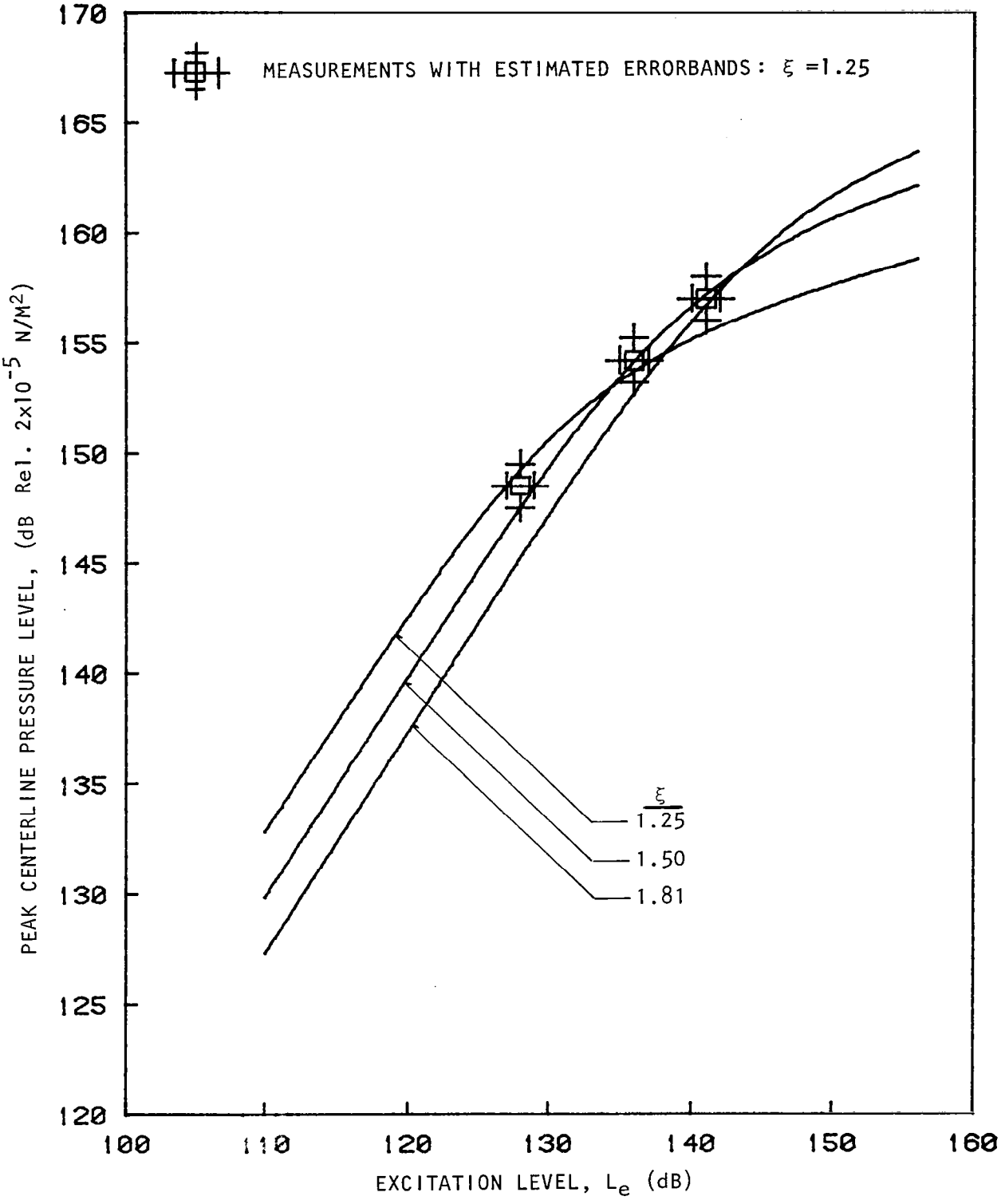

Figure 7.14 Effect of excitation level and Mach number on the peak centerline pressure level.
S_e = 0.5, t_r/t_o = 1.0 (Unheated), (0,0) Mode.

The departure from linear behavior occurs at an increasing value of excitation level as the jet pressure ratio increases. Thus at a fixed excitation level, nonlinear effects are more likely to occur at a lower value of jet Mach number. To see this increase in fine-scale turbulence levels, the variation of the peak turbulent kinetic energy with excitation level is shown in figure 7.15 for several values of jet pressure ratio. For a given pressure ratio, there is no change in the peak turbulent kinetic energy for low values of excitation. Beyond a certain threshold value, the peak turbulent kinetic energy increases. There appears to be no limit to this increase at very high levels of excitation. As the jet pressure ratio increases, the threshold level also increases -- indicating a higher excitation level to achieve the same peak turbulent kinetic energy as the pressure ratio is increased.

It should also be noted that the peak turbulent kinetic energy of the unexcited jet is predicted to decrease as the pressure ratio is increased. Moore (ref. 6) suggested, on the basis of observed changes in the broadband jet-noise radiation levels, that the threshold occurs at an excitation level equivalent to 0.08% of the jet dynamic head. This value is shown in figure 7.15, and the agreement with the predictions is very good. However, it is important to remember that the response of the jet to excitation is a function of the excitation Strouhal number, and the same result would not be achieved for other values of S_e. However, the prediction of the threshold level as a function of excitation Strouhal number presents no difficulties, and the results could be compared with the behavior observed in the present measurements or those by Moore (ref. 6, figure 39).

7.2.5 Temperature Effects

It has been calculated before (ref. 46) that as the total temperature of the jet is increased, at a fixed jet pressure ratio, the local growth rate of the instability waves or large turbulent structures increases. For the case of an unexcited jet, if the arguments of Tam and Chen (ref. 34) are extended to the jet, this would be expected to result in a more rapid mixing process. Figure 7.16 shows the axial variation of the jet half-width for both unexcited and excited jets for an unheated jet and for a jet with a total temperature ratio of 2.75. In the case of the unexcited jet, the jet is seen to spread more rapidly in the heated jet case. This is the effect of a significant variation in the jet density that appears in the integrals of equations (7-35). It should be noted that the shape of the mean velocity and turbulent kinetic energy are assumed to be unchanged. The rate of spread of the jet is predicted to increase further when the jet is excited. Though the absolute changes are different when heated and unheated jets are excited, the qualitative changes appear to be the same.

Figure 7.17 shows the axial variation of the maximum turbulent kinetic energy for the same conditions of heating. In the unexcited jet, the value of $\bar{q}$ is much greater. For the case of isotropic turbulence, the difference would be equivalent to a change from 13% to 15% in the turbulence intensity. The effects of the same excitation on both the heated and unheated jets is seen to be similar. The axial location of the peak in the turbulent kinetic energy is closer to the jet exit in the heated case. This is a result of

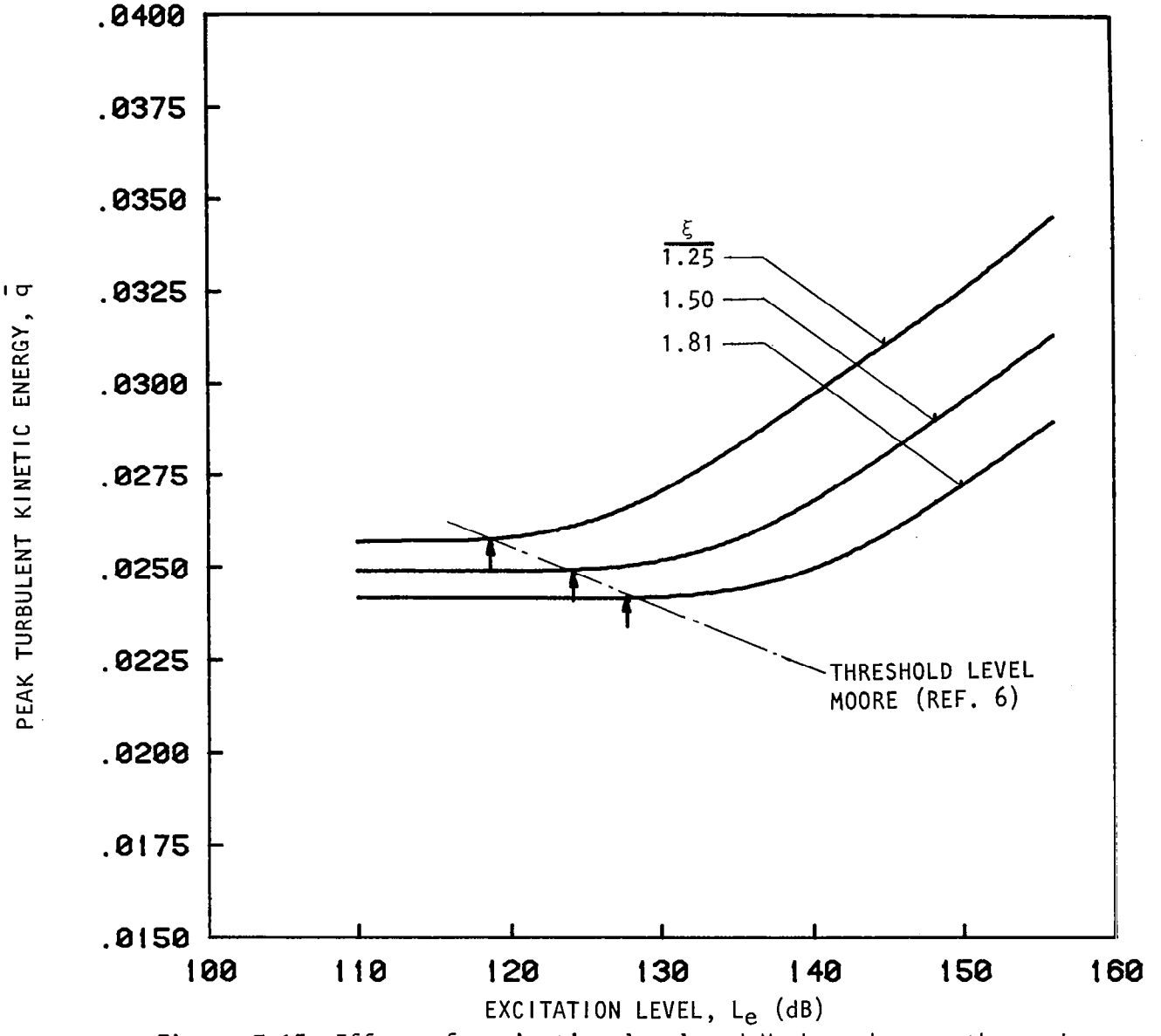

Figure 7.15 Effect of excitation level and Mach number on the peak turbulent kinetic energy.
S_e = 0.5, t_r/t_o = 1.0 (Unheated), (0,0) Mode.

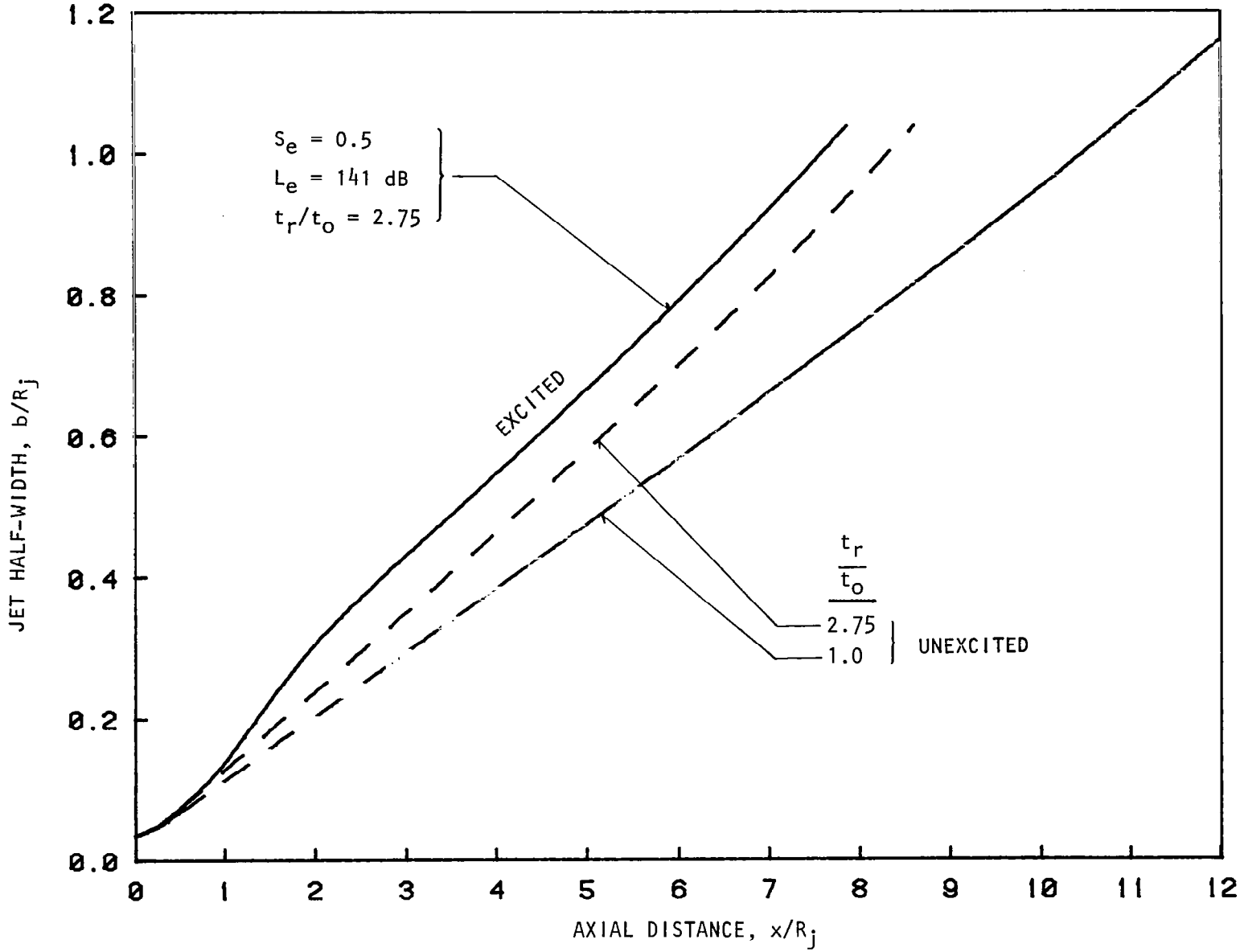

Figure 7.16 Predictied effect of excitation on jet half-width for heated jets.
ξ = 1.25, (0,0) Mode.

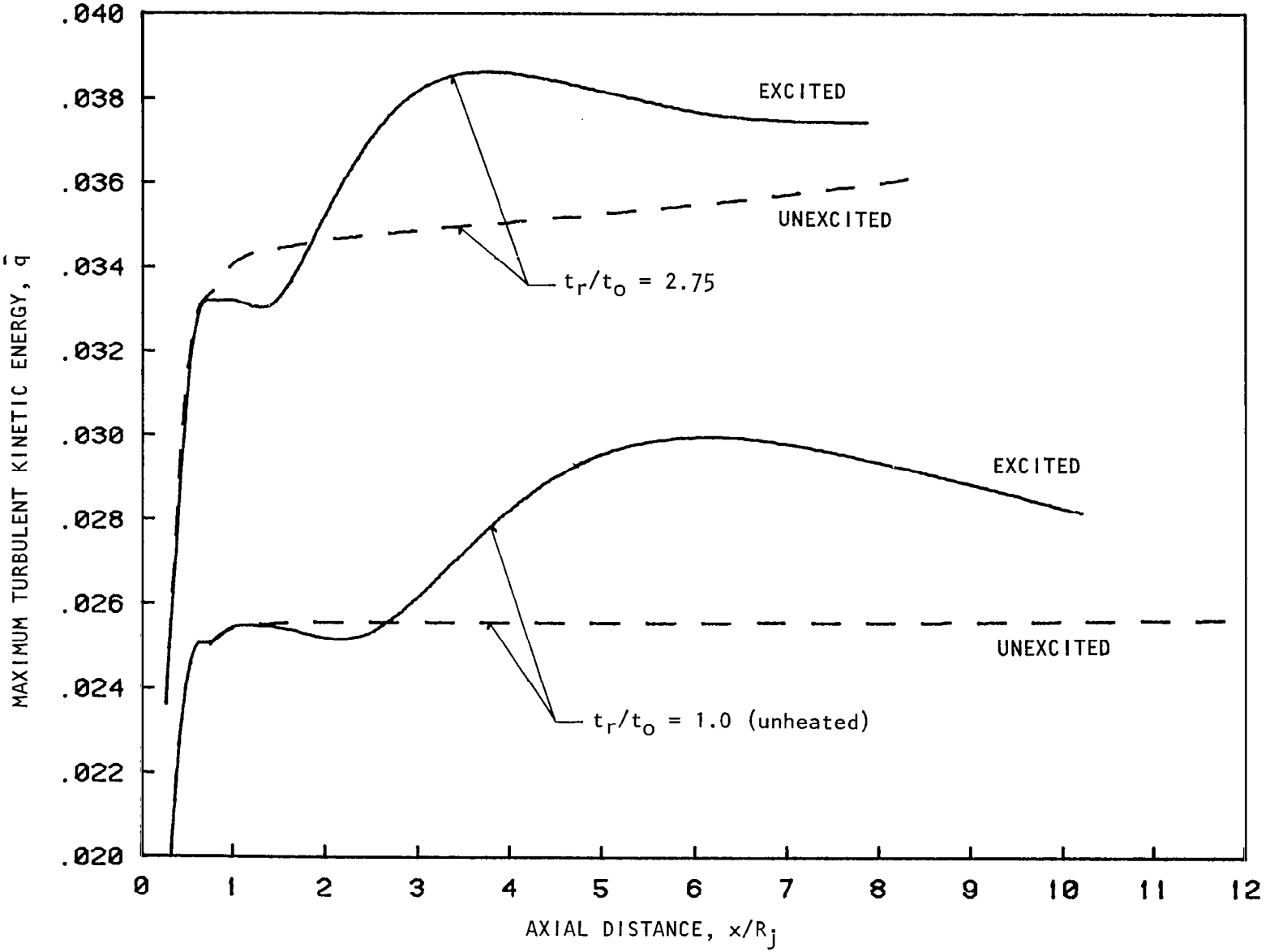

Figure 7.17 Predicted effect of excitation on the maximum turbulent kinetic energy for heated jets (ξ = 1.25).
L_e = 141 dB, S_e = 0.5, (0,0) Mode.

the greater jet spreading rate for these conditions. Since the dynamic head of the jet depends on the pressure ratio only, and is independent of the total temperature ratio, the threshold level might also be expected to be independent of the amount of heating. However further calculations are necessary to confirm this suggestion.

7.2.6 Mode-order Effects

As a final consideration, the effect of changing the mode number of the excitation is considered. For the axisymmetric or plane mode (0,0), the pressure fluctuation, associated with the excitation, is independent of radius within the duct, and its radial velocity is zero. As commented above, these properties are assumed to continue downstream of the nozzle in the jet flow. The other azimuthal mode to be considered is the helical (1,0) mode. For this mode, the pressure fluctuation is zero on the jet axis, and is a maximum along the jet lip line (according to the Born approximation). The radial velocity fluctuation is not zero, and both components of the jet receptivity problem must be included as described in section 7.1.1. The excitation level is defined as the maximum amplitude of the exciting wave at the jet exit. This value is thus given by the excitation amplitude at the jet lip.

Figure 7.18 shows the axial variation of the jet half-width for the same excitation level and Strouhal number, for both the plane and the helical mode. For these conditions, the increase in the jet spreading rate is greater for the plane mode. The same result is found if the maximum turbulent kinetic energy is considered. The increase in $\bar{q}$ is much less for the helical (1,0) mode. For this mode,the instability wave or large turbulent structures' pressure fluctuation is less than that for the plane mode excitation. Since the pressure fluctuation for the excited helical mode is zero on the jet centerline, a comparison may not be made meaningfully at that radial location. The pressure fluctuations have been compared at the edge of the potential core. This is shown in figure 7.19. The peak amplitude reached by the excited (1,0) mode is approximately 10 dB less than the plane mode. In the early stages of the instability wave growth, the two modes parallel each other indicating that it is not the rate of growth of the two modes that is different but the jet receptivity.

As with the other effects that have been discussed above, it is difficult to draw firm conclusions by making parametric changes along single lines in the parameter space when the bahavior is clearly a function of all the parameters simultaneously. For the case of the effect of mode number, for example, the instability wave or large turbulent structures at lower excitation Strouhal numbers continue to grow past the end of the potential core (ref. 47), whereas all the plane modes are decaying in this region. The flow development downstream of the end of the potential core has not been included in the present calculations, but it appears likely that a (1,0) mode excitation will have the greatest effect in this region.

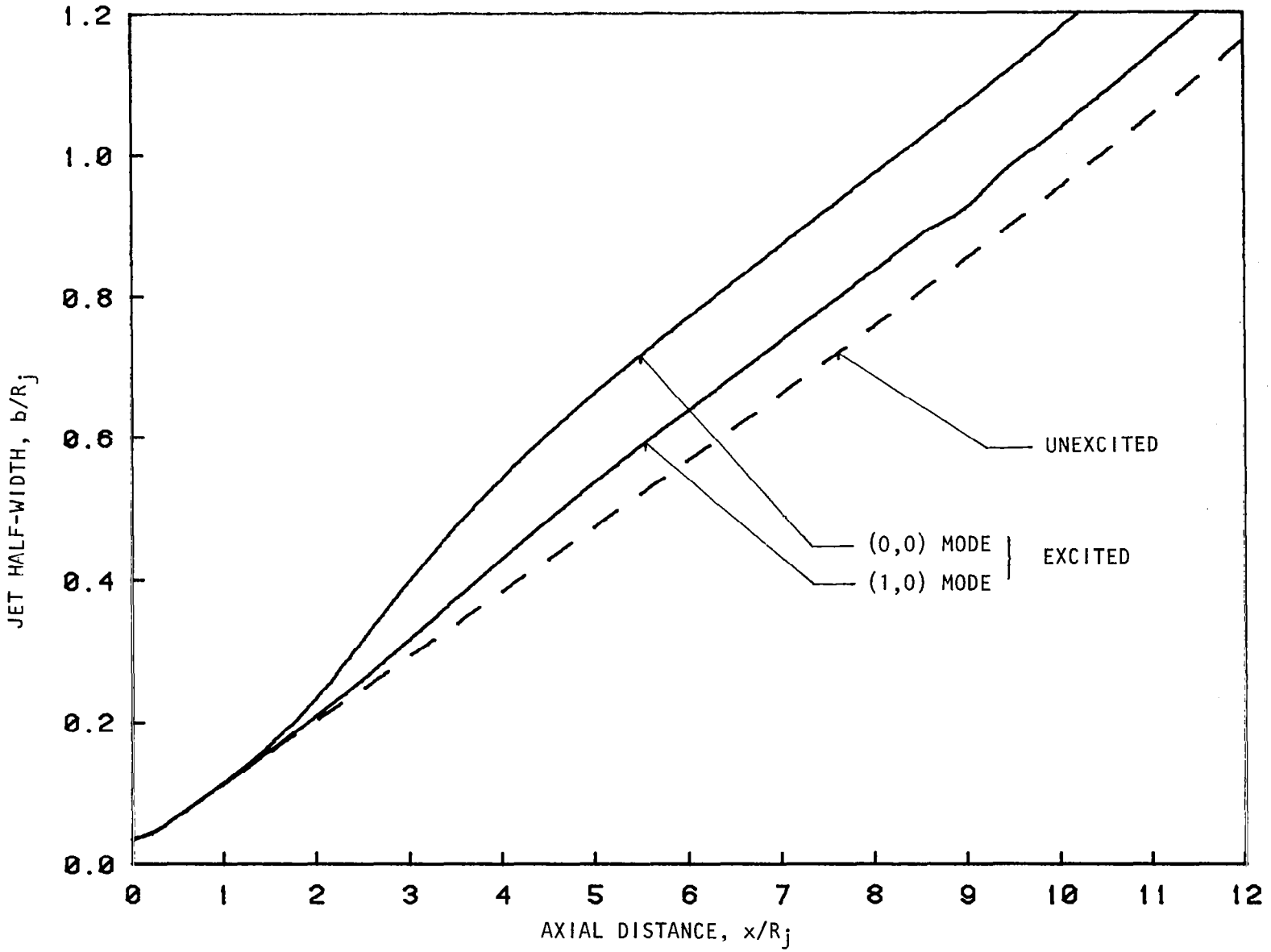

Figure 7.18 Predicted effect of excitation mode number on the jet width $\xi = 1.25$, $t_r/t_o = 1.0$, $L_e = 141$ dB, $S_e = 0.5$.

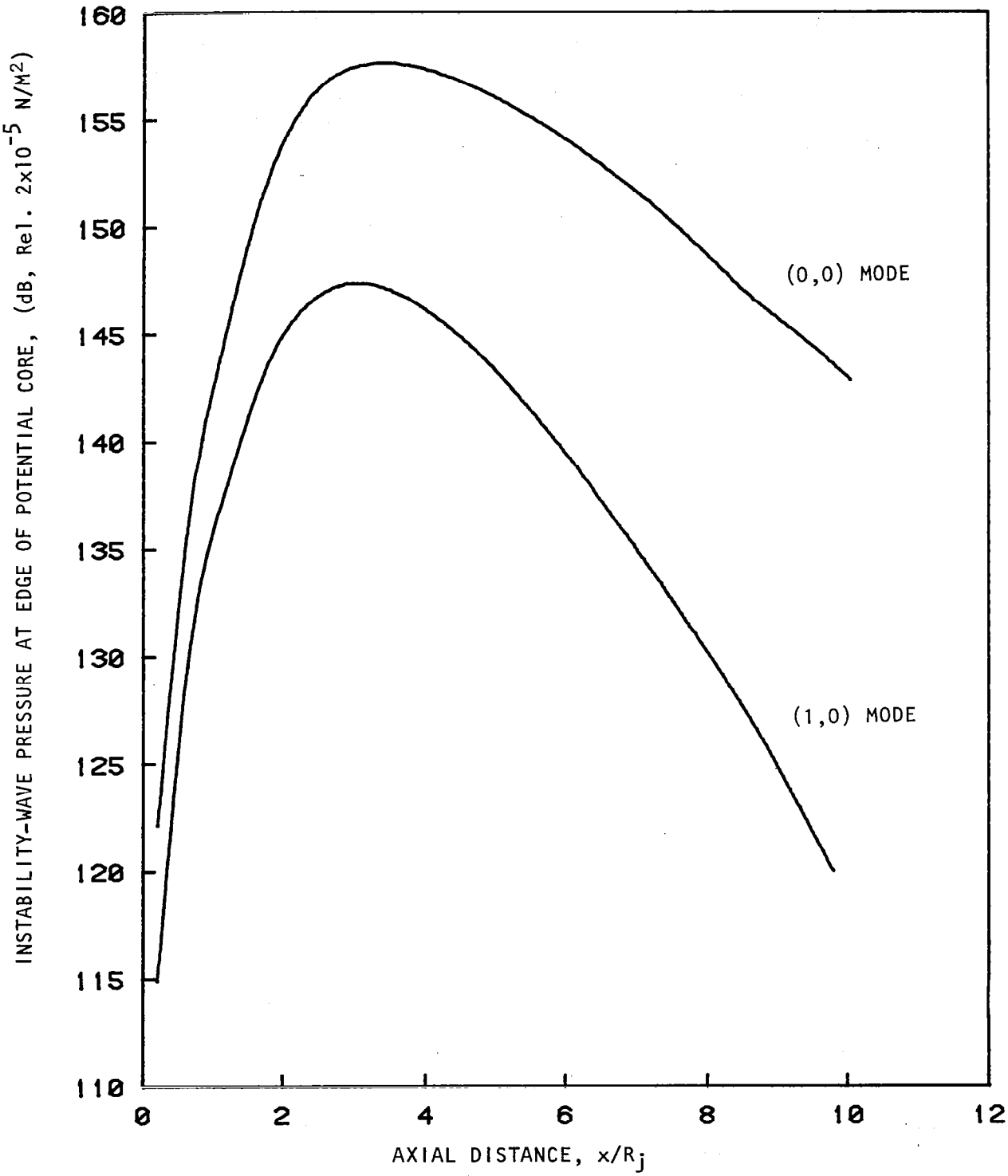

Figure 7.19 Predicted effect of the excitation mode number on the axial variation of the excited instability wave.
ξ = 1.25, t_r/t_o = 1.0, L_e = 141 dB, S_e = 0.5 .

7.2.7 Interaction of Excitation and Instability Wave

In the results presented so far, the amplitude of the excited instability wave and the propagating acoustic wave have been shown separately as, for example, in figure 7.8. This is justified as the relative magnitudes of the two waves are usually well separated. However, in certain special cases this separation in magnitude is not present, and the measured axial variation in the pressure is the sum of the two components. Such a set of measurements was obtained by Moore (ref. 6) for a low jet velocity, $U_j = 0.15\ a_o$ and a high excitation Strouhal number, $S_e = 0.98$. The measurements are shown in figure 7.20. For the case of no flow, the acoustic pressure decays in the usual fashion along the jet centerline. However, when the excitation is applied, a series of peaks and troughs appears. In the upper portion of figure 7.20, the predictions using the present analysis are shown. The acoustic excitation is seen to decay slowly along the jet axis. The excited instability wave grows rapidly in the initial region of the jet, and then also decays slowly. The amplitudes of both the excited and excitation wave are of the same order of magnitude for most of the potential core. Thus the measured pressure is the sum of the two components with account to be taken of their relative phases. The wavelength of the acoustic wave, for a Strouhal number of 1.0, is given by

$$\lambda = 2.0 \frac{a_o}{u_j} R_j \tag{7.43}$$

which for this case is about $13.0R_j$. The wavelength of the excited instability wave is about $2.0R_j$; thus their sum involves successive addition and cancellation every two radii. The calculated sum is also shown in figure 7.20. The predicted behavior is seen to match the measured effects very closely. To ensure that the amplitude of the two waves was of the same order, it is necessary to assume a larger value of initial jet width, $b_o = 0.085$. However, this appears justified in view of Moore's experimental facility. The excellent agreement between the measurements and the predictions is felt to give overwhelming confidence that the physical model chosen in the prediction scheme here is correct.

7.3. FLIGHT EFFECTS

When a jet is in flight, the external flow introduces important modifications to its mean-velocity profile. This in turn brings about significant changes in the characteristics and development of the large-scale as well as fine-scale turbulence in the mixing layer of the jet. As a result, the phenomenon of broadband noise amplification due to upstream tone excitation becomes far more complicated than in the static case. Because of the limitation of time and manpower resources available to the present project, theoretical investigation on the effects of flight has been

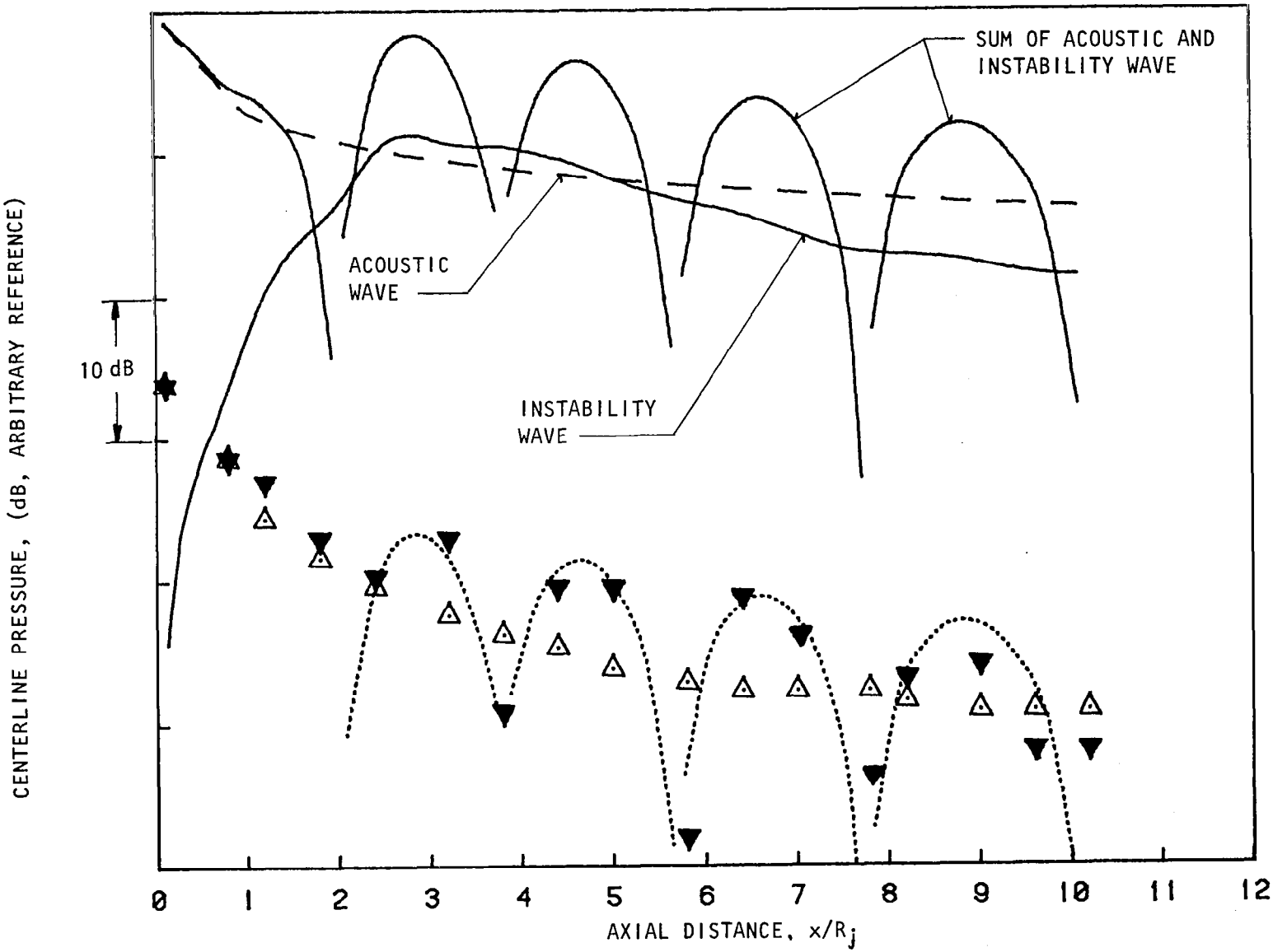

Figure 7.20 Prediction (- - -, ——) of centerline pressure fluctuation as sum of acoustic wave and excited instability wave and comparison with measurements (△,▼) by Moore (ref. 6).
△, No flow; ▼, $u_j = 0.15\ a_o$, $S_e = 0.98$; ..... , prediction: $U_j = 0.15\ a_o$; St = 1.0.

somewhat restricted in scope. Quantitative analysis has been carried out only with respect to certain specific isolated aspects of the overall processes. Based on these separate investigations, qualitative conclusions regarding broadband-noise amplification by upstream-tone excitation, however, will be provided at the end of this subsection.

7.3.1 Mean-Velocity Profiles

When a jet is in flight, an external boundary layer develops on the nozzle. Because of this boundary layer, the full effect of flight is not felt by the jet flow until a distance of one or two diameters downstream of the nozzle exit. This distance depends strongly on the boundary-layer thickness. Immediately downstream of the nozzle exit a wake-like flow region develops. This wake-like mean flow characteristic is extremely important and because of it, the jet behaves very much like that in a static environment.

Measurements of the initial jet-velocity profiles have been carried out by Morris (ref. 48). Based on his data, the axial-velocity profile can be adequately approximated by the following analytical functions. These functions are also shown graphically in figure 7.21.

$$\bar{u}(r) = \begin{cases} 1 & r \le h \\ \bar{u}_g(r) + \bar{u}_s(r) & h < r \le h_f \\ \bar{u}_f & h_f < r \end{cases} \qquad (7\text{-}44)$$

where $\bar{u}_f$ is the flight velocity, and

$$\bar{u}_g = (1.0 - u_*) \exp\left[-\ell n(2) \left(\frac{r-h}{b}\right)^2\right]$$

$$\bar{u}_s = \begin{cases} u_* + \dfrac{\bar{u}_f - u_*}{2b_f(h_f - h - b_f)^2}\left[(5b_f - 2h_f + 2h)(r-h)^2 + \dfrac{2(h_f-h)-4b_f}{h_f-h-b_f}(r-h)^3\right] & ; \; h \le r \le (h_f - b_f) \\ \bar{u}_f - \dfrac{(\bar{u}_f - \bar{u}_\alpha)}{2b_f^2}(r - h_f)^2 & ; \; (h_f - b_f) < r \le h_f \end{cases}$$

$$\bar{u}_s = 0 \text{ for } u_x > \bar{u}_f$$

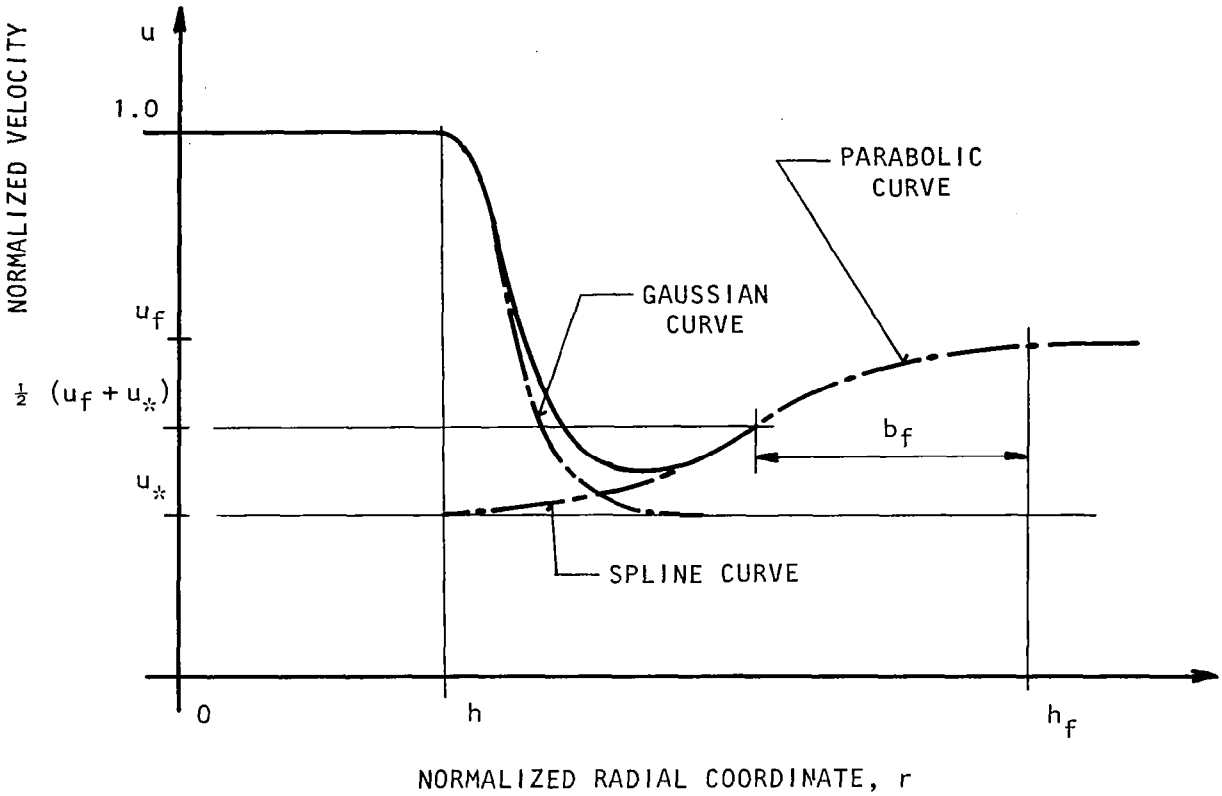

Figure 7.21 Schematic diagram of equation(7-44)indicated by the solid curve.

Inside the mixing layer, equation (7-44) consists of a linear superposition of two functions $\bar{u}_g$ and $\bar{u}_s$-- representing the inner and outer portions of the mixing layer. $\bar{u}_g$ is the usual Gaussian profile of a jet characterized by the parameters h and b as in equation (7-1).

$\bar{u}_s$ is the outer mixing-layer velocity profile. Here, it is divided into two segments, joined together at $r = h_f - b_f$, and has continuous first derivative. The outer segment is approximated by a parabolic curve with zero slope at $r = h_f$, the outer edge of the mixing layer. The inner segment consists of a spline curve with velocity equal to u_* at the edge of the potential core $r = h$.

The parameter u_* is a measure of the velocity defect of the wake-like flow of the mixing layer. When u_* is equal to $\bar{u}_f$, the flight velocity, the outer mixing layer of equation (7-44) vanishes, and the jet attains a fully-developed mixing-layer velocity profile with respect to the external flow. Figure 7.22 shows a comparison of equation (7-44) with the measured data given in reference 48 for a jet with Mach number 0.47 and flight velocity 0.384. In this figure the following values have been used to obtain a good fit to the measurements.

$$h = 0.96, \quad b = 0.04, \quad u_* = 0.2$$
$$h_f = 2.3, \quad b_f = 1.0$$

It can be seen from this figure that equation (7-44) can indeed fit the measured initial velocity profile of a jet under flight simulation quite well. In all the subsequent computations of this section, the jet-velocity profile will be assumed to be that given by equation (7-44) unless stated otherwise.

7.3.2 Growth Rate of the Excited Large-Scale Instability Waves

The presence of an external flow reduces the average velocity shear-gradient across the mixing layer of the jet. As a result, the growth rates of the excited large-scale instability waves are expected to be reduced. Slightly downstream of the nozzle exit, the inner mixing layer is thin, and the instability-wave motion is confined to a small thickness in the radial direction. If the external boundary layer of the nozzle is sufficiently thick, the presence of the external flow will, therefore, not be felt directly except through the reduction in the velocity-shear of the inner mixing layer. For a given jet-flow condition and excitation Strouhal number, the growth rate of an excited instability wave can be calculated quantitatively by solving the eigenvalue problem of equation (7-15) and boundary condition (7-16). A typical example of the reduction in growth rate, as the flight velocity increases, is given in figure 7.23. In this figure, it is assumed that u_* is equal to $0.3\ \bar{u}_f$. As can be seen in this figure, the reduction in spatial-growth rate is nearly proportional to the flight velocity. The implication of the reduction in growth rate of the excited instability waves due to flight effect on the broadband-noise amplification phenomenon will be discussed later.

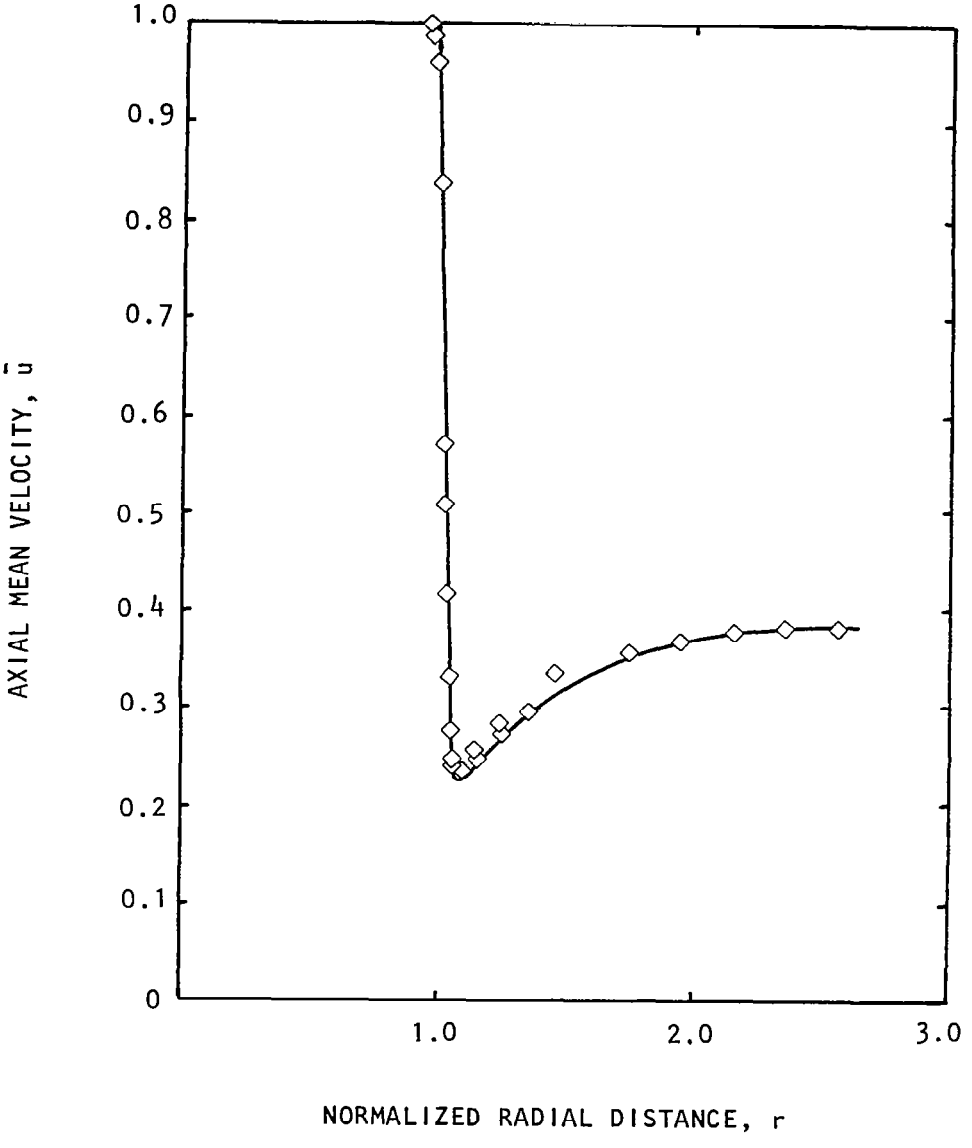

Figure 7.22 Initial velocity profile. $M_j = 0.47$, $\bar{u}_f = 0.384$, $x = 0.2$ ——, equation (7-44) with $u_x = 0.2$; $h_f = 2.3$; $h = 0.96$, $b_f = 1.0$, and $b = 0.04$; ◇, measurements (ref. 48)

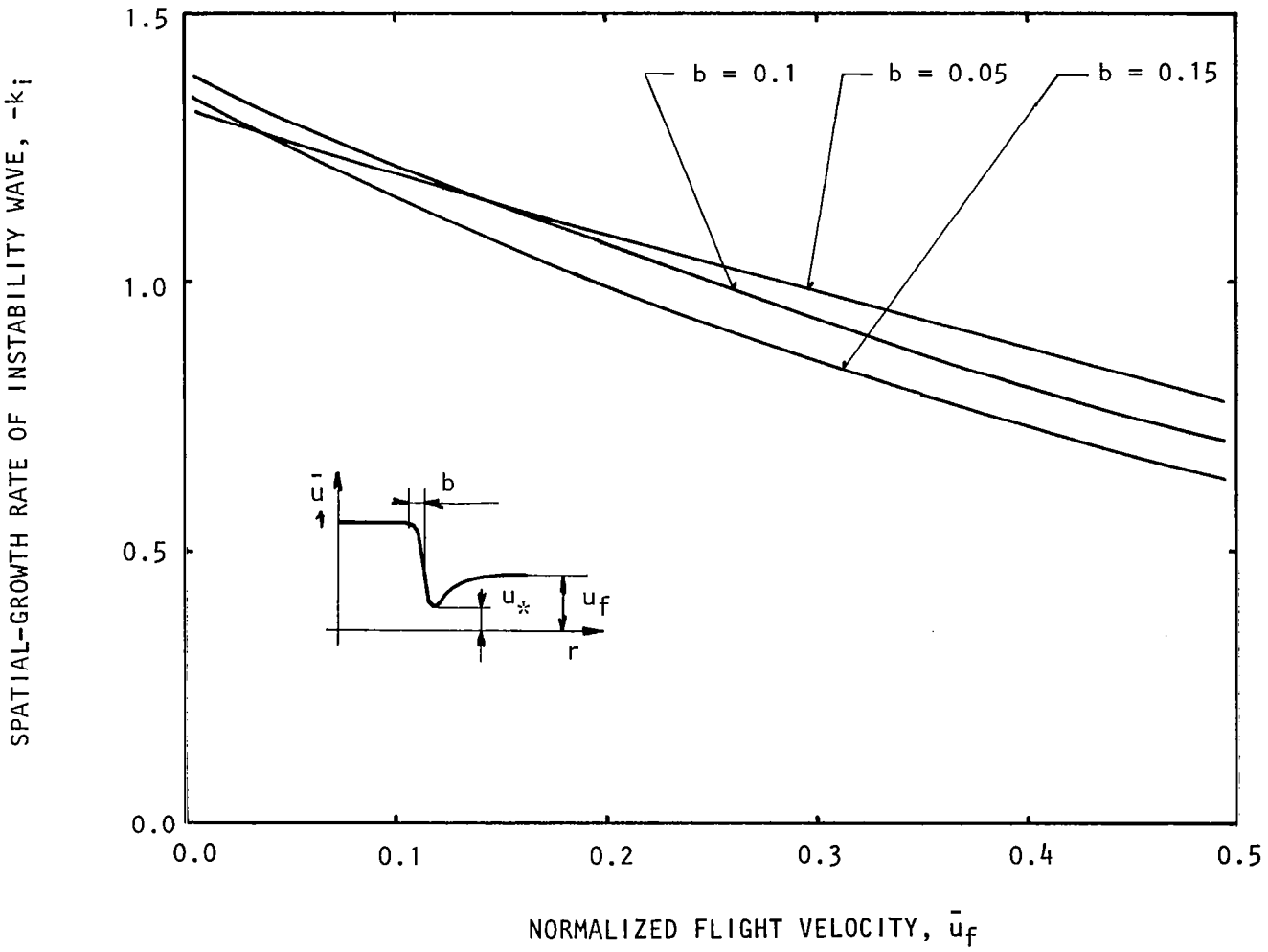

Figure 7.23 Reduction of growth rate as flight velocity increases.
$\xi = 1.25$, (0,0) Mode, $S_e = 0.5$, $U_* = 0.3\ \bar{u}_f$, $t_r/t_o = 1.0$ (Unheated).

7.3.3 Receptivity

As has been noted above, at the nozzle exit, the mean-velocity profile of a jet in flight is practically the same as in the static case provided the external boundary layer is reasonably thick. Thus, in the initial region of the jet, where the coupling between an upstream tone and the excited instability wave is most effective, it appears that the effect of flight is insignificant. If this is true, the amplitude of the excited instability wave in this region will be the same as that in the static case. To test this hypothesis, the analysis of subsection 7.1.1 has been extended to the case of flight using the mean-flow profile of equation (7-44). From equation (7-35d), the complex amplitude of the excited instability wave is given by the solution of the equation

$$\frac{dA}{dx} = ikA + C_p \hat{p} \tag{7-45}$$

for plane-wave excitation. In equation (7-45), k is the eigenvalue (the complex wave number) of the instability wave, and C_p is the pressure coupling coefficient. Over the initial region of the jet, the values k and C_p do not change appreciably. Further, if the Born approximation is invoked, $\hat{p}$ may be regarded as a constant. Within these approximations the solution of (7-45), satisfying initial condition (7-38c), is

$$A(x) = \frac{C_p}{ik} \left(e^{ikx} - 1\right) \tag{7-46}$$

It is seen from equation (7-46) that the unstable component of the excited wave, effectively, has an initial amplitude of

$$|A(0)| = \left|\frac{C_p}{k}\right| \tag{7-47}$$

Therefore, by computing the right-hand side of equation (7-47), it is possible to assess the effect of flight on the initial amplitude of the unstable component of the excited wave.

Figure 7.24 shows a typical example of the variation of the initial amplitude of the unstable component of the excited wave with respect to the forward flight velocity $\bar{u}_f$. In this example, an unheated jet with a Mach number of 0.575 has been used. The values of the pertinent mean flow parameters are,

$$b = 0.05, \quad h_f = 2.3, \quad b_f = 1.0, \quad u_* = 0.3\ \bar{u}_f$$

Thus, it is seen that over the flight-velocity range of $0 \leq \bar{u}_f \leq 0.5$ and Strouhal number range of $0.3 \leq S_e \leq 1.0$, for which the jet is most sensitive

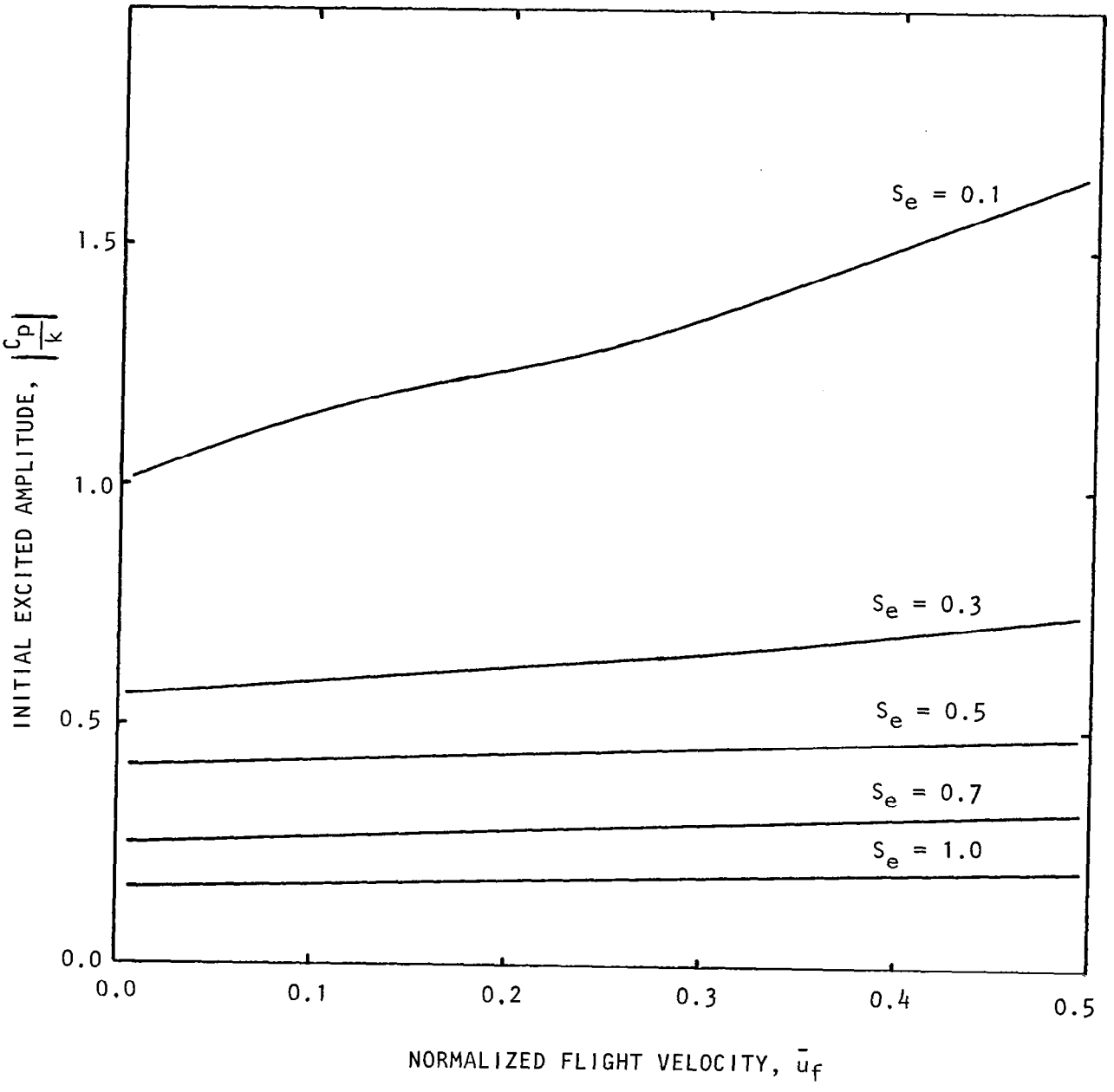

Figure 7.24 Initial amplitude of the unstable component of the excited wave. Plane wave mode. b = 0.05, M_j = 0.575, t_r/t_o = 1.0.

to excitation, the initial amplitude of the instability wave is, for all intents and purposes, independent of the flight speed. Figure 7.25 shows the computed results for a heated jet with $t_r/t_o = 2.7$. If consideration is limited to forward flight velocity not exceeding 0.4, then the same conclusion also holds. Equations (7-45) and (7-46), strictly speaking, are applicable only if the upstream tone is of the plane-wave mode. However, upstream of the nozzle exit, the radial velocity associated with the tone must be zero at r = 1, in order to satisfy the boundary condition at the nozzle wall. Therefore, at distances slightly downstream of the nozzle exit, it is expected that the radial velocity fluctuations due to the upstream tone at the edge of the potential core are small. That is to say, over the initial region of the jet, the velocity coupling between the tone and the instability wave is weak compared to the pressure coupling. Keeping this in mind, it is clear that equation (7-47) can also be used to estimate whether forward flight has any significant influence on the receptivity problem for upstream tones consisting of higher-order spinning modes. Figure 7.26 is a plot of the values of $|C_p/k|$ as a function of $\bar{u}_f$ at different Strouhal numbers for the helical (1,0) mode. Again it is seen that within the parameter range stated above, the initial amplitude of the unstable wave component is practically independent of the flight speed. Thus, it is possible to say that because of the existence of an external boundary layer outside the nozzle, the forward flight effect (up to $\bar{u}_f = 0.5$) has only a limited influence on the receptivity of large-scale instability waves of a jet to upstream tones. This is true for hot or cold jets, and for plane waves or higher-order modes of excitation within the sensitive Strouhal number range of the jet.

7.3.4 Effect of Flight on Broadband Noise Amplification

The evolution of the excited large turbulence structures in a jet is controlled by several factors. These factors are: (1) the initial amplitude of the unstable component of the excited wave, (2) the spatial growth rate, and (3) the available distance for growth. The first two factors have been discussed above. With an external flow, the average velocity gradient across the mixing layer of a jet is reduced. It follows, therefore, that the rate of mixing is also reduced, resulting in a longer jet-core region over which instability waves can grow. Thus, although the effect of flight decreases the spatial-growth rate of the excited large-scale instability waves, they can grow over a longer distance. The net result of these two compensating effects together with the limited influence of flight on receptivity is that the large-scale instability waves grow to about the same amplitude in both the flight and the static case. Because of this, it is expected that the increase in fine-scale turbulence would most likely be about the same in both cases. The practical implication of this is that the total increase of broadband noise of a jet due to upstream tone excitation is nearly independent of flight velocity. This is one of the main results of this subsection. Of course, the external flow would modify the angular distribution of the radiated noise intensity due to the shrouding effect. A detailed investigation of this aspect of the noise-amplification phenomenon is, however, beyond the scope of the present study.

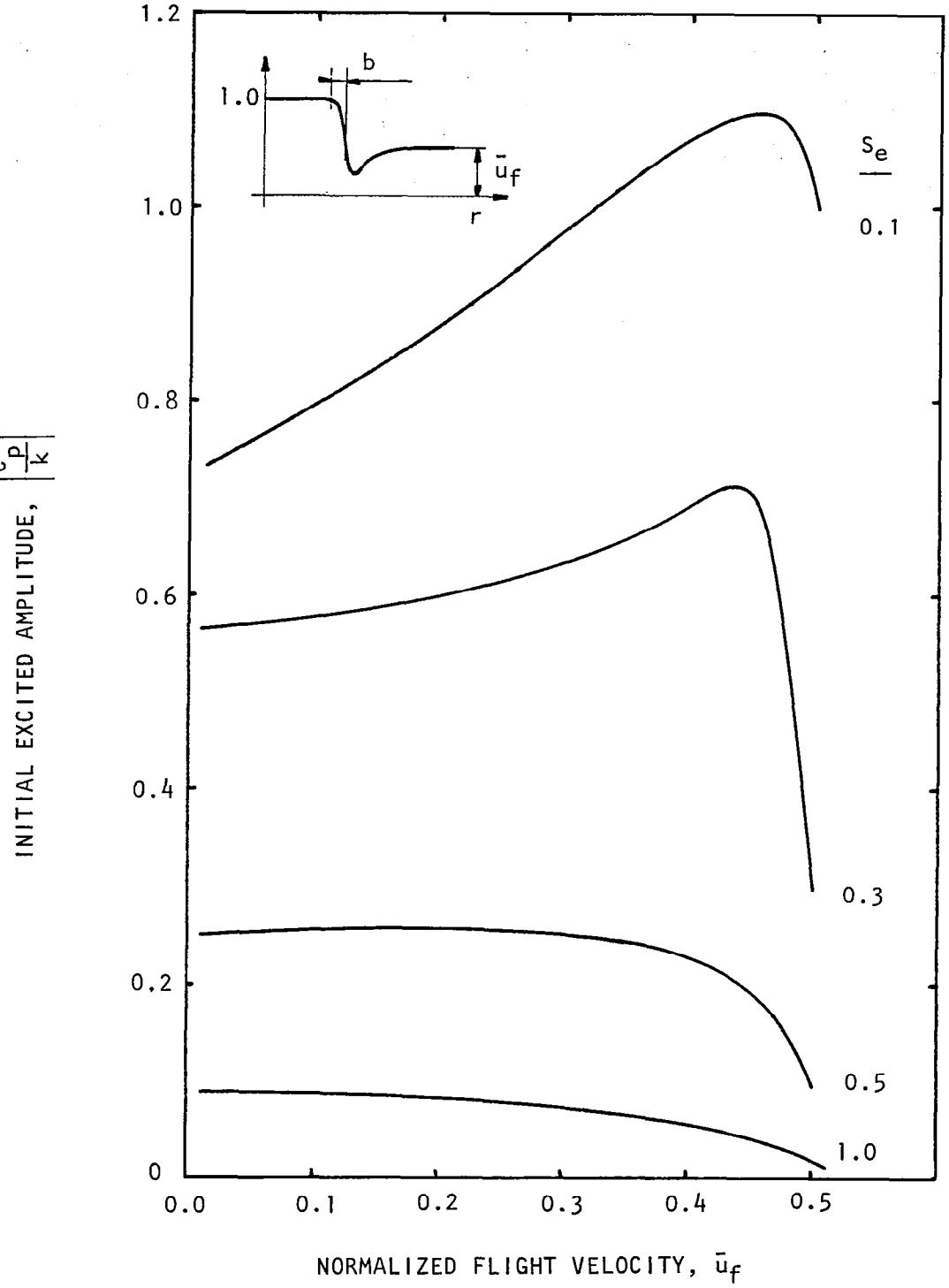

Figure 7.25 Initial amplitude of the unstable component of the excited wave in heated jets.
$t_r/t_o = 2.7$

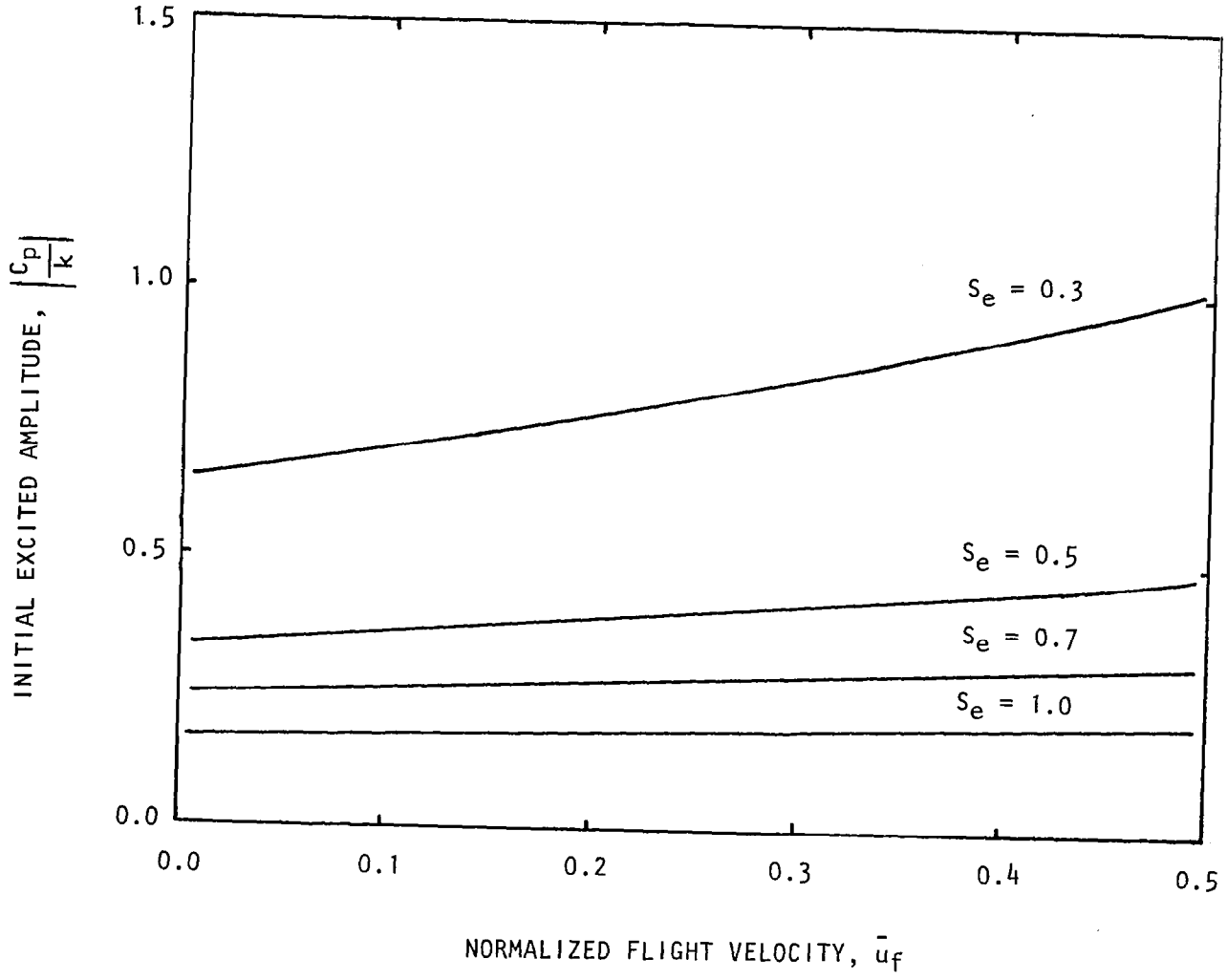

Figure 7.26 Initial amplitude of the unstable component of the excited wave. t_r/t_o = 1.0, (1,0) Mode.

8.0 CONCLUSIONS

A fairly detailed study to understand the phenomenon of broadband jet-noise amplification has been carried out. This has been achieved by acquiring simultaneous acoustic, mean velocity, turbulence, and instability-wave pressure data with and without forward velocity effects. Some optical data have also been qcquired to improve the understanding further. Limited data for heated jets have also been obtained.

A theoretical model has been developed as a part of this study to explain the jet-noise amplification phenomenon, and is described in section 7.0. After all the experimental results and the theoretical models are put together, the jet-noise amplification can be fairly well described by the schematic representation shown below in figure 8.1.

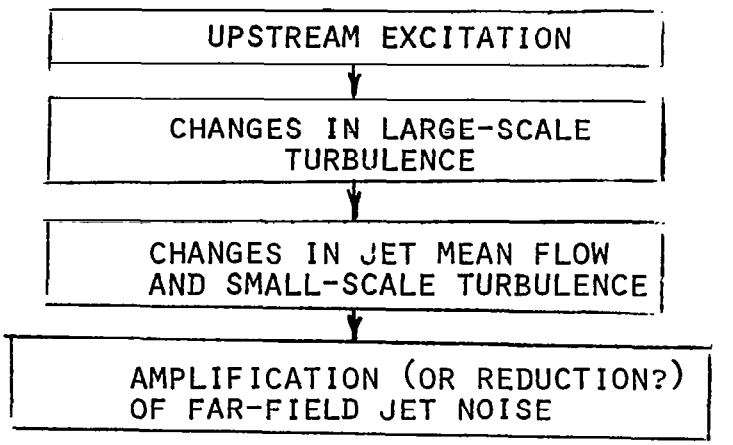

Figure 8.1 Schematic representation of jet noise amplification by upstream excitation

The first part of the problem concerns the excitation of the large-scale turbulence structure. It is now well known that these large-scale structures are an inherent part of a fully-developed turbulent free-shear flow. When a shear layer is excited by discrete-tone sound waves of appropriate frequency, not only is the randomness of the large-scale turbulence structure drastically reduced, but also its amplitude is greatly enhanced.

The second part of the process involves the coupling between the large-scale structure and the fine-scale turbulence based on the premise that even in the unexcited jet, these two are intimately related. Thus, if the large-scale structure controls the mixing process (with ambient air), and hence the mean and turbulent flow properties in an unexcited jet, then the augmented large-scale structure in an excited jet can be expected to produce significant changes in the fine-scale turbulence values, as indeed seen in this study.

The final link in the process concerns the raltionship between the jet-flow characteristics and the noise radiated to the far-field. Here, on the basis of classical aerodynamic noise theories, it is straightforward and logical to infer that an excited jet with significantly modified mean flow and turbulence levels will generate different noise levels compared with those of an unexcited jet.

As mentioned in section 2.0, the existence of the changes in large-scale and small-scale jet flow properties, with upstream excitation, is acknowledged widely by jet noise researchers, but when it comes to the changes in noise fields between unexcited and excited jets, two schools of thought have clearly emerged recently. In one case, it is argued that the increase in jet noise is a direct result of the amplified large-scale turbulence while the small-scale turbulence plays a relatively weaker role in the noise generation process. This is the explanation put forward in a recent theoretical study by Ffowcs Williams and Kempton (ref. 13). On the other hand, the position taken by other researchers places more importance on the increase in small-scale turbulence in an excited jet. Here, it is argued that although the phase-locked large-scale turbulence structure is at the root of the noise amplification process, the actual noise generation mechanism lies in the small-scale turbulence.

Based upon our results we support the second explanation for two reasons. First, except for heated jets or unheated jets with relatively high supersonic jet Mach numbers (M_j>1.5), the phase velocity of the excited large-scale instability waves is subsonic relative to the ambient fluid. It can be shown theoretically (refs. 14,38) that such subsonic instability waves are very inefficient in generating sound waves directly. Second, the broadband jet noise observed in these experiments and in those of others (refs. 5,6,9) is almost uniform at all frequencies. If it were the large-scale structure that was directly responsible for the noise amplification, the noise increase would occur only over a narrow frequency band, centered around the natural frequency of the instability wave, which will also correspond to the frequency of excitation.

The above statements are further confirmed if the peak turbulence intensities associated with the large-scale structure and the small-scale structure are plotted against forward velocity as shown in figure 8.2. It is seen here that for a given upstream excitation level of 141 dB, the change in the large-scale turbulence is negligible with forward velocity, but the small-scale turbulence decreases with increasing forward velocity, both for the unexcited as well as the excited jet. As expected, the small-scale turbulence levels are higher for the excited jet; the effect of forward velocity is similar to that for the unexcited jet. It is noticed that the difference between the turbulence-intensity levels for the excited and unexcited conditions does not alter significantly with forward velocity. Also, since the corresponding difference in far-field noise also did not change significantly, it is reasonable to conclude that, ultimately, it is the changes in small-scale turbulence that are responsible for jet-noise amplification.

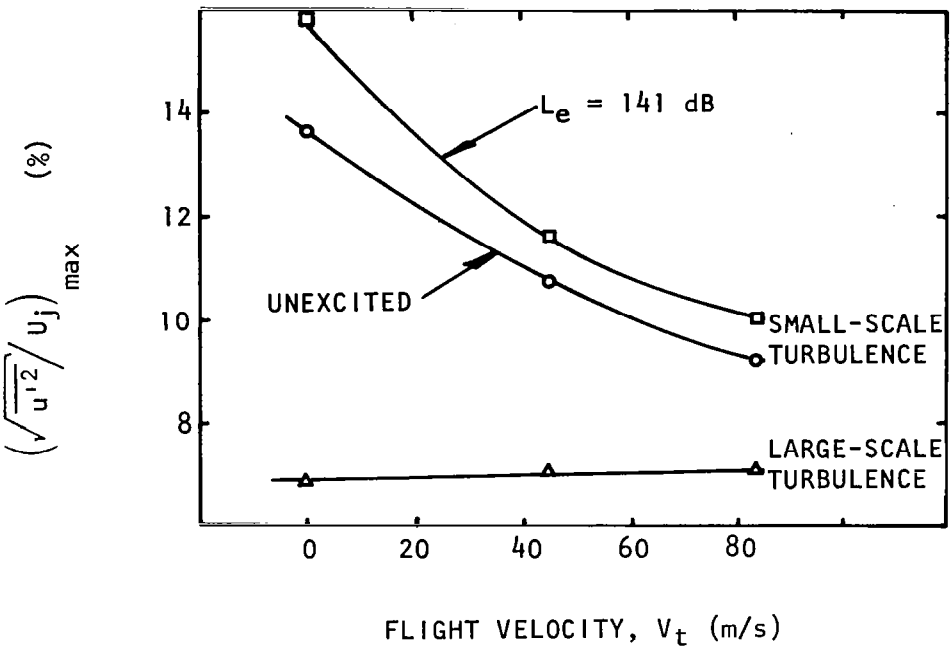

Figure 8.2 Variation of peak centerline turbulence intensities with forward velocity, V_t. M_j = 0.58, U_j = 190 m/s, Unheated, S_e = 0.5, (0,0) mode.

Following these conclusions of general nature some specific conclusions, derived mostly from the results for the unheated jets, can be listed as follows:

1. Excited large-scale structure indeed exists within extremely narrow band of frequency, and its center frequency is equal to that of the excitation signal itself.

2. The preferential Strouhal number at which maximum broadband jet-noise amplification is obtained (at a fixed excitation level) lies between 0.4 and 0.8, depending upon whether one is considering 1/3-octave band SPLs and PWLs, or the OASPLs and OAPWLs, or for that matter the angle of noise measurements. S_e = 0.5 can be considered to be a reasonable mean Strouhal number for maximum amplification.

3. With increasing excitation levels: (a) the mean velocities decay faster, (b) turbulence intensities increase, and (c) broadband jet-noise amplifications increase.

4. Threshold levels for jet-noise amplification can be taken to be 0.08% of the jet dynamic head, but only for the unheated jets.

5. For a fixed excitation level, jet noise amplification decreases as the jet Mach number increases.

6. Limited data acquired for the heated jets showed little effect of upstream excitation on broadband jet noise.

7. Excited large-scale structure amplitudes are not affected by flight velocity.

8. Broadband jet-noise amplification is the same for static and the flight case, thus indicating that the relative-velocity effects are the same for the excited and the unexcited jets.

9. It is the small-scale turbulence, and not the large-scale turbulence, that generates the additional broadband noise upon excitation by upstream discrete tones.

The present study has thus answered the two questions posed at the outset (see page 5). The study has also made it clear that if the internal noise levels in a real aircraft engine are high enough, broadband jet-noise amplification could easily account for the discrepancies between the results from well designed model-scale jets and full-scale engines whether tested statically or in flight.

APPENDIX A

DETECTION OF THE MODE STRUCTURE AT THE NOZZLE EXIT

Before incorporating the method of mode detection given in subsection 3.4.1, it was necessary to know the precise levels of the acoustic pressures at each of the 12 locations around the inner periphery of the nozzle exit, as sensed by the miniature, Knowles microphones (see figure 3.3). Since the signals at these microphones were contaminated with flow noise and other background noise sources, cross-spectra between the microphone signal at each location and the electronic signal fed to the acoustic drivers were obtained. After suitable number of ensemble averaging, and by measuring the amplitude of the electronic signal, the background noise, which was not coherent with the electronic signal, was virtually eliminated. Spectral Dynamics Type SD 360 real-time analyzer was used to determine the cross-power spectra. The analyzer also provided the phases between the electronic signal and the acoustic signals, and thus in effect the phase relationship along the periphery of the nozzle exit. These amplitudes and phases were fed to a computer program which incorporates the equations given in subsection 3.4.1. After few iterations between examining the computer output and the adjustments of the four driver voltages and their relative phases, the desired modes were obtained at the nozzle exit plane.

A typical computer output is shown in figure A.1.

The initial part of this printout describes the aerodynamic and desired upstream acoustic conditions as indicated by items (A) and (B) in the figure. Item (C) provides the sound pressure levels and phases at the source section as measured by the four microphones located in the 2.54 cm ducts connected to each of the four acoustic drivers. These values are a good-enough indication if a given mode has been achieved. Nozzle SPL distribution (item (D)) are then printed out together with their phases. Here, angles 30° to 360° refer to each of the 12 microphone locations around the nozzle-exit periphery. Both the corrected (for frequency response) and the uncorrected values as indicated on the SD-360 display are printed out.

The diagnostic information relating to mode decomposition is printed out on the second page of the printout as indicated by items (E) thru (H). Contribution of each mode is printed out under item (D). For example, as seen in figure A.1, the (0,0) mode has an amplitude of 95.9 dB, whereas the (1,0) mode has an amplitude of 67.4 dB. Comparison of the (0,0) mode amplitude with that of the higher amplitudes clearly indicates that the (0,0) mode was dominant in this case. This is further confirmed by the analysis of items (F) and (G). Finally, the least square-fit of the data is compared with the measured data as indicated by item (H).

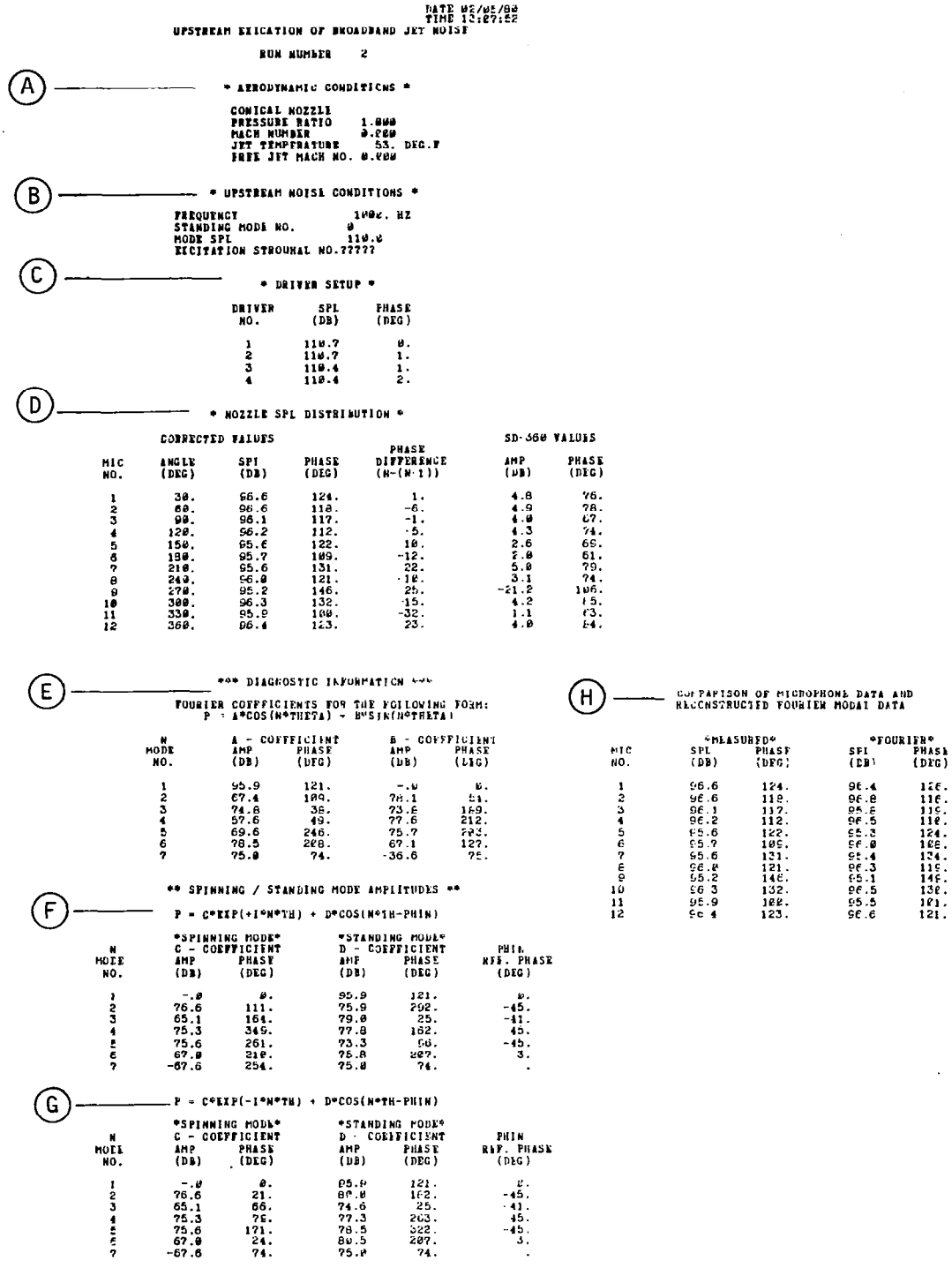

DATE 05/05/80
TIME 13:27:52

UPSTREAM EXICATION OF BROADBAND JET NOISE

RUN NUMBER 2

(A) * AERODYNAMIC CONDITIONS *

CONICAL NOZZLE
PRESSURE RATIO 1.800
MACH NUMBER 0.900
JET TEMPERATURE 53. DEG.F
REFE JET MACH NO. 0.900

(B) * UPSTREAM NOISE CONDITIONS *

FREQUENCY 1000. HZ
STANDING MODE NO. 0
MODE SPL 110.0
EXCITATION STROUHAL NO.?????

(C) * DRIVER SETUP *

DRIVER NO.	SPL (DB)	PHASE (DEG)
1	110.7	0.
2	110.7	1.
3	110.4	1.
4	110.4	2.

(D) * NOZZLE SPL DISTRIBUTION *

MIC NO.	CORRECTED VALUES ANGLE (DEG)	SPL (DB)	PHASE (DEG)	PHASE DIFFERENCE (N-(N-1))	SD-360 VALUES AMP (DB)	PHASE (DEG)
1	30.	96.6	124.	1.	4.8	96.
2	60.	96.6	118.	-6.	4.9	78.
3	90.	96.1	117.	-1.	4.0	67.
4	120.	96.2	112.	-5.	4.3	74.
5	150.	95.6	122.	10.	2.6	69.
6	180.	95.7	109.	-12.	2.0	61.
7	210.	95.6	131.	22.	5.0	79.
8	240.	96.0	121.	-10.	3.1	74.
9	270.	95.2	146.	25.	-21.2	106.
10	300.	96.3	132.	-15.	4.2	65.
11	330.	95.9	100.	-32.	1.1	83.
12	360.	96.4	123.	23.	4.0	84.

(E) *** DIAGNOSTIC INFORMATION ***

FOURIER COFFFICIENTS FOR THE FOLLOWING FORM:
P = A*COS(N*THETA) + B*SIN(N*THETA)

N MODE NO.	A - COFFFICIENT AMP (DB)	A - COFFFICIENT PHASE (DEG)	B - COFFFICIENT AMP (DB)	B - COFFFICIENT PHASE (DEG)
1	95.9	121.	-.0	0.
2	67.4	109.	78.1	51.
3	74.8	36.	73.8	169.
4	57.6	49.	77.6	212.
5	69.6	246.	75.7	293.
6	78.5	288.	67.1	127.
7	75.0	74.	-36.6	75.

(H) COMPARISON OF MICROPHONE DATA AND RECONSTRUCTED FOURIER MODAL DATA

MIC NO.	*MEASURED* SPL (DB)	*MEASURED* PHASE (DEG)	*FOURIER* SPL (DB)	*FOURIER* PHASE (DEG)
1	96.6	124.	96.4	126.
2	96.6	118.	96.0	116.
3	96.1	117.	95.6	115.
4	96.2	112.	96.5	110.
5	95.6	122.	95.3	124.
6	95.7	109.	96.0	108.
7	95.6	131.	95.4	134.
8	96.0	121.	96.3	119.
9	95.2	146.	95.1	146.
10	96.3	132.	96.5	132.
11	95.9	100.	95.5	101.
12	96.4	123.	96.6	121.

(F) ** SPINNING / STANDING MODE AMPLITUDES **

P = C*EXP(+I*N*TH) + D*COS(N*TH-PHIN)

N MODE NO.	*SPINNING MODE* C - COEFFICIENT AMP (DB)	*SPINNING MODE* C - COEFFICIENT PHASE (DEG)	*STANDING MODE* D - COEFFICIENT AMP (DB)	*STANDING MODE* D - COEFFICIENT PHASE (DEG)	PHIN REF. PHASE (DEG)
1	-.0	0.	95.9	121.	0.
2	76.6	111.	75.9	292.	-45.
3	65.1	164.	79.0	25.	-41.
4	75.3	349.	77.8	182.	45.
5	75.6	261.	73.3	90.	-45.
6	67.0	210.	75.8	207.	3.
7	-67.6	254.	75.0	74.	.

(G) P = C*EXP(-I*N*TH) + D*COS(N*TH-PHIN)

N MODE NO.	*SPINNING MODE* C - COEFFICIENT AMP (DB)	*SPINNING MODE* C - COEFFICIENT PHASE (DEG)	*STANDING MODE* D - COEFFICIENT AMP (DB)	*STANDING MODE* D - COEFFICIENT PHASE (DEG)	PHIN REF. PHASE (DEG)
1	-.0	0.	95.9	121.	0.
2	76.6	21.	89.8	182.	-45.
3	65.1	66.	74.6	25.	-41.
4	75.3	78.	77.3	203.	45.
5	75.6	171.	78.5	322.	-45.
6	67.0	24.	80.5	207.	3.
7	-67.6	74.	75.0	74.	.

Figure A.1 Typical computer output for detection of mode structure at the nozzle exit.

APPENDIX B

MEASUREMENT OF LARGE-SCALE TURBULENCE PRESSURE

The pressure magnitudes associated with the large-scale turbulence were measured by a 0.635-cm B&K Microphone fitted with a nose cone. The microphone itself was mounted on a suitable fairing with variable thickness along its length as shown in figure B.1. By adopting this design of the fairing, the discrete-tone noise normally associated with vortex shedding from bodies immersed in flows was virtually eliminated.

The total signal sensed by the microphone in the flow contains contributions from the small scale-turbulence, jet noise, ambient noise, the upstream acoustic signals, and the signal of interest--the large-scale turbulence. Since the upstream acoustic pressure signal and the large-scale turbulence pressures are coherent with the electronic signal fed to the acoustic driver, it was possible to use a coherence analysis whereby the contributions from other sources were minimized. Actually, a cross-power spectrum between the electronic signal and the microphone signal was obtained, and the resultant spectrum was basically the mean product of the acoustic-signal amplitude (which was constant and known *a priori*) and the sum of the acoustic and the large-scale turbulence-pressure amplitudes. As discussed in subsection 5.1, the acoustic signal was dominant only close to the nozzle exit, and thus farther away from the nozzle exit, the resultant cross-power spectra provided the actual amplitude of the large-scale turbulence pressure.

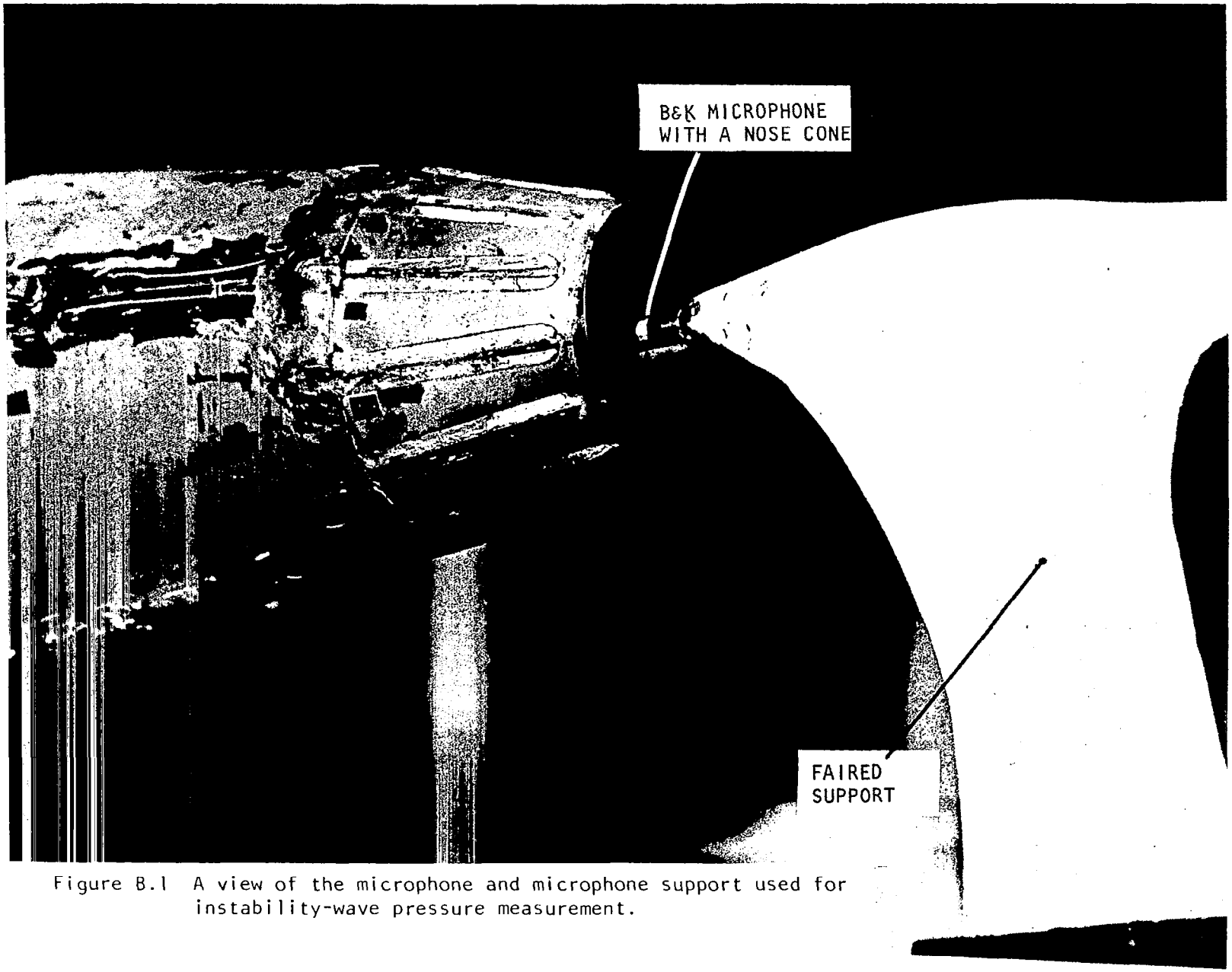

Figure B.1 A view of the microphone and microphone support used for instability-wave pressure measurement.

APPENDIX C
SUPPORTING EQUATIONS

C.1 EQUATIONS FOR THE MEAN FLOW WAVE MOTION AND FINE-SCALE TURBULENCE OF EXCITED JETS

The equations of motion for the mean flow, coherent wave, and turbulence of excited jet can be obtained by first taking the phase and the time average of the viscous compressible flow equations, and then form the differences of these equations. In the following, these equations are simplified by noting that the density fluctuation ρ' of the fine-scale turbulence is not too important (see ref. 41), and will be neglected. In other words, the fine-scale turbulence is assumed to be nearly incompressible. Also the magnitude of triple correlation terms of the unsteady motion of the jet are small. They are identically equal to zero if the motion is sinusoidal. For simplicity, their contributions to the equations of motion will be omitted.

The mean flow equations, assuming axisymmetry, are:

Continuity:

$$\frac{1}{r}\frac{\partial}{\partial r}\left[(\bar{\rho}\bar{v} + \overline{\tilde{\rho}\tilde{v}})r\right] + \frac{\partial}{\partial x}\left[\bar{\rho}\bar{u} + \overline{\tilde{\rho}\tilde{u}}\right] = 0 \qquad \text{(C-1)}$$

x - momentum:

$$\frac{1}{r}\frac{\partial}{\partial r}\left[(\bar{\rho}\bar{u}\bar{v} + \bar{\rho}\overline{\tilde{u}\tilde{v}} + \bar{\rho}\overline{u'v'} + \overline{\tilde{\rho}\tilde{v}}\bar{u} + \overline{\tilde{\rho}\tilde{u}}\bar{v})r\right]$$

$$+ \frac{\partial}{\partial x}\left[\bar{\rho}\bar{u}^2 + \bar{\rho}\overline{\tilde{u}^2 + u'^2} + 2\overline{\tilde{\rho}\tilde{u}}\bar{u}\right] = -\frac{\partial \bar{p}}{\partial x} + \frac{1}{R_e}\left[\frac{\partial^2 \bar{u}}{\partial x^2} + \frac{1}{r}\frac{\partial}{\partial r}\left(r\frac{\partial \bar{u}}{\partial r}\right)\right] \qquad \text{(C-2)}$$

The wave disturbance equations are:

$$\frac{\partial \tilde{\rho}}{\partial t} + \frac{1}{r}\frac{\partial}{\partial r}\left[(\bar{\rho}\tilde{v} + \tilde{\rho}\bar{v} + \tilde{\rho}\tilde{v} - \overline{\tilde{\rho}\tilde{v}})r\right] + \frac{1}{r}\frac{\partial}{\partial \theta}\left[\bar{\rho}\tilde{w} + \tilde{\rho}\bar{w} + \tilde{\rho}\tilde{w} - \overline{\tilde{\rho}\tilde{w}}\right]$$

$$+ \frac{\partial}{\partial x}\left[\bar{\rho}\tilde{u} + \tilde{\rho}\bar{u} + \tilde{\rho}\tilde{u} - \overline{\tilde{\rho}\tilde{u}}\right] = 0 \qquad \text{(C-3)}$$

$$\bar{\rho}\frac{\partial\tilde{u}}{\partial t} + \frac{\partial\tilde{\rho}\tilde{u}}{\partial t} + \bar{\rho}\tilde{v}\frac{\partial\bar{u}}{\partial r} + \frac{1}{r}\frac{\partial}{\partial r}\Big[(\bar{\rho}\tilde{u}\bar{v} + \bar{\rho}\tilde{u}\tilde{v} - \bar{\rho}\widetilde{\tilde{u}\tilde{v}} + \bar{\rho}\langle u'v'\rangle$$

$$- \bar{\rho}\overline{u'v'})r\Big] + \tilde{\rho}\bar{v}\frac{\partial\bar{u}}{\partial r} + \tilde{\rho}\tilde{v}\frac{\partial\bar{u}}{\partial r} - \widetilde{\tilde{\rho}\tilde{v}}\frac{\partial\bar{u}}{\partial r} + \frac{1}{r}\frac{\partial}{\partial r}\Big[(\tilde{\rho}\tilde{u}\bar{v} - \widetilde{\tilde{\rho}\tilde{u}\bar{v}}$$

$$+ \tilde{\rho}\tilde{u}\tilde{v} + \tilde{\rho}\langle u'v'\rangle)r\Big] - \frac{\bar{u}}{r}\frac{\partial}{\partial r}\Big[(\langle\rho'v'\rangle - \overline{\rho'v'})r\Big] + \frac{1}{r}\frac{\partial}{\partial\theta}\Big[\bar{\rho}\tilde{u}\bar{w} + \bar{\rho}\tilde{u}\tilde{w} - \bar{\rho}\widetilde{\tilde{u}\tilde{w}}$$

$$- \bar{\rho}\widetilde{\tilde{u}\tilde{w}} + \bar{\rho}\langle u'w'\rangle - \bar{\rho}\overline{u'w'} + \tilde{\rho}\tilde{u}\bar{w} - \widetilde{\tilde{\rho}\tilde{u}\bar{w}} + \tilde{\rho}\tilde{u}\tilde{w} + \tilde{\rho}\langle u'w'\rangle - \langle\rho'w'\rangle\bar{u}$$

$$+ \overline{\rho'w'\bar{u}}\Big] + \bar{\rho}\tilde{u}\frac{\partial\bar{u}}{\partial x} + \frac{\partial}{\partial x}\Big[\bar{\rho}\tilde{u}\tilde{u} + \bar{\rho}\tilde{u}^2 + \bar{\rho}\widetilde{\tilde{u}^2} + \bar{\rho}\langle u'^2\rangle - \bar{\rho}\overline{u'^2}\Big]$$

$$+ \tilde{\rho}\bar{u}\frac{\partial\bar{u}}{\partial x} + \tilde{\rho}\bar{u}\frac{\partial\bar{u}}{\partial x} + \tilde{\rho}\tilde{u}\frac{\partial\bar{u}}{\partial x} + \frac{\partial}{\partial x}\Big[\tilde{\rho}\tilde{u}\tilde{u} - \widetilde{\tilde{\rho}\tilde{u}\tilde{u}}\Big] - \widetilde{\tilde{\rho}\tilde{u}}\frac{\partial\bar{u}}{\partial x}$$

$$+ \frac{\partial}{\partial x}\Big[\tilde{\rho}\tilde{u}^2 + \tilde{\rho}\langle u'^2\rangle\Big] - \bar{u}\frac{\partial}{\partial x}\Big[\langle\rho'u'\rangle - \overline{\rho'u'}\Big] = -\frac{\partial\bar{p}}{\partial x}$$

$$+ \frac{1}{R_e}\Big[\frac{\partial^2\tilde{u}}{\partial x^2} + \frac{1}{r}\frac{\partial}{\partial r}\Big(r\frac{\partial\tilde{u}}{\partial r}\Big) + \frac{1}{r^2}\frac{\partial^2\tilde{u}}{\partial\theta^2}\Big] \qquad \text{(C-4)}$$

and

$$\bar{\rho}\frac{\partial\tilde{v}}{\partial t} + \frac{\partial\tilde{\rho}\tilde{v}}{\partial t} + \bar{\rho}\tilde{v}\frac{\partial\bar{v}}{\partial r} + \tilde{\rho}\bar{v}\frac{\partial\bar{v}}{\partial r} + \tilde{\rho}\tilde{v}\frac{\partial\bar{v}}{\partial r} - \widetilde{\tilde{\rho}\tilde{v}}\frac{\partial\bar{v}}{\partial r}$$

$$+ \frac{1}{r}\frac{\partial}{\partial r}\Big[(\bar{\rho}\bar{v}\tilde{v} + \bar{\rho}\tilde{v}^2 - \bar{\rho}\widetilde{\tilde{v}^2} + \bar{\rho}\langle v'^2\rangle - \bar{\rho}\overline{v'^2} + \tilde{\rho}\bar{v}\tilde{v} + \tilde{\rho}\tilde{v}^2 + \tilde{\rho}\langle v'^2\rangle)r\Big]$$

$$+ \frac{1}{r}\frac{\partial}{\partial\theta}\Big[\bar{\rho}\tilde{v}\bar{w} + \bar{\rho}\tilde{v}\tilde{w} - \bar{\rho}\widetilde{\tilde{v}\tilde{w}} + \bar{\rho}\langle v'w'\rangle - \bar{\rho}\overline{\langle v'w'\rangle} + \tilde{\rho}\tilde{v}\bar{w} - \widetilde{\tilde{\rho}\tilde{v}\bar{w}}$$

$$+ \tilde{\rho}\tilde{v}\tilde{w} + \tilde{\rho}\langle v'w'\rangle\Big] + (\bar{\rho}\tilde{u} + \tilde{\rho}\bar{u} + \tilde{\rho}\tilde{u} - \widetilde{\tilde{\rho}\tilde{u}})\frac{\partial\bar{v}}{\partial x} +$$

$$\frac{\partial}{\partial x}\Big[\bar{\rho}\tilde{v}\tilde{u} + \bar{\rho}\tilde{v}\tilde{u} - \bar{\rho}\overline{\tilde{v}\tilde{u}} + \bar{\rho}\langle u'v'\rangle - \bar{\rho}\overline{u'v'} + \tilde{\rho}\tilde{v}\bar{u} - \overline{\tilde{\rho}\tilde{v}\bar{u}}$$

$$+ \tilde{\rho}\bar{v}\tilde{u} + \tilde{\rho}\langle u'v'\rangle\Big] - \frac{1}{r}\Big[\bar{\rho}\tilde{w}^2 - \bar{\rho}\overline{\tilde{w}^2} + \bar{\rho}\langle w'^2\rangle - \bar{\rho}\,\overline{w'^2} + 2\,\bar{\rho}\bar{w}\tilde{w}$$

$$+ \tilde{\rho}w^2 + \tilde{\rho}\tilde{w}^2 + \tilde{\rho}\langle w'^2\rangle + 2\tilde{\rho}\bar{w}\tilde{w} - 2\overline{\tilde{\rho}\tilde{w}\bar{w}}\Big] = -\frac{\partial\tilde{p}}{\partial r}$$

$$+ \frac{1}{R_e}\Big[\frac{\partial^2\tilde{v}}{\partial x^2} + \frac{1}{r}\frac{\partial}{\partial r}\Big(r\frac{\partial\tilde{v}}{\partial r}\Big) + \frac{1}{r^2}\frac{\partial^2\tilde{v}}{\partial\theta^2} - \frac{\tilde{v}}{r^2} - \frac{2}{r^2}\frac{\partial\tilde{w}}{\partial\theta}\Big] \qquad \text{(C-5)}$$

Similarly,

$$\bar{\rho}\frac{\partial\tilde{w}}{\partial t} + \frac{\partial\tilde{\rho}\tilde{w}}{\partial t} + \frac{1}{r}\frac{\partial}{\partial r}\Big(\bar{\rho}\bar{v}\tilde{w} + \bar{\rho}\tilde{v}\bar{w} - \bar{\rho}\overline{\tilde{v}\tilde{w}} + \bar{\rho}\langle v'w'\rangle - \bar{\rho}\overline{v'w'}$$

$$+ \tilde{\rho}\bar{v}\tilde{w} + \overline{\tilde{\rho}\tilde{w}\bar{v}} + \tilde{\rho}\tilde{v}\bar{w} + \tilde{\rho}\langle v'w'\rangle\Big)r\Big] + \frac{1}{r}\frac{\partial}{\partial\theta}\Big[\bar{\rho}\tilde{w}^2 - \bar{\rho}\overline{\tilde{w}^2} + \bar{\rho}\langle w'^2\rangle$$

$$- \bar{\rho}\overline{w'^2} + \tilde{\rho}\tilde{w}^2 + \tilde{\rho}\langle w'^2\rangle\Big] + \frac{\partial}{\partial x}\Big[\bar{\rho}\tilde{w}\bar{u} + \bar{\rho}\tilde{w}\tilde{u} - \bar{\rho}\overline{\tilde{w}\tilde{u}} + \bar{\rho}\langle w'u'\rangle$$

$$- \bar{\rho}\overline{w'u'} + \tilde{\rho}\tilde{w}\bar{u} - \overline{\tilde{\rho}\tilde{w}\bar{u}} + \tilde{\rho}\tilde{w}\tilde{u} + \tilde{\rho}\langle w'u'\rangle\Big] + \frac{1}{r}\Big[\bar{\rho}\bar{v}\tilde{w} + \bar{\rho}\tilde{v}\bar{w}$$

$$- \bar{\rho}\overline{\tilde{v}\tilde{w}} + \bar{\rho}\langle v'w'\rangle - \bar{\rho}\overline{v'w'} + \tilde{\rho}\bar{v}\tilde{w} - \overline{\tilde{\rho}\tilde{w}\bar{v}} + \tilde{\rho}\tilde{v}\bar{w} + \tilde{\rho}\langle v'w'\rangle\Big] = -\frac{1}{r}\frac{\partial\tilde{p}}{\partial\theta}$$

$$+ \frac{1}{R_e}\Big[\frac{\partial^2\tilde{w}}{\partial x^2} + \frac{1}{r}\frac{\partial}{\partial r}\Big(r\frac{\partial\tilde{w}}{\partial r}\Big) + \frac{1}{r^2}\frac{\partial^2\tilde{w}}{\partial\theta^2} - \frac{\tilde{w}}{r^2} + \frac{2}{r^2}\frac{\partial\tilde{v}}{\partial\theta}\Big] \qquad \text{(C-6)}$$

and

$$\frac{\partial\tilde{p}}{\partial t} + \frac{1}{r}\frac{\partial}{\partial r}\Big[(\bar{p}\tilde{v} + \tilde{p}\bar{v} + \tilde{p}\tilde{v} - \overline{\tilde{p}\tilde{v}} + \langle p'v'\rangle - \overline{p'v'})r\Big]$$

$$+ \frac{1}{r}\frac{\partial}{\partial\theta}\Big[\bar{p}\tilde{w} + \tilde{p}\bar{w} - \overline{\tilde{p}\tilde{w}} + \langle p'w'\rangle - \overline{p'w'}\Big]$$

$$+ \frac{\partial}{\partial x}\Big[\bar{p}\tilde{u} + \tilde{p}\bar{u} + \tilde{p}\tilde{u} - \overline{\tilde{p}\tilde{u}} + \langle p'u'\rangle - \overline{p'u'}\Big] +$$

$$(\gamma-1)\ \bar{p}\left[\frac{1}{r}\frac{\partial\tilde{v}v}{\partial r}+\frac{1}{r}\frac{\partial\tilde{w}}{\partial\theta}+\frac{\partial\tilde{u}}{\partial x}\right]+(\gamma-1)\ \tilde{p}\left[\frac{1}{r}\frac{\partial\bar{v}r}{\partial r}+\frac{\partial\bar{u}}{\partial x}\right]$$

$$+(\gamma-1)\ \tilde{p}\left[\frac{1}{r}\frac{\partial\tilde{v}r}{\partial r}+\frac{1}{r}\frac{\partial\tilde{w}}{\partial\theta}+\frac{\partial\tilde{u}}{\partial x}\right]-(\gamma-1)\ \overline{\tilde{p}\left[\frac{1}{r}\frac{\partial\tilde{v}r}{\partial r}+\frac{1}{r}\frac{\partial\tilde{w}}{\partial\theta}\quad\frac{\partial\tilde{u}}{\partial x}\right]}$$

$$+(\gamma-1)<p'(\frac{1}{r}\frac{\partial v'r}{\partial r}+\frac{1}{r}\frac{\partial w'}{\partial\theta}+\frac{\partial u'}{\partial x})>-(\gamma-1)\ \overline{p'(\frac{1}{r}\frac{\partial v'r}{\partial r}+\frac{1}{r}\frac{\partial w'}{\partial\theta}+\frac{\partial u'}{\partial x})}=0 \qquad (C\text{-}7)$$

In line with the assumption that the fine-scale turbulence is nearly incompressible, the effect of the density fluctuation, $\tilde{\rho}$, associated with the excited wave motion on the fine-scale turbulent motion of the jet has been neglected in the following equations.

$$\rho\frac{\partial u'}{\partial t}+\frac{1}{r}\frac{\partial}{\partial r}\left[(\tilde{\rho}\bar{u}v'+\bar{\rho}\tilde{u}v'+\bar{\rho}u'\bar{v}+\bar{\rho}u'\tilde{v}+\bar{\rho}u'v'-\bar{\rho}<u'v'>)r\right]$$

$$+\frac{1}{r}\frac{\partial}{\partial\theta}\left[\bar{\rho}\bar{u}w'+\bar{\rho}\tilde{u}w'+\bar{\rho}u'\tilde{w}+\bar{\rho}u'w'-\bar{\rho}<u'w'>\right]$$

$$+\frac{\partial}{\partial x}\left[2\ \bar{\rho}\bar{u}u'+\bar{\rho}u'^2-\bar{\rho}<u'^2>+2\ \bar{\rho}\tilde{u}u'\right]=-\frac{\partial p'}{\partial x}$$

$$+\frac{1}{Re}\left[\frac{\partial^2u'}{\partial x^2}+\frac{1}{r}\frac{\partial}{\partial r}\left(r\frac{\partial u'}{\partial r}\right)+\frac{1}{r^2}\frac{\partial^2u'}{\partial\theta^2}\right] \qquad (C\text{-}8)$$

and

$$\bar{\rho}\frac{\partial v'}{\partial t}+\frac{1}{r}\frac{\partial}{\partial r}\left[(2\ \bar{\rho}\bar{v}v'+2\ \bar{\rho}\tilde{v}v'+\bar{\rho}v'^2-\bar{\rho}<v'^2>)r\right]$$

$$+\frac{1}{r}\frac{\partial}{\partial\theta}\left[\bar{\rho}\bar{v}w'+\bar{\rho}\tilde{v}w'+\bar{\rho}v'\tilde{w}+\bar{\rho}v'w'-\bar{\rho}<v'w'>\right]$$

$$+\frac{\partial}{\partial x}\left[\bar{\rho}\bar{v}u'+\bar{\rho}\tilde{v}u'+\bar{\rho}v'\bar{u}+\bar{\rho}v'\tilde{u}+\bar{\rho}v'u'-\bar{\rho}<u'v'>\right]$$

$$-\frac{1}{r}\left[\bar{\rho}w'^2-\bar{\rho}<w'^2>+2\ \bar{\rho}\bar{w}w'+2\ \bar{\rho}\tilde{w}w'\right]=-\frac{\partial p'}{\partial r}$$

$$+\frac{1}{Re}\left[\frac{\partial^2v'}{\partial x^2}+\frac{1}{r}\frac{\partial}{\partial r}\left(r\frac{\partial v'}{\partial r}\right)+\frac{1}{r^2}\frac{\partial^2v'}{\partial\theta^2}-\frac{v'}{r^2}-\frac{2}{r^2}\frac{\partial w'}{\partial\theta}\right] \qquad (C\text{-}9)$$

Similarly,

$$\bar{\rho}\frac{\partial w'}{\partial t} + \frac{1}{r}\frac{\partial}{\partial r}\left[(\bar{\rho}\bar{v}w' + \bar{\rho}\tilde{v}w' + \bar{\rho}v'\tilde{w} + \bar{\rho}v'w' - \bar{\rho}\langle v'w'\rangle)r\right]$$

$$+ \frac{1}{r}\frac{\partial}{\partial\theta}\left[2\,\bar{\rho}\tilde{w}w' + \bar{\rho}w'^2 - \bar{\rho}\langle w'^2\rangle\right] + \frac{\partial}{\partial x}\left[\bar{\rho}\tilde{w}u' + \bar{\rho}w'\bar{u} + \bar{\rho}w'\tilde{u} + \bar{\rho}w'u'\right.$$

$$\left. - \bar{\rho}\langle w'u'\rangle\right] + \frac{1}{r}\left[\bar{\rho}\bar{v}w' + \bar{\rho}\tilde{v}w' + \bar{\rho}v'\tilde{w} + \bar{\rho}v'w' - \bar{\rho}\langle v'w'\rangle\right]$$

$$= -\frac{1}{r}\frac{\partial p'}{\partial\theta} + \frac{1}{Re}\left[\frac{\partial^2 w'}{\partial x^2} + \frac{1}{r}\frac{\partial}{\partial r}\left(r\frac{\partial w'}{\partial v}\right) + \frac{1}{r^2}\frac{\partial^2 w'}{\partial\theta^2} - \frac{w'}{r^2} + \frac{2}{r^2}\frac{\partial v'}{\partial\theta}\right] \qquad \text{(C-10)}$$

C.2 THE INSTABILITY WAVE-ENERGY EQUATION CALCULATED BY THE LOCALLY-PARALLEL FLOW APPROXIMATION

In cylindrical coordinates, the equations for the instability waves with eddy viscosity to simulate the effect of fine-scale turbulence are:

$$\bar{\rho}\left[\frac{\partial\tilde{v}}{\partial t} + \bar{u}\frac{\partial\tilde{v}}{\partial x}\right] = -\frac{\partial\tilde{p}}{\partial r} + \mu_t\left[\frac{\partial^2\tilde{v}}{\partial x^2} + \frac{1}{r}\frac{\partial}{\partial r}\left(r\frac{\partial\tilde{v}}{\partial r}\right) + \frac{1}{r^2}\frac{\partial^2\tilde{v}}{\partial\theta^2} - \frac{\tilde{v}}{r^2} - \frac{2}{r}\frac{\partial\tilde{w}}{\partial\theta}\right] \qquad \text{(C-11a)}$$

$$\bar{\rho}\left[\frac{\partial\tilde{w}}{\partial t} + \bar{u}\frac{\partial\tilde{w}}{\partial x}\right] = -\frac{1}{r}\frac{\partial\tilde{p}}{\partial\theta} + \mu_t\left[\frac{\partial^2\tilde{w}}{\partial x^2} + \frac{1}{r}\frac{\partial}{\partial r}\left(r\frac{\partial\tilde{w}}{\partial r}\right) + \frac{1}{r^2}\frac{\partial^2\tilde{w}}{\partial\theta^2}\right.$$

$$\left. - \frac{\tilde{w}}{r^2} + \frac{2}{r}\frac{\partial\tilde{v}}{\partial\theta}\right] \qquad \text{(C-11b)}$$

$$\bar{\rho}\left[\frac{\partial\tilde{u}}{\partial t} + \bar{u}\frac{\partial\tilde{u}}{\partial x} + \tilde{v}\frac{\partial\bar{u}}{\partial r}\right] = -\frac{\partial\tilde{p}}{\partial x} + \mu_t\left[\frac{\partial^2\tilde{u}}{\partial x^2} + \frac{1}{r}\frac{\partial}{\partial r}\left(r\frac{\partial\tilde{u}}{\partial r}\right) + \frac{1}{r^2}\frac{\partial^2\tilde{u}}{\partial\theta^2}\right] \qquad \text{(C-11c)}$$

$$\frac{\partial\tilde{p}}{\partial t} + \bar{u}\frac{\partial\tilde{p}}{\partial x} + \gamma\bar{p}\left[\frac{1}{r}\frac{\partial\tilde{v}r}{\partial r} + \frac{1}{r}\frac{\partial\tilde{w}}{\partial\theta} + \frac{\partial\tilde{u}}{\partial x}\right] = 0 \qquad \text{(C-11d)}$$

where $\mu_t = \bar{\rho}\varepsilon_t$ is the eddy-viscosity coefficient. Under the locally-parallel flow approximation, the solution has the typical form:

$$\tilde{p} = R_e \left\{ a(x)\ \hat{p}(r,x) \exp\left[i \left(\int_o^x k_r dx + n\theta - \Omega t \right) \right] \right\}$$

$$= a(x)\ |\hat{p}|\ \cos\left\{ H + \alpha_p \right\} \qquad \text{(C-12)}$$

where, $a(x) = \exp\left[- \int_o^x k_i dx \right]$

$$H = \int_o^x k_r dx + k\theta - \Omega t$$

where, α_p is the phase of $\hat{p}$.

Here, k_r and k_i are the real and imaginary parts of the eigenvalue k_n. $\hat{p}$ is the eigenfunction. Its x-dependence, however, is to be ignored under the locally-parallel flow approximation. It is to be noted that a(x) is equal to the absolute value of A(x) of equation (7-18), i.e.,

$$a(x) = | A(x) | \qquad \text{(C-13a)}$$

and

$$\frac{d\ a(x)}{dx} = \frac{d\ |A(x)|}{dx} = - k_i \qquad \text{(C-13b)}$$

Substitution of equation (C-12) into equation (C-11) gives:

$$-\Omega\bar{\rho} \frac{\partial \tilde{v}}{\partial H} + \bar{\rho}\bar{u} \left[- k_i \tilde{v} + k_r \frac{\partial \tilde{v}}{\partial H} \right] = - \frac{\partial \tilde{p}}{\partial r} + \mu_t \left[(-k_i + k_r \frac{\partial}{\partial H})^2 \tilde{v} \right.$$

$$\left. + \frac{1}{r} \frac{\partial}{\partial r} (r \frac{\partial \tilde{v}}{\partial r}) + \frac{n^2}{r^2} \frac{\partial^2 \tilde{v}}{\partial H^2} - \frac{\tilde{v}}{r^2} - \frac{2n}{r} \frac{\partial \tilde{w}}{\partial H} \right] \qquad \text{(C-14a)}$$

$$-\Omega\bar{\rho} \frac{\partial \tilde{w}}{\partial H} + \bar{\rho}\bar{u} \left[-k_i \tilde{w} + k_r \frac{\partial \tilde{w}}{\partial H} \right] = - \frac{n}{r} \frac{\partial \tilde{p}}{\partial H} + \mu_t \left[(-k_i + k_r \frac{\partial}{\partial H})^2 \tilde{w} \right.$$

$$\left. + \frac{1}{r} \frac{\partial}{\partial r} (r \frac{\partial \tilde{w}}{\partial r}) + \frac{n^2}{r^2} \frac{\partial^2 \tilde{w}}{\partial H^2} - \frac{\tilde{w}}{r^2} + \frac{2n}{r} \frac{\partial \tilde{v}}{\partial H} \right] \qquad \text{(C-14b)}$$

$$- \Omega\bar{\rho} \frac{\partial \tilde{u}}{\partial H} + \bar{\rho}\ \bar{u} \left[-k_i \tilde{u} + k_r \frac{\partial \tilde{u}}{\partial H} \right] + \bar{\rho}\ \tilde{v} \frac{\partial \bar{u}}{\partial r} = - k_i \tilde{p} - k_r \frac{\partial \tilde{p}}{\partial H} +$$

$$\mu_t \left[(-k_i + k_r \frac{\partial}{\partial H})^2 \tilde{u} + \frac{1}{r} \frac{\partial}{\partial r} \left(r \frac{\partial \tilde{u}}{\partial r} \right) + \frac{n^2}{r^2} \frac{\partial \tilde{u}}{\partial H} \right] \qquad \text{(C-14c)}$$

$$- \Omega \frac{\partial \tilde{p}}{\partial H} + \bar{u} \left(-k_i \tilde{p} + h_r \frac{\partial \tilde{p}}{\partial H} \right) + \gamma \bar{p} \left[\frac{1}{r} \frac{\partial vr}{\partial r} + \frac{n}{r} \frac{\partial \tilde{w}}{\partial H} - k_i \tilde{u} + k_r \frac{\partial \tilde{u}}{\partial H} \right] = 0 \qquad \text{(C-14 d)}$$

Now the integral of the time average of equation (C-14a) weighted by $\tilde{v}r$ is,

$$- k_i \int_0^\infty \bar{\rho} \bar{u} \overline{\tilde{v}^2} \, r dr = \int_0^\infty \overline{\frac{\tilde{p}}{r} \frac{\partial \tilde{v} r}{\partial r}} \, r dr$$

$$+ \int_0^\infty \mu_t \, \overline{\tilde{v} \left[(- k_i + k_r \frac{\partial}{\partial H})^2 \tilde{v} + \frac{1}{r} \frac{\partial}{\partial r} \left(r \frac{\partial \tilde{v}}{\partial r} \right) + \frac{n^2}{r^2} \frac{\partial^2 \tilde{v}}{\partial H^2} - \frac{\tilde{v}}{r^2} \frac{2n}{r} \frac{\partial \tilde{w}}{\partial H} \right]} \, r dr \qquad \text{(C-15)}$$

If the locally parallel flow approximation is relaxed, the true x-derivative is given by

$$\frac{\partial \tilde{v}}{\partial x} = - k_i \tilde{v} + k_r \frac{\partial \tilde{v}}{\partial H} + \left(\frac{\partial \tilde{v}}{\partial x} \right)_{\substack{\text{on the x-dependence} \\ \text{of the eigenfunction}}} \qquad \text{(C-16)}$$

where, numerically, the second term is the largest.

In the eddy viscosity terms of equation (C-15), an approximation can be made to replace the first term by $\overline{- \frac{\partial \tilde{v}}{\partial x}}^2$ (after integration by parts over H). When this is done and on combining equation (C-15) with similar integrals obtained from equations (C-14b) and (C-14c), it is straightforward to find,

$$- k_i \int_0^\infty \left[\bar{\rho} \bar{u} \overline{(\tilde{u}^2 + \tilde{v}^2 + \tilde{w}^2)} + 2 \overline{\tilde{p} \tilde{u}} \right] r dr = - \int_0^\infty \bar{\rho} \, \overline{\tilde{u} \tilde{v}} \frac{\partial \bar{u}}{\partial r} \, r dr$$

$$+ \int_0^\infty \tilde{p} \left[\frac{1}{r} \frac{\partial}{\partial r} (r \tilde{v}) + \frac{1}{r} \frac{\partial \tilde{w}}{\partial \theta} - k_i \tilde{u} + k_r \frac{\partial \tilde{u}}{\partial H} \right] r dr$$

$$- \int_0^\infty \phi \, r dr \qquad \text{(C-17)}$$

where $\int_0^\infty \phi \, r dr$ is the turbulence dissipation integral of equations (7-27)

and (7-29). The corresponding integral of equation (C-14d) is

$$- k_i \int_0^\infty \frac{\bar{u}\overline{\tilde{p}^2}}{r\bar{\rho}} \, rdr + \int_0^\infty \overline{\tilde{p}\left[\frac{1}{r}\frac{\partial \tilde{v}r}{\partial r} + \frac{1}{r}\frac{\partial \tilde{w}}{\partial \theta} - k_s\tilde{u} + k_r\frac{\partial \tilde{u}}{\partial H}\right]} \, rdr \qquad \text{(C-18)}$$

On combining equations (C-17) and (C-18), one finds

$$- 2\, k_i \int_0^\infty \left[\frac{1}{2}\bar{\rho}\bar{u}\,\overline{(\tilde{u}^2 + \tilde{v}^2 + \tilde{w}^2)} + \frac{\bar{u}\overline{\tilde{p}^2}}{2r\bar{\rho}} + \overline{\tilde{p}\tilde{u}}\right] rdr$$

$$= - \int_0^\infty \bar{\rho}\,\overline{\tilde{u}\tilde{v}}\,\frac{\partial \bar{u}}{\partial r}\, rdr - \int_0^\infty \phi \, rdr \qquad \text{(C-19)}$$

Now if the eigenfunctions are normalized according to equation (7-17), then equation (C-19) becomes

$$2\, k_i\, |A|^2 = \int_0^\infty \bar{\rho}\,\overline{\tilde{u}\tilde{v}}\,\frac{\partial \bar{u}}{\partial r}\, rdr + \int_0^\infty \phi \, rdr \qquad \text{(C-20)}$$

By equation (C-13b) and normalization condition (7-17), the left hand side of equation (C-20) can be written as a total derivative of x:

$$\frac{d}{dx}\int_0^\infty \left[\frac{1}{2}\bar{\rho}\bar{u}\,\overline{(\tilde{u}^2 + \tilde{v}^2 + \tilde{w}^2)} + \frac{\bar{u}\overline{\tilde{p}^2}}{2r\bar{\rho}} + \overline{\tilde{p}\tilde{u}}\right] rdr$$

$$= - \int_0^\infty \bar{\rho}\,\overline{\tilde{u}\tilde{v}}\,\frac{\partial \bar{u}}{\partial r}\, rdr - \int_0^\infty \phi \, rdr \qquad \text{(C-21)}$$

(C-18) is a relation involving the potential energy of the wave motion. This equation can be rewritten approximately as

$$\frac{d}{dx}\int_0^\infty \frac{\bar{u}\overline{\tilde{p}^2}}{2\gamma\bar{p}} \, rdr + \int_0^\infty \overline{\tilde{p}\left[\frac{1}{r}\frac{\partial \tilde{v}r}{\partial r} + \frac{1}{r}\frac{\partial \tilde{w}}{\partial \theta} + \frac{\partial \tilde{u}}{\partial x}\right]} rdr = 0 \qquad \text{(C-22)}$$

By means of equation (C-22), equation (C-21) can finally be cast into the form

$$\frac{d}{dx}\int_0^\infty \left[\frac{1}{2}\bar{\rho}\bar{u}\,\overline{(\tilde{u}^2+\tilde{v}^2+\tilde{w}^2)} + \overline{\tilde{p}\tilde{u}} \right] r\,dr = -\int_0^\infty \bar{\rho}\,\overline{\tilde{u}\tilde{v}}\,\frac{\partial \bar{u}}{\partial r}\,r\,dr$$

$$+\int_0^\infty \overline{\tilde{p}\left[\frac{1}{r}\frac{\partial \tilde{v}r}{\partial r} + \frac{\partial \tilde{w}}{\partial \theta} + \frac{\partial \tilde{u}}{\partial x} \right]}\,r\,dr - \int_0^\infty \phi\,r\,dr \qquad \text{(C-23)}$$

On comparing equations (C-23) and (7-29), it is clear that they are identical. That is to say, the locally-parallel flow instability wave solution satisfies the integral wave-energy equation to a reasonably good degree of accuracy.

APPENDIX D

REPRESENTATIVE FLOW DATA

In this appendix are presented representative plots of actual measured flow-data points and their deviations from the smoothed curves through them that were presented in the description of flow results in section 5.0.

The figures of section 5.0, to which the figures in this appendix correspond, are tabulated in Table D-1 below together with a brief description of the type of data presented in each figure.

Table D-1 Appendix figures versus section 5.0 figures

FIGURE NUMBER IN THIS APPENDIX	CORRESPONDING FIGURE NUMBER IN SECTION 5.0	TYPE OF DATA
D.1(a)	5.8	MEAN VELOCITY
D.1(b)	5.8	TURBULENCE INTENSITY
D.2(a)	5.14	MEAN VELOCITY AND TURBULENCE INTENSITY (UNEXCITED JET)
D.2(b)	5.14	MEAN VELOCITY AND TURBULENCE INTENSITY (EXCITED JET)
D.3	5.16	TURBULENCE INTENSITY
D.4(a)	5.19	MEAN VELOCITY
D.4(b)	5.19	TURBULENCE INTENSITY
D.5	5.26(b)	TURBULENCE INTENSITY
D.6	5.27(a)	MEAN VELOCITY
D.7	5.28(a)	MEAN VELOCITY
D.8(a)	5.39(a)	TURBULENCE INTENSITY
D.8(b)	5.39(b)	MEAN VELOCITY

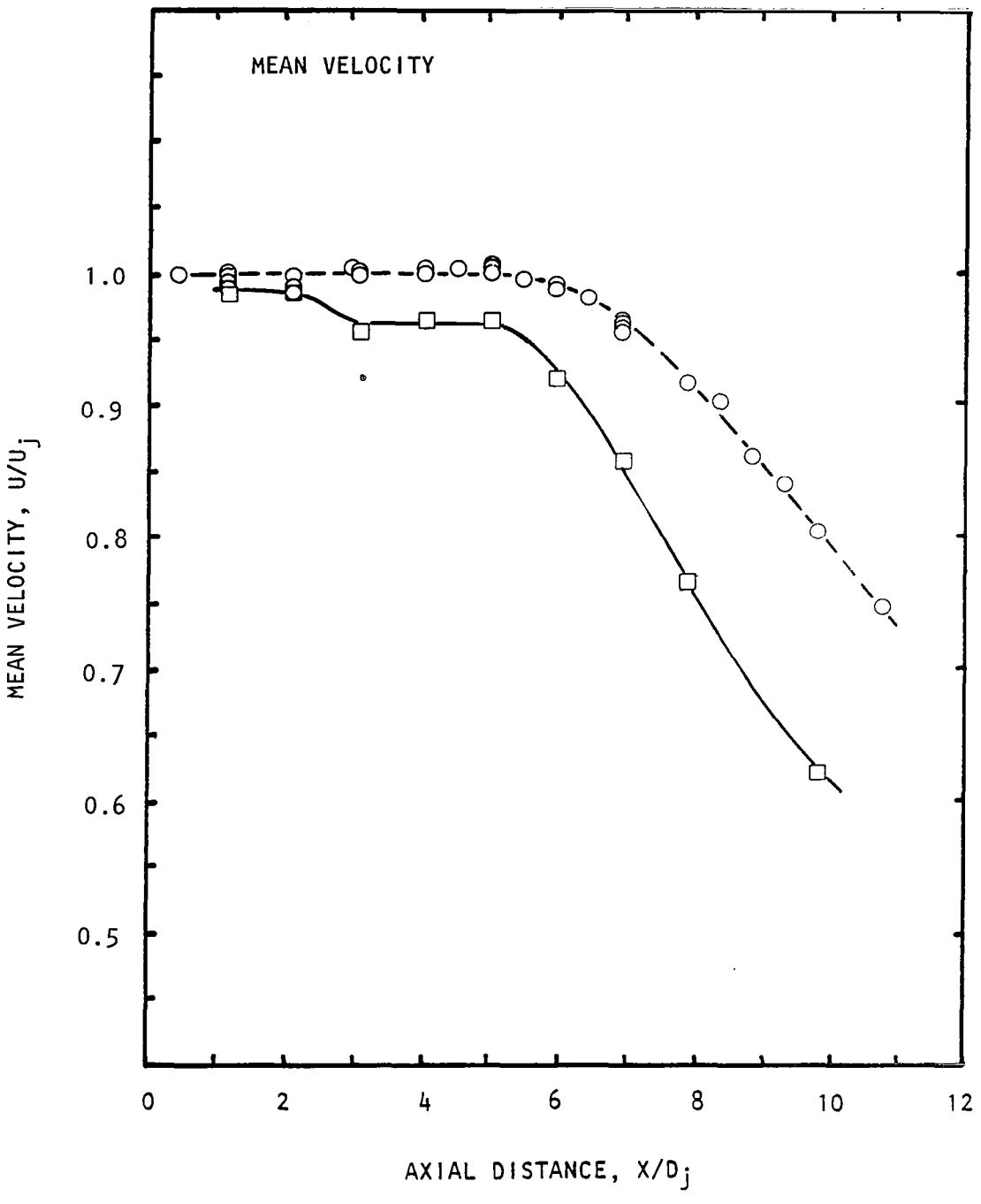

Figure D.1(a) Excitation-level effects on centerline distributions. M_j = 0.58, U_j = 195 m/s, Unheated, Static, S_e = 0.5, (0,0) Mode.
L_e: ○ , Unexcited; □ , 141 dB.
(Also see figure 5.8)

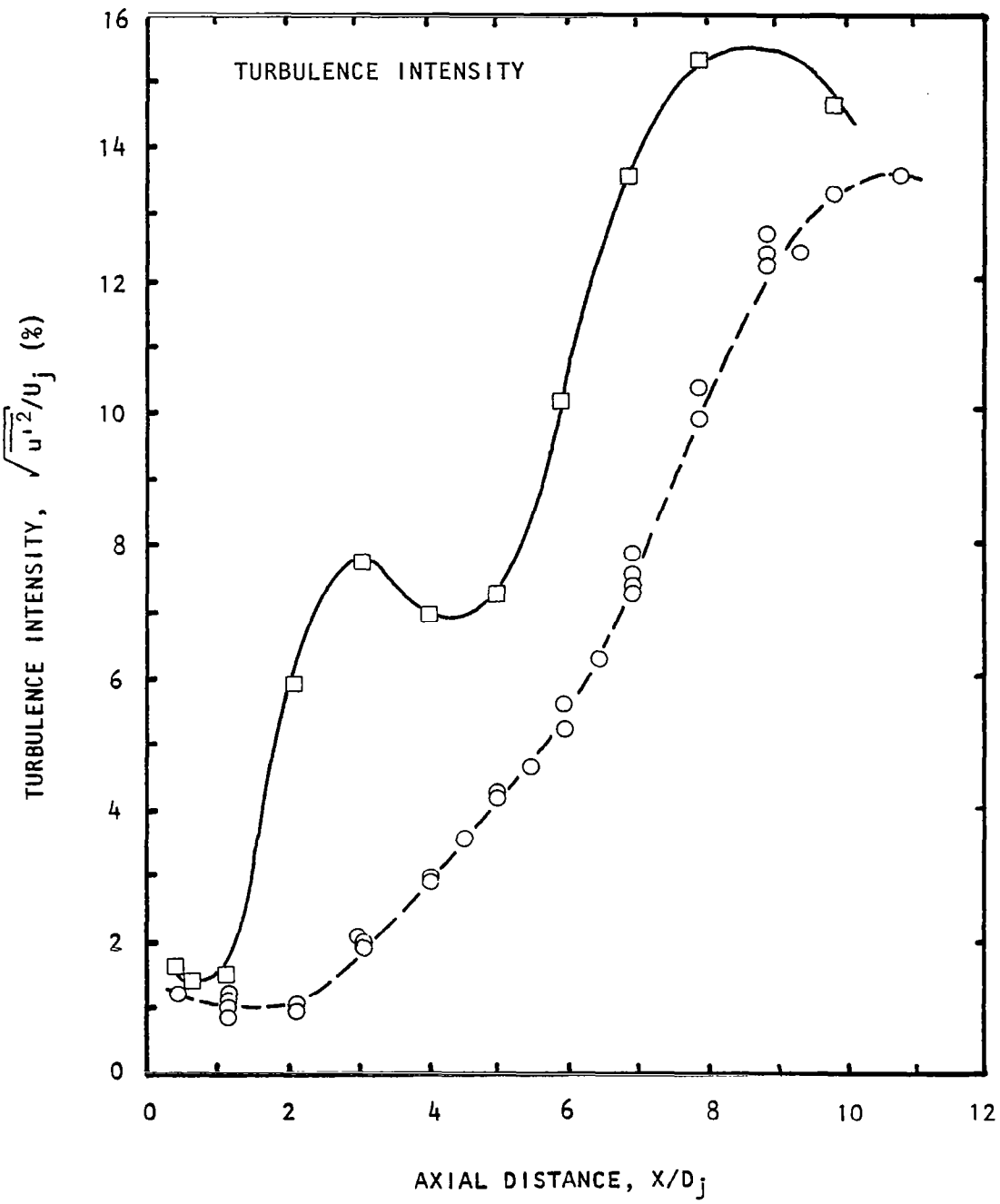

Figure D.1(b) Excitation-level effects on centerline distributions.
Mj = 0.58, U_j = 195 m/s, Unheated, Static, S_e = 0.5,
(0,0) Mode.
L_e: O , Unexcited; □, 141 dB.
(Also see figure 5.8)

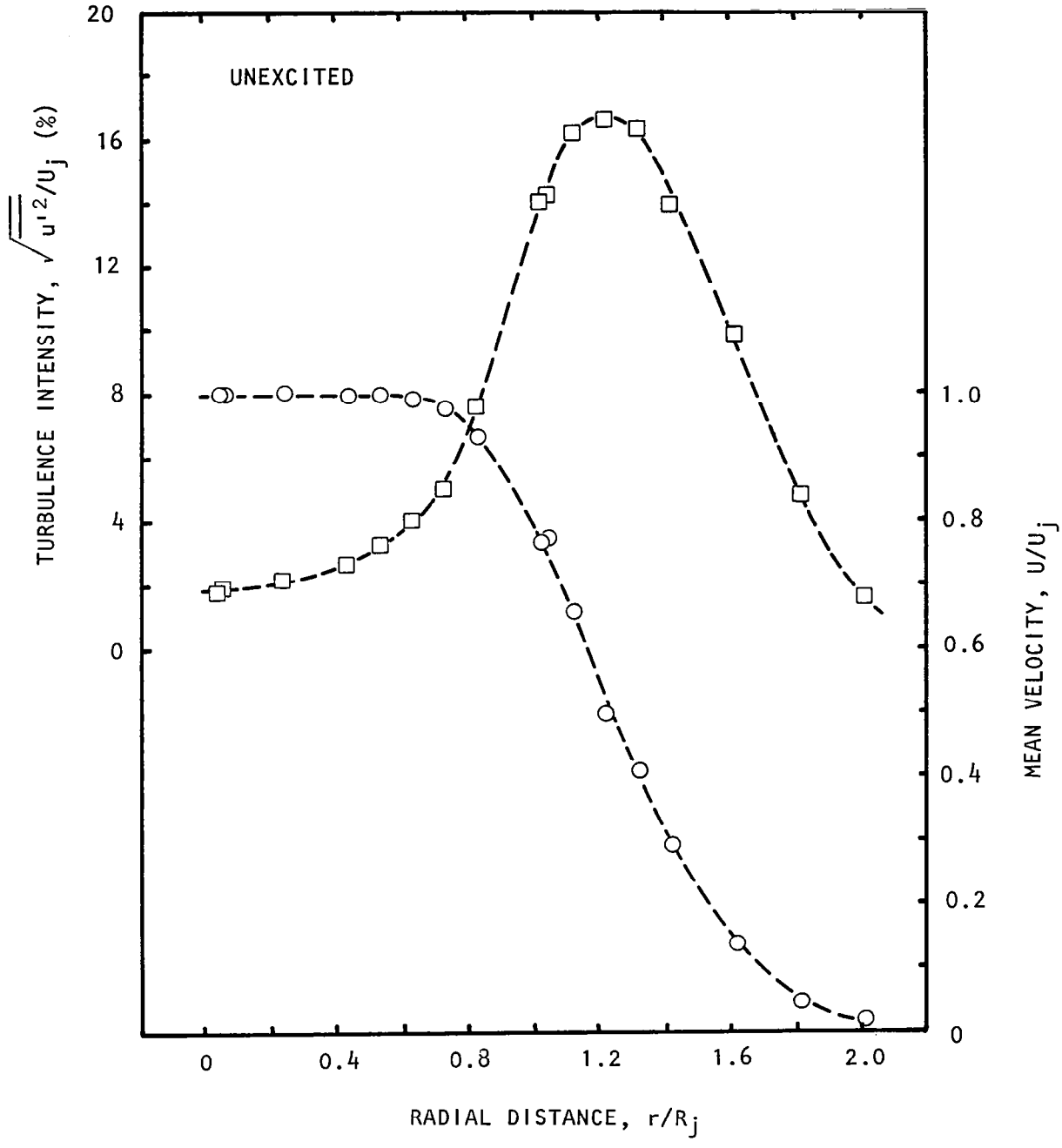

Figure D.2(a) Excitation effects on radial distribution of axial components of mean velocity (○) and turbulence intensity (□) at x/D = 3. M_j = 0.58, U_j = 195 m/s. Unheated, Static. (Also see figure 5.14)

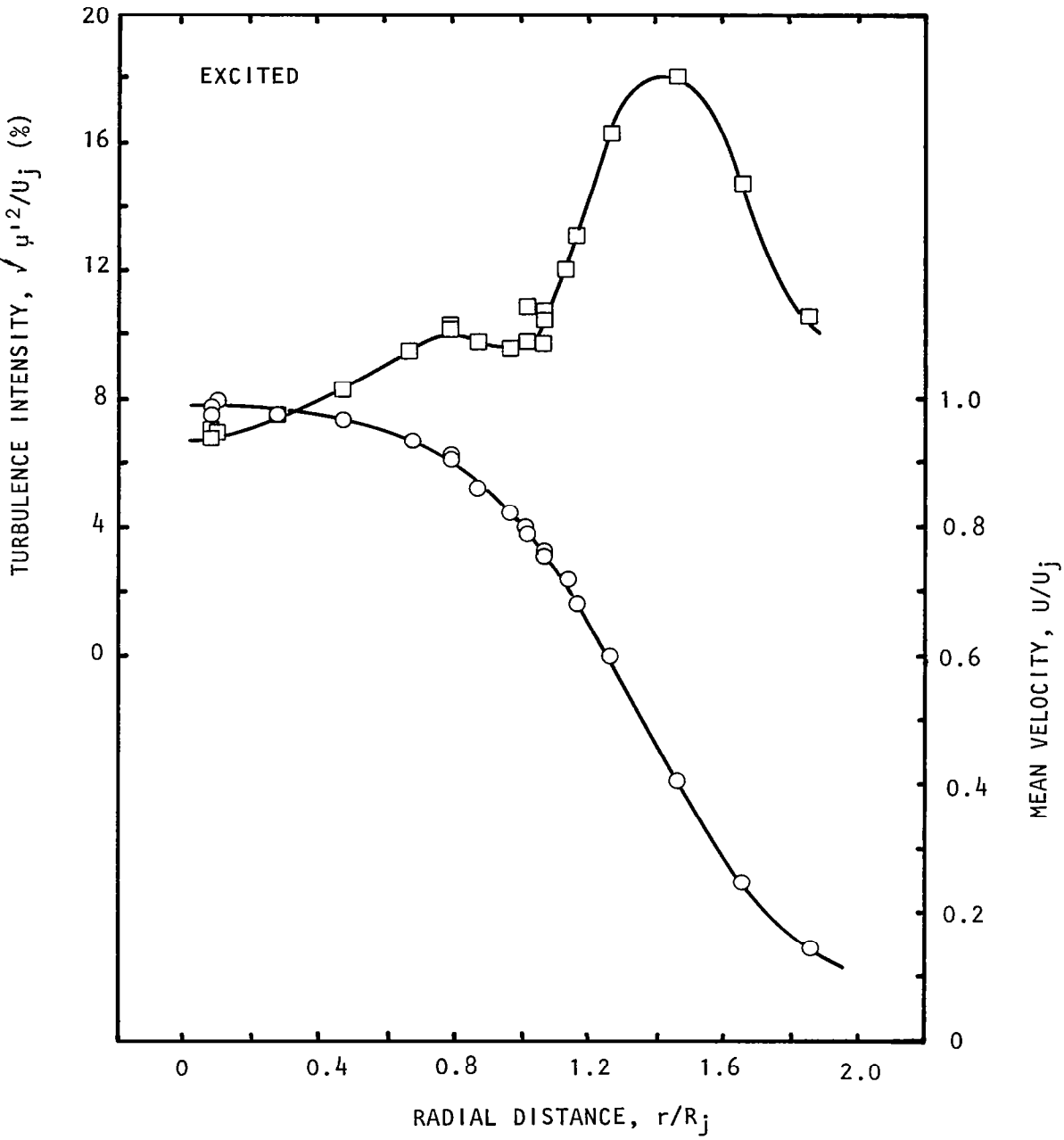

Figure D.2(b) Excitation effects on radial distribution of axial components of mean velocity (O) and turbulence intensity (□) at $x/D_j = 3$. $M_j = 0.58$, $U_j = 195$ m/s, Unheated, Static, $L_e = 141$ dB, $S_e = 0.5$.
(Also see figure 5.14)

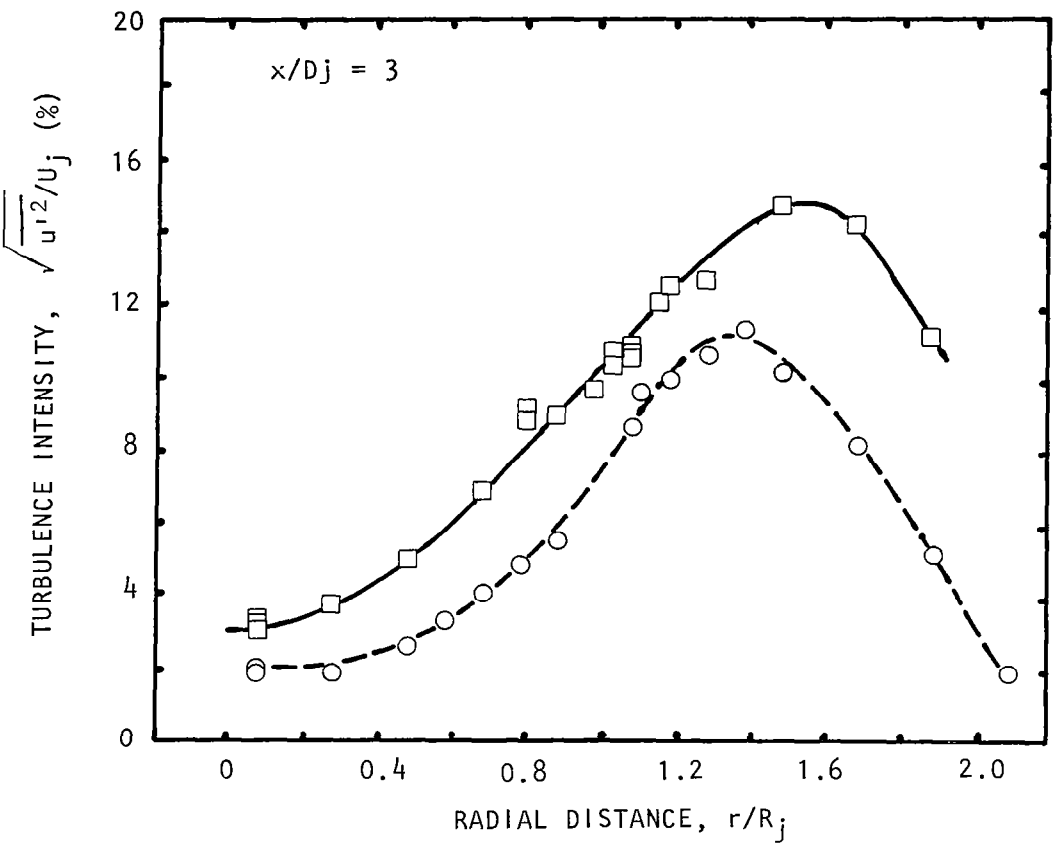

Figure D.3 Excitation effects on radial distribution of radial component of turbulence intensity at $x/D_j = 3$, $M_j = 0.58$, $U_j = 195$ m/s, Unheated, Static, $S_e = 0.5$, $L_e = 141$ dB, (0,0) Mode.
(○) Unexcited, (□) Excited
(Also see figure 5.16.)

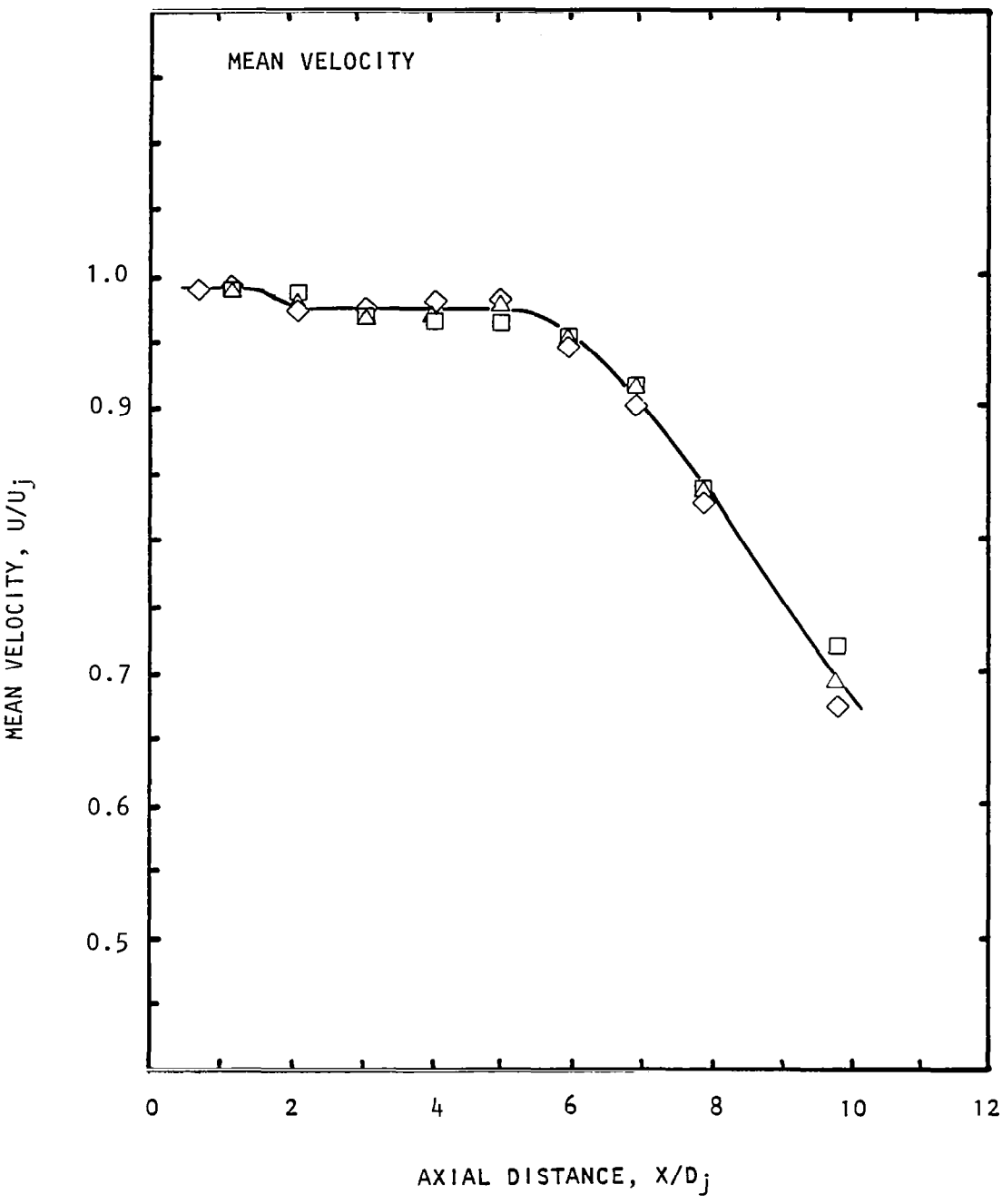

Figure D.4(a) Strouhal-number effects on centerline distribution.
M_j = 0.58, U_j = 195 m/s, Unheated, Static, L_e = 136 dB,
(0,0) Mode.
S_e: □ , 0.4; △ , 0.5; ◇ , 0.6.
(Also see figure 5.19.)

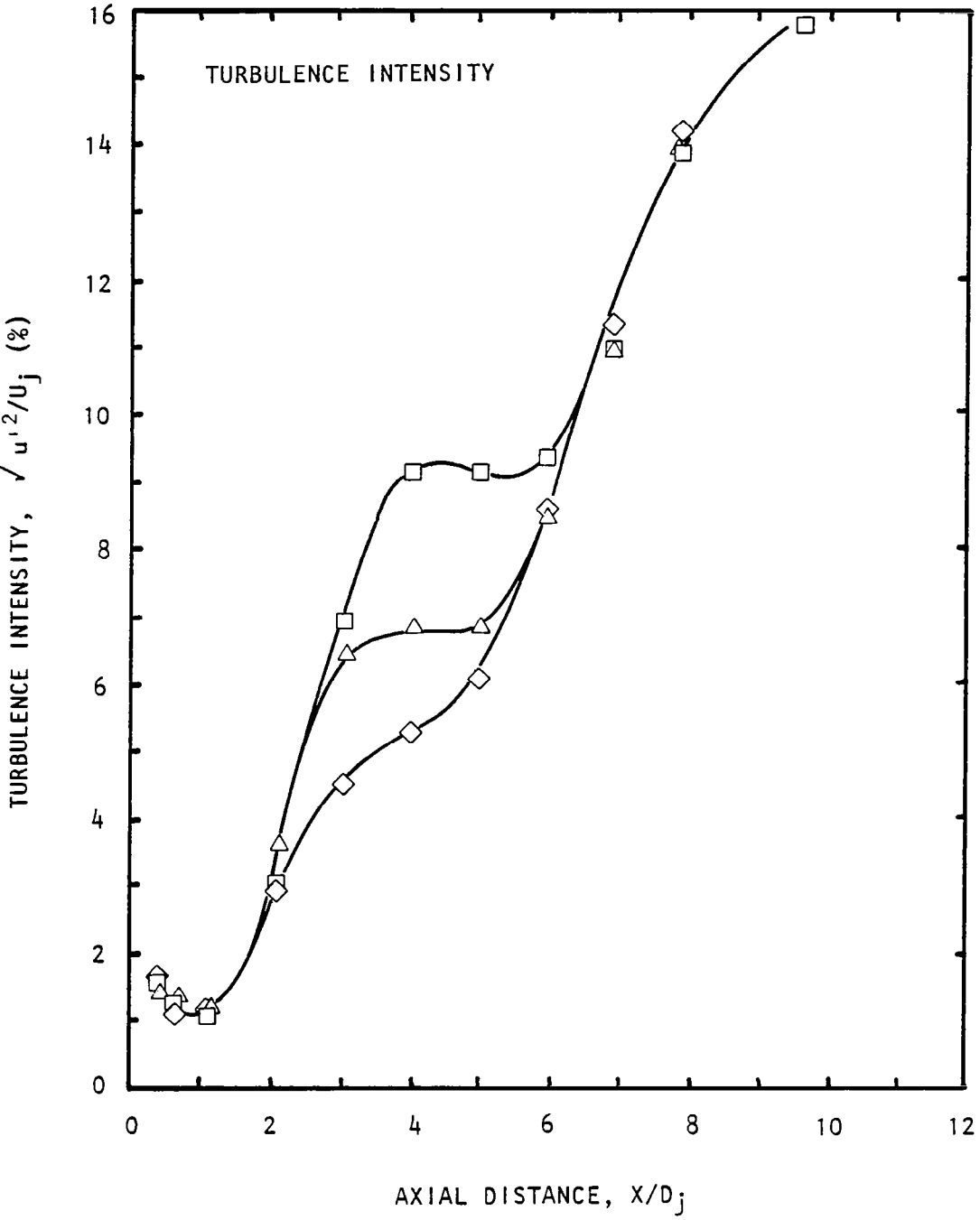

Figure D.4(b) Strouhal-number effects on centerline distributions.
M_j = 0.58, U_j = 195 m/s, Unheated, Static, L_e = 136 dB,
(0,0) Mode.
S_e: □, 0.4; △, 0.5; ◇, 0.6.
(Also see figure 5.19)

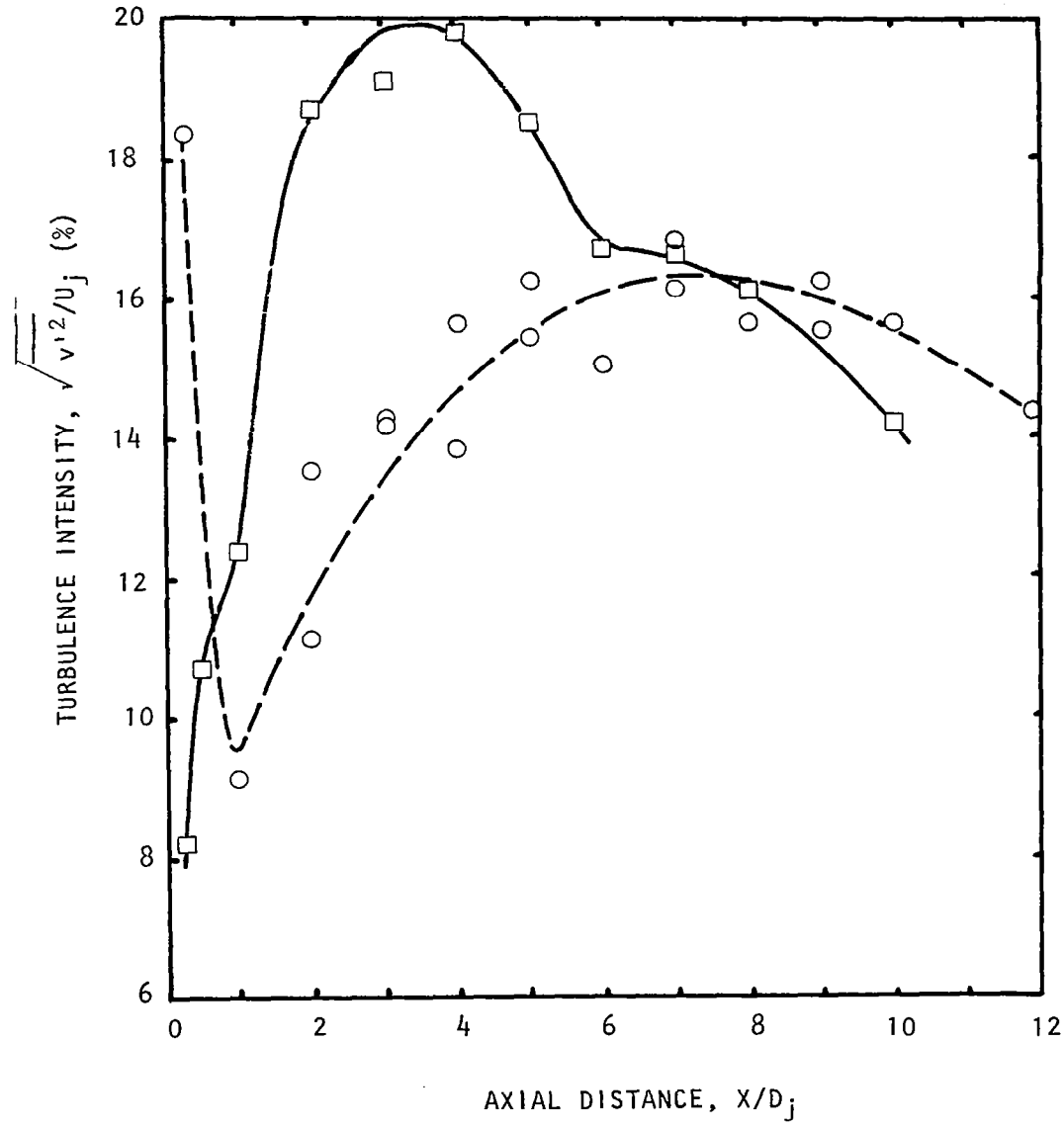

Figure D.5 Excitation-level effects on the lip-line distribution of turbulence intensities.
M_j = 0.58, U_j = 195 m/s, Unheated, Static,
S_e = 1.0, (1,0) Mode.
L_e: O, Unexcited; □ , 136 dB.
(Also see figure 5.26(b))

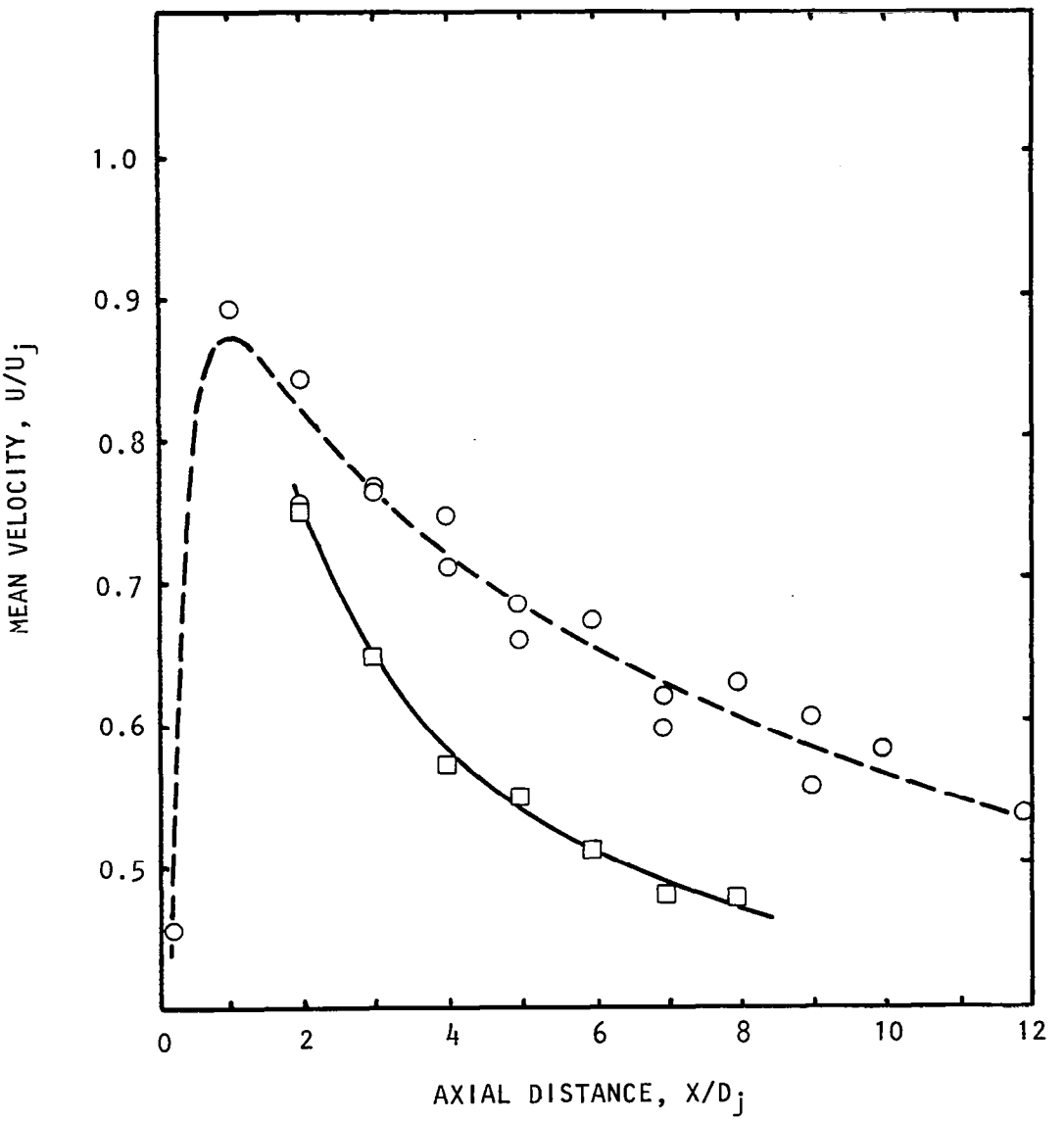

Figure D.6 Excitation-level effects on the lip-line distribution of mean velocities.
M_j = 0.58, U_j = 195 m/s, Unheated, Static,
S_e = 0.5, (0,0) Mode.
L_e: ○ , Unexcited; □ , 141 dB.
(Also see figure 5.27(a))

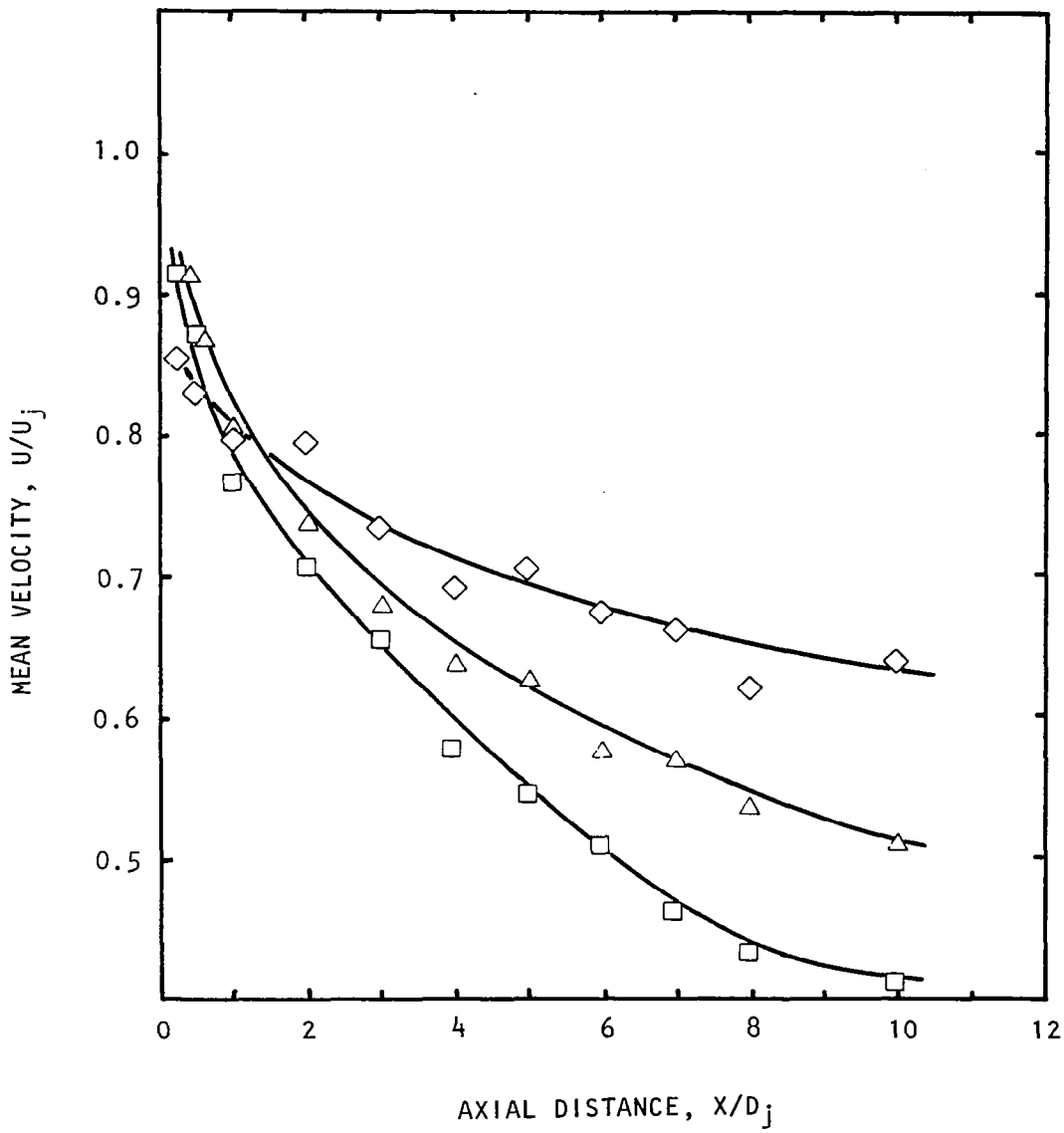

Figure D.7 Flight-velocity effects on lip-line distribution of mean velocities.
M_j = 0.58, U_j = 195 m/s, Unheated, Static,
L_e = 136 dB, S_e - 1.0, (1,0) Mode.
V_t: □ , 0 m/s; △ , 45 m/s; ◇ , 90 m/s.
(Also see figure 5.28(a)

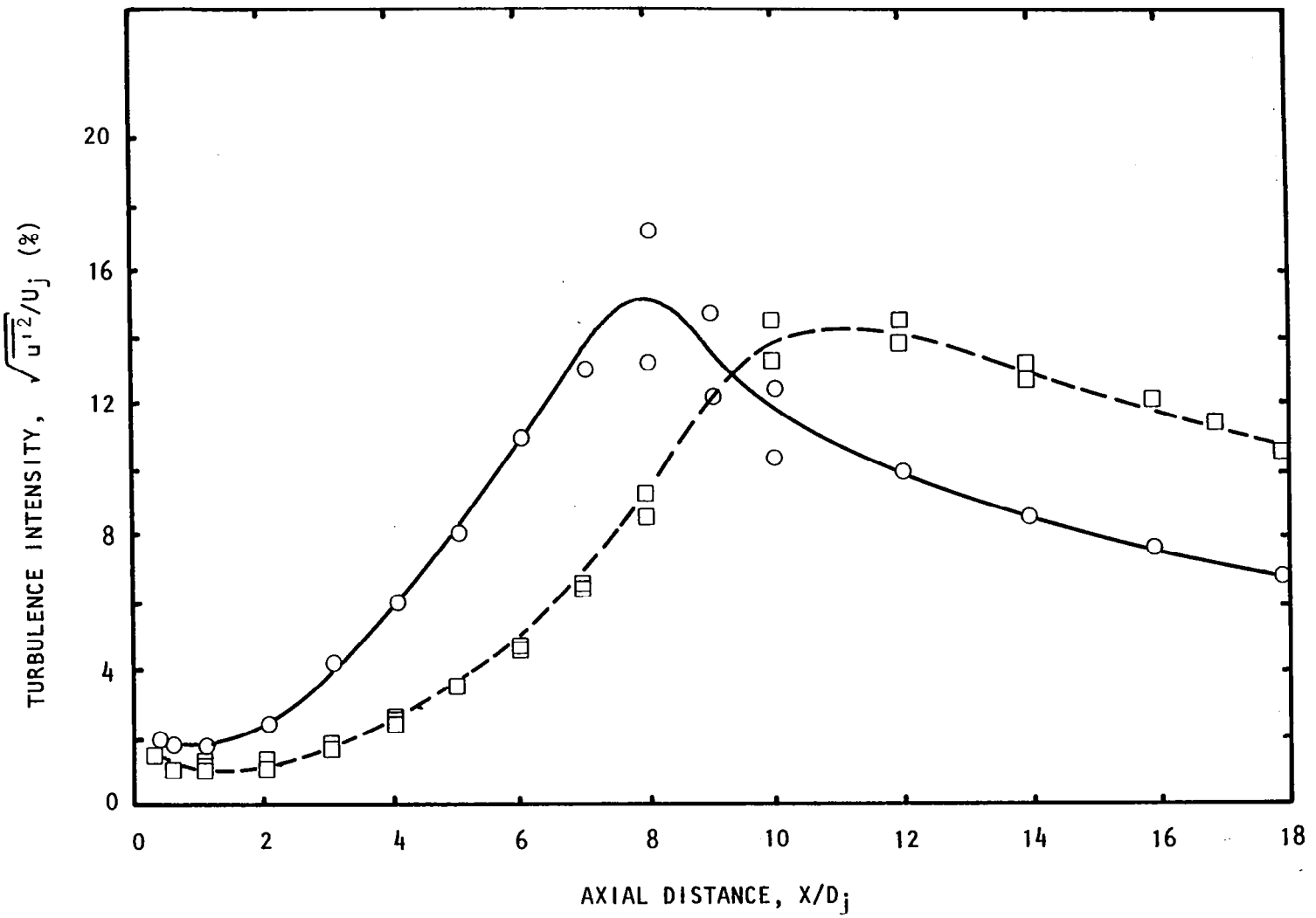

Figure D.8(a) Reservoir-temperature effects on centerline distribution of turbulence intensity.
M_j = 0.78, Static, Unexcited.
○ Heated (t_r = 800k), U_j = 428 m/s
□ , Unheated, U_j = 258 m/s
(Also see figure 5.39(a))

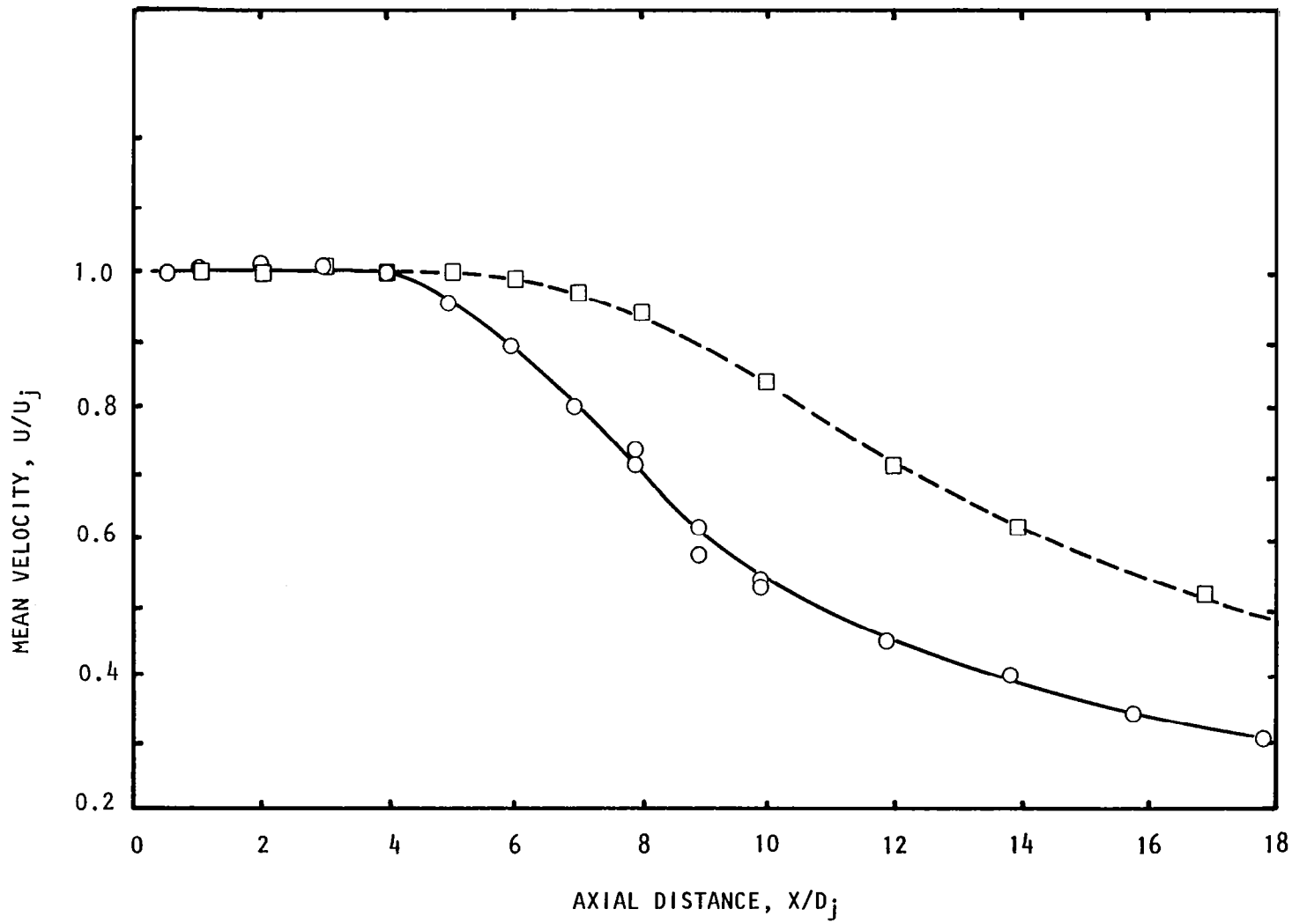

Figure D.8(b) Reservoir-temperature effects on centerline distribution of mean velocity.
M_j = 0.78, Static, Unexcited.
○ , Heated (t_r = 800k), U_j = 428 m/s
□ , Unheated, U_j = 258 m/s
(Also see figure 5.39(b))

APPENDIX E

LIST OF SYMBOLS

Symbols used in section 7.0 entitled "Theory and Comparison with Experiments" have been defined, where and as necessary, in the text itself. Only the symbols relevant to the rest of the report are therefore, being listed here.

b	half jet width
C_{ph}	phase velocity
D_j	jet-exit diameter
f_e	frequency of excitation
f_j	frequency in the jet noise spectra
k	wave number
L_e	level of excitation at the jet exit, in dB
M_j	fully expanded jet Mach number
M_t	flight or tunnel Mach number
P_o	ambient pressure
P_r	reservoir pressure
r	radial coordinate
R_j	jet exit radius
S_e	excitation Strouhal number, fD_j/U_j
t_o	ambient temperature
t_r	reservoir temperature

t_j	static temperature of the jet
U or u	mean velocity
U_j or u_j	jet exit velocity
u'	axial component of fluctuating velocity
u'_E	value of u' for excited conditions
u'_u	value of u' for unexcited conditions
$\tilde{u}$	instability-wave velocity
V_t	flight or tunnel velocity, m/s
v'	radial component of fluctuating velocity
x, X	axial distance from the nozzle-exit plane
x_c	length of the potential core
θ	emission angle with the downstream jet axis
ξ	jet operating pressure ratio, p_r/p_o
ϕ	phase

REFERENCES

1. Bushell, K. W.: A Survey of Low Velocity and Coaxial Jet Noise with Application to Prediction. *J. Sound and Vib.*, Vol. 46, 1971, pp. 477-500.

2. Ahuja, K. K.; and Bushell, K. W.: An Experimental Study of Subsonic Jet Noise and Comparison with Theory. *J. Sound and Vib.*, Vol. 30, No. 30, 1973, pp. 317-341.

3. Ahuja, K. K.; Tester, B. J.; and Tanna, H. K.: The Free Jet as a Simulator of Forward Velocity Effects on Jet Noise. NASA CR-3056, 1978.

4. Crow, S. C.; and Champagne, F. H.: Orderly Structures in Jet Turbulence. *J. Fluid Mech.*, Vol. 48, 1971, pp. 547-591.

5. Bechert, D.; and Pfizenmaier, E.: On the Amplification of Broadband Jet Noise by Pure Tone Excitation. *J. Sound and Vib.*, Vol. 43, 1975, pp. 581-587.

6. Moore, C. J.: The Role of Shear-Layer Instability Waves in Jet Exhaust Noise. *J. Fluid Mech.*, Vol. 80, 1977, pp. 321-367.

7. Deneuville, P.; and Jacques, J.: Jet Noise Amplification: A Practically Important Problem. AIAA Paper No. 77-1368, 1977.

8. Schmidt, C.: Aerodynamic Characterization of Excited Jets. *J. Sound and Vib.*, Vol. 61, 1978, pp. 148-152.

9. Jubelin, B.: New Experimental Studies on Jet Noise Amplification. AIAA Paper No. 80-0961, 1980.

10. Leconte, J.: On the Influence of Musical Sounds on the Flame of a Jet of Coal-Gas. *Phil. Mag.*, Vol. 15, 1858, pp. 235-239.

11. Tyndall, J.: On the Action of Sonorous Vibrations on Gaseous and Liquid Jets. *Phil. Mag.*, Vol. 33, 1867, pp. 375-391.

12. Tanna, H. K.; and Morris, P. J.: Inflight Simulation Experiments on Turbulent Jet Mixing Noise. *J. Sound and Vib.*, Vol. 53, pp. 389-405.

13. Ffowcs Williams, J. E.; and Kempton, A. J.: The Noise from the Large Structure of a Jet. *J. Fluid Mech.*, Vol. 84, 1978, pp. 673-694.

14. Morris, P. J.; and Tam, C.K.W.: Near and Far-Field Noise From Large-Scale Instabilities of Axisymmetric Jets. AIAA Paper No. 77-1351, 1977.

15. Reshotko, E.: Boundary Layer Instability and Transition. *Ann. Rev. Fluid Mech.*, Vol. 8, 1976, pp. 311-349.

16. Tam, C.K.W.: Excitation of Instability Waves in a Two-Dimensional Shear Layer by Sound. *J. Fluid Mech.*, Vol. 89, 1978, pp. 357-371.

17. Tam, C.K.W.; and Block, P.J.W.: On the Tones and Pressure Oscillations Induced by Flow Over Rectangular Cavities. *J. Fluid Mech.*, Vol. 89, 1978, pp. 373-399.

18. Tam, C.K.W.: The Excitation of Tollmien-Schlichting Waves in Low Subsonic Boundary Layers by Free Stream Sound Waves. *J. Fluid Mech.*, Vol. 109, 1981, pp. 483-501.

19. Shapiro, P.: The Influence of Sound Upon Laminar Boundary Layer Instability. Acoustics and Vibration Laboratory Report No. 83458-85560-1 (M.I.T.), 1977.

20. Kachanov, Y. S.; Kozlov, V. V.; and Levchenko, V. Y.: Experiments on the Generation of Tollmien-Schlichting Waves by External Disturbances. Physical Gas Dynamics (Aerophysical Investigations, Issue C), Collected Scientific Papers (In Russian), Institute of Theoretical and Applied Mechanics, Novosibirsk, 1976, pp. 96-99.

21. Ko, D.R.S.; Kubota, T.; and Lees, L.: Finite Disturbance Effect on the Stability of a Laminar Incompressible Wake Behind a Flat Plate. *J. Fluid Mech.*, Vol. 40, 1970, pp. 315-341.

22. Tam, C.K.W.: Supersonic Jet Noise Generated by Large-Scale Disturbances. *J. Sound and Vib.*, Vol. 38, 1975, pp. 51-79.

23. Chan, Y. Y.: Nonlinear Spatial Wave Development in an Axisymmetric Jet. Aero Report LR-585, National Research Council, Canada, National Aeronautical Establishment, 1975.

24. Liu, J.T.C.: Developing Large-Scale Wave-Like Eddies and the Near Noise Field. *J. Fluid Mech.*, Vol. 62, 1974, pp. 437-464.

25. Morris, P. J.: Flow Characteristics of the Large-Scale Wave-Like Structure of a Supersonic Round Jet. *J. Sound and Vib.*, Vol. 53, 1977, pp. 223-244.

26. Plumblee, Jr., H. E.: The Lockheed Laser Velocimeter. Appendix II of the Generation and Radiation of Supersonic Jet Noise, Volume I, Technical Report AFAPL-TR-76-65, 1976, pp. 107-124.

27. Plumblee, H. E.; Dean, P. D.; Wynne, G. A.; and Burrin, R. H.: Sound Propagation in and Radiation from Acoustically Lined Ducts: A Comparison of Experiment and Theory. NASA CR-2306, 1973.

28. Whiffen, M. C.; and Ahuja, K. K.: An Improved Schlieren System and Some New Results on Acoustically Excited Jets. *J. Sound and Vib.*, Submitted for publication, 1982.

29. Bechert, D.; and Pfizenmaier, E.: Optical Compensation Measurements on the Unsteady Exit Condition at a Nozzle Discharge Edge. *J. Fluid Mech.*, Vol. 71, 1975, pp. 123-144.

30. Morse, P. M.; and Ingard, K. U.: Theoretical Acoustics, *McGraw-Hill Book Co., Inc.*, 1968, pp. 467-607.

31. Plumblee, H. E.; Burrin, R. H.; Lau, J. C.; Morfey, C. L.; Morris, P. J.; Smith, D. M.; Tanna, H. K.; Tester, B. J.; and Whiffen, M. C.: Measurement of Turbulent Jet Structure, Ch. 6 of The Generation and Radiation of Supersonic Jet Noise, Volume II, Technical Report AFAPL-TR-76-65.

32. Ahuja, K. K.: Noise Studies of Cold and Heated Model Jets at Supersonic and High Subsonic Speeds with Particular Reference to Noise Reduction. Ph.D. Thesis, Mechanical Engrg., Syracuse University, June 1976.

33. Tam, C.K.W.: The Effects of Upstream Tones on the Large Scale Instability Waves and Noise of Jets. Mechanics of Sound Generation in Flows. ed. E. A. Muller. IUTAM/ICA/AIAA-Symposium, Göttingen, 1979, pp. 41-47.

34. Tam, C.K.W.; and Chen, K. C.: A Statistical Model of Turbulence in Two-Dimensional Mixing Layers. *J. Fluid Mech.*, Vol. 92, 1979, pp. 303-326.

35. Plaschko, P.: Stochastic Model Theory for Coherent Turbulent Structures in Circular Jets. *Phys. Fluids*, Vol. 24, 1981, pp. 187-193.

36. Lau, J. C.: Mach Number and Temperature Effects on Jets. AIAA Paper 78-1152, 1978.

37. Chan, Y. Y.: Spatial Waves in Turbulent Jets. *Phys. Fluids*, Vol. 17, 1974, pp. 46-53.

38. Tam, C.K.W.; and Morris, P.J.: The Radiation of Sound by the Instability Waves of a Compressible Plane Turbulent Shear Layer. *J. Fluid Mech.*, Vol. 98, 1980, pp. 349-381.

39. Hussain, A.K.M.F.; and Reynolds, W. C.: The Mechanics of an Organized Wave in Turbulent Shear Flow. *J. Fluid Mech.*, Vol. 41, 1970, pp. 241-258.

40. Launder, B. E.; Morse, A.; Rodi, W.; and Spalding, D. B.: Prediction of Free Shear Flows -- A Comparison of the Performance of Six Turbulent Models in Free Turbulent Shear Flows. NASA SP-321, 1973, pp. 361-422.

41. Bradshaw, P.: Compressible Turbulent Shear Layers. *Ann. Rev. Fluid Mech.*, Vol. 9, 1977, pp. 33-54.

42. Wiggnanski, I.; and Fiedler, H. E.: The Two-Dimensional Mixing Region. *J. Fluid Mech.*, Vol. 41, 1970, pp. 327-361.

43. Morris, P. J.: A Model for Broadband Jet Noise Amplification, AIAA Paper No. 80-1004, 1980.

44. Morris, P. J.: The Viscous Stability of Compressible Axisymmetric Jets. Submitted for publication to *AIAA Journal*, 1981.

45. Armstrong, R. R.: Influence of Mach Number on Coherent Structure Relevant to Jet Noise. *AIAA Journal*, Vol. 19, 1981, pp. 677-683.

46. Michalke, A.: Instabilitat Eines Kompressiblen Runden Freistrahls Unter Berücksichtigung des Einflusses der Strahlgrenzschichtdicke, *Z. Flugwiss*, Vol. 19, 1971, pp. 319-328.

47. Morris, P. J.: The Spatial Viscous Instability of Axisymmetric Jets. *J. Fluid Mech.*, Vol. 77, 1976, pp. 511-529.

48. Morris, P. J.: Effect of Forward Velocity on the Structure of a Turbulent Jet. Part 4 of Effects of Forward Velocity on Turbulent Jet Mixing Noise, Harry E. Plumblee, Jr., ed., NASA CR-2702, 1976.

1. Report No.	2. Government Accession No.	3. Recipient's Catalog No.
NASA CR-3538		

4. Title and Subtitle	5. Report Date
TONE-EXCITED JET - THEORY AND EXPERIMENTS	November 1982
	6. Performing Organization Code

7. Author(s)	8. Performing Organization Report No.
K. K. Ahuja, J. Lepicovsky, C. K. W. Tam, P. J. Morris, and R. H. Burrin	LG82ER0031
	10. Work Unit No.

9. Performing Organization Name and Address	11. Contract or Grant No.
Lockheed-Georgia Company Dept. 72-74, Zone 403 Marietta, Georgia 30066	NAS3-21987
	13. Type of Report and Period Covered
12. Sponsoring Agency Name and Address	Contractor Report
National Aeronautics and Space Adminstration Washington, D. C. 20546	14. Sponsoring Agency Code 505-32-02 (E-1174)

15. Supplementary Notes

Final report. Project Manager. Allen M. Karchmer, Fluid Mechanics and Acoustics Division, NASA Lewis Research Center, Cleveland, Ohio 44135. K.K. Ahuja and J. Lepicovsky, Lockheed-Georgia Company, Marietta, Georgia 30066; C. K. W. Tam, The Florida State University, Tallahassee, Florida 32306; P.J. Morris, Pennsylvania State University, University Park, Pennsylvania 16802; and R.H. Burrin, Lockheed-Georgia Company, Marietta, Georgia 30066.

16. Abstract

A detailed study to understand the phenomenon of broadband jet-noise amplification produced by upstream discrete-tone sound excitation has been carried out. This has been achieved by simultaneous acquisition of the acoustic, mean velocity, turbulence intensities, and instability-wave pressure data. A 5.08-cm diameter jet has been tested for this purpose under static and also flight-simulation conditions. An open-jet wind tunnel has been used to simulate the flight effects. Limited data on heated jets have also been obtained. To improve the physical understanding of the flow modifications, brought about by the upstream discrete-tone excitation, ensemble-averaged schlieren photographs of the jets have also been taken. Parallel to the experimental study, a mathematical model of the processes that lead to broadband-noise amplification by upstream tones has been developed. Excitation of large-scale turbulence by upstream tones is first calculated. A model to predict the changes in small-scale turbulence is then developed. By numerically integrating the resultant set of equations, the enhanced small-scale turbulence distribution in a jet under various excitation conditions is obtained. The resulting changes in small-scale turbulence have been attributed to broadband amplification of jet noise. Excellent agreement has been found between the theory and the experiments. It has also shown that the relative velocity effects are the same for the excited and the unexcited jets.

17. Key Words (Suggested by Author(s))	18. Distribution Statement
Jet noise; Broadband jet noise amplification; Large scale turbulence; Instability waves; Small scale turbulence; Discrete tone excitation; Flight effects on jet flow and noise; Receptivity; Time-averaged Schlieren photography	Unclassified - unlimited STAR Category 71

19. Security Classif. (of this report)	20. Security Classif. (of this page)	21. No. of Pages	22. Price*
Unclassified	Unclassified	243	All

* For sale by the National Technical Information Service, Springfield, Virginia 22161

NASA-Langley, 1982